Numerical simulation and experimental investigation of the forming of tailored fibre placement preforms : a mixed embedded-ALE finite element formulation

Jessy Simon

CENTRALE NANTES

THESE DE DOCTORAT DE

L'ÉCOLE CENTRALE DE NANTES

ECOLE DOCTORALE N° 602
Sciences pour l'Ingénieur
Spécialité : **Mécanique des solides, des matériaux, des structures et des surfaces**

Par
Jessy SIMON

Numerical Simulation and Experimental Investigation of the Forming of Tailored Fibre Placement Preforms: a Mixed Embedded-ALE Finite Element Formulation

Thèse présentée et soutenue à l'Ecole Centrale de Nantes le 9 juin 2022
Unité de recherche : UMR 6183, Institut de Recherche en Génie Civil et Mécanique (GeM)

Rapporteurs avant soutenance :

Marie-Ange BUENO Professeure des Universités, ENSISA, Mulhouse
Michael SUTCLIFFE Professeur, Cambridge University, U.K.

Composition du Jury :

Président : Damien SOULAT Professeur des universités, ENSAIT, Roubaix

Examinateur : Jonathan P BELNOUE Maître de conférences, Bristol University, U.K.

Dir. de thèse : Christophe BINETRUY Professeur des universités, Ecole Centrale de Nantes
Co-dir. de thèse : Nahiene HAMILA Professeur des universités, ENI Brest
Co-encadrant : Sébastien COMAS-CARDONA Professeur des universités, Ecole Centrale de Nantes

Invité

Benjamin MASSETEAU Ingénieur de recherche, IRT Jules Verne, Bouguenais

Acknowledgments

First and foremost, I would like to express my deepest gratitude to my supervisors, Prof. Christophe Binétruy, Prof. Nahiene Hamila and Prof. Sébastien Comas-Cardona for their invaluable advice and continuous support. The intellectually stimulating work environment they built naturally instilled in me a passion for academic research. I also could not have undertaken this journey without my defense committee, who generously provided knowledge and expertise as well as an important acknowledgement of the work carried out. I am also thankful to IRT Jules Verne and to the Research Institute in Civil and Mechanical Engineering (GeM) who financed my research. In particular, I would like to offer my special thanks to Dr. Benjamin Masseteau and M. Jean-Michel Lebrun for their technical support.

I would like to thank my friends, lab mates, colleagues and research team for a cherished time spent together in the lab, and in social settings. It is their kind help and support that have made my study and life in Nantes a wonderful time.

Finally, I would like to express my gratitude to my parents and Lénaïg for their love and support. Without their tremendous understanding and encouragement in the past few years, it would be impossible for me to complete my study. Make my parents proud has always been a major source of motivation for me.

Introduction

Manufacturing parts in an environmentally sustainable way is the challenge aeronautics, automotive and energy industries are facing with today. Increasing the stiffness-to-weight ratio of parts and reducing material wastage while maintaining highly competitive manufacturing process is a permanent issue for these industries. Fibre-reinforced composite materials have been widely developed to tackle this challenge over the past decades. Unidirectional plies stacked together to produce laminates or conventional textiles made by weaving, stitching or knitting allow manufacturing parts with improved stiffness-to-weight ratio compared to their metallic counter parts. However, with the emergence of additive manufacturing, topologically optimized metallic structures have become very attractive for the industry by providing a higher degree of design freedom. To further enhance topologically optimized structures, additive manufacturing of continuous fibre-reinforced composites has also been developed. It allows manufacturing parts having both optimized topology and material orientations, which again increases the stiffness-to-weight ratio compared to metallic parts made by additive manufacturing.

Generally, additive manufacturing of continuous fibre-reinforced composites consists in depositing fibres only where needed (or desired) with the possibility to prescribe curvilinear paths. There is a growing interest in these technologies due to the constant progress made in improving productivity and design complexity. Manufacturing processes falling into this class differ from the way they mix the fibres and the matrix as well as the deposition strategy. Continuous Filament Fabrication (CFF) technologies consist in depositing fibre tows which are pre-impregnated or in-situ-impregnated. Automated Fibre Placement (AFP), Continuous Tow Shearing (CTS) and Tailored Fibre Placement (TFP) can also be classified as additive manufacturing technologies. They differ from (CFF) by the width of deposited material. As AFP, CFF can directly manufacture 3D parts. However, depositing fibres directly on complex doubly-curved parts without defects can be challenging for these technologies. Another solution to manufacture 3D parts consists in a two-step approach where a flat preform is firstly produced before being transformed into a 3D shape via forming. This solution enables lowering cost-production and reduce defects. Forming of fibrous reinforcements is a widely used process to manufacture 3D shell-like composite parts. This process has been widely studied by the scientific community in case of conventional textiles. However, the forming of fibre-steered flat preforms received relatively little attention compared to conventional textiles. Since fibre steered preforms are more likely to provide a better mechanical solution, investigating the forming of such preforms is a necessary step to proposed a reliable manufacturing solution of optimised 3D shell-like composite part from flat fibre-steered preforms.

In this thesis, a hybrid solution combining the TFP technology and forming to manufacture highly doubly-curved parts is proposed. The main objective of this work consists in developing a numerical tool to predict the forming of flat TFP preforms. To validate this tool, full-scale simulations of complex doubly-curved part along with their experimental forming are addressed.

Since the TFP technology received little attention from the scientific community, this work also aims at demonstrating the ability of the proposed hybrid solution to manufacture complex parts with optimal final fibre orientations. This work was funded by IRT Jules Verne as part of the Ph.D program PERFORM.

This thesis starts by an introductory chapter which gives the necessary background to understand the challenges of the forming of fibrous reinforcements in general. It first introduces forming of conventional textiles before focusing on fibre-steered technologies, and in particular, the TFP technology. It highlights the capabilities of this technology as well as the missing numerical tools to fully leverage its potential. It ends with the objectives and outline of this work. The second chapter presents the modelling strategy adopted to address the forming of flat TFP preforms. The latter is based on the Finite Element Method (FEM) and uses the embedded element approach which assumes no-slip between the preform's constituents. The formulation, implementation and numerical validation of the modelling features are described. The next chapter aims at validating the proposed modelling approach. To this end, two full-scale simulations along with their experimental counter-parts are performed. They consists in the forming of both hemisphere and tetrahedral parts from flat TFP preforms especially designed to obtained orthotropic final orientations. The last chapter enhanced the proposed modelling strategy with a mixed embedded-ALE (Arbitrary Eulerian-Lagrangian) formulation. It allows to model fibre slippage in the TFP preform without modifying the initial ingredients of the modelling approach. In particular, pull-out experiments are carried out to characterize the friction behaviour.

Contents

List of Figures

List of Tables

List of source codes

Chapter 1

Forming of continuous fibre-reinforced composite materials : From regular fabrics to fibre-steered preforms

Abstract

This introductory chapter begins with a general definition of composite materials before focusing on continuous fibre-reinforced composites which is the class of composite materials this study is concerned with. The forming processes used to manufacture 3D parts from flat continuous reinforcements are presented as well as some conventional textiles which have been widely studied over the last decades. Section 1.2 is an insight of the experimental aspects and the different modelling strategies developed so far in conventional textiles' forming as well as their limitations for manufacturing optimized 3D parts. Although conventional textiles are not the subject of this study, this section provides the necessary background for understanding the issues and challenges in forming. Besides, it gives a general overview for the modelling strategy developed in chapter 2. In section 1.3, after highlighting the limitations of regular fabrics to form optimized complex shapes, fibre placement technologies allowing manufacturing optimised fibre-steered preforms are presented. Existing fibre placement technologies are reviewed in particular the Tailored Fibre Placement (TFP) technology which is the one of interest in this thesis. Section 1.4 focuses on the TFP technology. A detailed presentation of the preforming tool is followed by a review of the main applications studied so far to benefit from the high degree of design freedom offered by the TFP technology in case of 2D parts manufacturing. Finally the last section (section 1.5) presents challenges to be addressed to manufacture optimized 3D composite parts through the forming of flat TFP preforms. The introductory chapter ends with the presentation of the objectives and the outline of this thesis.

Contents

1.1 Introduction to continuous fibre-reinforced composite materials and forming

Introduction

This first section of the introductory chapter presents the general background of the study. It begins by defining composite materials before introducing continuous fibre-reinforced composites which are the ones discussed in this study. Next, some of the conventional fibrous reinforcements most commonly used in the composite industry are presented before describing some forming processes that allow 3D composite parts to be manufactured from flat fibrous reinforcements.

1.1.1 Composite materials

1.1.1.1 General definition

Manufacturing light, high performance and low-cost parts is one of the main interest of industries such as aerospace, automotive or energy industry. In this sense, composite materials have been largely developed over the last decades since they offer specific properties higher than their metallic counterparts.

Composite materials are formed by combining two or more materials which exhibit different properties. By mixing different material, properties can be achieved that none of the raw materials has on its own. It is an heterogeneous material since its constituents do not dissolve or blend with each other. Concrete which is basically made of cement, stones, sand and water is perhaps the best-known man-made example of what composite materials are. Concrete is obtained by adding water to cement to form a paste that encapsulates the stones, sand and possibly reinforcement steel. Each constituent has a special function in the final material. Binding and reinforcing are the two main functionalities. The constituent which binds the

reinforcements together is defined as the matrix. Composite materials properties depends on the intrinsic properties of the constituents as well as the interactions they create when mixed together. The final properties also depend strongly on the processes used to form them.

In short, a composite material consists of a binder (the matrix) which surrounds a stronger material (the reinforcement). Depending on the desired properties, other materials can be added to modify properties such as electrical or thermal conductivity for example.

1.1.1.2 Classification of composites: Polymer Matrix Composites

Many composite materials have been developed or naturally exist such as wood. Engineered composite materials can be classified into three main categories depending on the type of matrix used which are Metal Matrix Composites (MMC), Ceramic Matrix Composites (CMC) and Polymer Matrix Composites (PMC). This thesis focuses on PMC and more specifically on composites made of polymer composites and called fibre-reinforced composites.

Two classes of polymer matrix exist. Thermoset polymers are liquid and need to be polymerized with heat to become permanently rigid so that they cannot soften under high temperatures whereas thermoplastics can be reversibly processed to become rigid at low temperatures or soften at high temperatures. The reversibility of the process confers better recycling properties to thermoplastic polymer composites. Fibres can be synthetic materials such as carbon and glass which offer higher mechanical properties or natural fibres such as flax and hemp which increase the recyclability of the composites when combined with thermoplastics.

1.1.1.3 Fibre-reinforced composites

Fibre-reinforced composites differs from the nature of polymer and fibre materials used but also from the length of the fibres. On one hand, discontinuous fibre composite are made of short or long fibres, i.e. from 1 mm to several centimetres. Sheet moulding compounds (SMCs) is a class of low-cost chopped fibre composites intensively used by the automotive industry since it provides moderate mechanical properties with very high production rates and the ability to form complex shapes. Discontinuous fibre-reinforced composites mostly exhibit nearly isotropic properties in case of randomly distributed orientations. Fibre distribution and orientations strongly influence the final mechanical properties of the part Fu (1996). On the other hand, continuous fibre-reinforced composites involve fibres as long as the part itself i.e. up to several meters. The orientation distribution generally leads to one or more preferential directions leading to highly anisotropic properties. Thousands of fibres can be assembled to form tows. Fig. 1.1 shows schematic representations of short and continuous fibre-reinforced composite materials. Discontinuous fibre-reinforced composites made of short fibres have better formability than continuous fibre-reinforced composites and are therefore used for highly non-developable 3D parts.

Transition

This study focuses on continuous fibre-reinforced composites. The following section presents some of the conventional fibrous reinforcements most commonly used in the composite industry.

1.1.2 Conventional textiles

Conventional textiles are continuous fibre reinforcements which either have a well-defined structure or consist of an arbitrary arrangement of fibres. Fig. 1.3 shows the different material scales of a composite part made from a conventional textiles. This type of fibrous reinforcement is made of continuous fibre tows whose cohesion is ensured by its internal geometry. Weaving,

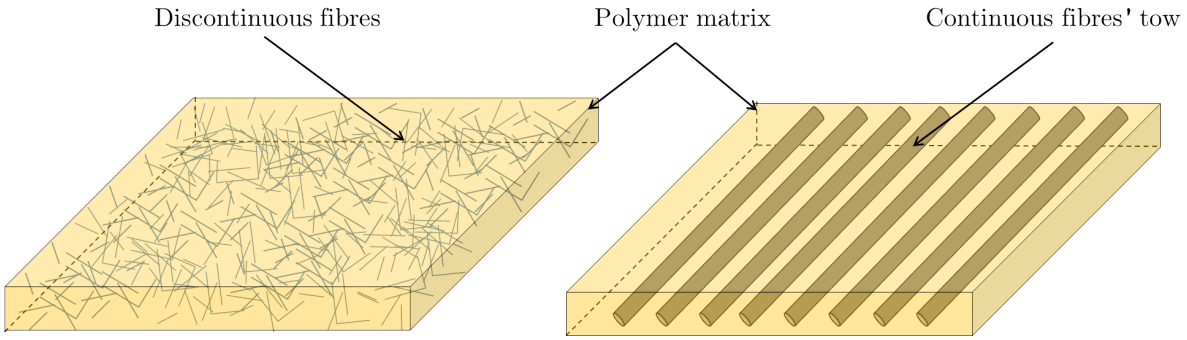

Figure 1.1: Discontinuous fibre-reinforced composites (left) vs continuous fibre-reinforced composites (right)

knitting, braiding or stitching are the main methods for assembling fibre tows. Due to its architecture, this type of reinforcement contains one to three main fibre orientations in its initial state. Since fibre tows are quasi-inextensible, the fabric deformation is nearly null in these directions. Fig. 1.2 from Akkerman and Haanappel (2015) shows different type of structured reinforcements as well as two non-structured reinforcements (chopped strand mat and continuous filament mat).

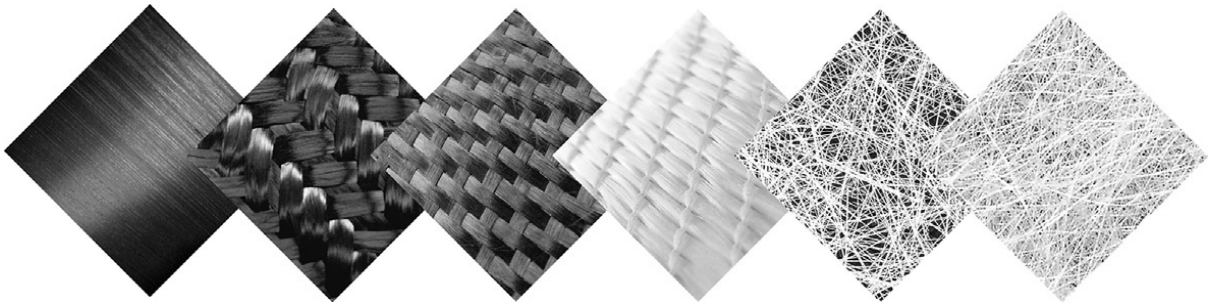

Figure 1.2: Various reinforcements in polymer composites. From left to right: unidirectional ply, triaxial braided fabric, biaxial woven fabric, stitched or noncrimp fabric, chopped strand mat, continuous filament mat. (Akkerman and Haanappel, 2015)

1.1.2.1 Unidirectional reinforcements

A first method to create a reinforcement is to form a layer containing continuous fibres aligned in a single orientation which are called unidirectional reinforcement (UD). However, fibres only exhibit high resistance when loaded in that direction. Consequently, manufacturing a part by stacking UD layers oriented in the same orientation would give very weak transversal properties and an early failure of the matrix would occur in the transverse direction. UD layers of different orientations are stacked to create a composite part able to resist complex loading paths (Fig. 1.4). The resulting composite laminate's properties strongly depend on the different orientations as well as the stacking sequence whose unbalance and asymmetry can lead to desired or undesired couplings between the different deformation modes like between tension and bending. A laminate usually contains from ten to one hundred layers to obtain the required properties and part thickness.

1.1.2.2 Non-crimp fabrics

Non-crimp fabrics (NCF) are made of multiple unidirectional plies stitched together with through-thickness stitching yarn. This reinforcement was developed to increase the in-plane

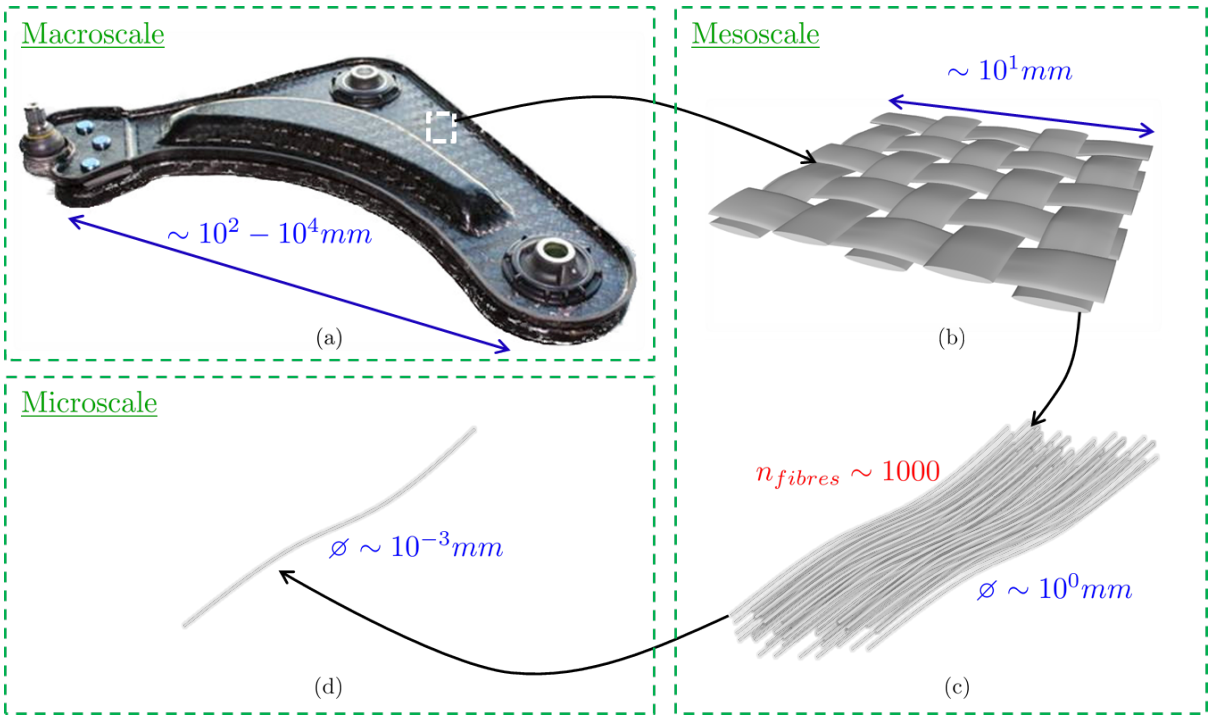

Figure 1.3: Material scales in a composite part: (a) A fibre-reinforced composite part (Guillon et al., 2016) (b) made from a fibrous reinforcement (c) obtained by assembling fibre tows (d) containing thousands of fibres

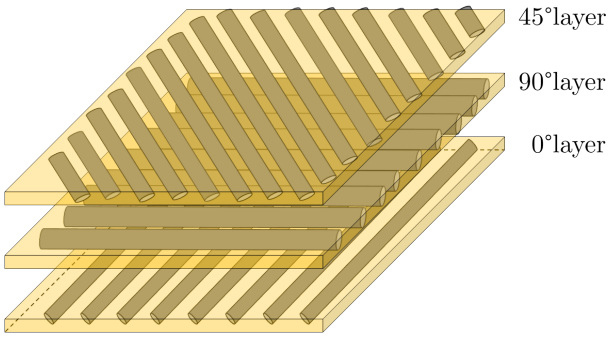

Figure 1.4: Stacking of unidirectional layers (UD laminate)

tensile stiffness of composites and to improve formability compared to UDs thanks to the stitching which bonds the layers together and reduces wrinkling defects. However, the stitching yarn leads to other defects. Different stitching points like chain stitch and tricot stitch can be used for layer's assembling. Fig. 1.5 shows a numerical model of the internal geometry of 0/90° chain stitched NCF created using TexGen (Brown and Long (2021)). The resulting internal structure can be either formed of several plies with well-separated tows or with the stitching yarn penetrating the tows.

1.1.2.3 Woven fabrics

In 2D or 3D woven fabrics, the cohesion is ensured by the interactions between adjacent and crossing fibre tows which depends on the weaving pattern. 2D woven fabrics are made by interweaving two networks of tows called weft and warp directions. 3D woven fabrics can be seen as an extension of 2D woven fabrics to the through-the-thickness dimension in which warp and weft yarns intertwine through several layers. Fig. 1.6 shows different weaving patterns for 2D and

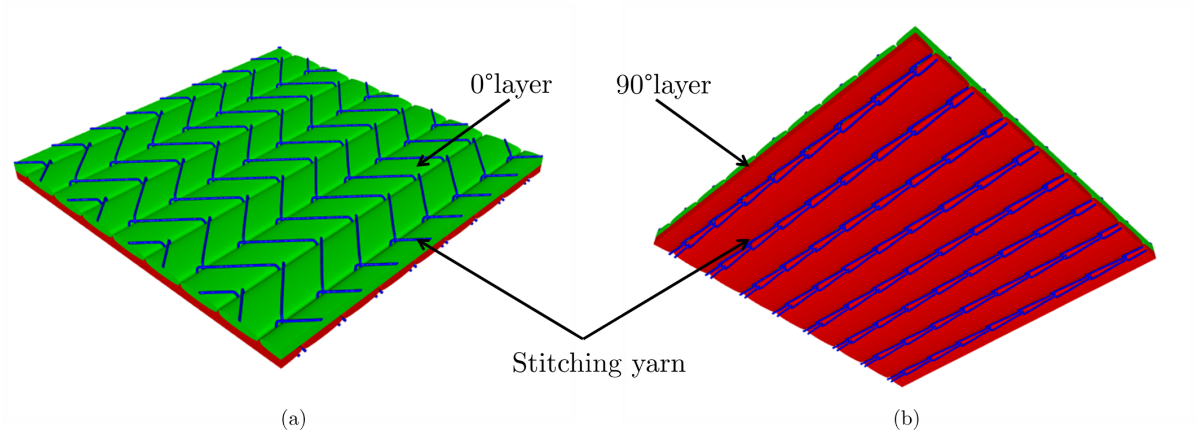

Figure 1.5: Internal geometry of a 2 layer chain stitched NCF : (a) top view and (b) bottom view

3D woven fabrics. Due to the weaving, fibre tows are undulated compared to UDs or NCF. This crimp has been shown to have a negative impact on the mechanical properties of the final part (Lomov and Verpoest, 2005; Hivet and Boisse, 2008). 3D woven fabrics allow manufacturing thick parts with better resistance to delamination compared to parts manufactured with 2D woven fabric layers, which is a required property for blade rotor in jet aircraft engine for instance.

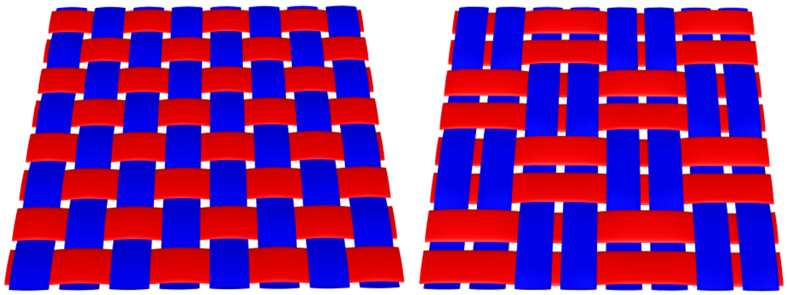

(a) 2D weaves: Plain weave (left) and 2x2 twill weave (right)

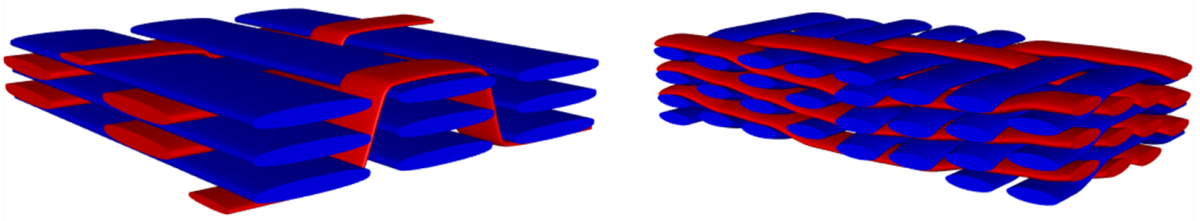

(b) 3D weaves: Orthogonal weave (left) and angle interlock weave (right)

Figure 1.6: 2D and 3D weaving pattern examples

Knitted fabrics

Knitted reinforcement is a technical textile used in parts like elastomeric hoses in the automotive industry which require large deformation ability. Several knitting patterns exists. Fig. 1.7 shows the internal geometry of a plain knit.

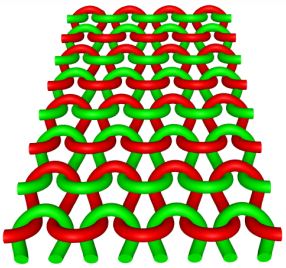

Figure 1.7: Internal geometry of a plain knit

Transition

Conventional textiles encompass a broad category of fibrous reinforcement. To manufacture 3D continuous fibre-reinforced composites from flat fibrous reinforcements, several forming processes exist and differ according to the nature of the polymer and the nature of the fibrous reinforcements.

1.1.3 Forming processes

1.1.3.1 General principle

Many processes exist to form fibre-reinforced composites. This study focuses on forming processes allowing manufacturing 3D parts from initial flat fibrous reinforcements. The manufacturing of 3D fibre-reinforced composite parts is composed of three major steps which are executed in different order depending on the involved process.

One of these steps is the mixing of the fibrous reinforcement with the polymer matrix and is called impregnation. During this step, a liquid thermosetting polymer or melted thermoplastic polymer flows within the reinforcement. Another step consists in transforming the flat reinforcement into a 3D surface and is generally named draping or forming. Finally, the last step is the consolidation phase which removes residual porosities and allows obtaining the final thickness and fibre content, followed by the solidification of the polymer matrix by crystallisation for thermoplastics and by polymerization for thermoset resins. Concerning the relative order of the impregnation and draping phases, if the impregnation phase is performed first, the fibrous reinforcement which already contains the polymer before being draped is named pre-impregnated reinforcement (prepregs). After draping, an additional impregnation phase can be necessary depending on the type of prepregs.

The forming process used depends on the nature of the fibrous reinforcement and the polymer matrix. They can be subdivided into processes for thermosetting polymers and those for thermoplastic polymers. The following briefly presents some of these forming processes.

1.1.3.2 Thermosetting processes

Hand lay-up of thermoset composites consists in manually placing the reinforcement layer on a mould surface where a release agent has been applied before. Then the liquid resin is applied on the reinforcement or the layer can be wet before being draped. This operation is repeated for each layer constituting the part and the resin is then cured at ambient or elevated temperature to consolidate the part. Vacuum bagging also consists in manually placing reinforcement layers on a open mould. If pre-impregnated layers are used, once vacuum bagged, the mould is placed inside an autoclave or oven where heat and pressure are applied for consolidation. For non-impregnated layers, the resin is injected under pressure into the bag before curing. Hand lay-up

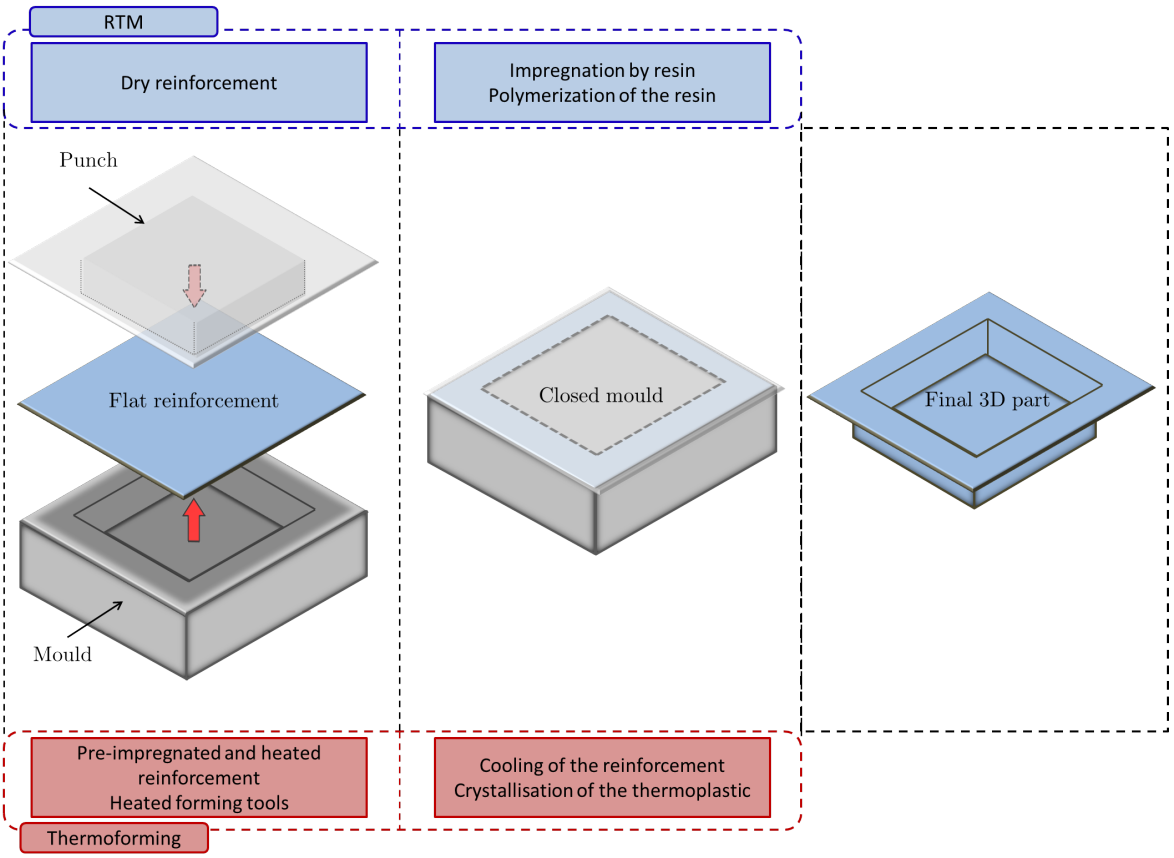

Figure 1.8: Forming process: (a) Mould closing to conform the reinforcement to the mould surface, (b) consolidation phase (or impregnation for RTM), (c) release of the final part

is a time-consuming operation and depends on the operator.

Resin transfer moulding (RTM) (Fig. 1.8) is a 2-step process which consists in forming fibrous reinforcements in a matched die mould to manufacture the fibrous preform. The fibrous preform is transferred into the injection tooling, where the thermoset resin is injected under low pressure and low temperature. The resin flows within the reinforcement and is finally cured to obtain a rigid part.

1.1.3.3 Thermoplastic processes

Hand lay-up of thermoplastic fibre-reinforced composites is also possible using prepregs which are vacuum bagged after draping before being placed in an autoclave for consolidation.

Thermoforming (Fig. 1.8) starts with a heating phase allowing decreasing the matrix stiffness in the prepreg reinforcements before being formed inside a pre-heated mould and then cooled to become rigid.

Conclusion

Composite materials are formed by combining two or more materials which exhibit different but complementary properties. Among them, those combining a polymer matrix with continuous reinforcing fibres are particularly well suited for structural engineering applications. Thermosetting or thermoplastic polymers together with synthetic continuous fibres are largely used and developed in the composite industry. Continuous fibres gathered into tows can then be assembled by weaving, stitching or knitting to form complex conventional textiles used in forming applications. To manufacture 3D shell-like structures using continuous fibres, the forming process combined to impregnation of the fibres by the polymer, consolidation and solidification of the polymer consists in transforming a initially flat fibrous reinforcement into a 3D structure. The next section will present some aspects and challenges in the numerical modelling and experimental characterisation of this type of continuous fibre reinforcements.

1.2 Forming: features and challenges in numerical modelling and experimental characterisation of conventional textiles

Introduction

This second section of the introductory chapter aims at highlighting the main concepts developed and used in the field of conventional textile forming. It gives a general overview of the modelling strategies adopted in previous works. More details are available in the following reviews (Pickett et al., 2005; Gereke et al., 2013a). This section begins with a description of the fabric kinematics and forming defects a model has to provide information about. To this end, deformation mechanisms in 2D woven fabrics, NCF or 3D interlocks are first analysed. Then, some models are described and compared according to the way they represent the fabric as well as the analysis scale they used. In the latter, a distinction between continuous and discrete models is done before presenting a class of model which takes benefits from both, namely, semi-discrete models. Afterwards, some methods to characterize their mechanical properties which are required in the numerical models are described.

1.2.1 Fabrics kinematics, process-induced defects and their treatments

1.2.1.1 Kinematics

Modelling the forming of fabrics requires knowing the deformation mechanisms a fabric can undergo. 2D woven fabrics, NCF and 3D interlocks are made of a specific arrangement of unidirectional fibre tows as shown in the previous section. Obviously, the deformation mechanisms occurring in fabrics are directly related to their internal geometry. In such fibrous structures, interactions between constituents are numerous and sometimes challenging to integrate in a numerically efficient model. The typical interactions or deformation mechanisms are listed hereafter for fabrics with some of them specific to stitched fabrics and illustrated in Fig. 1.9:

- Tow compaction
- In-plane shear
- Inter-tow slippage
- Cross-over point slippage
- Tow-to-stitch slippage

- Stitch tension
- Stitch slippage

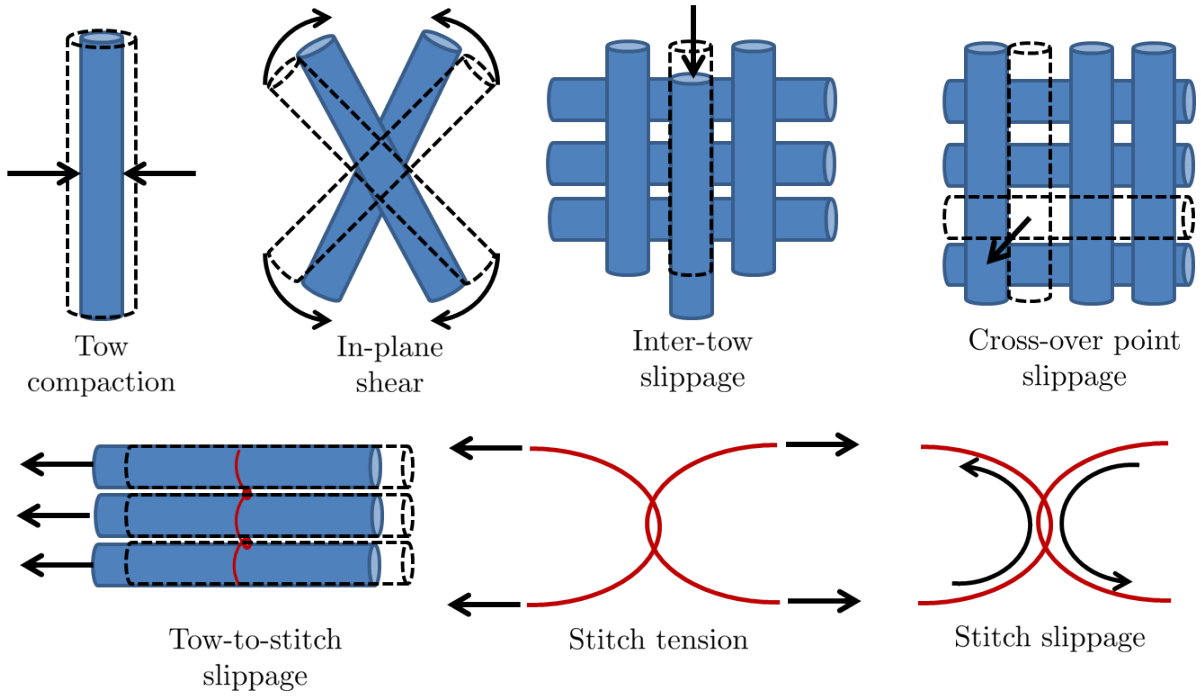

Figure 1.9: Deformation modes of conventional textiles (Reproduced from Creech and Pickett (2006))

This list underlines the variety and complexity of the interactions in fabrics. Besides, coupling between them exists. For instance, the tow compaction, which can result from interactions with the forming tools, is also dependent on in-plane shearing, especially in woven fabrics where shear locking phenomena appears once the compaction due to weft and warp yarns contact is the preponderant deformation mode (Boisse et al., 2011). Another coupling example is the asymmetric contribution of the stitch tension to in-plane shear in NCF demonstrated in bias extension tests by Creech and Pickett (2006). Bias extension test is a characterization method of conventional textiles which will be presented in the sequel. Contrary to woven fabrics in which cross-overs ensure relatively strong bonds between the two tow directions, in NCF the relative slippage between layers is more likely to happen and depends on the stitching. Creech and Pickett (2006) observed fibre slippage during bias extension tests of NCF as illustrated in Fig. 1.10.

1.2.1.2 Forming defects

Due to the quasi-inextensibility in the fibre directions, woven fabrics and NCF formability is mainly driven by its ability to allow large in-plane shearing which is characterized by angle changes between the warp and weft tows at crossovers in woven fabrics and between plies in NCF. Fig. 1.11 shows a model of a plain weave in its initial state and after applying in-plane shear of 15°. In 2D woven fabrics, the weaving pattern plays a preponderant role since it is directly related to the mechanical properties of the fabric. Huang et al. (2021b) investigated both experimentally and numerically the forming of a glass plain weave and a carbon satin weave on square box and hemisphere geometries. A high ratio of in-plane shear stiffness to bending stiffness was shown to increase the tendency to wrinkles, which are forming defects illustrated in Fig. 1.12 (a). 3D interlocks are less likely to wrinkle due to their higher bending

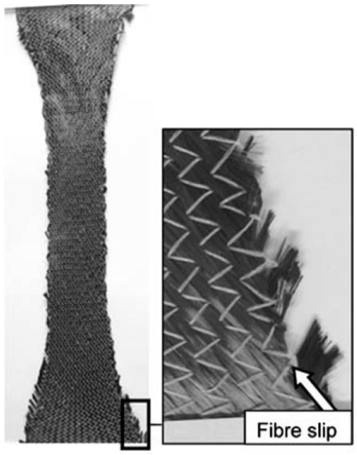

Figure 1.10: Tow slippage in bias extension test of NCF (Creech and Pickett, 2006)

stiffness directly related to their higher thickness. The stitching pattern in NCF also influences its formability (Steer, 2019).

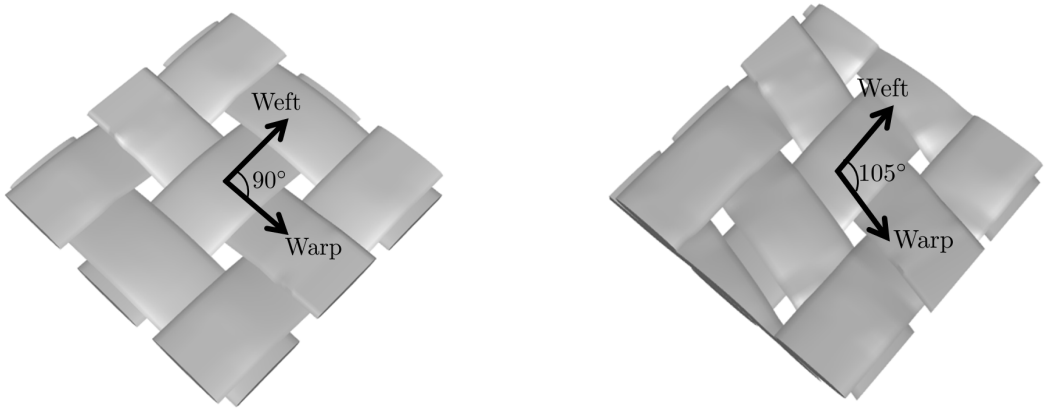

(a) Initial state **(b)** 15° shearing

Figure 1.11: Shear deformation of a 2D plain woven cell

Fabrics' kinematics is complex, coupled and have a strong impact on the forming process result. Some of them have been related to the onset of defects as in Boisse et al. (2011) where shear locking due to tow compaction was shown to be responsible for the onset of wrinkles in 2D woven fabrics. A high load in the yarn direction can lead to relative slippages between the yarns of a same ply or between the plies. The latter has been observed in prismatic shape forming of a glass plain woven as shown in Fig. 1.12 (b) by Allaoui et al. (2014). In the latter reference and in Ouagne et al. (2013), out of plane buckles in 2D woven fabrics which can be seen as wrinkles at the scale of the fibre tows where shown to create inhomogeneity of the part thickness. Lee et al. (2007) observed in-plane buckling of the tows in hemisphere shape forming of NCF.

Moreover, the impregnation and flow of polymer in the fibrous reinforcement can also create defects. For instance, in forming processes like compression moulding the impregnation of polymer generates high interaction forces with the fabrics. Hautefeuille et al. (2019) studied in-plane movement of fibre tows induced by the hydrodynamics forces generated during the compression of saturated fibrous reinforcement. Richardson and Zhang (2000) initially visualized this phenomenon in RTM even with reduced injection pressure. The impregnation of the fibrous reinforcement is another area of work in the field of fibre-reinforced composites which is strongly related to the study of the mechanical behaviour of dry fibrous reinforcements. The

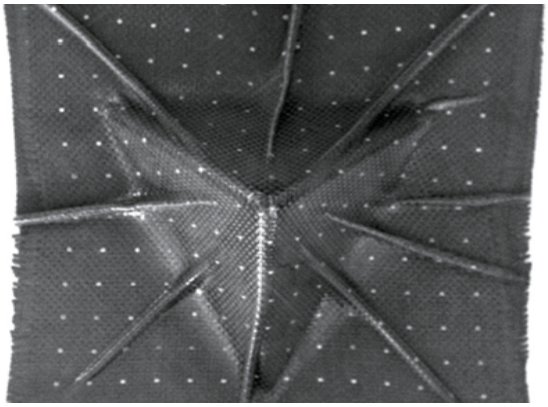

(a) Wrinkles during tetrahedral shape double diaphragm forming of 2 layer plain weaves [+45/-45°, 0/90°] (Thompson et al., 2020)

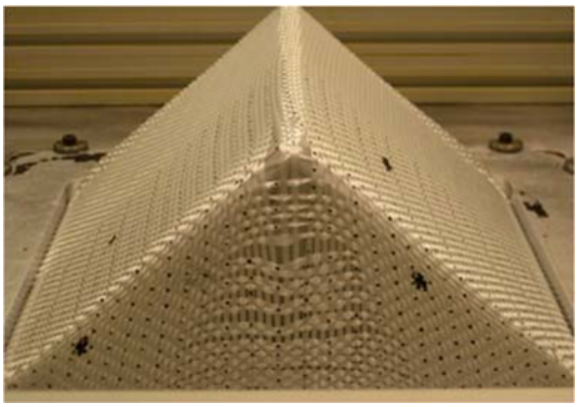

(b) Tow slippage in prismatic shape forming of a glass plain woven (Allaoui et al., 2014)

Figure 1.12: Examples of defects in woven fabrics forming

quality of the impregnation depends on the fibre orientations. Consequently, knowing the fibre orientations after forming is necessary for determining the permeability properties of the fibrous reinforcement and predict the result of the impregnation process. Voids formation is a major defect appearing during the impregnation. The reader can refer to Mehdikhani et al. (2019) for a review of their formation, characteristics and effects on the mechanical properties of fibre-reinforced composites.

1.2.1.3 Correction of defects

To avoid defects, some forming tools have been developed. For instance, blank-holders that apply tension in the fibre tows can reduce or eliminate wrinkles (Allaoui et al., 2011). However, a wrong design of these tools can also result in tow slippage due to too high blank-holder forces and also tow buckling. Capelle et al. (2014); Rashidi and Milani (2018) developed a specific blank-holder system to remove wrinkles without creating tow buckling or excessive tension strain or yarn slippage. Consequently, interactions with the forming tools has to be taken into account in modelling.

Transition

The accuracy of a model will be evaluated from its ability to account for the deformation mechanisms of conventional textiles since they are needed for predicting the onset of defects during forming processes. Besides, a good prediction of the final fibre orientations is required for computing the permeability properties as well as the final mechanical properties of the manufactured part. The next section introduces some models which are classified according to the way they represent the fabric as well as the analysis scale they used.

1.2.2 Modelling of conventional textiles in forming applications

Models mainly differ from the number of scales introduced to describe the behaviour of fabrics and the way they are considered. For the latter, two main options are possible. In the first one, the fabric is viewed as a continuum whereas in the other one the modelling is based on the detailed representation of its internal geometric features. In one hand, the concept of continuum allows representing the fabric as an equivalent homogeneous material using computationally efficient constitutive laws. This strategy is generally used at the industrial stage and assumes

the fabric to have a periodic structure, which is a common assumption for thin fabrics like 2D woven fabrics or NCF. On the other hand, the discrete approach allows a better description of the fabric behaviour and is mainly developed at the research level due to higher computational efforts. Between these two concepts, a third one, called semi-discrete representation, aims at taking advantage from the previous approaches by superimposing discrete features on a continuum. Models also differ from the constitutive law they used to describe the behaviour of the fabric features or the whole fabric itself. Reviews of these different types of modelling strategies can be found in (Syerko et al., 2012; Gereke et al., 2013b; Syerko et al., 2015; Bussetta and Correia, 2018; Liang and Boisse, 2021).

1.2.2.1 Discrete models

In the discrete approach, Durville (Durville, 2005, 2010) studied the behaviour of the fabric at the microscopic scale, by modelling all the fibres constituting the tows (Fig. 1.13 (a)). Deformable section beam elements where used to represent the fibres and the contact between them was modelled. This approach gave good results and highlighted the importance to consider the fibrous nature of the fibre tows. However, such a degree of discretisation is not adapted to the modelling of a whole piece of fabric due to its numerical cost. Moreover, modelling all the interactions in fabrics require a geometrically realistic model. Most of these interactions arise from contact between the constituents, namely tow-to-tow or tow-to-stitch or even fibre-to-fibre contacts. Wang and Sun (2001) used a different approach to model fibre tows based on digital rod elements pin-jointed to each other and forming a flexible chain as the length of the rod tends to zero (Fig. 1.13 (b)). The size of the rod had to be small enough to preserve the physical property, i.e. flexibility of the fibre tow.

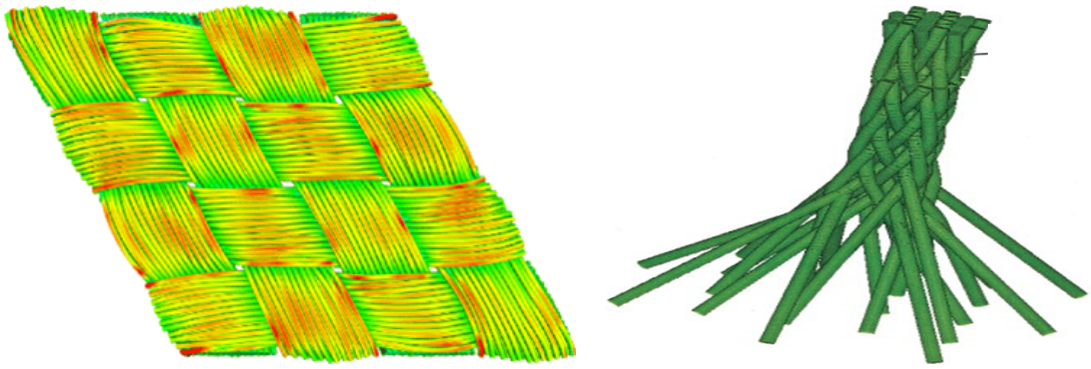

(a) Plain weave sample after in-plane shear (Durville, 2010)

(b) 3D preform braided by digital-element simulation model (Wang and Sun, 2001)

Figure 1.13: Examples of discrete models

Fortunately, classic fabrics exhibit periodic structures from which a unit cell can be identified. An example of woven fabric unit cell representation from Charmetant et al. (2011) is shown in Fig. 1.14. Based on this property, mesoscopic models have been developed (Boisse et al., 2005b; Charmetant et al., 2011; Gatouillat et al., 2013; Nguyen et al., 2013; Thompson et al., 2018). They aim at modelling the behaviour of a unit cell of a fabric to capture the true deformation mechanisms. Using this unit cell, the whole fabric behaviour can be modelled by translating the unit cell and imposing appropriate periodic boundary conditions between the unit cells. At this scale, tows are generally the smallest discrete features of the fabric and is modelled as a continuum. The difference between the models developed at this scale mainly lies is the constitutive law adopted to represent fibre tows which must take into account their fibrous nature. The first models were based on a hypoelastic constitutive law (Boisse et al., 2005a; Badel et al., 2008). The main drawback of this approach is the incomplete recovery

of the strain deformation in a closing loading path. To bypass this issue, hyperelastic models were used. For example, in Charmetant et al. (2011), the strain energy is considered as a sum of the contribution of each deformation mode of the tow taken separately, namely, elongation, compaction, distortion and longitudinal shear. In spite of the uncoupling between the strain modes, this approach gave good results for biaxial tension test and picture frame test which will be described in the next section. However, such constitutive law requires some additional efforts to identify all the material parameters. Carrying out physical experiments on a unit cell is not straightforward. To overcome this issue, standard macro scale tests were used and simulated with the mesoscopic model to identify the material parameters as it will be shown in the next section.

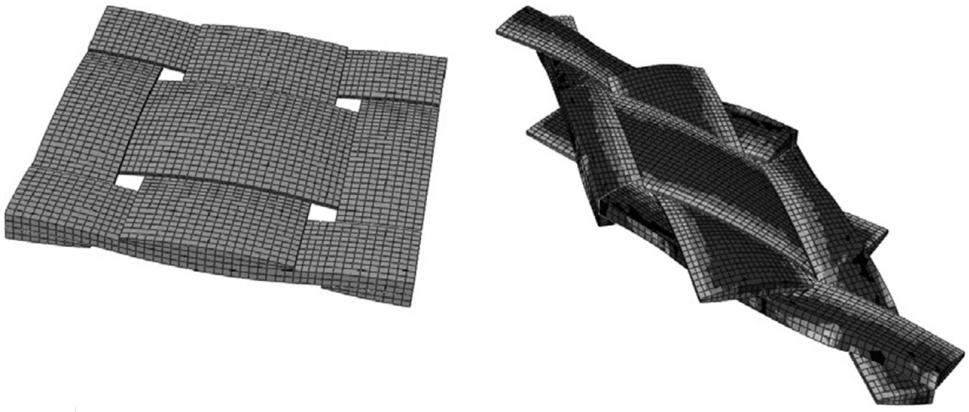

(a) (b)

Figure 1.14: Plain woven unit cell: (a) initial state and (b) deformed state (Charmetant et al., 2011)

Mesoscopic model's interest is driven by its ability to model the interactions between the structural elements of fabrics. Representing fibre tows as a continuum is a compromise between accuracy and simplicity whose admissibility depends on the constitutive law used to account for their fibrous nature. This type of model requires material parameters to be identified as well as a reliable reproduction of the unit cell geometry. It is generally time consuming, which explains its limited use at the laboratory scale. However, discrete models at the mesoscopic scale provide useful information about fabric deformations which are necessary for a clear understanding of deformation mechanisms and for quantifying their relative importance. Their accuracy allows replacing expensive and time consuming experimental tests by realizing them virtually (Boisse et al., 2005a).

1.2.2.2 Continuous models

As opposed to discrete models, the continuous approach consists in representing the fabric as a homogeneous material using computationally efficient constitutive laws. The fabric is considered as a continuum with anisotropic properties as well as large shear and bending deformations. This kind of model aims at representing the fabric behaviour at the macro scale since all the structural features of fabrics are condensed in a constitutive law. Among them, rate dependent constitutive models (Khan et al., 2010; Badel et al., 2009) as well as non-orthogonal rate independent models (Peng and Cao, 2005) and hyperelastic models (Aimene et al., 2008; Charmetant et al., 2012) were developed. This class of model generally assumes an uncoupling between tensile and shear, and neglect biaxial effects in woven fabrics. They simplify the consideration of the true deformation mechanisms but suffer from cumbersome homogenisation procedures with a necessary update of the directions of anisotropy to accurately take into account the change of fibre orientations (Dong et al., 2001). The continuous approach is not able to model the

relative sliding of yarns within a ply or between plies. Consequently, this modelling strategy is inappropriate to simulate defects like wrinkling, yarn fracture or slippage. However, (Zhu et al., 2011) developed a wrinkling criterion based on the yarn elastic properties of a woven fabric able to predict the onset of wrinkling.

The continuum approach is a computationally efficient numerical method usually used at the industrial stage to simulate macro-scale problems. This approach can be enriched through the use of discrete mesoscopic models in order to identify the main deformation modes or for realizing virtual mechanical testing to identify numerous material parameters when using hyperelastic constitutive laws.

1.2.2.3 Semi-discrete models

As an alternative to continuous and discrete modelling, the semi-discrete approach aims at finding a trade-off between the computational simplicity of a continuum representation with the accuracy of the discrete modelling of fabric features. These models superimposed discrete fabric features to a continuum.

Hamila et al. used 2D stress resultant elements to model woven fabrics (Hamila and Boisse, 2007, 2008). They firstly used a membrane element to model tensions and in-plane shear rigidities and then added the bending rigidities using neighbouring elements (Hamila et al., 2009). This final shell element possesses only displacement degrees of freedom (Fig. 1.15 (a)). The bending contribution was demonstrated to have a significant influence on the shape of the wrinkles whereas in-plane shear locking was determined to be responsible for their onset (Boisse et al., 2011). Each element represents several unit cells contrary to the discrete mesoscopic approach considering a unit cell. This model allows arbitrary warp and weft orientations in the shell element. The internal virtual work was considered as a sum of the independent contribution of tension, in-plane shear and bending rigidities to take into account the fibrous nature of the fabric. The simulations of the onset of wrinkling during forming and the shape of the wrinkles in woven fabric were in agreement with experimental observations. This shell element was also used in (Allaoui et al., 2011; Bel et al., 2012; Guzman-Maldonado et al., 2019; Huang et al., 2021a). In Bel et al. (2012), NCF forming was modelled using the previous shell element with a unidirectional anisotropy. The plies were represented separately with contact interactions. The through-thickness stitch contribution was simply modelled using bar elements connecting the plies (Fig. 1.15 (b)). Contrary to the mesoscopic approach in (Creech and Pickett, 2006), they did not use a true representation of the stitch pattern geometry but only took into account the through-thickness tension. They obtained forming simulation results in accordance with experiments and were able to represent inter-ply sliding. De Luycker et al. (2009) used a combination of hexahedral elements and truss to model the forming of 3D interlocks (Fig. 1.15 (c)). An isotropic hypoelastic material was used in the hexahedral elements to model the shear and transverse compression as well as all other yarn interactions in the preform which were considered to be second order rigidities compared to yarn tension stiffness. The truss elements allowed an explicit representation of the position of the yarns in the preform and an efficient tracking of the orientation changes. Other models have been proposed based on descriptions using a network of several springs types (shear, torsional, flexional, stretching) (Ben Boubaker et al., 2007) or a network of pin-jointed trusses (Sharma and Sutcliffe, 2004) or superposition of trusses and shell elements (Sidhu et al., 2001; Jauffres et al., 2010).

Transition

Semi-discrete modelling is particularly efficient to reflect the weakest deformation modes using a continuum representation and add discrete features in it to take into account preponderant deformation mechanisms. It is acknowledged to be a reliable trade-off

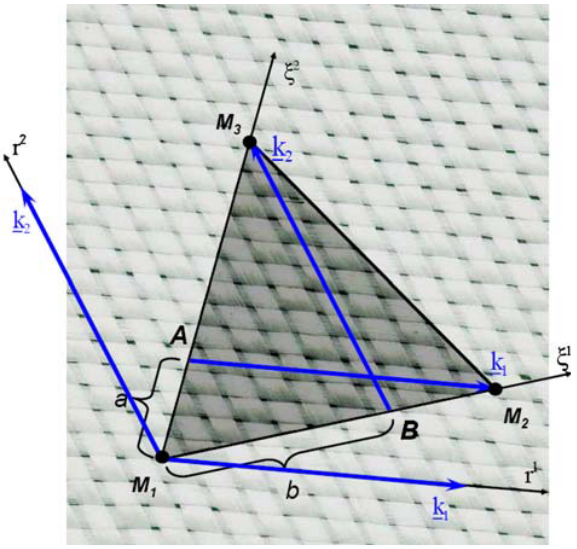

(a) Tree node finite element of Hamila and Boisse (2007) for woven fabrics

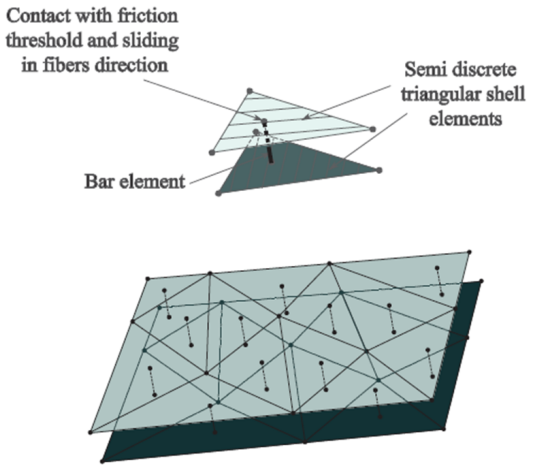

(b) NCF model in (Bel et al., 2012)

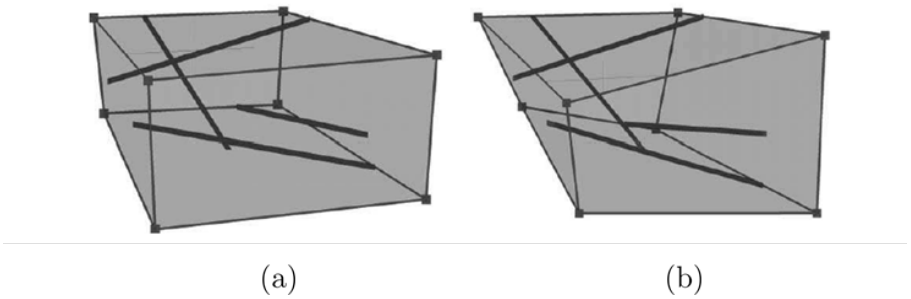

(c) 3D interlock model made of trusses embedded in 3D solids: (a) initial and (b) deformed state (De Luycker et al., 2009)

Figure 1.15: Discrete models' examples

between the simplicity of the model representation and its accuracy in modelling the main deformation mechanisms of fabrics. Whatever modelling technique is used, the identification of the required material parameters has to be carried out. The next section presents some of the main characterisation procedures for conventional textiles.

1.2.3 Characterisation of conventional textiles' mechanical properties

Characterising the mechanical properties of conventional textiles which are non-linear materials is necessary to provide the material parameters required in the numerical models. Uniaxial and biaxial tensions, in-plane shear, out-of-plane bending and friction are the main deformation modes and interactions studied in the literature. Depending on the complexity of the numerical models presented in the previous section, material properties associated with the latter deformation modes have to be evaluated. Besides, depending on the material scale used in the numerical model, the characterisations have to be carried out on single fibre, fibre tow or on a piece of conventional textile. This section describes some of the main characterisation procedures developed to identify the mechanical properties of conventional textiles. They are classified according to the studied deformation mode. The mechanical properties identified strongly depends on the nature of the fibre, the fibre tow assembling and the internal structure of the reinforcement.

(Gereke et al., 2013b; Liang and Boisse, 2021) reviewed these characterisation procedures.

1.2.3.1 Fibre direction tests

Characterisation carried out in the fibre direction are referred as axial tests and can be subdivided into tensile and compression modes. Generally, these tests provide information about tensile/compression modulus as well as the strength and elongation at break. It is well-accepted that fibres can be considered as quasi-inextensible whereas they easily break under compression. Measuring the tensile modulus of a single fibre is difficult due to its slenderness, however it has been carried out (Sinclair, 1950; Ilankeeran et al., 2012). Tensile tests can also be performed at the scale of the fibre tow (Xue and Hu, 2013; Moothoo et al., 2014; Ou et al., 2016). Modelling the tensile properties of fibre tows is not straightforward especially for natural fibre based tow which are made of discontinuous elementary fibres implying more variability than synthetic fibre bundles (Tham et al., 2019). For models which are not based on the modelling of fibres or fibre tows, testing the tensile properties of the reinforcement is necessary. However, tests at this material scale can also be used as validation test cases for lower scale models. From a single fibre to a fibre tow to a reinforcement, the tensile behaviour is very different. For instance, 2D woven fabrics exhibit strong linearities at the beginning of the uniaxial loading due to the crimp created by the weaving structure which also leads to a coupling between the tensile behaviour in the weft and warp directions (Buet-Gautier and Boisse, 2001; Launay et al., 2002). Biaxial tests of 2D woven fabrics allows characterising this coupling as shown in Fig. 1.16. Coupling between tensions in biaxial fabrics has also been studied for NCF (Lomov et al., 2005) and knitted fabrics (Luo and Verpoest, 2002).

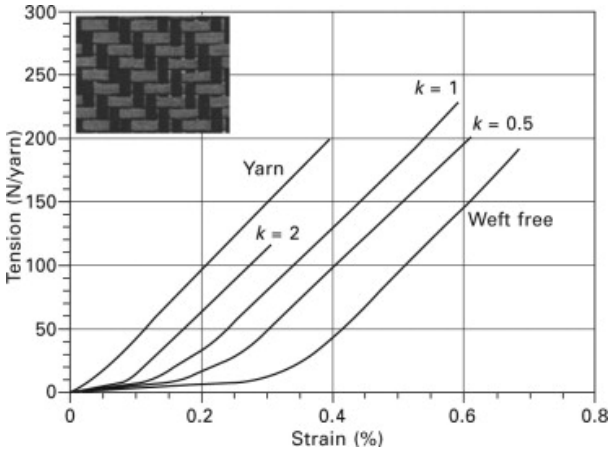

Figure 1.16: Biaxial tensile tests of a twill 2 x 2 carbon textile reinforcement: tension vs strain in the warp direction for different warp-to-weft tension ratio (Carvelli, 2011)

1.2.3.2 In-plane shear

In-plane shear of fibrous reinforcement is the deformation mode that received the greatest attention due to its predominance during forming. Two methods are mainly used, namely, the picture-frame test and the bias-extension test. Cao et al. (2008) made a compilation of the different experimental set-ups and their corresponding methods for interpreting results of picture frame and bias-extension tests on 2D woven fabrics.

An example of experimental set-up of the picture-frame is given in Fig. 1.17 from Schirmaier et al. (2016) which studied the forming behaviour of UD-NCF. Basically, a square sample of fabric is clamped in a frame made of four pin-jointed rods which have the same size. When loaded, the initial square frame turns into a rhombus generating rigid rotations between the two

fibre directions. Due to its sample size dependency and the difficulty to place correctly the fabric into the frame to avoid generating undesirable tension in the fibre direction, the bias-extension test can be preferred over the picture frame test.

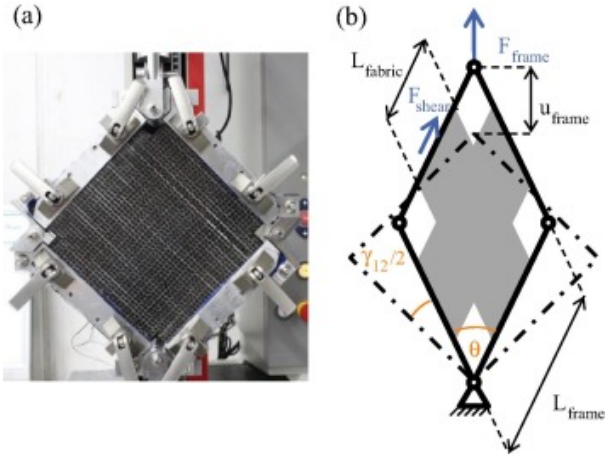

Figure 1.17: (a) Picture frame test setup in starting position and (b) schematic representation of the deformation of the picture frame (Schirmaier et al., 2016)

In the bias-extension test, a rectangular sample of UD or biaxial fabric is clamped on its smaller edges in a tensile device (Fig. 1.18 (a)). The rectangular shape is cut such that the tensile direction is the bisector of the angle between the two fibre directions. Theoretically, if the length-to-width ratio is greater than two, a constant shear angle is observed in the central area (zone C in Fig. 1.18) which can be directly computed from the force-displacement curve. However, to avoid biased results due to fibre slippage which are more likely to occur for high bending stiffness fabrics,Lomov et al. (2008) showed that optical measurements such as Digital Image Correlation (DIC) might give more reliable results for both bias-extension and picture frame tests. The deformed shape showed in Fig. 1.18 (c) is typical to woven fabrics and differs for other fibrous reinforcements. For examples, bias-extension tests were performed by Creech and Pickett (2006) on biaxial NCF which showed the asymmetric contribution of the stitch and by Schirmaier et al. (2016) on UD-NCF. Fig. 1.18 (d) shows the non-linear in-plane shear behaviour of 2D woven fabrics. At low shear angle, the shear force is small since the warp and weft tows are rotating. Once lateral contact and transverse compression between the tows occur, the shear force starts increasing strongly until reaching the so-called locking angle. Among the consequences of in-plane shear, lateral tow compression leads to local and inhomogeneous increasing of the reinforcement thickness.

1.2.3.3 Out-of-plane bending

Firstly neglected, out-of-plane bending gained a lot of interest once revealed to be strongly related to out-of-plane defects like wrinkles (Boisse et al., 2011; Hamila et al., 2009). Due to the fibrous nature of fibre tows, bending properties cannot be determined from in-plane properties as for continuum mediums. Two main tests have been used to characterize the bending rigidities of fabrics, namely, the cantilever bending test (Peirce, 1930) shown in Fig. 1.19 and Kawabata bending test (Kawabata, 1980). The cantilever bending test allows determining only elastic bending properties whereas the bending behaviour of fabrics showed to be non-linear. de Bilbao et al. (2010) developed another device allowing measuring the non-linearities of out-of-plane bending in fabrics.

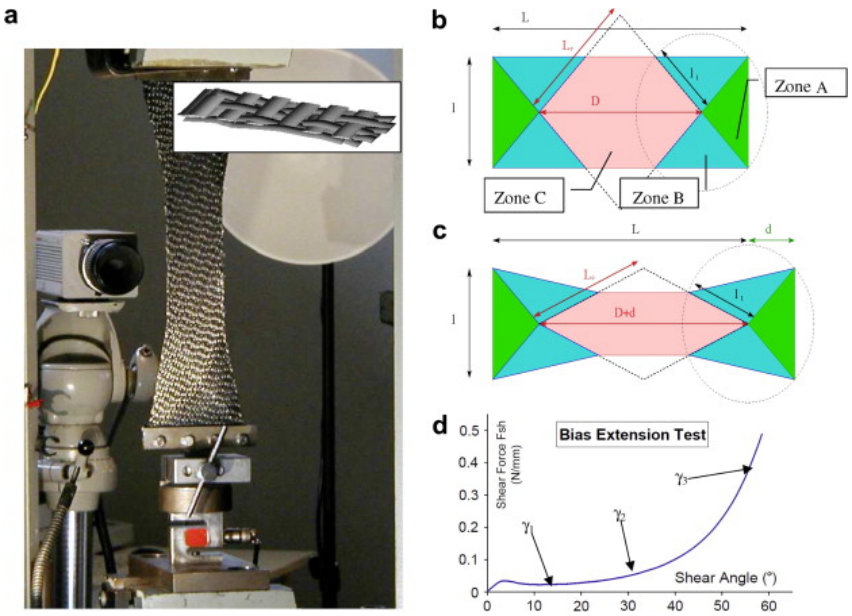

Figure 1.18: Bias extension test: (a) the device (inset: weave structure of the fabric G1151) (b) initial rectangular specimen with yarns oriented at ±45° (c) deformed specimen (d) shear load curve for G1151 interlock fabric (Lomov et al., 2008)

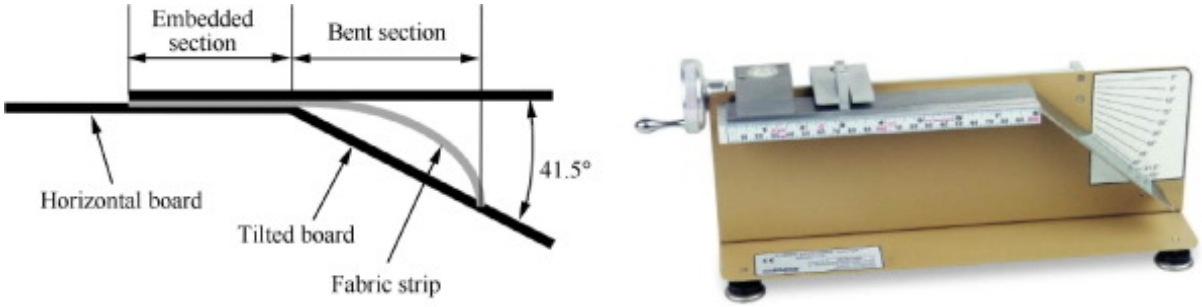

Figure 1.19: Standard cantilever bending test device (Liang and Boisse, 2021)

1.2.3.4 Friction

In addition to the characterisation of the fabrics' deformation modes, investigating the friction interactions with the forming tools and between layers is required. Gorczyca-Cole et al. (2007) carried out pull-out tests of commingled woven fabric placed between friction plates to measure the influence of the velocity, the polymer viscosity and the compaction pressure on the fabric-to-tools friction behaviour in thermostamping applications. Najjar et al. (2014) also showed the influence of the temperature and pressure on fabric-to-tools and fabric-to-fabric friction coefficient for a epoxy powdered carbon woven fabric used in aeronautical applications. Allaoui et al. (2015) studied dry fabric-to-fabric friction during ply-to-ply sliding which is due to the shock phenomenon between the transverse overhanging yarns of each ply shown in Fig. 1.20 and depends on the unit cell period of the woven fabric. Contrary to Gorczyca-Cole et al. (2007) which observed the independence of the fabric orientation on the fabric-to-tool friction, they showed its influence on the fabric-to-fabric friction behaviour.

For models representing explicitly tow-to-tow interactions, the friction behaviour between the tows needs to be characterized. Mulvihill et al. (2017) and Tourlonias et al. (2019) studied tow-to-tow friction and its dependency to normal loading. Mulvihill et al. (2017) investigated two orientations cases, namely, 0° and 90° whereas Tourlonias et al. (2019) measured the friction

coefficient between tows and between single fibres for different angle of intersection in this range. The friction coefficient was shown to decrease when the angle increases. The maximal value being obtained when fibres are almost parallel to each other.

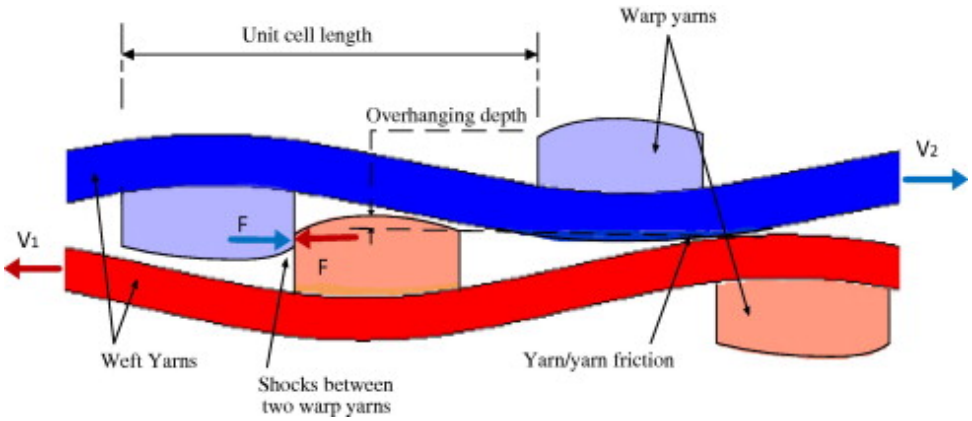

Figure 1.20: Phenomena occurring during fabric/fabric friction: yarn/yarn friction and shock phenomenon caused by overhanging yarns (Allaoui et al., 2015)

1.2.3.5 Some characterisation procedures for couplings

This overview of the characterisation methods developed for fibrous reinforcement was limited to the determination of the mechanical properties related to single deformation modes except for the biaxial tensile test. However, coupling exist between the deformation modes which cannot be neglected for a deep understanding of the forming behaviour. For instance, Colman et al. (2014) performed picture frame tests on pre-tensioned architecture fabrics to show the influence of tension over the shear behaviour. Kashani et al. (2016) highlighted the two-way coupling between tension and shear in woven fabrics by showing that fabric shear makes the tension behaviour more compliant. Salem et al. (2020) studied the effect of the shear angle on the pull-out force of single tow in a woven fabric.

Conclusion

Even if numerous experimental methods have been developed for fibrous reinforcement mechanical properties' characterisation, carrying them out still requires considerable efforts. Besides, the non-standardisation of most of these characterisation procedures make difficult the share of data within the scientific community. Due to the scale range covered by the characterisation methods, some of these tests can either be used as characterisation procedures or validation test cases. When developing a numerical model, it is important to firstly figure out which of these characterisation methods and experimental validation test cases will be used.

Despite major advances, the development of the numerical modelling and the experimental methods required to identify the material parameters is still in progress to understand the forming of conventional textiles. Taking into account the deformation modes' couplings as well as representing more accurately the fabric-to-tools and layer-to-layer interactions will be of first importance. However, even if a full understanding of conventional textiles would be achieved, would conventional textiles be the best fibrous reinforcements for manufacturing optimized 3D composite parts? The next section aims at highlighting the limits of conventional textiles to design and produce lightweight structural 3D parts, to bring to light fibre placement technologies that have been especially developed for this purpose. The latter gained a growing interest due to the constant progress made in improving productivity and design complexity.

1.3 Optimized FRC parts: towards fibre placement technologies

Introduction

The previous section reviewed the manufacturing of 3D composite parts by forming conventional textiles. This next section discusses the limitations of conventional textiles to manufacture optimized FRC parts. Among these limitations, material wastage and metal-like behaviour of the final part are highlighted. Then, existing fibre placement technologies are introduced as a remedy to these limitations. Automated Fibre Placement (AFP), Continuous Tow Shearing (CTS) and Tailored Fibre Placement (TFP) are described. Finally, challenges to be addressed in the design, manufacturing and modelling of fibre steered preforms are presented.

1.3.1 Expanding design possibilities: substituting conventional straight fibres by curvilinear ones

Fibre-reinforced composites have been initially developed to manufacture structures lighter than metallic ones. However, one of the major contradiction in the manufacturing of FRC parts using conventional textiles is that the final material often behaves quasi-isotropically as a result of the stacking sequence of unidirectional plies or biaxial textiles. Despite this apparent deficit in taking full advantage of the intrinsic anisotropy of fibres, isotropic FRC can save weight which makes them attractive in the industry.

1.3.1.1 Quasi-isotropy of straight fibre designs

Considering a rectangular plate made of unidirectional layers and submitted to pure traction might be the simplest example allowing to demonstrate this limitation in using conventional textiles to manufacture optimized FRC parts. The following is a simple thought process allowing determining the layers' configuration which maximizes the resistance of the part. First, as fibres are stronger when loaded in their direction, one may think about using only plies oriented in the tensile direction which is called 0°-direction. However, due to Poisson's effect in the orthogonal direction, namely 90°-direction, the matrix which is softer than the fibres will break long before reaching the maximal load capacity conferred by the fibres. Consequently, some plies are required in 90°-direction to counter Poisson's effect. Considering a part submitted to pure traction in real life applications is obviously very scarce. To prevent early breakage due to shear deformation induced by fibre misalignment or asymmetry of the part due to manufacturing defects or a slight deviation of the loading axis, a pair of ±45° ply is required. Consequently, the final part is finally made of four different directions providing the part quasi-isotropic mechanical properties, thereby loosing the intrinsic anisotropy of the elementary fibre.

1.3.1.2 First interest of curvilinear fibre designs

Hyer and Lee (1991) highlighted this point in FRC part by numerically comparing tensile and buckling load-bearing capacities of plates with a central circular hole for laminates made of straight and curvilinear fibre layers. A search gradient technique was used to determine the fibre orientations by maximizing the buckling load. In previous studies Hyer (1987) shows that 16-layers laminate with $[\pm 45, C_6]_s$ configuration where "C" stands for curvilinear fibre layer increases by 61% the tensile load-bearing capacity compared to a quasi-isotropic configuration $[\pm 45, 90, 0]_{2s}$. Fig. 1.21 illustrates both designs. In this study, aligning the principal directions of the fibrous material with the principal stress directions was assumed to give the part better structural strength. Fibres in the curvilinear layers encompass the hole which makes the layer continuous and removes high shear deformation due to initial high stress direction changes in

an isotropic part. A configuration where the pair of ±45° layer is replaced by curvilinear layer orthogonal to the "C-layers" forming an orthogonal curvilinear grid theoretically gives better results but will suffer from any shear deformation introduced in the part by fibre misalignments or a slight deviation of the traction's axis. Holes in plates are common for assembling parts in aeronautics. Removing stress concentrations at such geometric discontinuities using curvilinear fibres was seen as a very attractive solution and has expanded the design freedom of FRC parts.

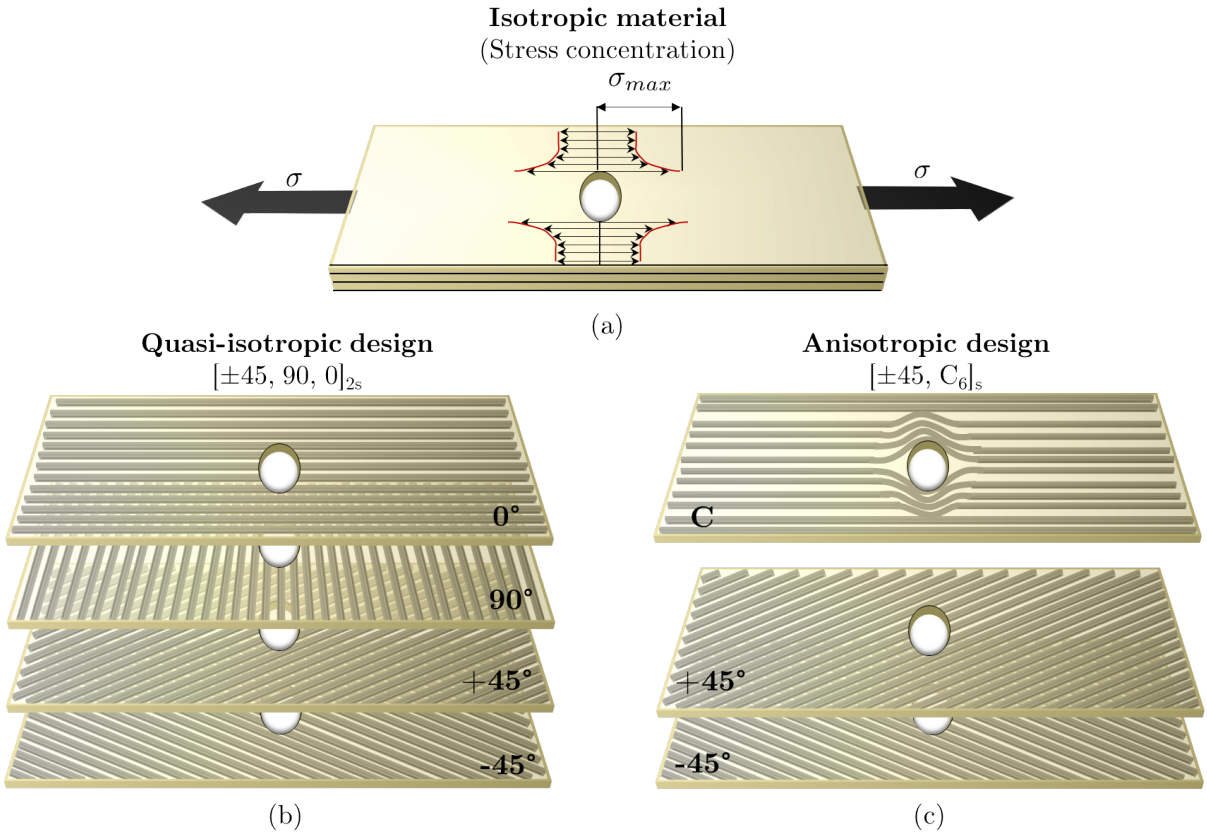

Figure 1.21: Removing stress concentration in tensioned plate with central circular hole: (a) Stress concentration for isotropic material, (b) quasi-isotropic FRC design leading to discontinuous plies and (c) anisotropic design using curvilinear fibre paths removing stress concentration

1.3.1.3 Variable stiffness and variable angle tow composites

Using curvilinear fibre layers rather than straight fibre layers was shown to considerably increase the mechanical performance of FRC by taking more advantage of the intrinsic anisotropy of fibres. Laminates made of such curvilinear fibre layers have been called Variable Stiffness Composite (VSC) or Variable Angle Tow (VAT). Ribeiro et al. (2014) reviewed the mechanical behaviour of VSC. Despite VSC laminates can be obtained using techniques other than curvilinear fibres, as shown in Fig. 1.22, these other techniques introduce either abrupt changes in thickness such as internal ply drops or major geometry variations such as stiffeners, which makes the curvilinear fibre approach more attractive. VAT design is not restricted to the removal of stress concentration at geometric discontinuities but it extends to the design of parts where both topological and material orientations optimisation are performed. The pioneering concept is to use fibre only where needed.

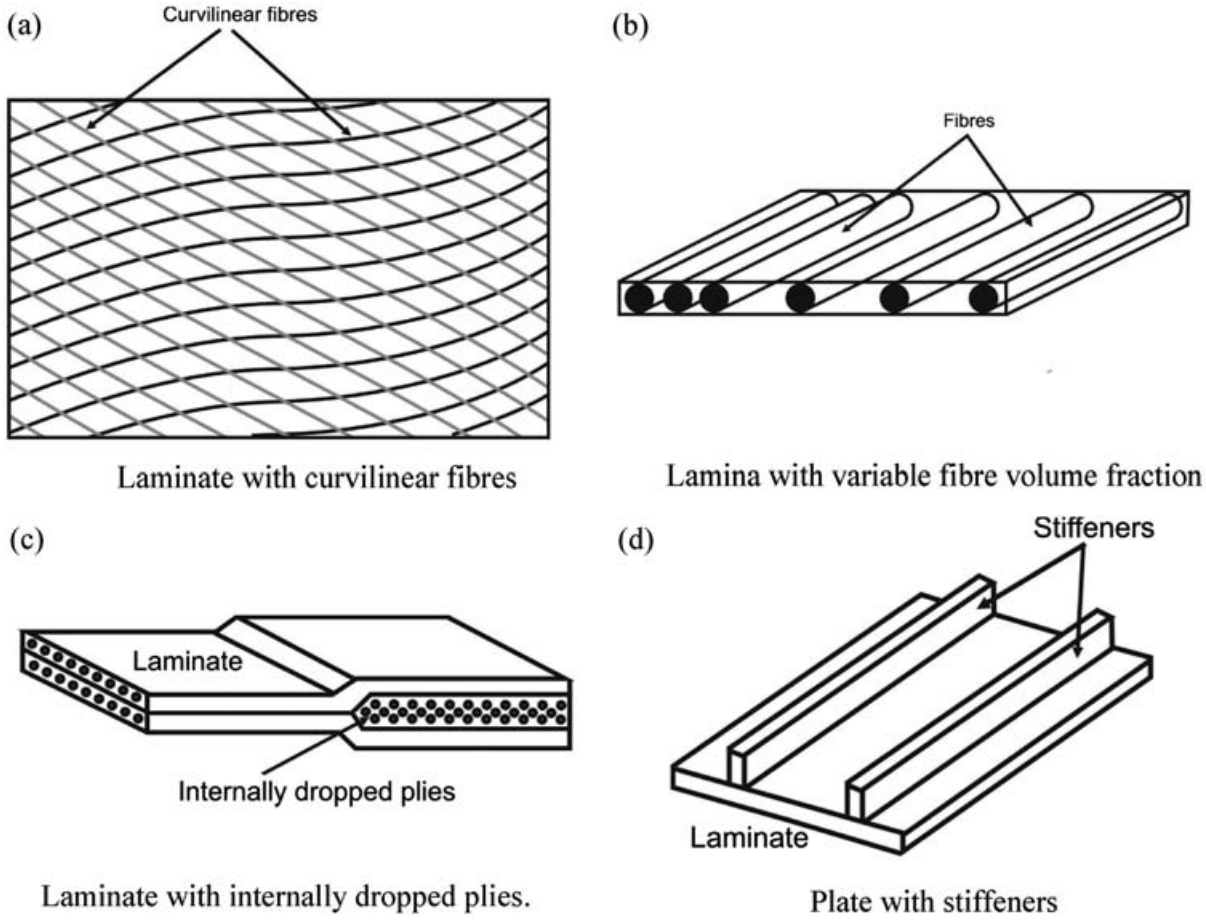

Figure 1.22: Examples of four types of variable stiffness composite panels (Ribeiro et al., 2014)

Transition

Consequently, by maximizing the use of anisotropy in FRC parts, material weight can be saved. Moreover, as discussed in the next section, fibre placement technologies allow manufacturing nearly nets-shape FRC parts avoiding material wastage, which is inherent in the use of conventional textiles. Nevertheless, by extending the design freedom, curvilinear fibre also complexify the characterisation of the mechanical properties of curvilinear FRC and their modelling. Besides, the optimal design now lies in a wider space. In the next section, different technologies for manufacturing curvilinear fibrous reinforcements are presented.

1.3.2 Introduction to the fibre placement technologies: AFP, CTS and TFP

The development of technologies to place fibres in a curvilinear way has been driven by the need to better take advantage of the anisotropy. Advances in robotics and computer aided design have accelerated the integration of these automated technologies in the most advanced industries. Among these technologies, Automated Fibre Placement (AFP), Continuous Tow Shearing (CTS) which can be seen as an enhancement of AFP and Tailored Fibre Placement (TFP) will be briefly presented. This section aims at describing the principle of each technology as well as the advantages their offer and the shortcomings they have. Sobhani Aragh et al. (2021) reviewed these fibre placement technologies.

1.3.2.1 Automated Fibre Placement

Automated Fibre Placement machine is based on the Automated Tape Laying concept, which was firstly developed to automate the hand lay-up of pre-impregnated materials on flat or slightly curved surfaces, and the Filament Winding process dedicated to surface with positive Gaussian curvature. AFP enhances those concepts by adding a mechanism to split the tape into several parallel tows, which allows manufacturing parts with more complex curvatures. The AFP machine consists in a robotised head, as illustrated in Fig. 1.23 including a roller to compact and stack the tows on the mould surface while a heat source heals-up the polymer contained in the incoming tapes creating cohesion with the mould's surface or the previously deposited layer. Flat or 3D surfaces can be used as forming tools. Lay-up speed, heat source temperature, roller compaction pressure and tow tension are processing parameters that have been studied and need precise adjustments for obtaining optimal part quality.

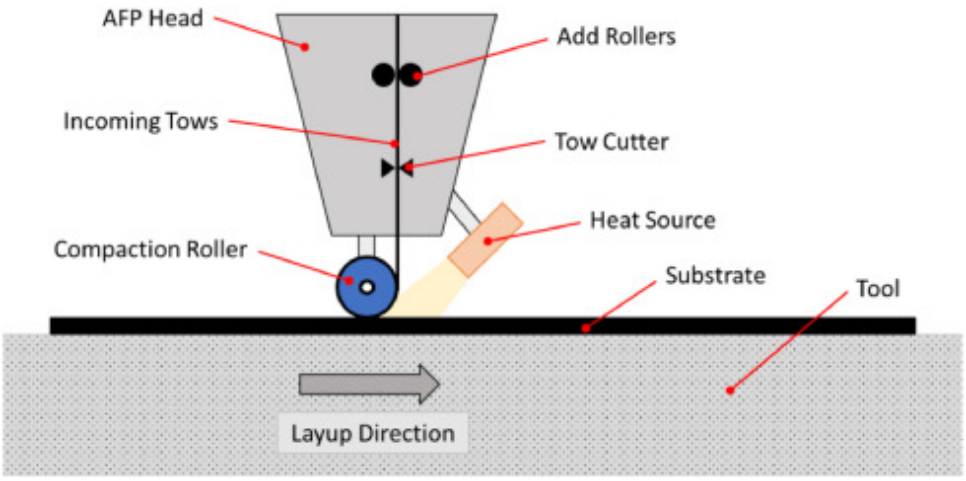

Figure 1.23: Simplified representation of an AFP head (Brasington et al., 2021)

AFP received the greatest attention from industry and in particular from aeronautics. The latter could explain the greater deployment of this technology and the amount of research devoted to it. In particular, many efforts have been undertaken since the 1980s to study the AFP technology, which has led to an in-depth understanding of the numerous manufacturing defects in AFP. Harik et al. (2018) classified these defects by describing their cause, explaining how to identify and prevent them and giving the immediate future consequences on the structural performances of the produced fibre-steered laminate. Among them tow gaps and overlaps as well as wrinkles are easily recognizable as shown in Fig. 1.24. Zhang et al. (2020) and Brasington et al. (2021) made a detailed review of the AFP process.

1.3.2.2 Continuous Tow Shearing

Continuous Tow Shearing is a relatively recent fibre placement technology based on the AFP concept and developed by Kim et al. (2012). CTS has been designed to remove tow gaps and overlaps present in VAT laminate manufactured using AFP. In this process, dry tows are used to enable shearing of their section and in-situ impregnation is achieved. The shear deformation avoids generating additional tension of the outer edge and compression of the inner edge due to the path curvature as occurring with AFP. Fig. 1.25 shows the improvement on the surface coverage by using the CTS technique over AFP. However, even if tow gaps and overlaps are removed, due to the shear deformation, there are induced angle variation between adjacent tows as well as thickness variation. Kim et al. showed that the thickness variation can be directly computed from the shear angle by assuming isochoric transformation of the tow's section. CTS technique reduces the minimum curvature radius of 500 mm for AFP to a few

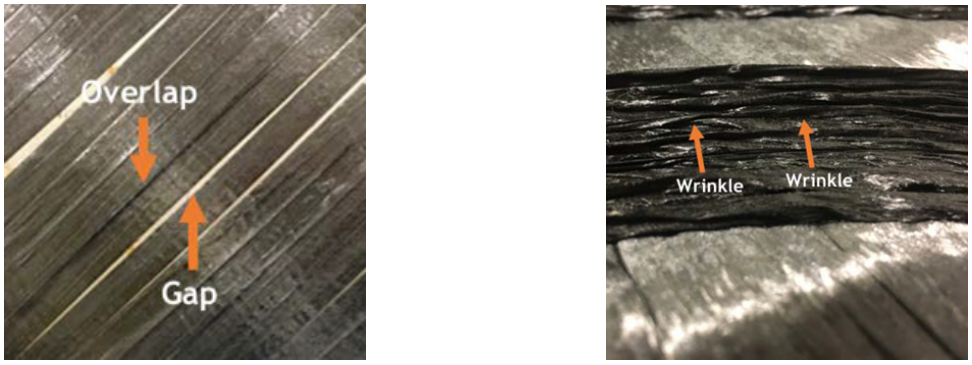

(a) Tow gaps and overlaps **(b)** Tow wrinkles

Figure 1.24: AFP manufacturing defects (Harik et al., 2018)

tens of millimetres depending on the tow material (Kim et al., 2012). However, CTS is still limited to the manufacturing of 2D parts and needs further development to be fully integrated in the composite industry.

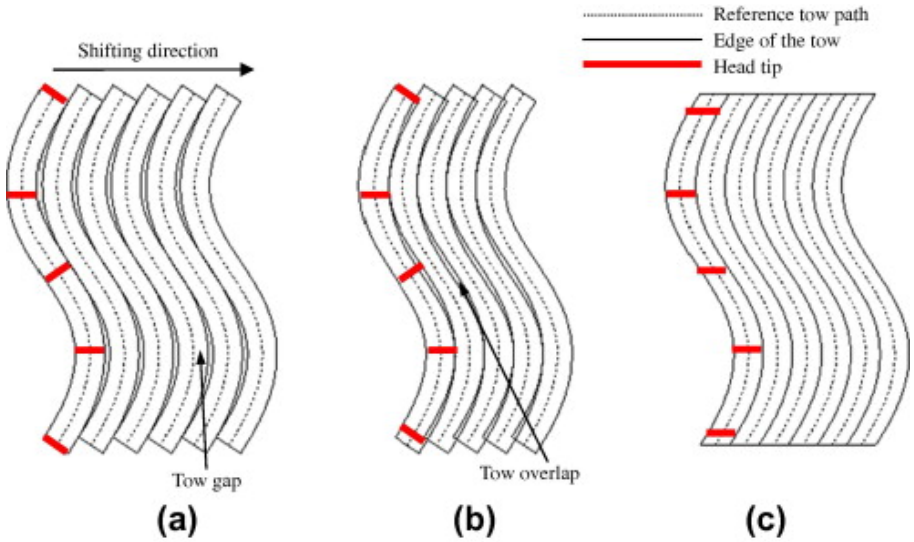

Figure 1.25: Difference of the tow arrangement and head rotation: (a) conventional AFP (tow gap), (b) conventional AFP (tow overlap), and (c) CTS. (Kim et al., 2012)

1.3.2.3 Tailored Fibre Placement

AFP and CTS are based on the placement of pre-impregnated tows whose cohesion with previously deposited material or mould surface is ensure by the successive heating and solidification of the polymer. In Tailored Fibre Placement whose principle is illustrated in Fig. 1.26, an embroidery head fixes a continuous tow on a flat backing material by realizing a zig-zag stitching. The tow can be dry or commingled and the backing material can be any material tolerant to stitching as thin plastic film or conventional thin textiles. The stitching yarn is generally made of (but not limited to) polyester. Compared to AFP and CTS, higher curvature can be achieved since U-turn are possible which makes TFP more attractive to manufacture small parts. Besides, the stitching yarn bonding the layers together gives better out-of-plane properties and higher deposition rate is achieved by using several heads working in parallel.

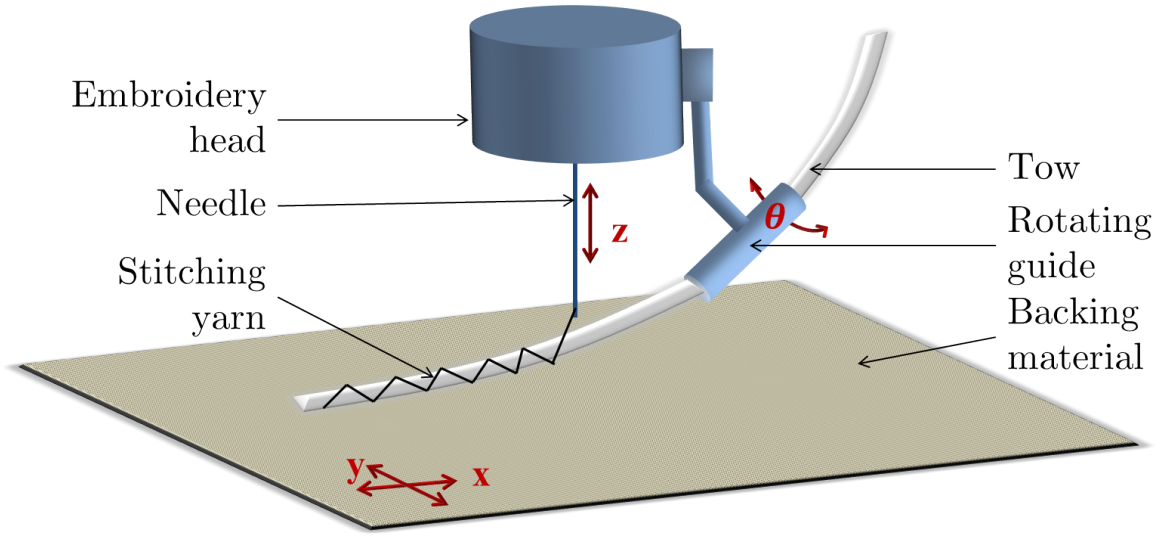

Figure 1.26: Schematic representation of Tailored Fibre Placement principle

Transition

Table 1.1 summarizes the advantages and drawbacks for the fibre placement technologies presented. They allow manufacturing either flat or 3D shell-like composite parts with curvilinear fibre paths that enlarges the design possibilities. Among these designs, those with the best mechanical performance are of interest to advanced industries. Therefore, identifying the optimal mechanical design for a given application is required to fully take advantage of the fibre placement technologies. The next section highlights this challenge.

1.3.3 Challenge in manufacturing FRC parts with optimal mechanical performances using curvilinear fibres

1.3.3.1 Definition of the optimisation problem

The development of technologies allowing manufacturing VAT laminates expanded the design freedom of FRC parts. However, determining the optimal composite part design for a given structural application is not straightforward and requires satisfying multiple objectives simultaneously. Even if the optimal design in terms of mechanical efficiency can be determined, the designer still has to deal with both manufacturing feasibility and production costs which have to be taken into account in the optimisation process as additional constraints or design parameters. Combining realistic simulations of mechanical performance analysis and manufacturability in a single optimisation loop requires enormous computation time making it difficult to be integrated at the industrial stage. To reduce computation cost of such optimisation process, Eck et al. (2015) used a process estimator for determining impregnation quality in RTM rather than using a complete process simulation in the main loop and finally checked the manufacturability of the optimisation result using a more realistic RTM simulation. To achieve such an optimisation process, reliable and fast simulation tools in the different steps of the process are required.

Curvilinear fibre layer design promised to outperform straight fibre layer design by taking more advantage of the intrinsic anisotropy of fibres. However, determining the optimal fibre paths giving the best mechanical performance for a given geometry with specific boundary conditions is a very broad field of research. The first difficulty is to determine the properties to optimize. Structural topology, strength or natural frequencies or a combination of them are some examples. Moreover, the optimal design will strongly depends on the boundary conditions the part is

Table 1.1: Advantages and drawbacks of fibre placement technologies

Fibre placement technology	Advantages	Drawbacks
AFP	Studied over decades Advanced process planning tools Auto-generation of FE models Well studied manufacturing defects and correlation with manufactruing parameters	Small curvature radius, gaps and overlaps Fibre discontinuities Expensive forming tools Limited to small surface curvatures
CTS	Gaps and overlaps are removed Fibre continuity Smooth thickness variations	Recent technology Small curvature radius (but higher than AFP) Thickness and fibre angle variations due to cross-section shearing
TFP	High curvature radius Fibre continuity 3D reinforcement by stitching Great variety of material combinations	Lack of numerical and optimisation studies Lack of control over manufacturing parameters Out-of-plane and in-plane wrinkles, gaps and overlaps

submitted to and will have to take into account every possible loadings.

1.3.3.2 Principal stress directions and loading path principles

The first study focusing on determining the optimal fibre orientations in FRC parts considered simple loading conditions for relatively simple 2D geometry (Hyer, 1987). Tosh and Kelly (2000) also investigated the optimal fibre orientation in open hole tensile laminates. They demonstrated that using principal stress directions, which correspond to tension and compression directions for optimally placing fibres as done in Hyer (1987), is only reliable when boundary conditions result in tension or compression dominant stress in the part. If both modes show equivalent magnitude in a given area, indicating the presence of shear, following this rule of thumb might not give the best mechanical performances unless using a ply for each main stress trajectory. Therefore, they introduced the theory of loading path which can be seen as the trajectory where a constant load can be observed from the point of application into the structure to the point of reaction out of this structure. The computation of loading paths is based on the integration of principal stresses though a section which gives a constant load along the trajectory. The normal to this section is arbitrary and has to be given. One of the differences with the concept of principal stress directions is that when following a loading path in the structure, the load to be carried by the material particles in the given section is constant whereas stress magnitude can change from a point to another. If only one deformation mode(tension or compression) is present in the part, then the loading paths give similar results to those obtained with the principal stress directions approach. A loading path only shows how a constant unit of load is transferred through the structure and potentially alternates between tensile, compressive or shear modes. It is worth noting that theoretically for the principal stress direction design, a ply for each tension and compression trajectories is required while a single ply where fibres are aligned with the loading paths is sufficient. In practice, to take into account any additional shear deformation, a complementary set of loadings path is required. Fig. 1.27 summarizes

the different main stresses and loading paths trajectories as well as trajectories obtained with dominant main stress and hybridation between main tensile stress and X-direction loading path for an isotropic material.

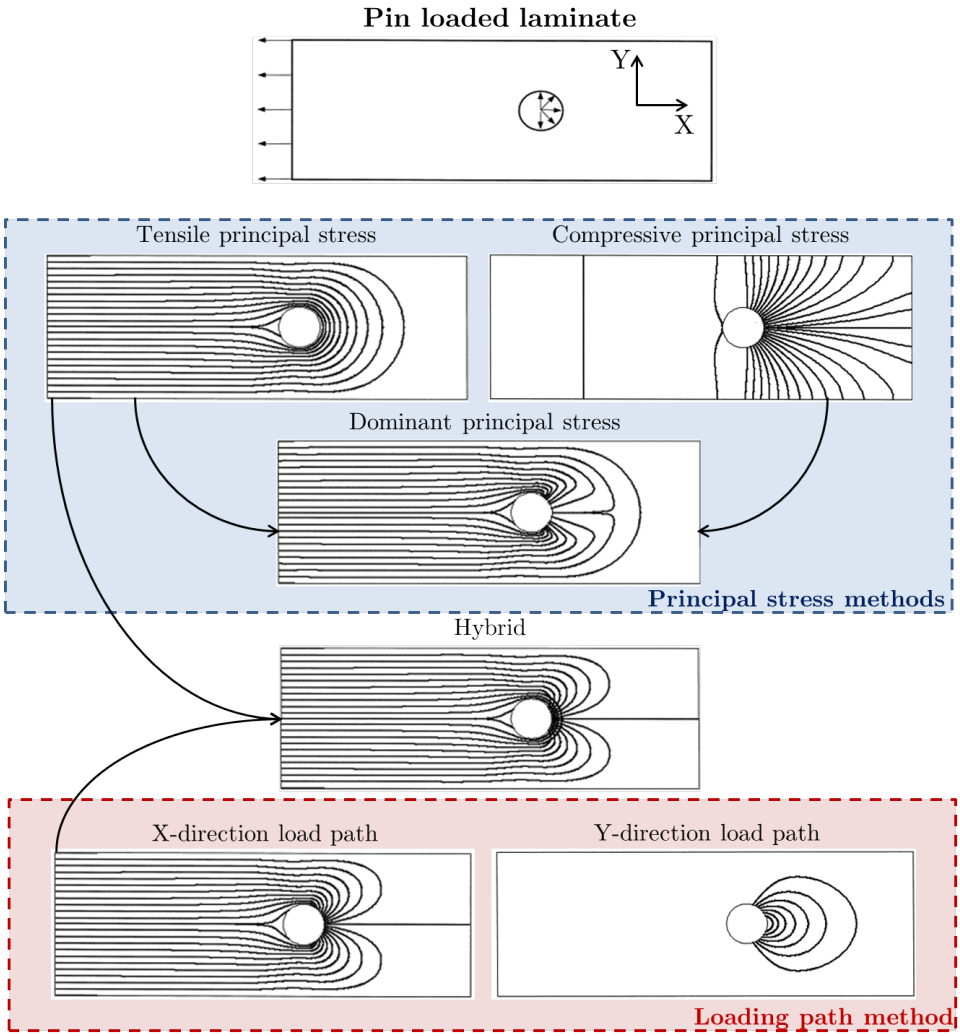

Figure 1.27: Pin loaded laminate design for isotropic material: Trajectories for main stresses and loading paths methods (adapted from Tosh and Kelly (2000))

Tosh and Kelly (2000) also showed that using anisotropic material modifies the computed loading paths. In other words, a loading path is dependent on the material orientations. Consequently, when using anisotropic material like curvilinear fibres, an iterative procedure is required to update the material orientations according to the loading path until changes between both become negligible. Zhao et al. (2021) proposed a comparative study between stress-based load path analysis and other non stress-based methods to determine load-path guided fibre trajectories in composite panels for various load cases.

1.3.3.3 Examples of advanced structural topology and material orientations optimisations

Structural optimisation for orthotropic materials based on strain methods (Pedersen, 1989), stress methods (Ma et al., 1994) and energy-based methods (Luo and Gea, 1998) were developed and showed to be efficient for some simple cases but not in general. The difficulty is to find a method which can be applied to any type of loading conditions. The latter works only determined the optimal material orientations for an orthotropic material in a fixed part geometry

to minimize the compliance. However, taking full advantage of the fibre placement technologies required simultaneous optimisation of the structural topology and the fibre angle all together with the manufacturing constraints which require the continuity and smoothness of the fibre path as well as its morphology, namely the fibre volume, thickness and spacing. Recent works were based on optimisation procedures for simultaneous structural topology and fibre orientation which include the latter manufacturing constraints.

Papapetrou et al. (2020) developed an optimisation procedure where the structural topology and fibre orientations are optimized simultaneously. To take into account the manufacturing constraints, an infill pattern method is then applied either at the end or in-between iterations which locally modifies the fibre orientations resulting from the current iteration to satisfy those constraints. The compliance is modified by the infill pattern method which implies fibre orientation's changes. Consequently, better results are obtained when using the method in-between iterations than at the end of the process since modifying the compliance also influences the structural topology. They used different methods for the structural topology and fibre orientation optimisations as well as the infill pattern strategy. Fig. 1.28 shows the optimized design obtained for these different methods for a cantilever beam study. The methods give different results respecting more or less the path continuity and smoothness. If the streamlines infill pattern method shows the best result in this case, it depends on the problem studied. It is also worth noting that applying the infill pattern method can result in a reduction of the structural compliance. This can be explained by the better continuity and smoothness of the path, which is not necessarily achieved in the initial optimized topology.

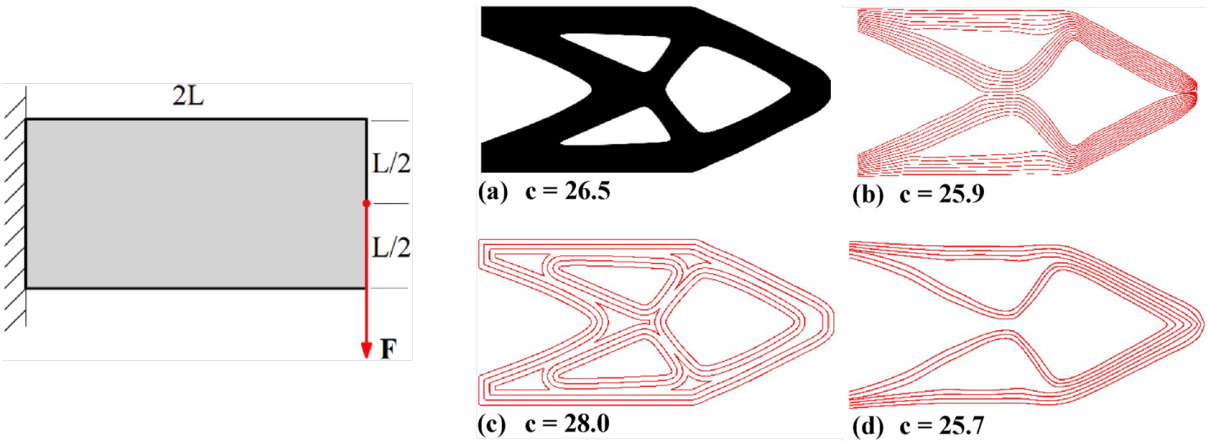

Figure 1.28: Cantilever beam with a point load applied at the free edge: (a) the optimized topology for the cantilever case, (b) the fiber paths created by the Equally-Space method, (c) the fiber paths created by the Offset method, (d) the fiber paths created by streamline method (adapted from Papapetrou et al. (2020))

Li et al. (2021) used a different method where the fibre path morphology is directly taken into account in the structural topology and fibre orientation optimisation process. They used a bi-material approach meaning that two density variables are required instead of one to identify if the element is empty, contains matrix or contains fibre. By setting some global and local constraints on the composite volume and local fibre fraction, the fibre path morphology is automatically generated. Fig. 1.29 shows the result for the optimisation of a Michell beam structure where the red lines correspond to the fibre and the blue color is the matrix.

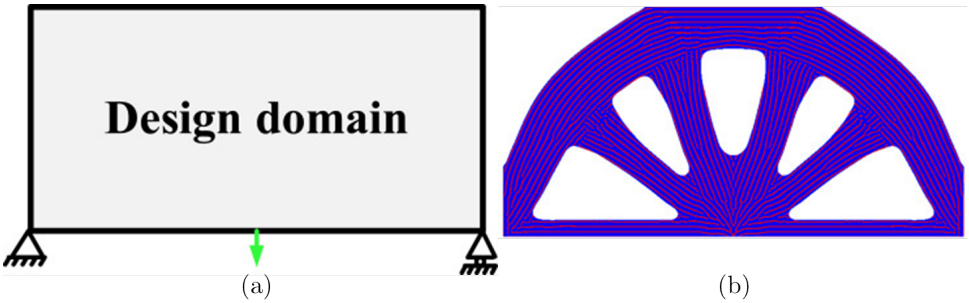

Figure 1.29: Michell beam structure optimisation: (a) Initial domain and loading. (b) The optimized Michell shape fiber-reinforced structure (adapted from Li et al. (2021))

Conclusion

The aforementioned advances in structural topology and fibre orientation optimisation allow the determination of optimal mechanical design for FRC 2D parts that can be manufactured using curvilinear fibres. However, they are limited to 2D parts and need further development to be adapted to the case of 3D shell-like structures. The construction of the fibre deposition path, called path planning, follows the determination of the optimal design. Even if the morphology of the fibre path is given by an optimisation tool, the designer still has to deal with some specific constraints of the fibre placement process used. For instance, in AFP, the path has to obey a minimum cut length and radius, while also avoiding some previously mentioned defects such as tow gaps, overlaps and wrinkles. Moreover, the process parameters to produce a part without defects have to be determined. Besides, simulating the deposition process is also required to ensure the proper manufacturability of the part.

Finally, an efficient and complete tool for the manufacturing of mechanically optimized FRC parts made with curvilinear fibres requires the following attributes:

- A fibre placement technology
- A structural topology and fibre orientation optimisation tool ensuring path continuity, smoothness and providing its morphology
- Multi-objectivity: applicable for any optimisation problem including structural topology and strength, stiffness, buckling stability, failure load and natural frequencies
- A path planning tool
- A manufacturing simulation tool
- A modelling approach to correlate manufacturing defects with manufacturing parameters
- An integrated on-line monitoring for detecting defects and accordingly correct the manufacturing parameters

A graphical representation of the general workflow describing interactions between process planning, design, manufacturing and inspection steps for the AFP technology is presented in Fig. 1.30.

Many efforts have been undertaken to develop such a tool for the AFP technology but other technologies such as TFP did not receive such attention. The next section provides a detailed review of the work achieved herein for the TFP technology and will highlight the missing critical tool that would make TFP technology as interesting as AFP is today.

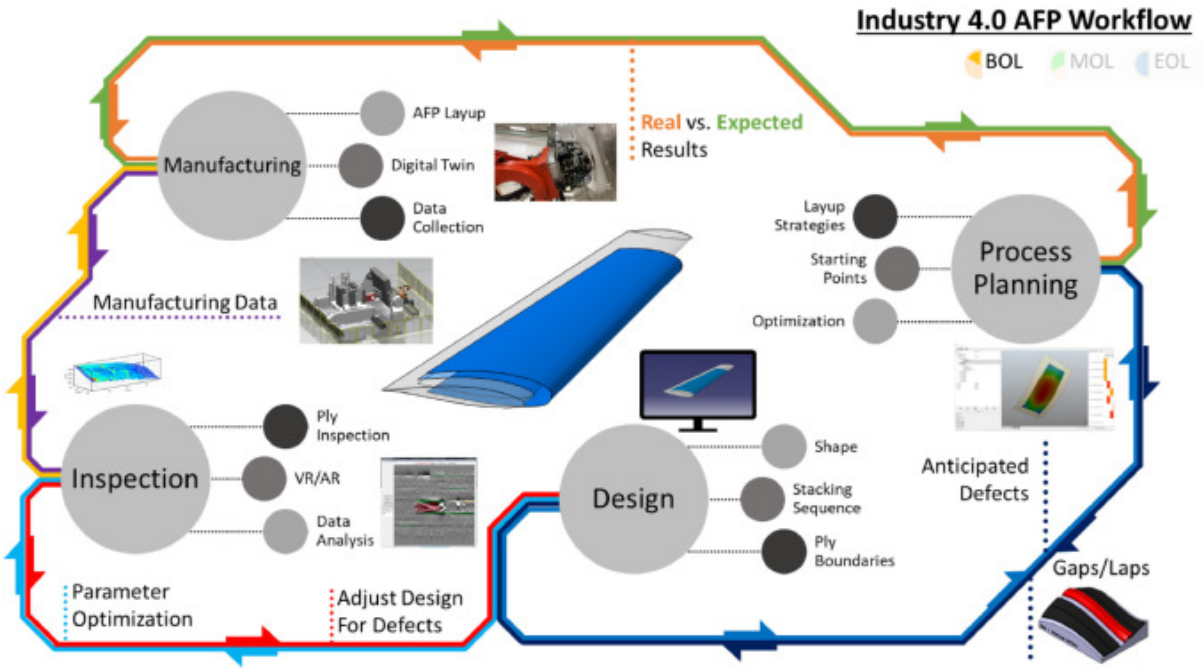

Figure 1.30: Graphical representation of closed loop AFP workflow (Harik, 2020)

1.4 The Tailored Fibre Placement technology: A high degree of design freedom

Introduction

Developed in the 1990s at Leibniz Institute of Polymer Research Dresden, TFP has received less attention compared to the AFP process. It can be explained by the fact that 3D composite parts cannot be manufactured directly by TFP contrary to AFP but requires a forming step which complicates the determination of the optimal design as it will be highlighted in this section. However, contrary to AFP which allows direct fibre deposition on 3D mould surface, forming initially flat preform to obtain 3D shell-like parts is still interesting especially when the complexity of the part generates to much defects using AFP. In this sense, Sun et al. (2021) manufactured 3D shell-like parts with small double curvature using a two-step approach consisting in AFP processing of flat preforms followed by a forming process. They showed that using this two-step approach rather than direct AFP processing onto complex 3D mould could provide easier and better manufacturability. Moreover, it reduces the overall cost due to shorter cycle times when depositing fibres on flat surface. Therefore, this two-step approach can also be used to manufacture 3D shell-like parts with TFP that allows even higher rate deposition than AFP on flat surfaces.
As mentioned earlier in section 1.2, in general, the forming of fibrous reinforcement inevitably implies fibre motions for complex double-curvature parts where the modelling is required to be used as a reliable process in the composite industry. However, as it will be shown in this section, no model exists to simulate the forming of TFP preforms and studies of VAT laminates made from TFP were mainly limited to 2D parts. Consequently, this study can be considered the first contribution to the numerical modelling of TFP preform forming. This section starts with a more detailed presentation of the TFP principle than those given in section 1.3. Moreover, the morphology of the flat preform and studies on the mechanical performances of flat laminates are presented. Next, a review of the works concerning the TFP technology is made. These studies essentially focused on demonstrating the potential of TFP in manufacturing optimal designs for 2D parts containing geometric discontinuities such as the well-known hole tension plate laminate problem introduced in section 1.3. Finally, this section ends with presenting the challenges to be addressed in the manufacturing of 3D optimized FRC parts made by TFP preform forming. Among those challenges, the modelling of TFP preform forming is of first importance and is the subject of this thesis whose objectives and outline are finally presented.

1.4.1 TFP preforming

1.4.1.1 Principle

A flat TFP preform is made of a continuous tow laid down on a backing material that remains in place thanks to double locked zig-zag stitching (Fig. 1.26). Rotation of the embroidery head together with the in-plane displacement of the pantograph allows prescribing curvilinear paths to the fibre tow with high precision. Similarly to additive manufacturing capabilities, variable planar orientations and thicknesses can be achieved in the preform as well as net-shape design avoiding costly and environmentally unsustainable material wastage. The tow direction can vary sharply since a U-turn is achievable making this technology more efficient in designing continuous and smooth fibre paths than AFP, where minimal radius might be to high for manufacturing small to medium parts. Besides, TFP offers a large choice of combinations for the backing material, fibre tows, and stitching yarn, which considerably enlarges the design

space of flat preforms and makes them suitable for any desired consolidation process. A single TFP preform can be made of several tow materials and the backing material can be a polymer film or woven or non-woven fabrics for instance. Dry or commingled tow is used depending on the consolidation process involved. The stitching yarn material is usually polyester although higher performance materials such as aramid are possible options to provide better resistance to delamination.

1.4.1.2 Processing parameters

Several parameters can be controlled to manufacture a TFP preform, they are listed hereafter.

- Stitch length
- Stitch width
- Upper-stitch tension
- Lower-stitch tension
- Incoming tow tension
- Stitching speed

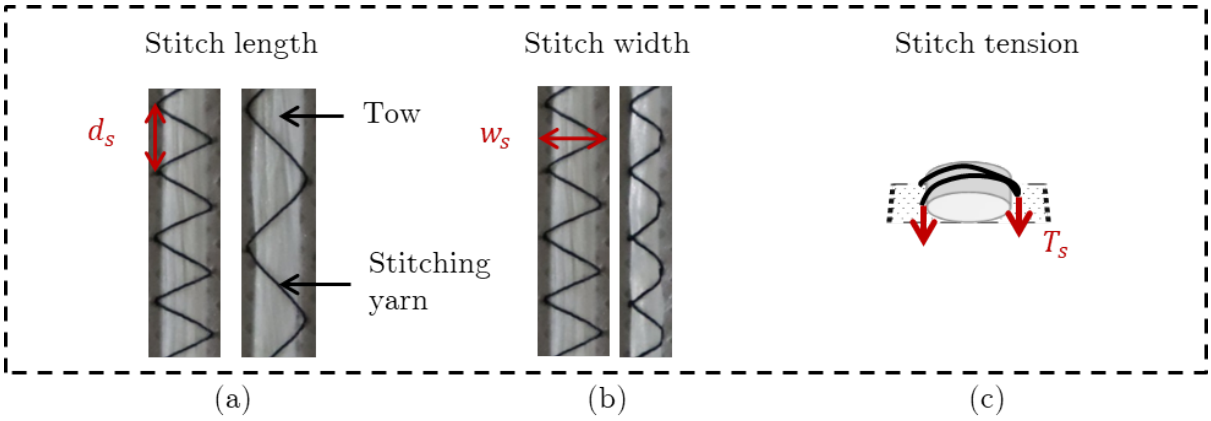

Figure 1.31: Stitching parameters: (a) Stitch length (d_s), (b) stitch width (w_s) and (c) stitch tension (T_s)

Firstly, two stitching parameters, namely, the stitch length and stitch width, illustrated in Fig. 1.31, can be considered as design parameters because they are defined during the path planning process. They influence the fibre tow placement and layer thickness. In this work, the choice was made to define the stitch length as the characteristic distance of the stitching pattern following the direction of the tow whereas the stitch width is the characteristic distance in the orthogonal direction of the tow. Other authors like Uhlig et al. (2016) adopted the opposite definition. Consequently when referencing results of other works with respect to these parameters, the names stitch length and stitch width will always referred to the definitions adopted in this work. Small stitch distances are required to achieve better trajectory accuracy for high in-plane curvatures or even a U-turn. The stitch width together with the tow morphology and cross-section behaviour can affect the layer thickness, since the tow can be more or less flattened on the backing material or compacted transversely, which makes it thicker and directly influencing the fibre density. One limitation of the TFP technology is the current impossibility to vary the stitch width at every point of the preform contrary to the stitch length. Another parameter, which is not a built-in feature of TFP machines, is the control of the upper stitch tension. An additional force sensor able to control the upper-stitch tension was added to the

TFP machine used in this work at IRT Jules Verne. This is a manufacturing parameter since it can be adjusted during the tow placement process, but is not remotely controlled and required manual intervention by the operator. The lower-stitch tension can be set by measuring the resistance of the delivery mechanism of the stitching yarn bobin. It can also be adjusted during the manufacturing if necessary, but changes are made by hand. Then, the incoming tow tension is ensured by the feeding tow mechanism. Finally the stitching speed is a manufacturing parameter that can be set through the machine controller, but cannot be specified in the placement planning process to adjust the speed at specified locations.

1.4.1.3 Process-induced defects

Similarly to AFP, the TFP technology suffers from process-induced defects that are inherent to placement processes requiring in-plane bending of fibre tows. As highlighted by Kim et al. (2011), a high path curvature leads to cross-sectional deformation of the tow which modifies the local fibre density (Fig. 1.32 (b)). Due to the tension applied to the incoming tow during the placement, the neutral axis of the tow tends to move inwards the center of curvature rather than being well distributed over the width of the stitching path, as it is the case in Fig. 1.32 (a), and leads to wrinkles.

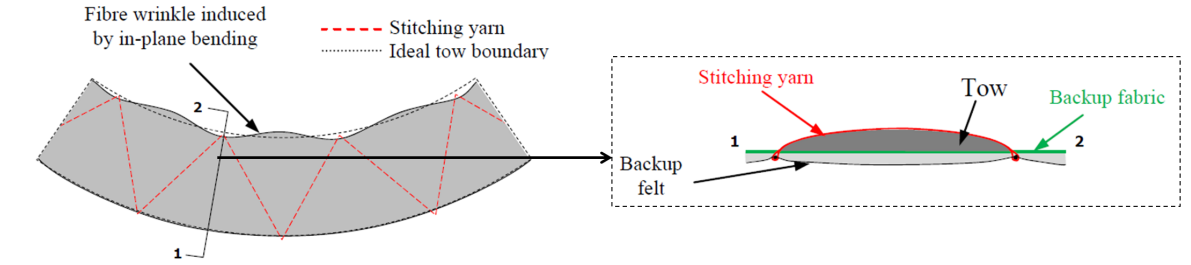

(a) Ideally placed fibre tow with small wrinkles

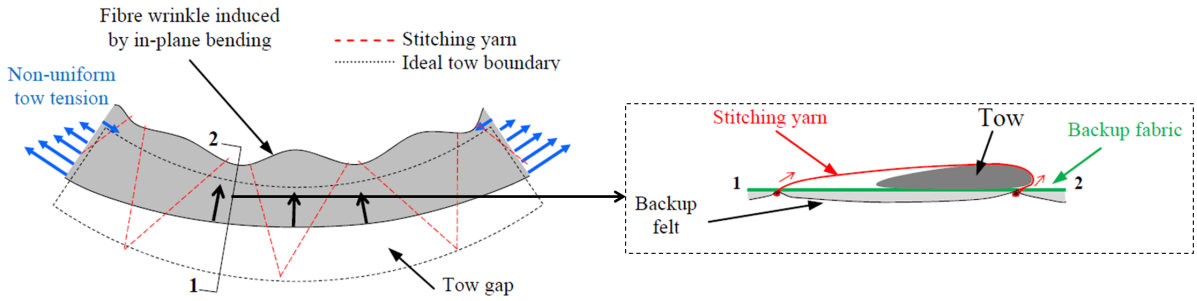

(b) High fibre tow wrinkling due to excessive incoming tow tension

Figure 1.32: TFP in-plane bending induced defect (adapted from Kim et al. (2011))

Moreover, due to the stitching pattern, the fibre tow has a slight in-plane undulation, making the fibre not perfectly aligned in a straight path (Fig. 1.33). Uhlig et al. (2019) studied the waviness and fibre volume content of continuous unidirectional carbon fibre reinforced plastics made by TFP. They studied the influence of the stitching yarn material as well as the stitch length and stitch width on the in-plane waviness of the tow using Fourier analysis and determined both mean fibre volume content within the tow and within the layer from optical micrography of the manufactured laminates. They showed that decreasing the stitch length and increasing the stitch width leads to an increase of the tow and layer fibre volume contents. Concerning the in-plane waviness, the higher the stitch length, the lower the waviness amplitude. In particular, the wavelength was shown to be equal to the stitch length. In a previous study Uhlig et al. (2016) modelled the geometry of an elementary cell in an unidirectional TFP laminate to describe the

effect of the stitching pattern on the fibre volume content. They where able to represent the in-plane and out-of plane waviness produced by the stitching yarn as shown in Fig. 1.34.

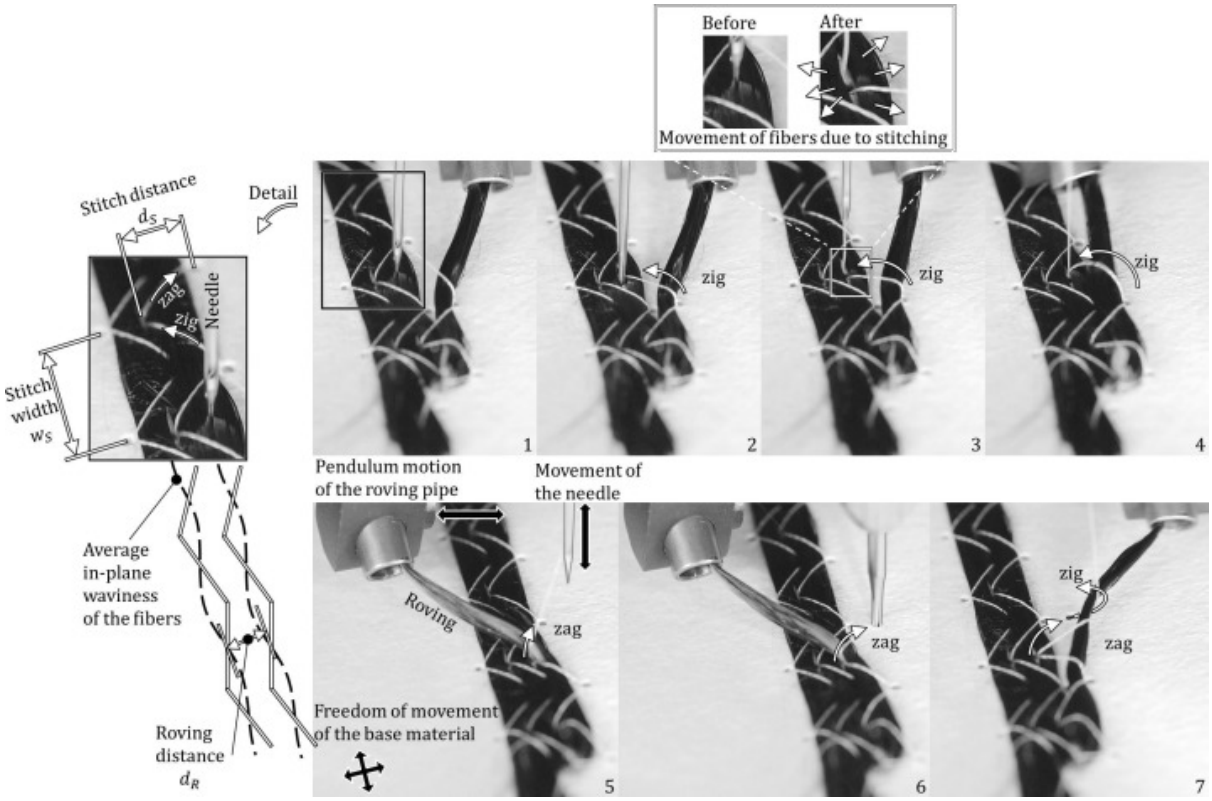

Figure 1.33: Snapshots of the TFP process (1–7) showing the placement of a third roving row and the sewing with a zigzag stitch pattern while the roving pipe moves from right to left. Details (left and top) with TFP process parameters and resulting fiber waviness due to stitching (Uhlig et al., 2016)

Uhlig et al. (2016) also showed that the presence of the stitching yarn creates rich resin pocket zone around the puncture point by locally displacing the tow. Providing more degree of freedom over the TFP parameters would considerably enhancing the TFP technology by allowing greater control over the fibre volume content in TFP layers. This also requires to develop models able to predict the properties of the TFP layer according to the TFP parameters as the mentioned studies did. Consequently, enabling the stitch width to be varied and assigned locally in the path planning process as well as controlling the stitch tension and the incoming to tension are improvements TFP machine designers should be concerned with.

The effects of increasing the stitching parameters on TFP preform and fibre tow characteristics are summarized in Table 1.2. In this table, V_f^{tow} stands for fibre volume content in tow, V_f^{layer} for fibre volume content in layer, A_{ip} for in-plane waviness amplitude, A_{op} for out-of-plane waviness amplitude and A_T for tow's cross section.

Another defect which is inherent to stitched fibrous reinforcements is the damage induced by the tow puncture. In Crothers et al. (1997) before the zig-zag stitching was developed for TFP, the fibre tow was punctured, which leads to fibre damage. Thanks to the zig-zag stitching, the puncture points are located on each side of the tow instead of inside. However, when manufacturing a multi-layer TFP preform in a single shot, the lower layers are punctured by the stitching yarn of the upper layer. Besides, when TFP is used as local reinforcement of another fibrous reinforcement, direct stitching on the fibrous reinforcement will damage its fibres. Crothers et al. (1997) compared the performances of different assembling methods to

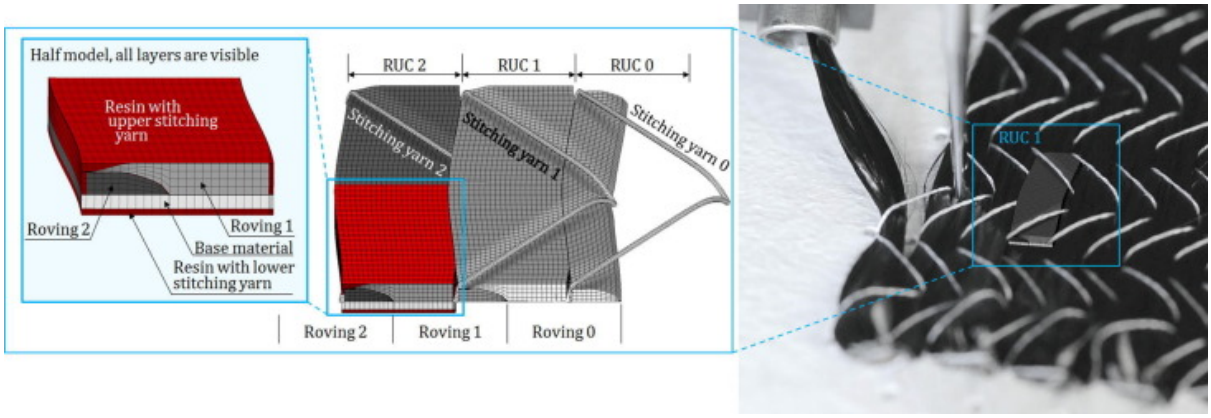

(a) Representative unit cell (RUC), where different layers are visible. All layers are shown in the half model (detail left). The stitching yarn is shown only in this illustration but is considered as resin material in the simulation. On the right the RUC is graphically embedded in the textile preform during the stitching process.

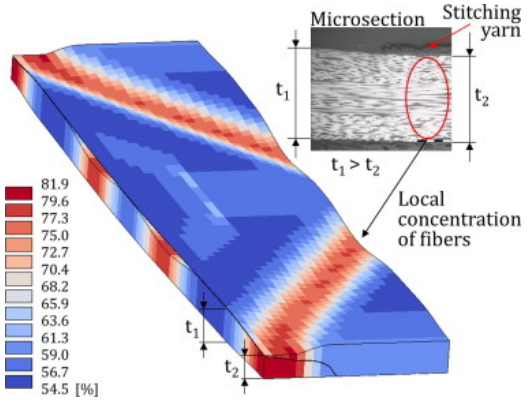

(b) Local fiber volume content of the CFRP volumes

Figure 1.34: In-plane and out-of-plane waviness in TFP layer (adapted from Uhlig et al. (2016))

bond the TFP reinforcement to the fibrous reinforcement without over-stitching it.

1.4.1.4 Mechanical performances

To demonstrate the potential of the TFP technology, it was necessary to investigate its mechanical performances in comparison with conventional fabrics or tape laminates manufactured with ATP. Besides, characterising the influences of the previously mentioned process-induced defects on the mechanical properties of TFP parts is required to ensure that they did not counteract the benefits resulting from optimal curvilinear fibre placement designs.

Mattheij et al. (1998) compared the static properties of glass and carbon UD-like TFP laminates with those of tape laminates and 2D woven fabrics. They showed that tensile strength of UD

Table 1.2: Effect of stitching parameters on TFP preform and fibre tow characteristics

Effect of \ Characteristics	V_f^{tow}	V_f^{layer}	A_{ip}	A_{op}	A_T
$\nearrow d_s$	$\searrow$	$\searrow$	$\searrow$	$\searrow$	x
$\nearrow w_s$	$\nearrow$	$\nearrow$	x	x	$\nearrow$ width $\searrow$ height
$\nearrow T_s$	$\nearrow$	$\nearrow$	$\nearrow$	$\nearrow$	$\searrow$

TFP was close to UD tape and higher than woven fabrics. However, the compressive strength was significantly lower than tapes and thereby affected also the flexural strength. The latter was attributed to the damage caused by the stitching process which splits apart single fibres inside the tow and also creates in-plane and out-of-plane waviness. Moreover, the ultimate tensile, compressive and flexural stresses of UD glass TFP are similar to those of UD tapes.

In the previously mentioned work by Uhlig et al. (2016), an elementary cell of unidirectional TFP laminates was modelled using FEM to measure the impact of the in-plane and out-of-plane waviness on the tensile strength of the laminate. They also performed experimental measurements with tensile tests that showed good agreement. They obtained about 2% reduction compared to an ideal unidirectional laminate with no waviness, which agreed with the observations of Mattheij et al. (1998).

Uhlig et al. (2010) compared several lay-up configurations of open-hole tension carbon fibre laminates made from NCF, TFP and braids. They performed static tensile tests to measure the strength as well as cyclic tensile tests to observed the damage behaviour of the different laminates. They showed that in general, TFP and NCF specimens provided similar tensile strength and damage behaviour during cyclic and tensile tests. Fig. 1.35 shows the failure mode of the different reinforcements for the $[+45/0/-45]_s$ lay-up configuration with and without cyclic preloading.

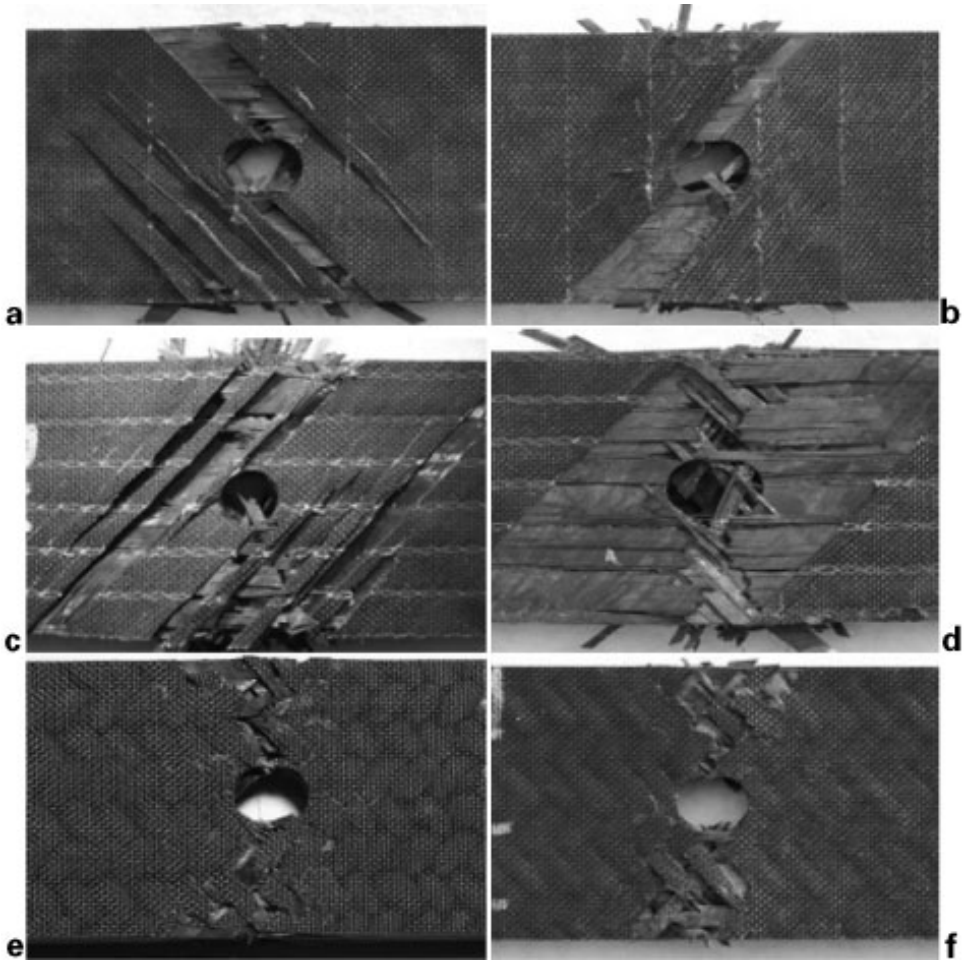

Figure 1.35: Fractographic images of tested $[+45/0/-45]_s$ specimens (a) TFP, (b) cyclic preloaded TFP, (c) NCF, (d) cyclic preloaded NCF, (e) braids, (f), cyclic preloaded braids (Uhlig et al., 2010)

Transition

TFP is an effective tool to manufacture preform with curvilinear fibre paths. Process-induced defects, such as in-plane and out-of-plane waviness, make UD TFP laminates not exactly as mechanically efficient as conventional laminates especially in compressive mode. TFP was not developed to manufacture straight fibre laminates. Manufacturing curvilinear fibre laminates with TFP allows outperforming conventional laminates by expanding the optimal design space. The next section reviews the main applications of TFP, especially for 2D parts.

1.4.2 A review of studied TFP applications for manufacturing 2D parts

The major field of application of TFP is the manufacturing of small to medium size lightweight composite structures in the aeronautic, automotive or energy industries. As reviewed by Mecnika et al. (2015) TFP can also be applied to the manufacturing of smart structures which incorporate deformation sensors or heating components for instance. This section presents some studies about the main applications of TFP for manufacturing lightweight composite structures. Therefore, it will give an insight of the motivations behind the development of the TFP technology and the expansion of its field of application.

1.4.2.1 Removing stress concentration at geometric discontinuities

As introduced in section 1.3, the first application of curvilinear fibres was the manufacturing of composite laminates containing geometric discontinuities such as open holes that are required for assembling structural components, especially in the aircraft industry. By using curvilinear fibres, stress concentration in such area can be removed, which considerably increases the structural strength of the part. Consequently, some studies investigated the ability of the TFP technology in manufacturing stress concentration free part in notched laminates. Most of the works presented hereafter used Finite Element Analysis (FEA) based on main stress directions to determine the optimal fibre orientations around the hole.

Crothers et al. (1997) studied the combination of conventional textile reinforcements with local TFP reinforcement around holes in single and double bolt loaded plates. A multi-axial warp knitted (MWK) E-glass fabrics with $[0/45/90/-45]$ lay-up configuration was used as based material and E-glass fibre tows (1x1200 tex and 2x1200 tex yarns) for the TFP reinforcement. Vacuum Injection Moulding (VIM) and Resin Film Infusion (RIF) were used for impregnation. The assembly of the MKW and the TFP reinforcement was performed differently to study the effect of stitching directly on the conventional textile reinforcement or using adhesive or hand stitching for assembling both components prepared separately by using another backing material for manufacturing the TFP reinforcement as illustrated in Fig. 1.36. Specific strength improvements varying between 15-55% were obtained depending on the assembling strategy compared to a laminate without TFP reinforcement. The second assembly strategy using adhesive to bond the impregnated conventional textile and TFP reinforcements shown the best result. It was attributed to an effect known as interleafing, reducing interlaminar shear between the bonded interfaces.

Gliesche (2003) also investigated the combination of multiaxial non-woven carbon fabrics with $[(-45/90/+45/0)2]_s$ lay-up configuration and a TFP reinforcement made of Tenax HTA 5331 12K carbon fibre tows impregnated with Epoxy Rütapox VE 3966. They directly stitched two TFP reinforcements on front and back side of the conventional textile around an open-hole. During the tensile tests, they used optical deformation measurements using the Grating Method to visualize the modification of the strain field when adding the TFP reinforcement. The specific fracture load values for the reinforced plate reached 94% of that of the unnotched

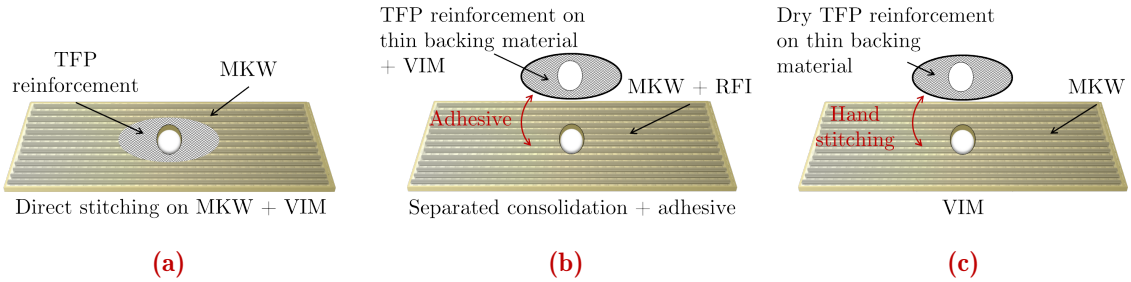

Figure 1.36: Different strategies to assemble conventional textile and TFP reinforcements (Crothers et al., 1997)

plate (reference), while the notched plate without reinforcement only reached 61%. Beside, the fracture occurred outside the reinforcement demonstrating their success in removing the stress concentration at the edge of the hole (Fig. 1.37 (a)).

Koricho et al. (2015) compared 4-ply TFP open-hole laminates made of S2-glass fibre tows of size 50K impregnated with SC-15 epoxy (Applied Poleramics Inc., CA) using vacuum assisted resin transfer method. Among the specimens shown in Fig. 1.37 (b) small and large curvatures around the hole were compared. The best curvilinear design (with small curvatures) reached 92.7% of no-hole specimen tensile strength.

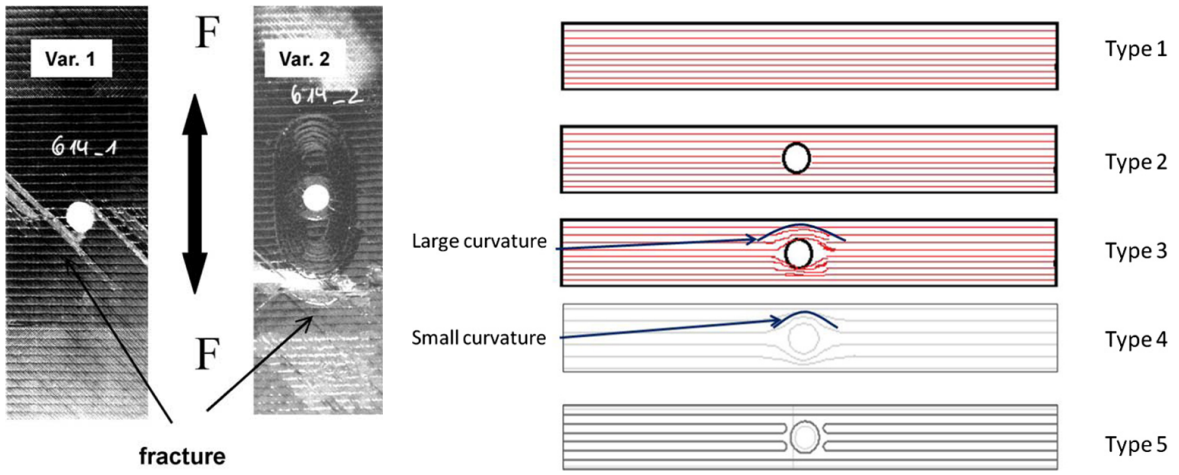

Figure 1.37: (a) Photograph of the plates with fracture (Gliesche, 2003), (b) Specimen profiles created using tailored fiber placement and conventional drilling. (Koricho et al., 2015)

The latter works manufactured thermoset polymer composites. A more recent study made by El-Dessouky et al. (2019) investigated the open-hole laminate problem using carbon/nylon 6 commingled fibre tows to study the properties of thermoplastic TFP laminates. They compared two different TFP patterns to add a circular reinforcement around the hole based on main stress directions principle. As Koricho et al., the laminates were produced only from TFP layers (seven) and did not use a conventional textile reinforcement as backing material as Crothers et al. (1997) and Gliesche (2003) did. The best design showed only 10% reduction in tensile strength compared to the un-notched specimen also made entirely by TFP.

Katagiri et al. (2021) studied the same problem with carbon TFP laminates impregnated with epoxy using Electrodeposition Resin Molding. They use this impregnation technology to show improvement in avoiding void formation which is unavoidable in curvilinear fibre laminates

produced by vacuum assist resin transfer moulding method (Koricho et al., 2015), due to the modification of the resin flow compared to unidirectional laminates. They also observed an improvement in tensile strength of TFP laminates with curvilinear fibres circumventing the hole compared to conventional drilled TFP laminates.

The most recent study about optimisation of open-hole tensile plate laminate made by combining a conventional reinforcement with TFP layers (Almeida et al., 2020) showed that using principal stress directions do not give the optimal design. To obtain a manufacturable TFP layout, they started with an arbitrary parametrisation of the initial TFP pattern. For this loading case, fibres were initially placed parallel to the loading axis. Then, the parameters controlling the pattern can be adjusted during the optimisation process and are constraint to an orthogonal displacement of the fibres. The optimisation is driven by compliance minimisation and both the thickness and the fibre orientation (through the parameters of the TFP pattern) are modified during the iterations. This strategy allows obtaining a manufacturable layout with curvilinear fibres placed only where needed. However, the required choice of an initial parametrisation can limit the degree of freedom of the optimisation process. The optimal solution of the proposed approach can be different from the true optimal design, especially for more complex geometries and loadings. Details about their optimisation tool called Direct Fiber Path Optimization (DFPO) can be found in Bittrich et al. (2019). Fig.1.38 shows the referenced fibre layout (a), the result obtained with the DFPO tool (b) and the principal stress design (c).

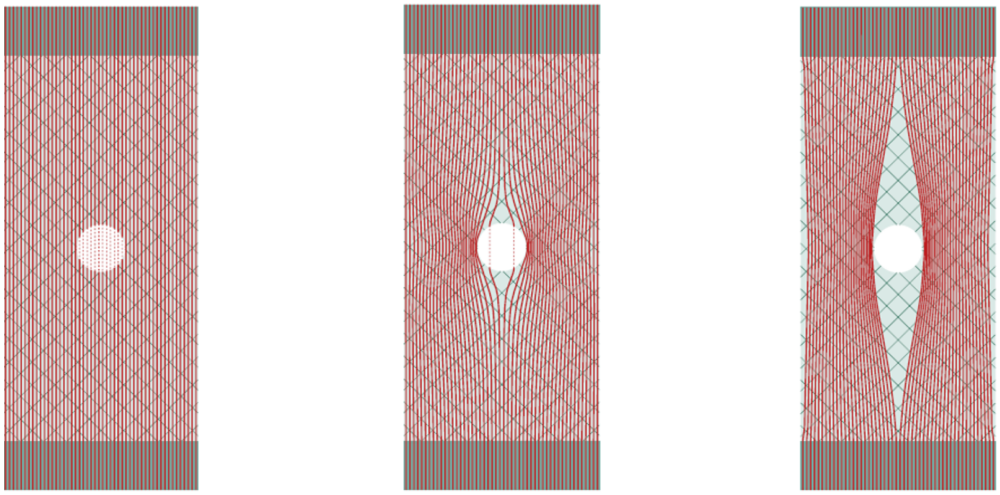

Figure 1.38: Fiber layouts for open-hole specimens: reference layout with equidistant and parallel fibres (a), stiffness optimization (DFPO) (b), and principal stress design (c). The TFP layer is placed on top of the base material(Bittrich et al., 2019)

All the previously cited works agreed that TFP has a great potential for local reinforcement applications in highly stressed regions due to the presence of geometric discontinuities such as open-holes. Adding TFP on top of another conventional textile or manufacturing a whole laminate with TFP both provide a considerable increase in tensile strength compared to no-reinforced open-hole laminates.

1.4.2.2 Manufacturing optimized lightweight structures

In general, TFP has been used to manufacture small to medium sized lightweight structures whose optimal design has been determined using structural topology and fibre orientation optimisations. For instance, Spickenheuer et al. (2008) studied the case of an unequally loaded tensile plate. They firstly determined the shape of the part using structural topology opti-

misation before determining the fibre orientation using an optimisation tool named Computer Aided Internal Optimisation (CAIO) specifically design for this purpose. Fig. 1.39 shows the initial design space (a) and the resulting design (b). CAIO was further enhanced to integrate multi-layer design optimisation. Details about this tool can be found in Voelkl et al. (2020), where they studied and discussed the efficiency of their method for multi-layer optimisation using a notched plate, a mounting bracket and a B-pillar demonstrator. Spickenheuer et al. pointed-out the simplicity of the studied case and the needs for investigating more complex parts with complex loadings. Moreover, using sequential optimisations for the topology and fibre orientations rather than a simultaneous method might be limited to this type of simply loaded and simple geometry cases.

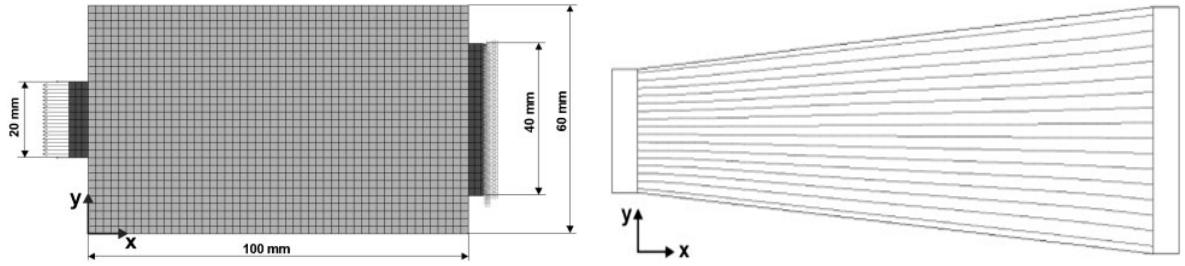

Figure 1.39: (a) Initial design space of the unequally loaded tensile plate, (b) Topology and fibre orientation results after sequential structural topology and fibre orientation optimisations (adapted from (Spickenheuer et al., 2008))

Uhlig et al. (2013) manufactured a load-adapted bladed rotor made of carbon fibre reinforcement using TFP and showed improvements in both burst rotational frequency and rotor mass. They obtained an operational speed about 35% higher than that of part made of aluminium alloy by combining tangential and radial TFP layers. However, they milled an initial disk shape to create the 17 blades and thereby did not benefit from the net-shape capability of the TFP technology. Fig. 1.40 summarizes the manufacturing process they used.

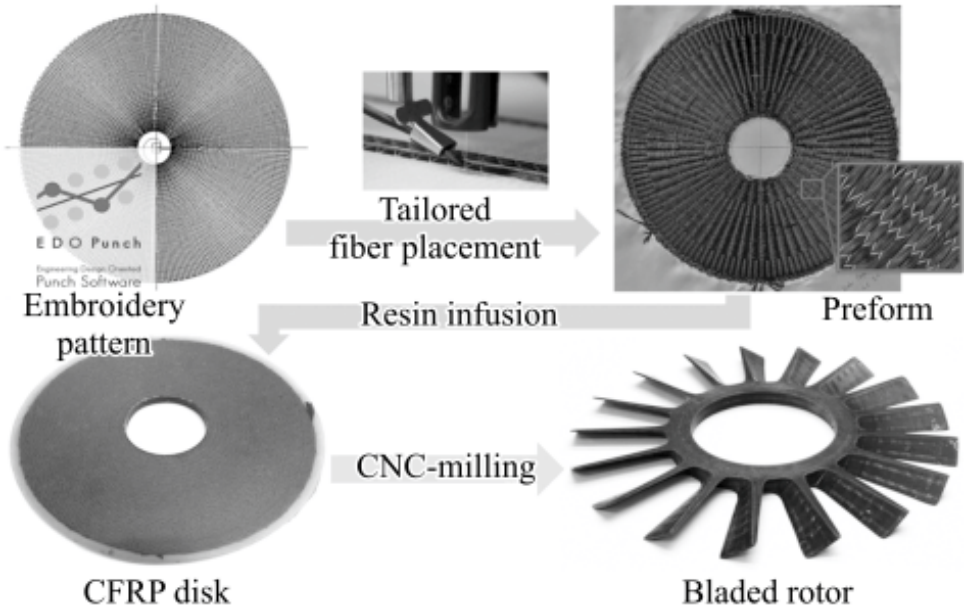

Figure 1.40: Manufacturing steps required for the bladed CFRP rotor developed (Uhlig et al., 2013)

Based on a sequential structural isotropic topology optimisation and a cross-section optimisation, Almeida et al. (2019) manufactured a brake booster with 330% enhancement of the specific stiffness compared to an isotropic stacking sequence of conventional reinforcements. The cross-section optimisation based on a genetic algorithm and performed after the structural topology optimisation provided information about the optimal TFP pattern or morphology, namely the roving orientation and spacing which ensured the manufacturability of the resulting fibre layout. They also showed that the cross-section optimisation allows increasing by 22% the specific stiffness of the brake booster compared to the structural topologically optimised design. Although an anisotropic structural topology optimisation tool as those presented in section 1.3 might give better results, since the fibre orientation influences the optimal topology, the specific stiffness improvement compared to a conventional straight fibre design is convincing. They also studied the specific stiffness of a brake booster design (PS) using 2-layer, following the main principal stress (1^{st} layer) and its transverse direction (2^{nd} layer). Fig. 1.41 shows the results for the four designs.

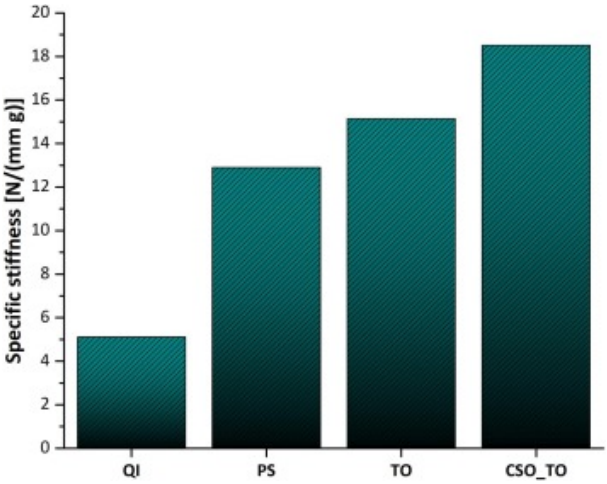

Figure 1.41: Specific stiffness for all brake boosters investigated in (Almeida et al., 2019): Quasi-Isotropic design (QI), Principal Stress design (PS), Topology Optimisation design (TO), Cross-Section Optimisation and Topology Optimisation design (CSO-TO)

The structural topology optimisation often leads to truss-like structure such as the optimal shape of the bicycle brake booster shown in Fig. 1.42 (a). One potential issue with this type of design is the determination of the TFP pattern at intersection points of branches. Richter et al. (2019) investigated several way to design the TFP pattern at intersection points in such truss-like structure. They studied a T-shape and Y-shape branching with tree different patterns (straight, fanned out and merging) shown in Fig. 1.42 (b). They showed both experimentally and numerically that the fanned-out design, where fibre tow spacing is increasing, leads to a better structural stiffness than parallel or merging patterns.

1.4.2.3 Expanding TFP capabilities to the design of 3D FRC parts

The main applications of TFP developed herein focused on manufacturing optimised 2D parts based on structural topology and fibre orientation optimisations. However, since a couple of years, some works have shown interest in using the TFP technology to manufacture 3D parts.

The first study by Fial et al. (2018) focused on manufacturing a small 3D shell-like part via TFP using folding mechanisms rather than true forming, which is known to eventually lead to defects like wrinkles as shown in section 1.2. Once they determined the optimal fibre path on the 3D structure, they used a numerical tool to determine the 2D TFP pattern (Fig. 1.43 (a)). During forming, fibre orientation changes are unavoidable, thereby they decided to cut the glass

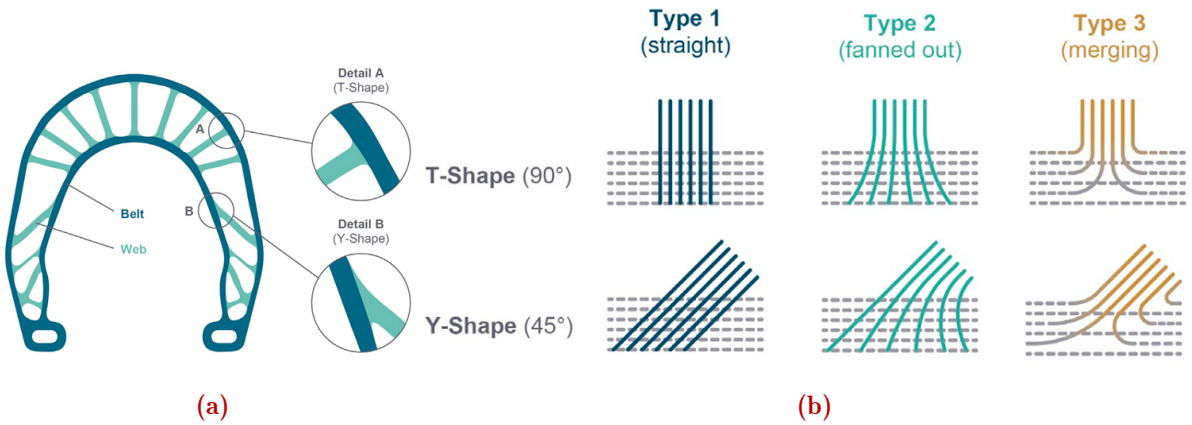

Figure 1.42: (a) A bicycle brake booster with a truss-like structure resulting from topology optimization and two marked distinctive intersection point configurations: T- and Y-shape-like geometries, (b) Illustration of the types of fibre patterns (adapted from (Richter et al., 2019))

fibre fabric that served as a backing material in the corner of the structure, which has double curvature. However, cutting the fibre in the corner will considerably weaken the structure in these regions. In order to reinforce those regions, they placed several fibre tows with the TFP machine that span the cut regions. Then, these fibre tows are pulled-out during the forming process and drove the folding of the backing material (Fig. 1.43 (b)). This way, they avoided complication with design implying true forming on double curvature parts. The determination of the stitching parameters allowing sufficient sliding of the fibre tows in the stitching path was achieved in a previous study (Bohler et al., 2015).

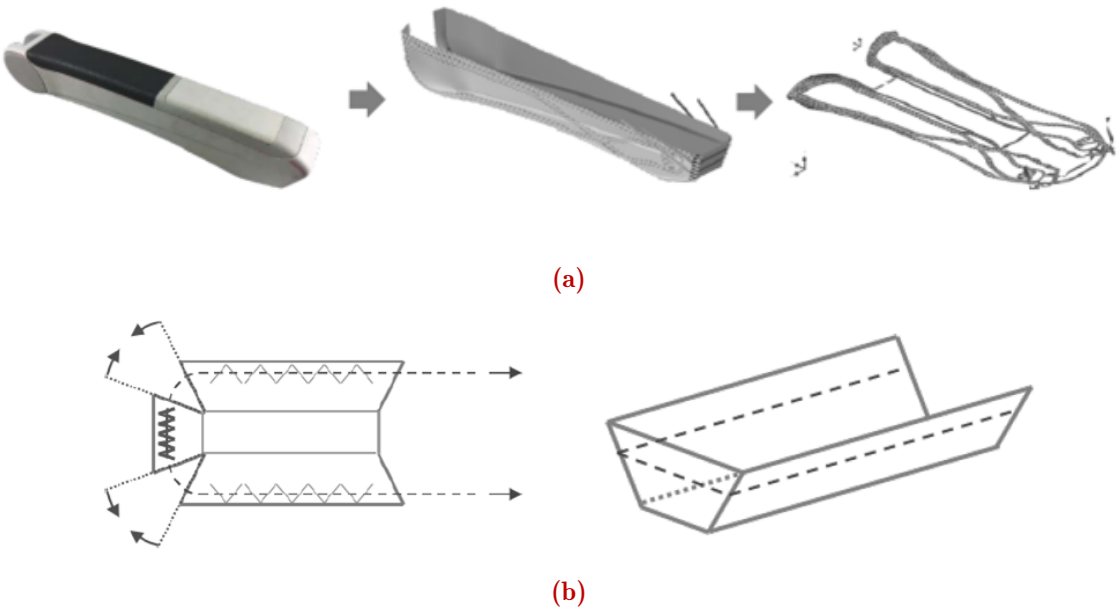

Figure 1.43: (a) Derivation of the 2-dimensional stitching paths from the target structure (left). Based on a numerical analysis a mesoscopic textile model is created (middle). A reverse draping simulation creates the flat pattern for the creation of the 2-dimensional preform (right). (b) Pre-cut base material with manipulated reinforcement yarn (dashed line) and final structure represented by the folded base material and one exemplary manipulated reinforcement yarn (dashed line) (adapted from Fial et al. (2018))

More recent works were also based on designing 3D parts manufactured by TFP and used the foldable property of the flax preform by adjusting the fibre orientations to tailor the bending stiffness in regions to be bent to form the 3D shape. The fact that they did not need a mould to form the flat reinforcement is one of the main advantages of their approach. Costalonga Martins et al. (2020) manufactured a stool of 1 kg able to support a load of 80 kg using curved folding principle and combined both TFP and Coreless Filament Winding (CFW) technologies. The flat shape was determined using a relatively simple structural topology optimisation tool. After the dry TFP preform has been created, the flat preform is infused before being folded into a spatial object and cured. Then, fibre tows are manually added using filament winding techniques. The manufacturing process and the final part are shown in Fig. 1.44.

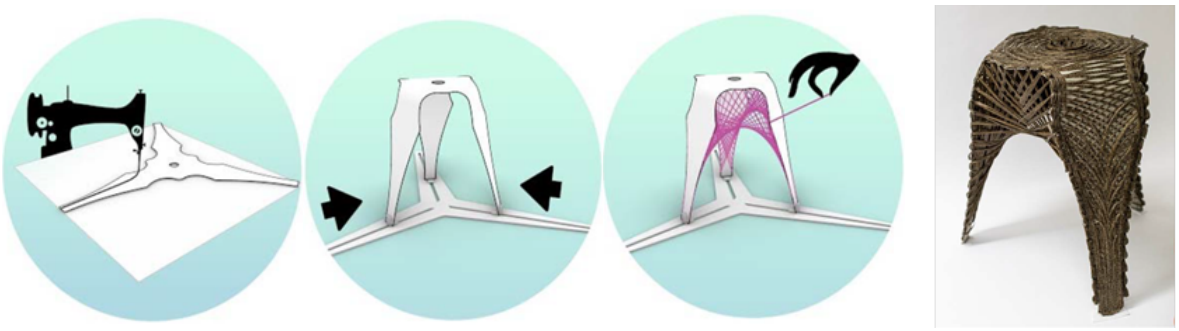

(a) (b) (c) (d)

Figure 1.44: FlexFlax Stool: (a) Stitch: A tailored natural fiber textile is designed and produced in its flat form. This textile is infused with resin to create a fiber composite; (b) Bend: The activated polymer is formed into shape, enabled by specific fiber bending patterns; (c) Weave: This form becomes a permanent winding frame, upon which natural fibers are placed through coreless filament winding. Once cured, the TFP and CFW elements become a co-dependent functional and structural system in the form of a stool. (d) Final prototype (adapted from Costalonga Martins et al. (2020))

However, this multi-method manufacturing process, especially the filament winding, was time consuming and labour-intensive. To simplify the manufacturing process, Rihaczek et al. (2020) enhanced the stool design by using TFP only and integrating more functionalities in the flat preform to be folded. They also developed a continuous parametric design to production workflow of curved folded Natural Fibre Reinforced Polymer (NFRP), namely bio-composites, to automate the process. They studied two forming processes, one based on a minimal scaffolding rods and the other by self-weight of the infused preform. The initially opened legs' surface of the stool were closed using additional manual stitching as shown in Fig. 1.45. They produced stools with different number of legs. Moreover, they also manufactured small kinetic structures enabling reversible transformation from flat to 3D structure. They made two samples to illustrate the concept of compliant curved hinges manufacturable using the TFP technology which are shown in Fig. 1.46. Another work similar in terms of design to production approach can be found in Sippach et al. (2020).

The last study which is worth noting, was done by Takezawa et al. (2021) who manufactured an automobile hood and a marine propeller blade, which both are doubly-curved shell structures. To form a flat TFP preform on such non-developable surfaces, they divided surfaces into developable strips by cutting the base material rather than cutting the reinforcing fibres, which would have resulted in the weakening of the structures. They developed a flattening algorithm able to flatten strips that have been determined on the initial 3D surface using sets of arbitrary orthogonal curves. The latter theoretically allowed them to choose between Gaussian, principal stress or stretch curves, which are all orthogonal sets of curves. The preform is made of two

Figure 1.45: Stitching of the legs (a) and forming of preform under self-weight (b). Closeup photography of the stitched legs after curing (c) (Rihaczek et al., 2020)

(a) Sample 1 **(b)** Sample 2

Figure 1.46: Initial (left) and folded states (right) for two samples with compliant curved hinges (Rihaczek et al., 2020)

separated layers, one whose fibres are aligned in each strip with the first curve and another one where fibres are aligned to the orthogonal curve. The whole manufacturing process from flattening to production is illustrated in Fig. 1.47. Their cutting strategy allows keeping connections between the strips which means that a continuous fibre path can be achieved between adjacent strips.

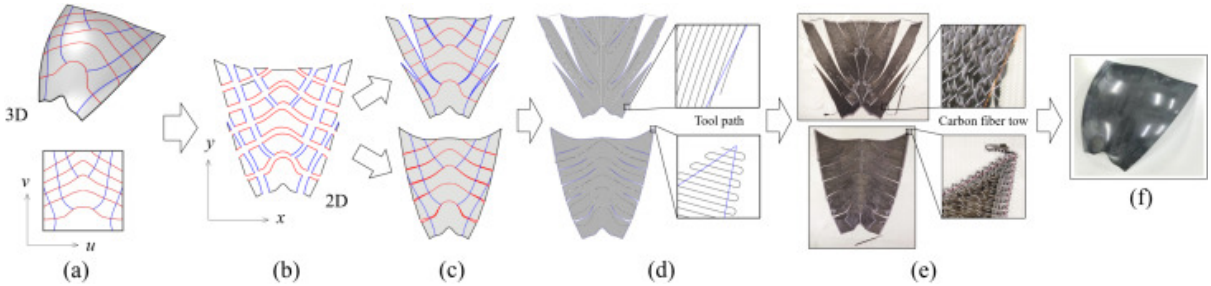

Figure 1.47: Overview: (a) tessellation of the input surface into structured quadrilateral patches (either in parametric or 3D space), (b) unfolding of these patches into quads, (c) aligning the flattened quads in two ways, (d) one stroke tool path generation, (e) tow placement on the flattened surface using the TFP embroidery machine to fabricate preforms, and (f) CFRP formation (Takezawa et al., 2021)

Transition

The different applications which have been presented make TFP an attractive technology for the manufacturing of FRC parts in the most advanced industries where reducing weight while maintaining the structural stiffness of the parts is needed. TFP allows taking more advantage of the intrinsic anisotropy of fibres by placing them only where needed

with the optimal orientation. Besides, its net-shape preforming capability allows drastic reduction of material wastage. Moreover, it has been shown that TFP can be used in combination with other conventional textiles or as a whole preforming tool, which makes it very versatile. The first development stage of TFP was focused on manufacturing structural topology and fibre orientation optimised 2D parts. However, recent efforts were undertaken to expand the applications of TFP to the manufacturing of optimised 3D parts by using either foldable preforms or forming with backing material cuts to facilitate the transformation. Therefore, transforming a flat TFP preform into a 3D shell-like structure without resorting to folding or backing material cuts is not straightforward. The last section of the introductory chapter presents the challenges to de addressed to fully exploit the TFP technology in the manufacturing of 3D FRC parts. This will lead to the challenges this work is concerned with.

1.4.3 Challenges in 3D optimized composite parts made by TFP preform forming

This section aims at highlighting the challenge to address in the manufacturing of 3D optimised composite parts made by TFP preform forming. Issues concerning the determination of optimal structure topology and material orientation in 3D shell-like structures are firstly presented. The second challenge specific to the manufacturing of 3D shell composites made by forming, is the determination of the flat TFP preform from the targeted final 3D part known as flattening.

1.4.3.1 Topological and material optimisations of 3D parts

Some examples of simultaneous structural topology and fibre orientation optimisation tools have been presented in section 1.3. Although these tools show promising results, they were applied to single layered 2D parts. Expanding the TFP technology to the manufacturing of optimised 3D FRC parts requires other optimisation tools. In the previously cited works limited to 2D parts, only in-plane properties where necessary to formulate the material model. However, for 3D surfaces, bending or torsional stiffness as well as their couplings with the in-plane properties might be required for an accurate representation of the material and to find the optimal design. Some of the previously cited works on manufacturing 3D parts did not necessarily investigated the best fibre orientation in terms of structural stiffness but choose the ones ensuring the formability of the part.

Safonov (2019) developed an algorithm for finding optimal density and fibre orientation distribution in 3D parts. They obtained promising numerical results for a 3D cube with vertical central load and the bending of a 3D cantilever beam. However, this tool was designed for 3D fibre printing technologies that manufacture 3D parts directly.

The previously mentioned tool CAIO (Voelkl et al., 2020) which was initially limited to single layer part design, was extended to multi-layer part design. Multi-layered preforms are required for parts submitted to multi-axial stress state. They studied a mounting bracket and a B-pillar demonstrators. Although their tool showed promising results, the optimisation is based on fibre angle changes only and do not modify the structural topology that is initially prescribed.

Determining the optimal geometry with the optimal fibre orientation of a FRC 3D parts manufacturable through forming of a flat TFP preform is not the aim of this work. Consequently, this required "virtual" tool is only supposed to exist or to be developed in the future.

1.4.3.2 Determination of the corresponding 2D TFP pattern: Flattening

The previous section 1.3 shows how challenging the manufacturing of optimised 2D parts using fibre placement technology can be. The manufacturing process from design to production implies

many challenges which have been summarized in the definition of the tool allowing taking full advantage of fibre placement in the conclusion of section 1.3. However, to manufacture 3D parts from flat TFP preforms an additional forming step is required, which in general (without using folding or cuts), implies large fibre orientation changes in conventional textiles for the most complex parts as shown in section 1.2. These changes are unavoidable since they are required for formability purpose. However, the virtual optimisation process allowing determining the geometry and fibre orientation is performed on the final 3D part, which will be formed from a flat preform. Consequently, it is necessary to predict how the fibre orientations will change during the forming process. Moreover, the 3D part design process has to include the formability of the resulting part. To this end, considering the geometry and fibre orientation of this optimised 3D part as known, its flattening is necessary to obtain the flat TFP pattern. The flattening simulation would allow checking the manufacturability of the 3D part by showing negligible deformation in the fibres directions that are assumed quasi-inextensible.

The work previously mentioned by Takezawa et al. (2021) used an interesting flattening method based on splitting a non-developable surface into developable patches determined by a given set of orthogonal curves. However, they investigated the use of Gaussian curves which facilitate the formability but did not determine the fibre orientation which gives the optimal structural stiffness. Flattening of non-developable 3D shell-like structures has already been investigated, especially in metallic sheet forming applications (Zhang et al., 2007; Zhu et al., 2013; Liu et al., 2016; Zhang et al., 2018; Yi et al., 2018; Wang et al., 2019), clothing design (Wang et al., 2002, 2005; Zhong and Xu, 2006; Casati et al., 2016; Yi et al., 2018), texture mapping (Yi et al., 2018) and also for 3D woven fabrics (Morioka et al., 2016) and CTS processing (Sun et al., 2021). Contrary to forming, flattening consists in finding a mapping between the material points of the 3D final part and the position of those material points in a plane that minimizes the deformation energy of the process.

1.4.3.3 Overview of the required tool to manufacture optimised 3D part by TFP

The tool required to manufacture optimised 3D shell-like structures through forming of flat TFP preforms is not so different from the definition stated in the conclusion of section 1.3. In addition to the listed attributes in this definition, the manufacturing step is now divided into two steps: flat TFP preforming and forming. Therefore the optimisation tool that provides the optimised 3D parts has to take into account another manufacturing constraint, which is the formability of the preform. Consequently, an additional tool able to check the formability of the optimised 3D parts is required. In this work, it is assumed to rely on an iterative approach where successive flattening of the 3D parts and forming of the resulting 2D pattern allow to find a compromise between optimal structural stiffness and formability. This approach is illustrated in Fig1.48.

Conclusion

Developing a tool allowing determining the flat TFP pattern to be manufactured from the 3D optimised part will be a necessary step to fully take advantage of the TFP technology in manufacturing 3D FRC parts. However, to the knowledge of the author, the forming behaviour of flat TFP preforms and its numerical modelling has not been investigated yet. Flattening which is the virtual reverse process of the physical forming process cannot be investigated experimentally. To validate a flattening method, experimental forming is required to verify that the flat preform allows obtaining the targeted 3D part after forming. Consequently, to avoid using costly trial-error based methods to validate the flattening method, developing a numerical tool to simulate the forming of TFP preforms is of first importance.

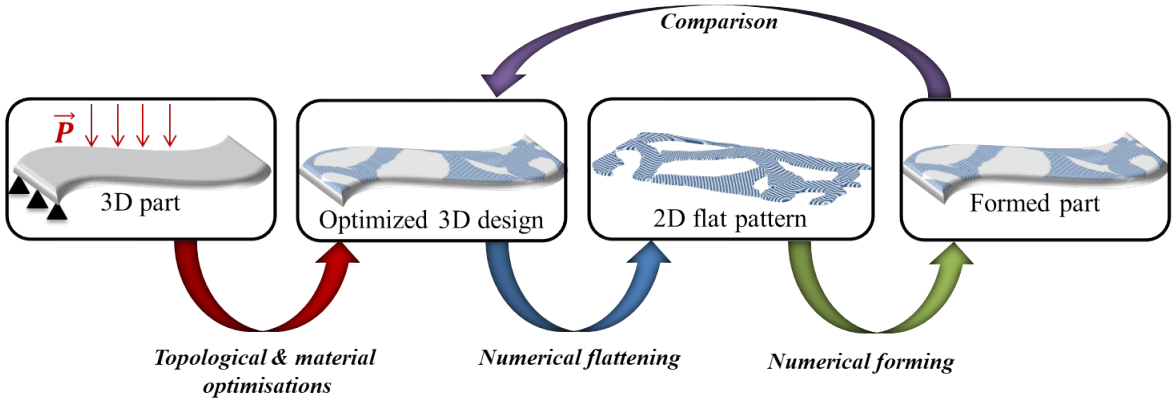

Figure 1.48: Formability tool principle: The optimised 3D part resulting from topological and material optimisations is numerically flattened and formed iteratively until a compromised between structural stiffness and formability is achieved

1.5 Objectives and outline of the thesis

This last section of the introductory chapter states the objectives of this thesis that focuses on the forming of TFP preforms. Finally, an outline of the thesis is given.

1.5.1 Forming modelling: a first step to understand the deformation mechanisms of TFP preforms

The section 1.4.2.3 presented some experimental studies on TFP preforms forming or folding. However, there is no model to numerically simulate the forming of TFP preforms. Consequently, as a first step to simulate the forming of TFP preforms, the deformation mechanisms of TFP preforms during forming has to be taken into account in the numerical model. Besides, it has been shown in the section 1.4.2 that TFP layers can be combined with conventional reinforcements or TFP technology can be used to manufacture a whole flat preform. Therefore, the modelling strategy to be developed requires describing both possibilities to take advantage of the versatility of TFP preforms. Due to the complexity of TFP preforms, which are made by stitching and combine several materials, a trade-off between accuracy and simplicity will be necessary to allow developing this first numerical model of TFP preform forming in a limited time.

The objectives of the thesis are summarised as follow:

- Develop a numerical model for the forming of TFP preforms able to address TFP layers stitched on conventional reinforcements or a removable backing material.
- Implement this model in a robust numerical solver.
- Validate the model through elementary numerical tests and full-scale forming simulations with experimental comparisons.
- Discuss the simulations' results of this first modelling strategy and improve it.

This work can be considered as a first contribution in the development of a numerical model for the forming of TFP preforms.

1.5.2 Outline of the thesis

Chapter 2 introduces the modelling strategy adopted to address the numerical forming of TFP preforms. Starting from the general morphology of a TFP preform and its possible kinemat-

ics, the motivations of the proposed approach are presented. In particular, it is based on an embedded element formulation which assumes no-slip between the TFP preform constituents. The numerical framework used for the simulation is presented before detailing the modelling strategy. Two models, named Model I and Model II, which represent TFP preforms with and without backing material respectively, are described. Their implementation features are given before addressing some elementary test cases.

Chapter 3 aims at validating the proposed modelling strategy. To this end, full-scale forming simulations based on hemispheric and tetrahedral punch geometries with curvilinear $0/90°$ fibre orientation is performed and compared with experimental results. The final targeted fibre orientations have been selected to demonstrate the potential of the TFP technology in manufacturing 3D shell-like structures with orthotropic final fibre orientations that cannot be achieved using conventional reinforcements. These full-scale simulations address the forming of TFP preforms without backing material (Model II). Model I, which represents TFP preforms with backing material, is studied numerically and shows a very stiff and unrealistic behaviour due to the no-slip condition of the fibre tows in the preform.

Chapter 4 presents the key features of an enriched modelling strategy to improve the models presented in **Chapter 2**. The improvement, based on the Arbitrary Lagrangian Eulerian (ALE) framework, aims at relaxing the no-slip assumption between the TFP preform constituents. The models are not revisited but enhanced to take into account the relative motion between the fibre tows and their surroundings. The ALE framework is firstly introduced. Then, some modelling strategies to take into account material flow in 1D finite elements are described before choosing the most suitable for enhancing the TFP preform models. Validation of the new feature with elementary test cases is performed. Next, characterisation of the friction behaviour required to feed the numerical models is carried out. It consists in a parametric study of pull-out experiments to develop a friction law taking into account the effect of the stitching parameters. Finally, the integration of the friction law into the TFP models is performed before extending the proposed mixed embedded-ALE formulation to the modelling of fibre slippage in conventional textiles.

Bibliography

Aimene, Y., Hagege, B., Sidoroff, F., Vidal-Sallé, E., Boisse, P., and Dridi, S. (2008). Hyperelastic Approach for Composite Reinforcement Forming Simulations. *International Journal of Material Forming*, 1(S1):811–814.

Akkerman, R. and Haanappel, S. (2015). Thermoplastic composites manufacturing by thermoforming. In *Advances in Composites Manufacturing and Process Design*, pages 111–129. Elsevier.

Allaoui, S., Boisse, P., Chatel, S., Hamila, N., Hivet, G., Soulat, D., and Vidal-Salle, E. (2011). Experimental and numerical analyses of textile reinforcement forming of a tetrahedral shape. *Composites Part A: Applied Science and Manufacturing*, 42(6):612–622.

Allaoui, S., Cellard, C., and Hivet, G. (2015). Effect of inter-ply sliding on the quality of multilayer interlock dry fabric preforms. *Composites Part A: Applied Science and Manufacturing*, 68:336–345.

Allaoui, S., Hivet, G., Soulat, D., Wendling, A., Ouagne, P., and Chatel, S. (2014). Experimental preforming of highly double curved shapes with a case corner using an interlock reinforcement. *International Journal of Material Forming*, 7(2):155–165.

Almeida, J. H. S., Bittrich, L., Nomura, T., and Spickenheuer, A. (2019). Cross-section optimization of topologically-optimized variable-axial anisotropic composite structures. *Composite Structures*, 225:111150.

Almeida, J. H. S., Bittrich, L., and Spickenheuer, A. (2020). Improving the open-hole tension characteristics with variable-axial composite laminates: Optimization, progressive damage modeling and experimental observations. *Composites Science and Technology*, 185:107889.

Badel, P., Gauthier, S., Vidal-Sallé, E., and Boisse, P. (2009). Rate constitutive equations for computational analyses of textile composite reinforcement mechanical behaviour during forming. *Composites Part A: Applied Science and Manufacturing*, 40(8):997–1007.

Badel, P., Vidal-Sallé, E., Maire, E., and Boisse, P. (2008). Simulation and tomography analysis of textile composite reinforcement deformation at the mesoscopic scale. *Composites Science and Technology*, 68(12):2433–2440.

Bel, S., Hamila, N., Boisse, P., and Dumont, F. (2012). Finite element model for NCF composite reinforcement preforming: Importance of inter-ply sliding. *Composites Part A: Applied Science and Manufacturing*, 43(12):2269–2277.

Ben Boubaker, B., Haussy, B., and Ganghoffer, J. (2007). Discrete models of woven structures. Macroscopic approach. *Composites Part B: Engineering*, 38(4):498–505.

Bittrich, L., Spickenheuer, A., Almeida Jr, H., Mueller, S., Kroll, L., and Heinrich, G. (2019). Optimizing Variable-Axial Fiber-Reinforced Composite Laminates: The Direct Fiber Path Optimization Concept. *Mathematical Problems in Engineering*, 2019:1–11.

Bohler, P., Carosella, S., Goetz, C., and Middendorf, P. (2015). Path Definition for Tailored Fiber Placement Structures Using Numerical Reverse Draping Approach. *Key Engineering Materials*, 651-653:446–451.

Boisse, P., Gasser, A., Hagege, B., and Billoet, J.-L. (2005a). Analysis of the mechanical behavior of woven fibrous material using virtual tests at the unit cell level. *Journal of Materials Science*, 40(22):5955–5962.

Boisse, P., Hamila, N., Vidal-Sallé, E., and Dumont, F. (2011). Simulation of wrinkling during

textile composite reinforcement forming. Influence of tensile, in-plane shear and bending stiffnesses. *Composites Science and Technology*, 71(5):683–692.

Boisse, P., Zouari, B., and Gasser, A. (2005b). A mesoscopic approach for the simulation of woven fibre composite forming. *Composites Science and Technology*, 65(3-4):429–436.

Brasington, A., Sacco, C., Halbritter, J., Wehbe, R., and Harik, R. (2021). Automated fiber placement: A review of history, current technologies, and future paths forward. *Composites Part C: Open Access*, 6:100182.

Brown, L. P. and Long, A. C. (2021). 8 - Modeling the geometry of textile reinforcements for composites: TexGen. In Boisse, P., editor, *Composite Reinforcements for Optimum Performance (Second Edition)*, Woodhead Publishing Series in Composites Science and Engineering, pages 237–265. Woodhead Publishing.

Buet-Gautier, K. and Boisse, P. (2001). Experimental analysis and modeling of biaxial mechanical behavior of woven composite reinforcements. *Experimental Mechanics*, 41(3):260–269.

Bussetta, P. and Correia, N. (2018). Numerical forming of continuous fibre reinforced composite material: A review. *Composites Part A: Applied Science and Manufacturing*, 113:12–31.

Cao, J., Akkerman, R., Boisse, P., Chen, J., Cheng, H. S., de Graaf, E. F., Gorczyca, J. L., Harrison, P., Hivet, G., Launay, J., Lee, W., Liu, L., Lomov, S. V., Long, A., de Luycker, E., Morestin, F., Padvoiskis, J., Peng, X. Q., Sherwood, J., Stoilova, T., Tao, X. M., Verpoest, I., Willems, A., Wiggers, J., Yu, T. X., and Zhu, B. (2008). Characterization of mechanical behavior of woven fabrics: Experimental methods and benchmark results. *Composites Part A: Applied Science and Manufacturing*, 39(6):1037–1053.

Capelle, E., Ouagne, P., Soulat, D., and Duriatti, D. (2014). Complex shape forming of flax woven fabrics: Design of specific blank-holder shapes to prevent defects. *Composites Part B: Engineering*, 62:29–36.

Carvelli, V. (2011). Biaxial tensile properties of reinforcements in composites. In *Composite Reinforcements for Optimum Performance*, pages 306–332. Elsevier.

Casati, R., Daviet, G., and Bertails-Descoubes, F. (2016). Inverse Elastic Cloth Design with Contact and Friction. page 12.

Charmetant, A., Orliac, J., Vidal-Sallé, E., and Boisse, P. (2012). Hyperelastic model for large deformation analyses of 3D interlock composite preforms. *Composites Science and Technology*, 72(12):1352–1360.

Charmetant, A., Vidal-Sallé, E., and Boisse, P. (2011). Hyperelastic modelling for mesoscopic analyses of composite reinforcements. *Composites Science and Technology*, 71(14):1623–1631.

Colman, A., Bridgens, B., Gosling, P., Jou, G.-T., and Hsu, X.-Y. (2014). Shear behaviour of architectural fabrics subjected to biaxial tensile loads. *Composites Part A: Applied Science and Manufacturing*, 66:163–174.

Costalonga Martins, V., Cutajar, S., van der Hoven, C., Baszyński, P., and Dahy, H. (2020). FlexFlax Stool: Validation of Moldless Fabrication of Complex Spatial Forms of Natural Fiber-Reinforced Polymer (NFRP) Structures through an Integrative Approach of Tailored Fiber Placement and Coreless Filament Winding Techniques. *Applied Sciences*, 10(9):3278.

Creech, G. and Pickett, A. K. (2006). Meso-modelling of Non-Crimp Fabric composites for coupled drape and failure analysis. *Journal of Materials Science*, 41(20):6725–6736.

Crothers, P., Drechsler, K., Feltin, D., Herszberg, I., and Kruckenberg, T. (1997). Tailored

fibre placement to minimise stress concentrations. *Composites Part A: Applied Science and Manufacturing*, 28(7):619–625.

de Bilbao, E., Soulat, D., Hivet, G., and Gasser, A. (2010). Experimental Study of Bending Behaviour of Reinforcements. *Experimental Mechanics*, 50(3):333–351.

De Luycker, E., Morestin, F., Boisse, P., and Marsal, D. (2009). Simulation of 3D interlock composite preforming. *Composite Structures*, 88(4):615–623.

Dong, L., Lekakou, C., and Bader, M. G. (2001). Processing of Composites: Simulations of the Draping of Fabrics with Updated Material Behaviour Law. *Journal of Composite Materials*, 35(2):138–163.

Durville, D. (2005). Numerical simulation of entangled materials mechanical properties. *Journal of Materials Science*, 40(22):5941–5948.

Durville, D. (2010). Simulation of the mechanical behaviour of woven fabrics at the scale of fibers. *International Journal of Material Forming*, 3(S2):1241–1251.

Eck, B., Comas-Cardona, S., Binetruy, C., and Aufrere, C. (2015). Multi-objective composite part mechanical optimization enhanced by a Process Estimator. *Composite Structures*, 119:620–629.

El-Dessouky, H., Saleh, M., Gautam, M., Han, G., Scaife, R., and Potluri, P. (2019). Tailored fibre placement of commingled carbon-thermoplastic fibres for notch-insensitive composites. *Composite Structures*, 214:348–358.

Fial, J., Harr, M., Böhler, P., and Middendorf, P. (2018). Automated wet compression moulding of load-path optimised TFP preforms with low cycle times. *IOP Conference Series: Materials Science and Engineering*, 406:012018.

Fu, S. (1996). Effects of fiber length and fiber orientation distributions on the tensile strength of short-fiber-reinforced polymers. *Composites Science and Technology*, 56(10):1179–1190.

Gatouillat, S., Bareggi, A., Vidal-Sallé, E., and Boisse, P. (2013). Meso modelling for composite preform shaping – Simulation of the loss of cohesion of the woven fibre network. *Composites Part A: Applied Science and Manufacturing*, 54:135–144.

Gereke, T., Döbrich, O., Hübner, M., and Cherif, C. (2013a). Experimental and computational composite textile reinforcement forming: A review. *Composites Part A: Applied Science and Manufacturing*, 46:1–10.

Gereke, T., Döbrich, O., Hübner, M., and Cherif, C. (2013b). Experimental and computational composite textile reinforcement forming: A review. *Composites Part A: Applied Science and Manufacturing*, 46:1–10.

Gliesche, K. (2003). Application of the tailored fibre placement (TFP) process for a local reinforcement on an “open-hole” tension plate from carbon/epoxy laminates. *Composites Science and Technology*, 63(1):81–88.

Gorczyca-Cole, J. L., Sherwood, J. A., and Chen, J. (2007). A friction model for thermostamping commingled glass–polypropylene woven fabrics. *Composites Part A: Applied Science and Manufacturing*, 38(2):393–406.

Guillon, D., Lemasçon, A., and Callens, C. (2016). QSP®: An innovative process based on tailored preforms for low cost and fast production of optimized thermoplastic composite parts. In *Proceedings of the ECCM*.

Guzman-Maldonado, E., Wang, P., Hamila, N., and Boisse, P. (2019). Experimental and numerical analysis of wrinkling during forming of multi-layered textile composites. *Composite Structures*, 208:213–223.

Hamila, N. and Boisse, P. (2007). A Meso–Macro Three Node Finite Element for Draping of Textile Composite Preforms. *Applied Composite Materials*, 14(4):235–250.

Hamila, N. and Boisse, P. (2008). Simulations of textile composite reinforcement draping using a new semi-discrete three node finite element. *Composites Part B: Engineering*, 39(6):999–1010.

Hamila, N., Boisse, P., Sabourin, F., and Brunet, M. (2009). A semi-discrete shell finite element for textile composite reinforcement forming simulation. *International Journal for Numerical Methods in Engineering*, 79(12):1443–1466.

Harik, R. (2020). next automated fiber placement: advancing composites manufacturing towards a new paradigm. *SAMPE J.*, pages 6–14.

Harik, R., Saidy, C., Williams, S., Gurdal, Z., and Grimsley, B. (2018). *Automated fiber placement defect identity cards: cause, anticipation, existence, significance, and progression.*

Hautefeuille, A., Comas-Cardona, S., and Binetruy, C. (2019). Mechanical signature and full-field measurement of flow-induced large in-plane deformation of fibrous reinforcements in composite processing. *Composites Part A: Applied Science and Manufacturing*, 118:213–222.

Hivet, G. and Boisse, P. (2008). Consistent mesoscopic mechanical behaviour model for woven composite reinforcements in biaxial tension. *Composites Part B: Engineering*, 39(2):345–361.

Huang, J., Boisse, P., and Hamila, N. (2021a). Simulation of the forming of tufted multilayer composite preforms. *Composites Part B: Engineering*, 220:108981.

Huang, J., Boisse, P., Hamila, N., Gnaba, I., Soulat, D., and Wang, P. (2021b). Experimental and numerical analysis of textile composite draping on a square box. Influence of the weave pattern. *Composite Structures*, 267:113844.

Hyer, M. W. and Lee, H. H. (1991). The use of curvilinear fiber format to improve buckling resistance of composite plates with central circular holes. *Composite Structures*, 18(3):239–261.

Hyer, M. W. C. (1987). Innovative design of composite structures: Use of curvilinear fiber format to improve structural efficiency. Technical report.

Ilankeeran, P., Mohite, P., and Kamle, S. (2012). Axial Tensile Testing of Single Fibres. *Modern Mechanical Engineering*, 02:151–156.

Jauffres, D., Sherwood, J., Morris, C., and Chen, J. (2010). Discrete mesoscopic modeling for the simulation of woven-fabric reinforcement forming. *International Journal of Material Forming*, 3:1205–1216.

Kashani, M. H., Rashidi, A., Crawford, B., and Milani, A. (2016). Analysis of a two-way tension-shear coupling in woven fabrics under combined loading tests: Global to local transformation of non-orthogonal normalized forces and displacements. *Composites Part A: Applied Science and Manufacturing*, 88:272–285.

Katagiri, K., Honda, S., Nakaya, S., Kimura, T., Yamaguchi, S., Sonomura, H., Ozaki, T., Kawakita, S., Takemura, M., and Sasaki, K. (2021). Tensile strength of CFRP with curvilinearly arranged carbon fiber along the principal stress direction fabricated by the electrodeposition resin molding. *Composites Part A: Applied Science and Manufacturing*, 143:106271.

Kawabata, S. (1980). *The standardization and analysis of hand evaluation.* Textile Machinery Society of Japan, Osaka, 2nd ed. edition. Open Library ID: OL19767923M.

Khan, M. A., Mabrouki, T., Vidal-Sallé, E., and Boisse, P. (2010). Numerical and experimental analyses of woven composite reinforcement forming using a hypoelastic behaviour. Application to the double dome benchmark. *Journal of Materials Processing Technology*, 210(2):378–388.

Kim, B. C., Hazra, K., Weaver, P., and Potter, K. (2011). *Limitations of fibre placement techniques for variable angle tow composites and their process-induced defects.* Journal Abbreviation: ICCM International Conferences on Composite Materials Publication Title: ICCM International Conferences on Composite Materials.

Kim, B. C., Potter, K., and Weaver, P. M. (2012). Continuous tow shearing for manufacturing variable angle tow composites. *Composites Part A: Applied Science and Manufacturing*, 43(8):1347–1356.

Koricho, E. G., Khomenko, A., Fristedt, T., and Haq, M. (2015). Innovative tailored fiber placement technique for enhanced damage resistance in notched composite laminate. *Composite Structures*, 120:378–385.

Launay, J., Lahmar, F., Boisse, P., and Vacher, P. (2002). Strain Measurement in Tests on Fibre Fabric by Image Correlation Method. *Advanced Composites Letters*, 11(1):096369350201100.

Lee, J. S., Hong, S. J., Yu, W.-R., and Kang, T. J. (2007). The effect of blank holder force on the stamp forming behavior of non-crimp fabric with a chain stitch. *Composites Science and Technology*, 67(3-4):357–366.

Li, H., Gao, L., Li, H., Li, X., and Tong, H. (2021). Full-scale topology optimization for fiber-reinforced structures with continuous fiber paths. *Computer Methods in Applied Mechanics and Engineering*, 377:113668.

Liang, B. and Boisse, P. (2021). A review of numerical analyses and experimental characterization methods for forming of textile reinforcements. *Chinese Journal of Aeronautics*, 34(8):143–163.

Liu, X., Li, S., Zheng, X., and Lin, M. (2016). Development of a flattening system for sheet metal with free-form surface. *Advances in Mechanical Engineering*, 8(2):168781401663051.

Lomov, S., Barburski, M., Stoilova, T., Verpoest, I., Akkerman, R., Loendersloot, R., and Thije, R. (2005). Carbon composites based on multiaxial multiply stitched preforms. Part 3: Biaxial tension, picture frame and compression tests of the preforms. *Composites Part A: Applied Science and Manufacturing*, 36(9):1188–1206.

Lomov, S., Boisse, P., Deluycker, E., Morestin, F., Vanclooster, K., Vandepitte, D., Verpoest, I., and Willems, A. (2008). Full-field strain measurements in textile deformability studies. *Composites Part A: Applied Science and Manufacturing*, 39(8):1232–1244.

Lomov, S. and Verpoest, I. (2005). Manufacturing and internal geometry of textiles. In *Design and Manufacture of Textile Composites*, pages 1–61. Elsevier.

Luo, J. H. and Gea, H. C. (1998). Optimal orientation of orthotropic materials using an energy based method. *Structural Optimization*, 15(3-4):230–236.

Luo, Y. and Verpoest, I. (2002). Biaxial tension and ultimate deformation of knitted fabric reinforcements. *Composites Part A: Applied Science and Manufacturing*, 33(2):197–203.

Ma, Z., Kikuchi, N., and Cheng, H.-C. (1994). Improved approach for determining the optimal orientation of orthotropic material. *Structural Optimization*, 8.

Mattheij, P., Gliesche, K., and Feltin, D. (1998). Tailored Fiber Placement-Mechanical Properties and Applications. *Journal of Reinforced Plastics and Composites*, 17(9):774–786. Publisher: SAGE Publications Ltd STM.

Mecnika, V., Hoerr, M., Krievins, I., Jockenhoevel, S., and Gries, T. (2015). Technical Embroidery for Smart Textiles: Review. *Materials Science. Textile and Clothing Technology*, 9:56.

Mehdikhani, M., Gorbatikh, L., Verpoest, I., and Lomov, S. V. (2019). Voids in fiber-reinforced polymer composites: A review on their formation, characteristics, and effects on mechanical performance. *Journal of Composite Materials*, 53(12):1579–1669.

Moothoo, J., Allaoui, S., Ouagne, P., and Soulat, D. (2014). A study of the tensile behaviour of flax tows and their potential for composite processing. *Materials & Design*, 55:764–772.

Morioka, K., Ohtake, Y., Suzuki, H., Nagai, Y., Hishida, H., Inagaki, K., Nakamura, T., and Watanabe, F. (2016). 3D woven composite design using a flattening simulation. *Computer-Aided Design*, 81:24–38.

Mulvihill, D. M., Smerdova, O., and Sutcliffe, M. P. (2017). Friction of carbon fibre tows. *Composites Part A: Applied Science and Manufacturing*, 93:185–198.

Najjar, W., Pupin, C., Legrand, X., Boude, S., Soulat, D., and Dal Santo, P. (2014). Analysis of frictional behaviour of carbon dry woven reinforcement. *Journal of Reinforced Plastics and Composites*, 33(11):1037–1047.

Nguyen, Q. T., Vidal-Sallé, E., Boisse, P., Park, C. H., Saouab, A., Bréard, J., and Hivet, G. (2013). Mesoscopic scale analyses of textile composite reinforcement compaction. *Composites Part B: Engineering*, 44(1):231–241.

Ou, Y., Zhu, D., Zhang, H., Huang, L., Yao, Y., Li, G., and Mobasher, B. (2016). Mechanical Characterization of the Tensile Properties of Glass Fiber and Its Reinforced Polymer (GFRP) Composite under Varying Strain Rates and Temperatures. *Polymers*, 8(5):196.

Ouagne, P., Soulat, D., Moothoo, J., Capelle, E., and Gueret, S. (2013). Complex shape forming of a flax woven fabric; analysis of the tow buckling and misalignment defect. *Composites Part A: Applied Science and Manufacturing*, 51:1–10.

Papapetrou, V. S., Patel, C., and Tamijani, A. Y. (2020). Stiffness-based optimization framework for the topology and fiber paths of continuous fiber composites. *Composites Part B: Engineering*, 183:107681.

Pedersen, P. (1989). On optimal orientation of orthotropic materials. *Structural optimization*, 1(2):101–106.

Peirce, F. T. (1930). 26—THE "HANDLE" OF CLOTH AS A MEASURABLE QUANTITY. *Journal of the Textile Institute Transactions*, 21(9):T377–T416.

Peng, X. and Cao, J. (2005). A continuum mechanics-based non-orthogonal constitutive model for woven composite fabrics. *Composites Part A: Applied Science and Manufacturing*, 36(6):859–874.

Pickett, A. K., Creech, G., and de Luca, P. (2005). Simplified and advanced simulation methods for prediction of fabric draping. *Revue Européenne des Éléments Finis*, 14(6-7):677–691.

Rashidi, A. and Milani, A. (2018). Passive control of wrinkles in woven fabric preforms using a geometrical modification of blank holders. *Composites Part A: Applied Science and Manufacturing*, 105:300–309.

Ribeiro, P., Akhavan, H., Teter, A., and Warmiński, J. (2014). A review on the mechanical behaviour of curvilinear fibre composite laminated panels. *Journal of Composite Materials*, 48(22):2761–2777.

Richardson, M. and Zhang, Z. (2000). Experimental investigation and flow visualisation of the resin transfer mould filling process for non-woven hemp reinforced phenolic composites. *Composites Part A: Applied Science and Manufacturing*, 31(12):1303–1310.

Richter, E., Spickenheuer, A., Bittrich, L., Uhlig, K., and Heinrich, G. (2019). Mechanical Design of Intersection Points of Tailored Fiber Placement Made Carbon Fiber Reinforced Plastic Truss-Like Structures. *Key Engineering Materials*, 809:452–460.

Rihaczek, G., Klammer, M., Başnak, O., Petrš, J., Grisin, B., Dahy, H., Carosella, S., and Middendorf, P. (2020). Curved Foldable Tailored Fiber Reinforcements for Moldless Customized Bio-Composite Structures. Proof of Concept: Biomimetic NFRP Stools. *Polymers*, 12(9):2000.

Safonov, A. A. (2019). 3D topology optimization of continuous fiber-reinforced structures via natural evolution method. *Composite Structures*, 215:289–297.

Salem, M. M., De Luycker, E., Delbe, K., Fazzini, M., and Ouagne, P. (2020). Experimental investigation of vegetal and synthetic fabrics cohesion in order to prevent the tow sliding defect via frictional and pull-out test. *Composites Part A: Applied Science and Manufacturing*, 139:106083.

Schirmaier, F., Weidenmann, K., Kärger, L., and Henning, F. (2016). Characterisation of the draping behaviour of unidirectional non-crimp fabrics (UD-NCF). *Composites Part A: Applied Science and Manufacturing*, 80:28–38.

Sharma, S. and Sutcliffe, M. (2004). A simplified finite element model for draping of woven material. *Composites Part A: Applied Science and Manufacturing*, 35(6):637–643.

Sidhu, R. M. J. S., Averill, R. C., Riaz, M., and Pourboghrat, F. (2001). Finite element analysis of textile composite preform stamping. *Composite Structures*, 52(3):483–497.

Sinclair, D. (1950). A Bending Method for Measurement of the Tensile Strength and Young's Modulus of Glass Fibers. *Journal of Applied Physics*, 21(5):380–386.

Sippach, T., Dahy, H., Uhlig, K., Grisin, B., Carosella, S., and Middendorf, P. (2020). Structural Optimization through Biomimetic-Inspired Material-Specific Application of Plant-Based Natural Fiber-Reinforced Polymer Composites (NFRP) for Future Sustainable Lightweight Architecture. *Polymers*, 12(12):3048.

Sobhani Aragh, B., Borzabadi Farahani, E., Xu, B., Ghasemnejad, H., and Mansur, W. (2021). Manufacturable insight into modelling and design considerations in fibre-steered composite laminates: State of the art and perspective. *Computer Methods in Applied Mechanics and Engineering*, 379:113752.

Spickenheuer, A., Schulz, M., Gliesche, K., and Heinrich, G. (2008). Using tailored fibre placement technology for stress adapted design of composite structures. *Plastics, Rubber and Composites*, 37(5):227–232.

Steer, Q. (2019). *Modélisation de la mise en forme des renforts fibreux cousus (NCF): Etude expérimentale et numérique de l'influence de la couture.* PhD thesis, Université de Lyon.

Sun, X., Belnoue, J. P.-H., Wang, W.-T., Kim, B. C., and Hallett, S. R. (2021). "Un-forming" fibre-steered preforms: Towards fast and reliable production of complex composites parts. *Composites Science and Technology*, 216:109060.

Syerko, E., Comas-Cardona, S., and Binetruy, C. (2012). Models of mechanical properties/behavior of dry fibrous materials at various scales in bending and tension: A review. *Composites Part A: Applied Science and Manufacturing*, 43(8):1365–1388.

Syerko, E., Comas-Cardona, S., and Binetruy, C. (2015). Models for shear properties/behavior of dry fibrous materials at various scales: a review. *International Journal of Material Forming*, 8(1):1–23.

Takezawa, M., Otoguro, Y., Matsuo, K., Shibutani, T., Sakurai, A., and Maekawa, T. (2021). Fabrication of doubly-curved CFRP shell structures with control over fiber directions. *Computer-Aided Design*, 136:103028.

Tham, M. W., Fazita, M. N., Abdul Khalil, H., Mahmud Zuhudi, N. Z., Jaafar, M., Rizal, S., and Haafiz, M. M. (2019). Tensile properties prediction of natural fibre composites using rule of mixtures: A review. *Journal of Reinforced Plastics and Composites*, 38(5):211–248.

Thompson, A., Belnoue, J., and Hallett, S. (2020). Modelling defect formation in textiles during the double diaphragm forming process. *Composites Part B: Engineering*, page 108357.

Thompson, A. J., El Said, B., Belnoue, J. P.-H., and Hallett, S. R. (2018). Modelling process induced deformations in 0/90 non-crimp fabrics at the meso-scale. *Composites Science and Technology*, 168:104–110.

Tosh, M. W. and Kelly, D. W. (2000). On the design, manufacture and testing of trajectorial fibre steering for carbon fibre composite laminates. page 14.

Tourlonias, M., Bueno, M.-A., Fassi, G., Aktas, I., and Wielhorski, Y. (2019). Influence of friction angle between carbon single fibres and tows: Experimental analysis and analytical model. *Composites Part A: Applied Science and Manufacturing*, 124:105478.

Uhlig, K., Bittrich, L., Spickenheuer, A., and Almeida, J. H. S. (2019). Waviness and fiber volume content analysis in continuous carbon fiber reinforced plastics made by tailored fiber placement. *Composite Structures*, 222:110910.

Uhlig, K., Spickenheuer, A., Bittrich, L., and Heinrich, G. (2013). Development of a Highly Stressed Bladed Rotor Made of a CFRP Using the Tailored Fiber Placement Technology. *Mechanics of Composite Materials*, 49(2):201–210.

Uhlig, K., Spickenheuer, A., Gliesche, K., and Karb, I. (2010). Strength of CFRP open hole laminates made from NCF, TFP and braided preforms under cyclic tensile loading. *Plastics, Rubber and Composites*, 39(6):247–255.

Uhlig, K., Tosch, M., Bittrich, L., Leipprand, A., Dey, S., Spickenheuer, A., and Heinrich, G. (2016). Meso-scaled finite element analysis of fiber reinforced plastics made by Tailored Fiber Placement. *Composite Structures*, 143:53–62.

Voelkl, H., Franz, M., Klein, D., and Wartzack, S. (2020). Computer Aided Internal Optimisation (CAIO) method for fibre trajectory optimisation: A deep dive to enhance applicability. *Design Science*, 6. Publisher: Cambridge University Press.

Wang, C., Zhang, X., Shen, G., and Wang, Y. (2019). One-step inverse isogeometric analysis for the simulation of sheet metal forming. *Computer Methods in Applied Mechanics and Engineering*, 349:458–476.

Wang, C. C., Tang, K., and Yeung, B. M. (2005). Freeform surface flattening based on fitting a woven mesh model. *Computer-Aided Design*, 37(8):799–814.

Wang, C. C. L., Smith, S. S.-F., and Yuen, M. M. F. (2002). Surface ¯attening based on energy model. page 11.

Wang, Y. and Sun, X. (2001). Digital-element simulation of textile processes. *Composites Science and Technology*, 61(2):311–319.

Xue, D. and Hu, H. (2013). Mechanical properties of biaxial weft-knitted flax composites. *Materials & Design*, 46:264–269.

Yi, B., Yang, Y., Zheng, R., Li, X., and Yi, M. (2018). Triangulated surface flattening based on the physical shell model. *Journal of Mechanical Science and Technology*, 32(5):2163–2171.

Zhang, L., Wang, X., Pei, J., and Zhou, Y. (2020). Review of automated fibre placement and its prospects for advanced composites. *Journal of Materials Science*, 55(17):7121–7155.

Zhang, X., Hu, S., Lang, Z., Guo, W., and Hu, P. (2007). Energy-Based Initial Guess Estimation Method for One-Step Simulation. *International Journal for Computational Methods in Engineering Science and Mechanics*, 8(6):411–417.

Zhang, X., Zhu, X., Wang, C., Liu, H., Zhou, Y., Gai, Y., Zhao, C., Zheng, G., Hang, Z., Hu, P., and Ma, Z.-D. (2018). Initial solution estimation for one-step inverse isogeometric analysis in sheet metal stamping. *Computer Methods in Applied Mechanics and Engineering*, 330:629–645.

Zhao, S., Wu, N., and Wang, Q. (2021). Load path-guided fiber trajectory in composite panels: A comparative study and a novel combined method. *Composite Structures*, 263:113689.

Zhong, Y. and Xu, B. (2006). A physically based method for triangulated surface flattening. *Computer-Aided Design*, 38(10):1062–1073.

Zhu, B., Yu, T. X., Zhang, H., and Tao, X. M. (2011). Experimental investigation of formability of commingled woven composite preform in stamping operation. *Composites Part B: Engineering*, 42(2):289–295.

Zhu, X.-F., Hu, P., Ma, Z.-D., Zhang, X., Li, W., Bao, J., and Liu, M. (2013). A new surface parameterization method based on one-step inverse forming for isogeometric analysis-suited geometry. *The International Journal of Advanced Manufacturing Technology*, 65(9-12):1215–1227.

Chapter 2

A first step towards the modelling of TFP preform forming

Abstract

This second chapter of the thesis is the core of the numerical developments. It focuses on the modelling strategy adopted to represent TFP preforms and model their behaviour during forming. Section 2.1 explains the choice of the modelling strategy among those already presented in section 1.2.2 of the introductory chapter. The need for the development of two semi-discrete models arises from the versatility of the TFP technology. Next, the embedded element approach, which constitutes the main part of the modelling approach, is introduced. Then, the numerical tool developed and used in this thesis is briefly presented. The next three sections have the same outline. They begin with presenting the formulation of a feature in the models, before describing and validating its implementation using elementary test cases. Section 2.2 discusses the modelling of fibre tows while section 2.3 focuses on the backing material. Finally, section 2.4 describes the stitching yarn modelling as well as its application to the two semi-discrete models.

Contents

2.1 Modelling strategy

Introduction

This section explains which modelling strategy was chosen to model TFP preforms. Firstly, the objectives to be fulfilled by the modelling approach are described before choosing one that is more likely to meet these objectives among the previously mentioned modelling strategies (Section 1.2.2), i.e. continuum, discrete and semi-discrete approaches. Finally, the general principle of the chosen modelling strategy of TFP preforms is presented as well as its fundamental hypothesis. This section aims at providing the reader the necessary materials to understand the foundation of the modelling approach while the formulation details will be presented in the next sections.

2.1.1 Introduction

2.1.1.1 Objectives

The modelling of TFP preform forming has to provide information about the fibre orientation and distribution in the final 3D part obtained after forming. Besides, the onset of defects has also to be predicted such as wrinkles observed in forming of conventional textiles in order to ensure the proper formability of the preform. TFP inherently offers a high degree of freedom for the design of tailored preforms. Therefore, the model has to take into account all the capabilities of TFP such as the placement of curvilinear fibres and the inhomogeneity of fibre tows distribution. Moreover, the backing material can be removed prior to forming. Consequently, two configurations are possible for the TFP preforms. A first one, where the backing material is still present during forming. This is the case if TFP is used to locally reinforced a conventional textile for instance. A second one where the backing material only serves to manufacture the preform. In this case, the TFP technology is used as a whole preforming method. To be efficient, the modelling has to address both configurations and exploit their similarities to avoid the development of two completely separated models.

2.1.1.2 Existing strategies

Various finite element models have been proposed that mainly differs from the scale used to represent the fibrous reinforcement and its behaviour as shown in section 1.2.2. The current task is to figure out which modelling strategy, among the continuum, discrete or semi-discrete approaches, will be the more appropriate to fulfil the previously mentioned objectives.

On one hand, modelling all the features of a TFP preform using a continuum approach would require a prior and deep understanding of the deformation mechanisms as well as the development of a robust homogenisation procedure for this strongly non-homogeneous material. Since this thesis is the first contribution to the numerical modelling of TFP preforms, condensing the deformation modes of all the constituents and their interactions in a single constitutive law seems too challenging at this stage. However, this approach could be suitable to model the impregnation step or the mechanical behaviour of the final part, as proposed by Spickenheuer et al. (2018), which used solid elements with variable material orientations and density.

On the other hand, adopting a full discrete approach would require modelling all the features of TFP preforms: fibre tows, stitching yarn as well as the backing material if present and the contact interactions between all these constituents, which would be extremely time consuming. Fig. 2.1 shows a 3D representative model of the microscopic structure of TFP preform and the interactions between its constituents with only one layer. Moreover, in general, numerical models contain material parameters that have to be characterised using dedicated experiments, which are often time consuming. The material parameters will be numerous if all the features are taken into account.

Transition

Consequently, in order to develop a first model able to represent the forming of TFP preforms, a trade-off between its accuracy, its efficiency and the simplicity of its development, is required. With this philosophy in mind, the semi-discrete modelling strategy is selected, where the modelling of some deformation modes or interactions is simplified. The next section explains how this modelling strategy can be applied to the modelling of TFP preforms.

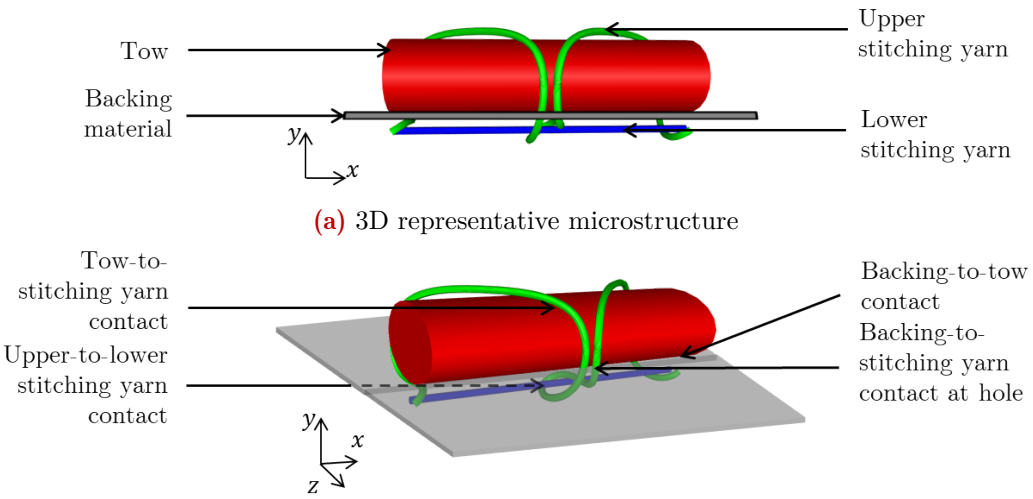

(a) 3D representative microstructure

(b) Interactions between the backing material, the fibre tows and the stitching yarn

Figure 2.1

2.1.2 Towards semi-discrete modelling of TFP preforms

The semi-discrete modelling strategy allows focusing on first order deformation modes while simplifying or neglecting higher order deformation modes and interactions to reduce the complexity of the underlying model. Therefore, more effort can be undertaken to study the predominant deformation modes and interactions. After comparison with experiments, deformation modes or interactions which have been firstly neglected but finally show to be important could be incorporated. The first step to establish the model is to discriminate the weak from the preponderant deformation modes and interactions. To this end, the behaviour and role of each constituent in the TFP preform is firstly described.

2.1.2.1 Role and mechanical behaviour of TFP preform components

Fig. 2.2 illustrates the role and behaviour of the constituents of TFP preforms as well as their interactions.

Fibre tows are the main component of a TFP preform that constitutes the core of the reinforcement or locally reinforce another fibrous reinforcement. Continuous fibre tows have preponderant tensile stiffness and generally low bending stiffness. However, as mentioned in section 1.2, the bending stiffness strongly influences the shape of wrinkles and is therefore required for a good prediction of this forming defect.

The backing material is necessary for the stitching operation. It can be any thin material tolerant to stitching. In-plane tension and shear as well as in-plane and out-of-plane bending might be required to accurately modelled this thin material depending on its nature. A polymer film allowing adding matrix in the final part can be soften during forming or a suitable backing material such as a water soluble PVA film can be removed prior to forming. Moreover, as mentioned is section 1.4.2, TFP layers can be stitched on top of another fibrous reinforcement. Consequently, on one hand, if the backing material is removed prior to forming or in a melted state during forming, its contribution might be neglected. On the other hand, if another fibrous reinforcement is used, an accurate modelling of the backing material is required.

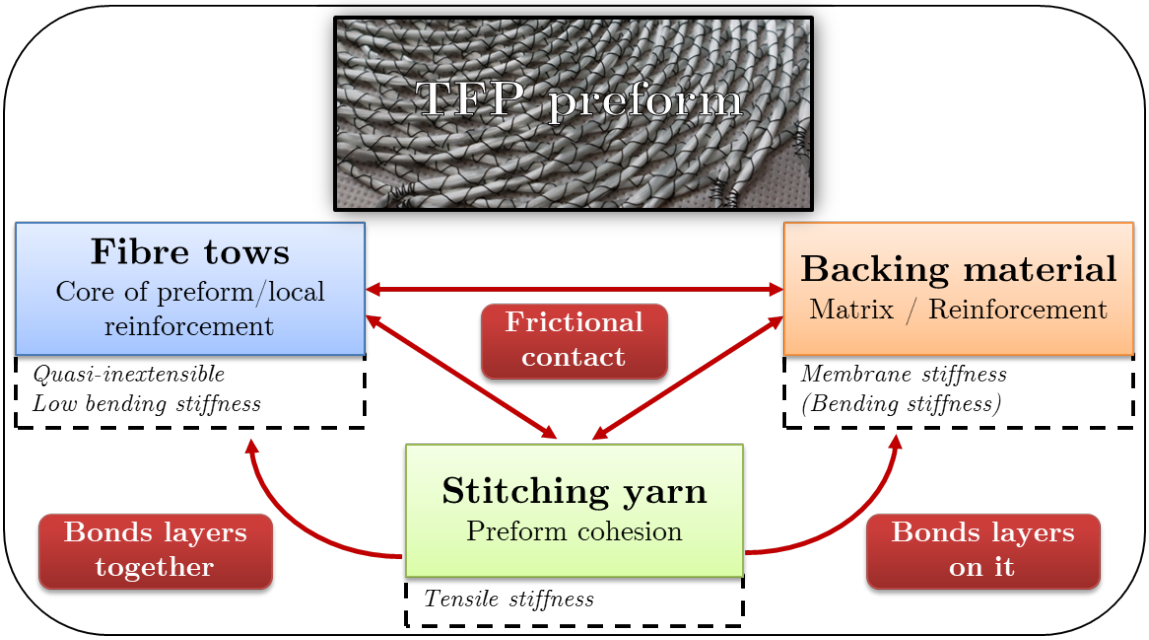

Figure 2.2: TFP preform's constituents: role, behaviour and mutual interactions

The stitching yarn ensures the fibre tows to be precisely placed and maintained on the backing material during the manufacturing of the flat preform. It is responsible for the cohesion between the fibre tows and the backing material as well as between the fibre tows within a layer or between layers. The stitching parameters, i.e. stitch length, width and tension, and the fibre tows spacing directly influence this cohesion. As shown in Fig. 2.3, oversticking increases the cohesion of the TFP preform. The stitching yarn material can be a polymer, meaning that it can be melted during the forming. In this case, it becomes very complex to control and predict the motion of the fibre tows.

2.1.2.2 Fundamental hypothesis

According to the identification of the role and behaviour of the different constituents of TFP preforms, the fundamental hypothesis of the modelling are given for each of them. Table 2.1 summarises the deformation modes and interactions that can occur in a TFP preform during forming as well as their modelling.

Fibre tows Continuously varying orientations is the main feature of TFP preforms. Therefore, it has been chosen to model explicitly the fibre tows using 1D finite elements to track these orientations during forming. Beam elements are required to take into account both axial and bending stiffness of fibre tows.

The Backing material is modelled using membrane or shell elements depending on its nature.

Stitching yarn Fibre tows either lie on a backing material or on top of the previously deposited layer and remain on it thanks to the stitching yarn. The stitching yarn is the constituent most likely to be difficult to model. In NCF, the contribution of the stitching yarn was shown to strongly influences the shear behaviour (Creech and Pickett, 2006; Bel et al., 2012). When stacking several layers in TFP preforms, the stitching yarn over-stitches the tows of the previous layers. Consequently, considering the fibre tows as being fixed on the backing material seems to be a reasonable assumption as a first step. In other word, the stitching yarn is considered to

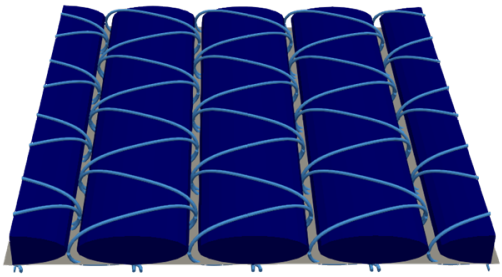

(a) Tow spacing without overstitching within the layer

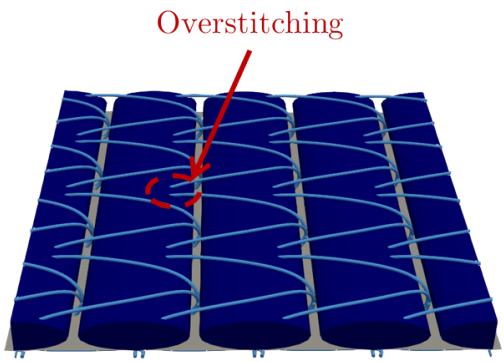

(b) Overstitching within the layer

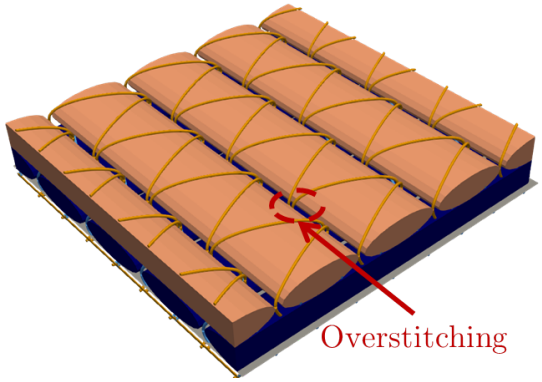

(c) Overstitching between layers

Figure 2.3: Overstitching increases cohesion between fibre tows

act as a bond between the tows and the backing material. This means that the sliding between the tows and the backing material is neglected. Therefore, the stitching yarn is not modelled explicitly but involves the transfer of forces between the tows and the backing material. If the backing material has been removed prior to forming or is in a melted state during forming, the stitching yarn is also assumed to act as a tight bond between layers. This means that their is no sliding between fibre tows of different layers. The case where the stitching yarn is melted would require modelling contacts between all the fibre tows and would be very expensive. Moreover, the preform cohesion would be very low and might lead to many defects in case of complex parts. Therefore, the stitching yarn is assumed to remain intact and ensures the preform cohesion during forming.

Although the fibre tows between the layers experience interactions due to friction and overstitching, it is not realistic to consider them as perfectly bounded to each other. The rotation of intersecting fibre tows, known as in-plane shear in conventional textiles, is not free. For simplicity, a linear elastic torsional spring is added at each fibre tows intersection that only takes into account the frictional resistance as well as the stitching yarn deformation due to the rotation of the intersecting fibre tows. In conventional textiles' models, the in-plane shear resistance is generally non-linear to take into account the lateral compaction of fibre tows. In the TFP preform models, this contribution due to fibre tows contact within layers is neglected.

2.1.2.3 Representation of the two semi-discrete models

Finally, two models will be developed, one with the backing material called Model I and the second one without backing material called Model II. Table 2.1 reports the modelling choices for the TFP preform's constituents. In both models, the stitching yarn is assumed to ensure a

Table 2.1: Modelling hypothesis for the constituents of TFP preforms and their interactions

Constituents and interactions	Characteristics	Modelling
Fibre tows	Predominant tensile stiffness and low bending stiffness (required for modelling wrinkles)	Explicit discretisation using 3D beam elements with undeformable cross-section
Backing material	In-plane stiffness and potentially bending stiffness	Explicit discretisation using 2D elements (3D membrane or shell)
Stitching yarn	Predominant tensile stiffness and negligible bending stiffness	Implicit modelling considering perfect bonding between tows of different layers and/or between tows and the backing material
Tow-to-backing material interaction	Tows in contact with the backing material exhibit friction if sliding	Forces in the fibre tows are fully transferred to the backing material
Tow-to-tow interaction between layers	Frictional rotation at intersections Lateral compaction and friction if sliding	Linear elastic torsional springs Not modelled
Tow-to-stitching yarn interaction	The stitching yarn deforms the tows' section and involves friction if sliding	Not modelled
Backing-material-to-stitching yarn interaction	The stitching yarn creates holes in the backing material and may slide through them	Not modelled
Tow-to-tow interaction within layer	Lateral compaction and friction if sliding	Not modelled

perfect cohesion either between the fibre tows and the backing material (Model I) or between layers (Model II). Fibre tows are modelled using beam elements and the thin backing material is modelled using 2D elements, which are either membrane or shell depending on its nature. The stitching yarn is implicitly modelled by embedding the fibre tows in the backing material (Model I) or by embedding the fibre tows of the next layer in the fibre tows of the previous layer as illustrated in Fig. 2.4. The general principle of the embedding constraint is presented in the next section.

Transition

Considering that the stitching yarn acts as a bond between the fibre tows and the backing material (Model I) or between the fibre tows of adjacent layers (Model II) is the main assumption of the TFP preform modelling strategy developed in this work. This assumption greatly simplifies the modelling of the stitching yarn, which is implicit, by avoiding the modelling of frictional contact interactions. The next section presents a method to model the stitching yarn bonding.

2.1.3 Introduction to the embedded element approach

This section aims at presenting the general principle of the embedded element approach and why it is appropriate for modelling TFP preforms. First the general principle is detailed before reviewing its use in the literature. Then, its application to the TFP preform models is described.

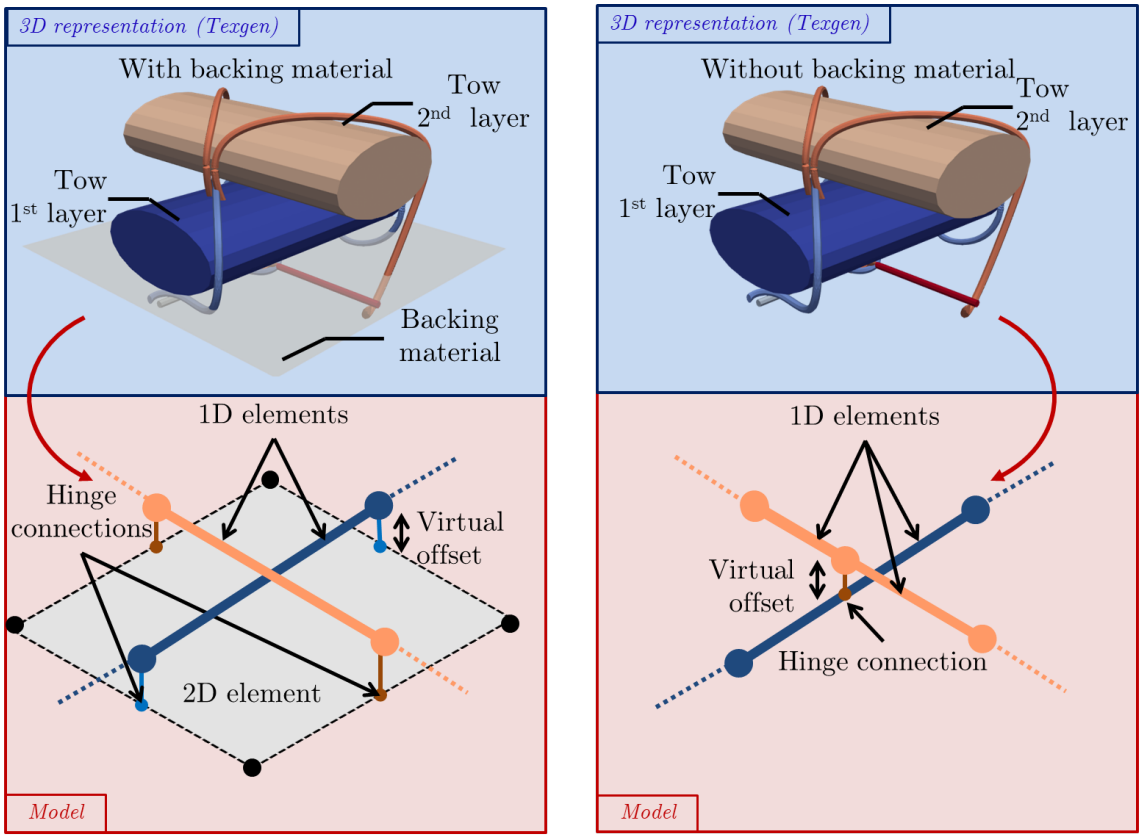

(a) Model I **(b)** Model II

Figure 2.4: TFP preform models: with (Model I) and without (Model II) backing material

2.1.3.1 Principle

Definition

The embedded element approach consists in embedding a body, called embedded body, in another body of higher dimension, called host body. The embedding constraint means that the material points constituting the embedded body are bound to the material points of the host body. Therefore, when the host body deforms, the embedded body deforms accordingly. When subjected to the same deformation, both bodies develop stress that adds up.

If these bodies are discretized using finite elements, then it consists in embedding elements in other elements of higher dimension. Consequently, 1D elements (truss) can be embedded in either 2D elements (membrane) or 3D solids. Similarly, 2D elements can be embedded in 3D solids. Besides, nodes, which can be seen as 0D elements, can be embedded in 1D, 2D or 3D elements. As a consequence of the compatibility between the deformation of the embedded and host bodies, the embedded elements and host elements have the same interpolation order. Fig. 2.5 illustrates some of the different options.

Kinematic constraint

If $\vec{\boldsymbol{x}}^e$ is a material point of the embedded body Ω_e, then it is associated to the virtual material point $\vec{\boldsymbol{x}}^h$ of the host body Ω_h having the same coordinates. Consequently, in a finite element representation, the position of a material point $\vec{\boldsymbol{x}}^e$ is related to the position of the host nodes by:

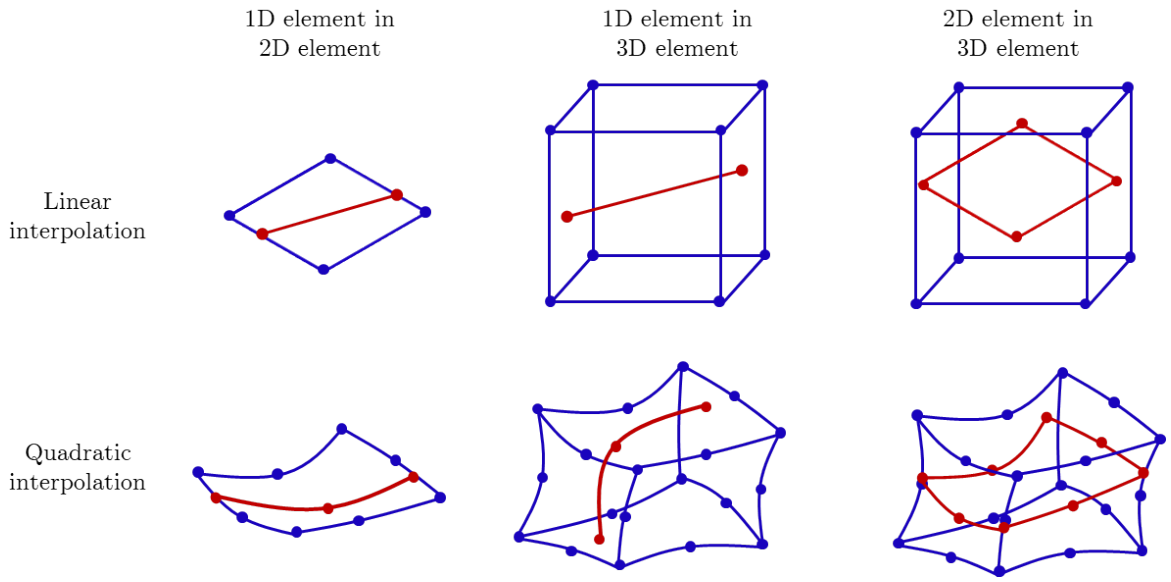

Figure 2.5: Examples of embedded element - host element combination with linear and quadratic interpolations

$$\vec{\boldsymbol{x}}^e = \sum_\alpha N_\alpha^h \left(\vec{\boldsymbol{\chi}}^e\right) \vec{\boldsymbol{x}}_\alpha^h \tag{2.1}$$

where $\vec{\boldsymbol{\chi}}^e$ is the natural coordinates of $\vec{\boldsymbol{x}}_e$ in the host element, N_v^h and $\vec{\boldsymbol{x}}_\alpha^h$ are respectively the shape function and position of the α^{th} node of the host element. The number of components of $\vec{\chi}^e$ is equal to the dimension of the host element.

Computation of the natural coordinates

To apply the embedding constraint, the natural coordinates $\vec{\boldsymbol{\chi}}^e$ of the embedded nodes are required. Therefore, the following equation must be solved for $\vec{\chi}^e$:

$$\vec{\boldsymbol{x}}^e - \sum_i N_i^h \left(\vec{\boldsymbol{\chi}}^e\right) \vec{\boldsymbol{x}}_i^h = \vec{\boldsymbol{0}} \tag{2.2}$$

To simplify the notations, $\vec{\boldsymbol{x}}_a^e$ is defined as: $\vec{\boldsymbol{x}}_a^e \left(\vec{\boldsymbol{\chi}}^e\right) = \sum_\alpha N_\alpha^h \left(\vec{\boldsymbol{\chi}}^e\right) \vec{\boldsymbol{x}}_\alpha^h$

In the general case, Eq 2.2 is nonlinear and can be solved iteratively using the Newton-Raphson method. The method consists in minimizing the scalar function:

$$f\left(\vec{\boldsymbol{\chi}}^e\right) = \left\|\vec{\boldsymbol{x}}^e - \vec{\boldsymbol{x}}_a^e\right\|^2 \tag{2.3}$$

At each iteration, the Newton-Raphson update is given by: $\vec{\boldsymbol{\chi}}_{n+1}^e = \vec{\boldsymbol{\chi}}_n^e + \Delta\vec{\boldsymbol{\chi}}^e$

where $\Delta\vec{\boldsymbol{\chi}}^e = -\boldsymbol{J}^{-1} \cdot \vec{\boldsymbol{R}}$ with J the Jacobian and $\vec{\boldsymbol{R}}$ the residual of the function f:

$$\underset{(nd_e \times 1)}{\vec{\boldsymbol{R}}} = \frac{1}{2} \frac{\partial f}{\partial \vec{\boldsymbol{\chi}}^e} \tag{2.4}$$

where nd_e is the dimension of the host element.

The Jacobian is computed according to:

$$\underset{(nd_e \times nd_e)}{[\boldsymbol{J}]} = \left[\frac{\partial \vec{\boldsymbol{R}}}{\partial \vec{\boldsymbol{\chi}}^e}\right] \tag{2.5}$$

$$J_{ij} = \frac{\partial R_i}{\partial \chi_j^e} = \frac{\partial \vec{\boldsymbol{g}}_i}{\partial \chi_j^e} \cdot (\vec{\boldsymbol{x}}_a^e - \vec{\boldsymbol{x}}^e) + \vec{\boldsymbol{g}}_i \cdot \vec{\mathbf{g}}_j \tag{2.6}$$

where $\vec{\boldsymbol{g}}_k$ is the k^{th} vector of the covariant basis of the host element defined as:

$$\vec{\boldsymbol{g}}_k = \frac{\partial \vec{\boldsymbol{x}}_a^e}{\partial \chi_k^e} = \sum_\alpha \frac{\partial N_\alpha^h(\vec{\boldsymbol{\chi}}^e)}{\partial \chi_k^e} \vec{\boldsymbol{x}}_\alpha^h \tag{2.7}$$

For a 2D element: $\underset{(2\times1)}{\vec{\boldsymbol{\chi}}^e} = \begin{bmatrix} \xi & \eta \end{bmatrix}^T$ and:

$$\underset{(2\times1)}{\vec{\boldsymbol{R}}} = \begin{bmatrix} \frac{\partial \vec{\boldsymbol{x}}_a^e}{\partial \xi} \cdot (\vec{\boldsymbol{x}}_a^e - \vec{\boldsymbol{x}}^e) & \frac{\partial \vec{\boldsymbol{x}}_a^e}{\partial \eta} \cdot (\vec{\boldsymbol{x}}_a^e - \vec{\boldsymbol{x}}^e) \end{bmatrix}^T$$

$$\underset{(2\times2)}{[\boldsymbol{J}]} = \begin{bmatrix} \frac{\partial R_1}{\partial \xi} & \frac{\partial R_1}{\partial \eta} \\ \frac{\partial R_2}{\partial \xi} & \frac{\partial R_2}{\partial \eta} \end{bmatrix}$$

Once the natural coordinates are computed for the nodes of the embedded elements, the position of each embedded element is perfectly defined from the position of its host element using Eq. 2.1. For a linear line or a linear triangle element as host element, this method converges in one step and the solution can also be computed analytically.

The algorithm to compute the natural coordinates of a point $\vec{\boldsymbol{x}^e}$ in an element is given in Alg. 1.

Algorithm 1 Computation of the natural coordinates of a point in an element using Newton-Raphson method

1: Initialize the natural coordinates $\vec{\boldsymbol{\chi}^e}$
2: Compute the coordinates of the element in a local basis ($\vec{\boldsymbol{X}^{el}}$) using the covariant vectors $\vec{\boldsymbol{g_k}}$ defined in Eq. 2.7
3: Compute the objective function f using Eq. 2.3
4: Initialize $i \leftarrow 0$
5: **while** $f > tol$ & $i < i_{max}$ **do**
6: Compute the residual $\vec{\boldsymbol{R}}$ at $\vec{\boldsymbol{\chi}^e}$ using Eq. 2.4
7: Compute the Jacobian $\boldsymbol{J}$ at $\vec{\boldsymbol{\chi}^e}$ using Eq. 2.5
8: Update $\vec{\boldsymbol{\chi}^e}$ as: $\vec{\boldsymbol{\chi}^e} \leftarrow \vec{\boldsymbol{\chi}^e} - \boldsymbol{J}^{-1}\vec{\boldsymbol{R}}$
9: Compute f
10: $i \leftarrow i + 1$
11: Return: $\vec{\boldsymbol{\chi}^e}$

2.1.3.2 A brief review of the embedded element approach

The embedded element approach has been used in different application fields and especially in fibre-reinforced concrete modelling. Besides it was also applied to 3D interlocks modelling and can be seen as a generalisation of some modelling techniques used for conventional textiles.

Fibre-reinforced concrete The first field of application of the embedded element approach is the modelling of fibre-reinforced concrete. Allwood and Bajarwan (1989) embedded steel bar elements in 2D concrete elements. One of their motivation in using this technique was to dissociate the concrete elements from the reinforcements. In fact, the reinforcement position used to be limited to the edges of the concrete elements, creating a strong dependency between the reinforcement layout and the concrete mesh. In other words, concrete and reinforcement shared the same nodes. The embedded element approach allows placing the reinforcements anywhere in the concrete elements and therefore was a major improvement to independently mesh the concrete and reinforcements and eased the modelling of complex reinforcement layouts. Cunha et al. (2012); Markou and Papadrakakis (2012) embedded reinforcing bars in 3D solid concrete elements. Markou and Papadrakakis (2012) proposed a method to efficiently generate the data associated with this modelling technique. In particular, the generation of the reinforcing elements with nodes required at the intersection with the concrete elements' boundaries as well as the computation of their natural coordinates.

3D interlocks De Luycker et al. (2009) embedded trusses in 3D solid elements to model 3D interlocks in forming simulations. Contrary to fibre-reinforced concrete modelling, the embedded elements and the host elements do not represent distinct physical domains as reinforcing bars and concrete but are used to split the deformation modes of this complex material. In fact, the trusses allow taking into account the tensile stiffness of the fibre tows as well as modelling explicitly their orientation in the 3D interlock. The other deformation modes such as compaction, transverse shear and bending are modelled in the 3D solid elements. Consequently, they used the embedded element approach to simplify the implementation of the mechanical behaviour of this complex fibrous architecture by splitting its deformation modes into two types of finite element, one embedded in the other.

Generalisation of some conventional textiles modelling Models where embedded elements have to share the same nodes of the host elements can be seen as special cases of the embedded element approach. Consequently, the embedded element approach can be considered as a generalisation of methods that superimpose different element types, such as the discrete pantographic models by (d'Agostino et al., 2015), which placed 1D elements (trusses and beams) along the diagonal of quadrangle elements, or the woven fabrics model by Harrison (2016), which embeds beam elements on the edge of membrane elements.

2.1.3.3 Application to the TFP preform models

As mentioned in the previous section, the embedded element approach has been used either to model bonding between two distinct physical domains or to split the modelling of the deformation modes into different element types.

In the TFP preform models, the stitching yarn is supposed to bond the fibre tows to the backing material (Model I) or the fibre tows of adjacent layers (Model II). Consequently, in Model I, the embedded element approach can be used to embed fibre tows modelled with beam elements in the backing material modelled with 2D elements. In Model II, the nodes of the beam elements representing the fibre tows of a layer at intersection with the beam elements representing the fibre tows of the previous layer can be embed in these beam elements. Consequently, in Fig. 2.4, the hinge connection will be model using the embedded element method. Details about its formulation and implementation will be given in section 2.4.

Transition

The embedded element approach will be used to model the bonding function brought by the stitching yarn. Its implementation will be detailed in a subsequent section. Before presenting the finite element formulation of the different features of the TFP preform models, the framework of the finite element solver used in this work is introduced.

2.1.4 Framework of the finite element solver

2.1.4.1 Global presentation

The finite element solver used in this thesis is based on the Fortran language. The generation of inputs and the post-processing of the outputs of this solver are achieved in Python. Python is widely used in the computation field and offer a large choice of open-source and reliable libraries to facilitate I/O operations and visualisation of complex simulations' results for instance. The finite element solver, named Femtran (Finite Element Method in forTRAN) in the remainder of this work, is based on previous in-house developments to simulate the forming of conventional textiles. Fortran is an old but computationally efficient language whose standards have been developed over the past decades. In particular, some effort were undertaken to better integrate the Oriented-Object Programming (OOP) paradigm which constitutes the base of the most widely used languages (C++, Python, Java). Consequently, in this work, the architecture of Femtran has been largely modified to better use the OOP features, which considerably increases the maintainability, reusability and readability of a code, especially when it is developed in-house by different developers.

Input data for the finite element model The definition of a finite element model starts with the creation of the bodies to be represented. These bodies are defined through their geometry before being discretize into finite elements to create a mesh. Meshes are defined by a set of nodes and a connectivity table describing their topology. Performing a mechanical analysis requires to define the mechanical properties of the bodies by assigning a material to its elements. A material section is also assigned to these bodies to define additional data such as the thickness for surface-like bodies or orientation for truss-like ones. The boundary conditions, which constraint the position or displacement of the bodies, is also required. Displacements, rotations, pointwise forces, distributed loads are examples of boundary conditions and loads to be set-up when defining a finite element model as well as contact interactions.

The OOP is particularly suited to represent the complexity of a finite element model which encompasses several types of complex data interacting with each other. For instance, finite elements are subdivided into different types according to their interpolation order or the number of integration points. However, all the finite element types share common attributes and methods. This is particularly adapted to OPP using the polymorphism feature. Each finite element belong to a given mesh which represent a body in the finite element model. This type of relation can be represented using the encapsulation feature of OOP.

High-level workflow Fig. 2.6 illustrates the high level flowchart when performing a simulation with the developed numerical tool. The creation of the geometry and the generation of the mesh are performed using external commercial software Abaqus or open-source software such as GMSH. The mesh information are parsed and added in a Model created from a Python script. Additional data such as the materials or the boundary conditions are added to the Model before writing the input file of the solver. Then, the simulation can be launched via the Femtran executable. During the simulation, outputs are regularly written for future analysis and display of the results.

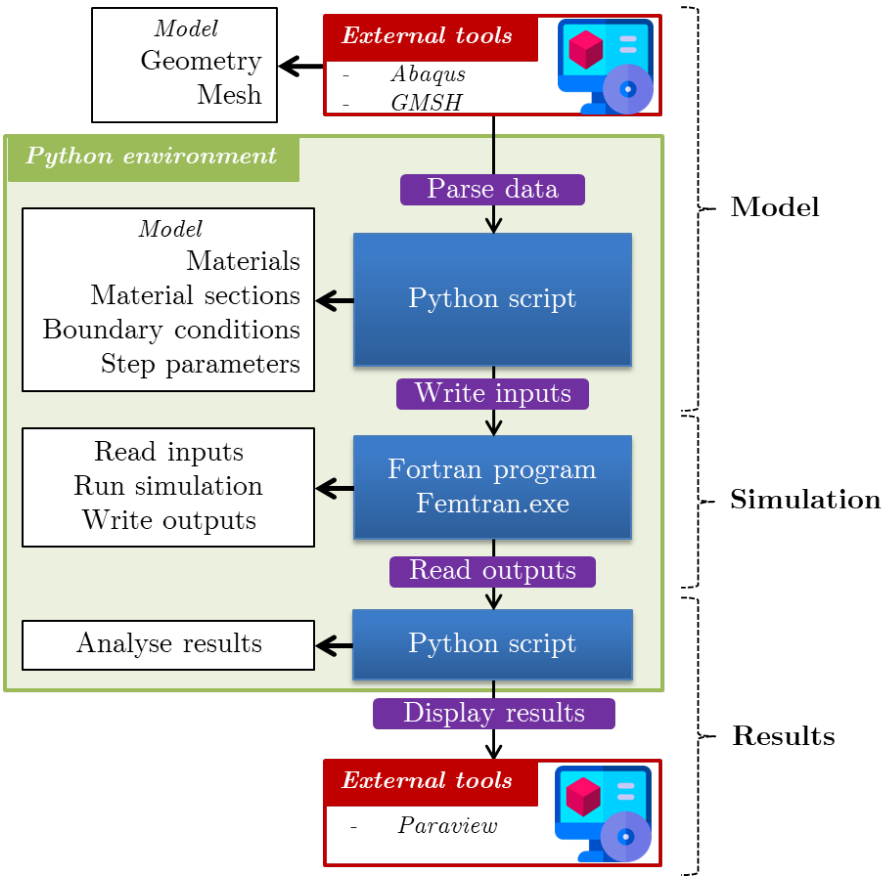

Figure 2.6: High-level flowchart of the numerical tool

Femtran data structure Fig. 2.7 displays the data structure of Femtran. The main entity is a Model which brings together all the data of the finite element model. The Assembly entity contains all the data concerning the topology of the model, which includes the nodes and the elements, but also some sets of nodes or elements that have been created to specify the boundary conditions for instance. The Step entity contains the data about the boundary conditions, the time integration scheme, etc. Each entity is represented using a derived type, which is the Fortran name for the concept of class in OOP.

In particular, the class *Material elements* is used to define the computation of the internal forces for a given set of elements with a pre-defined material. A *Material elements* is defined by a material and a type of element and is applied for a given set of elements. For instance, if a linear elastic behaviour is defined on a set of membrane elements containing both triangles and quadrangles, a *Material elements* is initialized for each element type. New classes defined as extensions of the *Material elements* class can be implemented to add new finite element behaviours. This data structure eases the enrichment of the finite element solver without requiring excessive changes elsewhere in the program.

2.1.4.2 Explicit solver

Equation of dynamic Femtran is an explicit solver. Explicit solvers are particularly efficient to solve contact interactions between rigid and deformable bodies as in forming of fibrous reinforcements. Moreover, implementing a new mechanical behaviour in such a solver only requires the computation of internal forces.

Femtran solves the following dynamic equation:

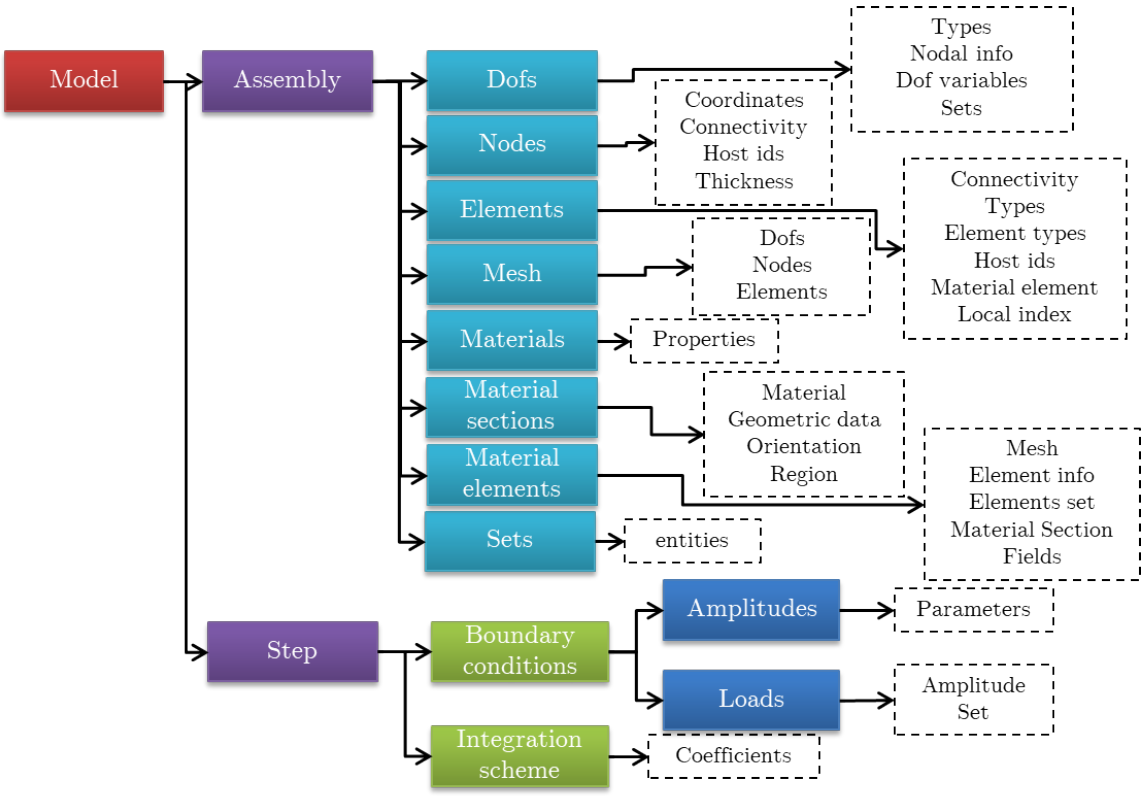

Figure 2.7: OOP data structure of Femtran

$$\boldsymbol{M\ddot{U} + C\dot{U} + F_{int} = F_{ext}} \tag{2.8}$$

where $\boldsymbol{M}$ is the lumped mass matrix, $\boldsymbol{C}$ is the damping vector proportional to the lumped mass matrix, $\boldsymbol{F_{int}}$ is the vector of internal forces and $\boldsymbol{F_{ext}}$ is the vector of external forces. $\boldsymbol{\ddot{U}}$, $\boldsymbol{\dot{U}}$ and $\boldsymbol{U}$ are respectively the vectors of acceleration, velocity and displacement also called kinematic variables.

Eq. 2.8 is solved using an explicit time integration scheme defined by:

$$\begin{aligned}
\boldsymbol{U_{n+1}} &= \boldsymbol{U_n} + \Delta t \boldsymbol{\dot{U}_n} + \frac{1}{2}\Delta t^2 \boldsymbol{\ddot{U}_n} \\
\boldsymbol{\dot{U}_{n+1}} &= \boldsymbol{\dot{U}_n} + \Delta t \boldsymbol{\ddot{U}_n} + \Delta t \beta \boldsymbol{\Delta \ddot{U}_n} \\
\boldsymbol{\ddot{U}_{n+1}} &= \boldsymbol{\ddot{U}_n} + \boldsymbol{\Delta \ddot{U}_n}
\end{aligned}$$

β is taken equal to 0.5. Therefore, the time integration scheme reduces to that of central differences.

Computation of contact interactions The contact interactions are solved using a forward increment Lagrangian multipliers method (Carpenter et al., 1991), which consists in a prediction-correction algorithm of the displacement of the nodes in contact. Contact interactions are defined by a contact pair and a contact law. The contact pair is made of two entities named primary and secondary. The primary entity is a set of 2D elements (primary faces) defining a surface while the secondary entity is a set of nodes (secondary nodes) which can come from a surface or a set of 1D elements. At each iteration, the displacement of the nodes are predicted by considering zero contact forces. Then, an algorithm iterates through each contact pair and looks for penetration of the secondary nodes into the primary faces. If penetrations occur, a

correction is applied to both the primary and secondary nodes' displacement of each contact pair iteratively until a criteria is reached. This criteria can be a minimal displacement correction which implies the convergence of the algorithm or a number of maximal iterations, which means that the contact algorithm failed. Once the contact interactions have been solved, the resulting contact forces are added to the external forces.

Femtran workflow Fig. 2.8 illustrates the workflow of Femtran. A Model entity is created by reading the input file. Once the model has been initialized, the mass of the finite elements is computed and lumped at the nodes. Then, the time stepping begins. First, the boundary conditions are applied. Next, the contact interactions are solved. Once all the external forces have been computed, the kinematic variables are computed using the time integration scheme. Then, the internal forces can be computed at the element level and assembled before the next iteration. Outputs are regularly saved throughout the simulation.

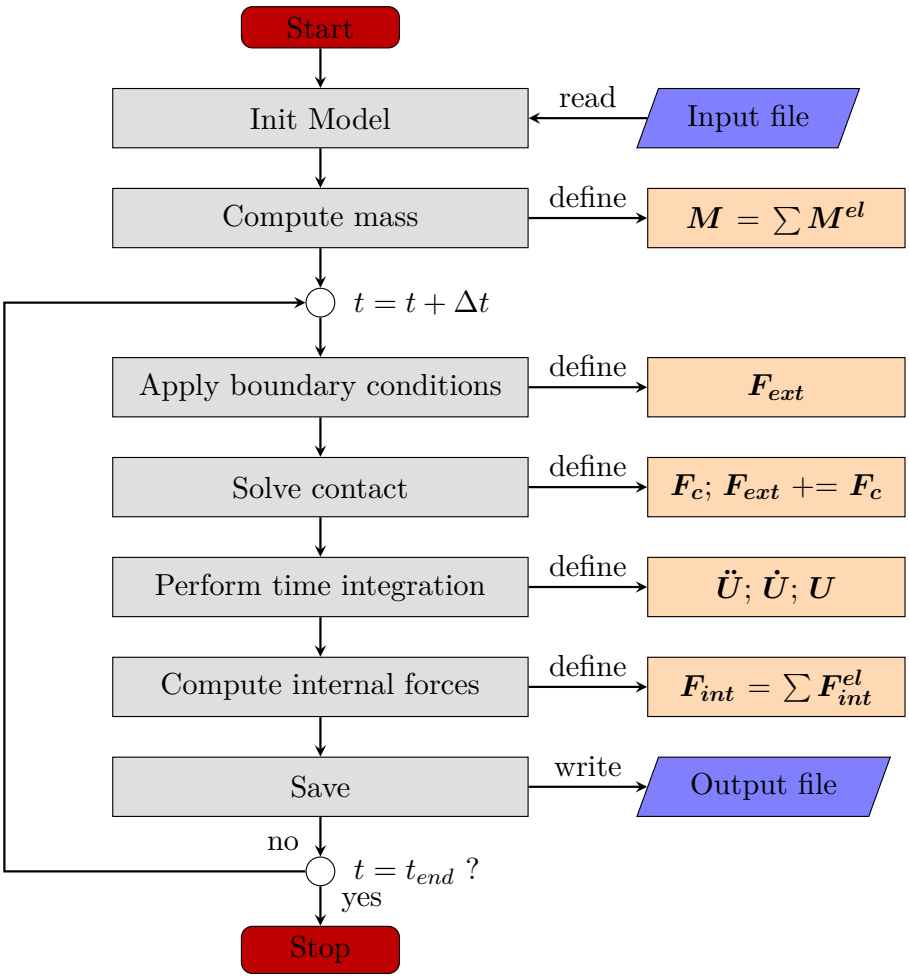

Figure 2.8: Femtran workflow

2.1.4.3 Implementing a finite element: example of a linear elastic 3D truss

This last section aims at briefly illustrating how the implementation of a new finite element mechanical behaviour is addressed. For simplicity, the example of a linear elastic 3D truss is detailed.

Extent the abstract derived type To add a new *Material elements* in the solver, a new derived type called *Linear_elastic_truss_t* is created using the source code 2.1. This new derived type

is built upon an abstract derived type whose implementation is given in the source code 2.2. The abstract derived type *Base_material_element_t* contains common attributes and methods (called procedures in Fortran) for all defined finite element mechanical behaviours. In particular, each finite element mechanical behaviour contains a set of elements (line 8) the mechanical behaviour is defined to and a 2D array *Fint_e* (line 28) of size $(n_{elements}, n_{dofs})$, which is used to store the values of the internal forces computed for all the elements in the element set. Among the procedures defined in the abstract type (lines 37-47), *initialize*, *init_data* and *compute_Fint* have to be overridden by the new derived type. Their role is described hereafter:

- *initialize*: it initializes the attributes of the derived type. In particular, it initializes the additional attributes required for this finite element mechanical behaviour such as E and S (line 3), which are 2D arrays storing the deformation and stress components for each element having this mechanical behaviour.
- *init_data*: it initializes the geometric and mechanical properties of the elements
- *compute_Fint*: it calculates the internal forces for all the elements having this mechanical behaviour.

Override the deferred procedures The implementation of the procedures to be overridden to define the derived type *Linear_elastic_truss_t* is given in the source codes 2.3, 2.4 and 2.5.

Source code 2.1: Fortran: Implementation of a derived type for the linear elastic 3D truss

```
1     !> A 3D linear elastic truss
2     Type, extends(Base_material_element_t) :: Linear_elastic_truss_t
3         Type(Element_tensors_t) :: E, S
4     contains
5         procedure, pass :: initialize => init_linear_elastic_truss
6         procedure, pass :: init_data => init_linear_elastic_truss_data
7         procedure, pass :: compute_Fint => linear_elastic_truss_Fint
8     End Type Linear_elastic_truss_t
```

Source code 2.2: Fortran: Implementation of the abstract derived type which is the base to define new mechanical behaviour

```
1  !> A abstract derived type (class) to handle material element data. Each material
       element derived type is built from this class
2      Type, abstract :: Base_material_element_t
3          !> A pointer to the mesh
4          Class(mesh_t), pointer :: mesh => null()
5          !> The element type info
6          Type(Element_infos_t), pointer :: infos => null()
7          !> The element set
8          Type(Set_t) :: elements_set = Set_t()
9          !> A 2d array to store geometric data of the elements (like section profile
       properties for beams)
10         double precision, dimension(:,:), allocatable :: geometry_data
11         !> A pointer to the material section derived type
12         Type(Material_section_t), pointer :: material_section => null()
13         !> A 2D array to store the material properties of the elements
14         double precision, dimension(:,:), allocatable :: properties
15         !> A 1d array derived type to store the thickness
16         Type(Nodal_scalars_t) :: tickness
17         !> A field container to set the fields available for outputs
18         Type(Fields_container_t) :: fields
```

```
19          !> A logical to know if the element mass must be computed in the current
    configuration
20          logical :: update_mass = .False.
21          !> A logical to know if the size of the element must be computed in the
    current configuration
22          logical :: update_size = .False.
23          !> A logical to know if the internal force assembly is done with custom
    parallelization
24          logical :: parallel_fint = .False.
25          !> A logical to know if the mass assembly is done with custom parallelization
26          logical :: parallel_mass = .True.
27          !> 2d arrays to store the internal forces and mass at the dofs of the elements
28          double precision, dimension(:,:), allocatable :: Fint_e, M_e
29          !> Dof mapping for vector assembly
30          Type(LocalToGlobalMapping_t) :: mapping
31          !> Internal forces assembly
32          Type(LocalToGlobalVector_t) :: Fint_assembly
33          !> Mass assembly
34          Type(LocalToGlobalVector_t) :: Mass_assembly
35      contains
36          !> A subroutine to initialize the global to local dof mapping for parallel
    vector assembling
37          procedure, pass :: dof_mapping => default_dof_mapping
38          !> A subroutine to compute the size of the elements
39          procedure, pass :: compute_size => compute_elements_size
40          !> A subroutine to compute the mass at the dofs
41          procedure, pass :: compute_mass => compute_elements_mass
42          !> A subroutine to initialize the material element derived type
43          procedure(initialize_base_material_elements), pass, deferred :: initialize
44          !> A subroutine to initialize the properties of the material elements
45          procedure(init_base_material_elements_data), pass, deferred :: init_data
46          !> A subroutine to compute the internal forces at the element level
47          procedure(compute_internal_forces), pass, deferred :: compute_Fint
48      End Type Base_material_element_t
```

Source code 2.3: Fortran: Implementation of the procedure *initialize* for the linear elastic 3D truss

```
1  Subroutine init_linear_elastic_truss(self, mesh, elementInfos, materialSection,
       elementsSet, integrationScheme)
2
3      integer, parameter :: dim=3, nComponents=1
4
5      ! Inputs
6      Class(Linear_elastic_truss_t), target, intent(inout) :: self
7      Class(Mesh_t), target, intent(in) :: mesh
8      Type(Element_infos_t), target, intent(in) :: elementInfos
9      Type(Material_section_t), target, intent(in) :: materialSection
10     Type(Set_t), intent(in) :: elementsSet
11     Type(Integration_scheme_t), target, intent(in), optional :: integrationScheme
12
13     ! Body
14     call init_base_material_element(self,&
15                             mesh,& !> The Mesh_t derived type of the finite element
       model
16                             elementInfos,& !> A derived type representing the finite
       element type
```

```
17                              materialSection,& !> A derived type representing a
    material section
18                              elementsSet,& !> The elements having this material
    behaviour
19                              1,& !> The number of geometric data
20                              1,& !> The number of properties
21                              2,& !> The number of fields
22                              parallelFint=.True.)
23
24          ! initialize strain and stress fields
25      call init_field(self%E,&
26                      Field_enum%e_tensors%E,&
27                      nComponents,&
28                      self%infos%n_gauss,&
29                      self%elements_set%n_entities,&
30                      self%elements_set,&
31                      [XX_c])
32      call init_field(self%S,&
33                      Field_enum%e_tensors%S,&
34                      nComponents,&
35                      self%infos%n_gauss,&
36                      self%elements_set%n_entities,&
37                      self%elements_set,&
38                      [XX_c])
39          ! add the fields outputs in the container
40      call self%fields%set(1, self%E)
41      call self%fields%set(2, self%S)
42      call self%init_data()
43
44  End Subroutine init_linear_elastic_truss
```

Source code 2.4: Fortran: Implementation of the procedure *init_data* for the linear elastic 3D truss

```
1   Subroutine init_linear_elastic_truss_data(self)
2
3       ! Inputs
4       Class(Linear_elastic_truss_t), target, intent(inout) :: self
5
6       ! Body
7           ! area density
8       self%properties(1, :) = self%material_section%material%properties(1)*self%
        material_section%geometric_data(1)  ! rho
9           ! initial cross section
10      self%geometry_data(1, :) = self%material_section%geometric_data(1)  ! A0
11
12  End Subroutine init_linear_elastic_truss_data
```

Source code 2.5: Fortran: Implementation of the procedure *compute_Fint* for the linear elastic 3D truss

```
1   Subroutine linear_elastic_truss_Fint(self)
2
3       integer, parameter :: dim=3, elDim=1, nDofs=3, nComponents=1, iA0=1, iL0=2,
        ilambda=2, imu=3
4
5       ! Inputs
```

```
6       Class(Linear_elastic_truss_t), intent(inout) :: self
7
8       ! Locals
9       integer :: j, iNode, gElement, lNode, iElement, iDof, ldof
10      integer, dimension(:) :: dofs(nDofs), gDofs(nDofs), nodeDofs(nDofs)
11      double precision, dimension(:) :: g1(dim), e1(dim)
12      double precision :: lambda, mu, nu, l, E, A, V
13      !> 2D arrays of float
14      double precision, dimension(:,:) :: elementCoords(dim, self%infos%n_nodes), B(self
        %infos%n_nodes),&
15                                          dU(nDofs, self%infos%n_nodes), dUg(self%infos%
        n_nodes)
16      !> The derived type storing the varibales defined at the degrees of freedom
17      Type(Dof_variables_t), pointer :: var
18
19      ! Body
20      nodeDofs = [(j, j=1, nDofs)]
21          ! material properties
22      lambda = self%material_section%material%properties(ilambda)
23      mu = self%material_section%material%properties(imu)
24          ! compute Poisson's ratio
25      nu = lambda/(2.d+00*(lambda + mu))
26          !calculate Young's modulus
27      E = mu*(3.d+00*lambda + 2.d+00*mu)/(lambda + mu)
28      !$OMP PARALLEL PRIVATE(gElement, gdofs, iNode, lNode, elementCoords, idof, ldof,
        dU, g1, l, e1, dUg, V, B)
29          !$OMP DO
30      !> loop over all elements in the set
31      do iElement=1, self%elements_set%n_entities
32          !> get the global id of the element in the finite element model
33          gElement=self%elements_set%entities(iElement)
34              !> get the element coordinates and the increment of displacement at dofs
35          do  iNode=1,self%infos%n_nodes
36              !> get the global id of the node
37              lNode=self%mesh%elements%connectivity(iNode, gElement)
38              !> store the coordinates of the node
39              elementCoords(:, iNode) = self%mesh%nodes%coordinates(:, lNode)
40              !> get the global ids of the displacement dofs of the node
41              gDofs = nodeDofs + self%mesh%dofs%nodal_infos(2, lNode)
42              !> Loop over the displacement dofs of the node and store the increment of
        displacement
43              do iDof=1, nDofs
44                  var => self%mesh%dofs%variables(self%mesh%dofs%var_indx(self%mesh%dofs
        %infos(gDofs(iDof), 3)))
45                  ldof = self%mesh%dofs%infos(gDofs(iDof), 2)
46                  dU(iDof, iNode) = var%at(ldof, var%indx(i_dU))
47              end do
48          end do
49              !> compute the covariante vector g1
50          g1 = matmul(elementCoords + 0.5d+00*dU, self%infos%dNi_gauss(:, 1, 1))
51          l = 2.d+00 * sqrt(sum(g1**2))
52              !> normalize g1
53          e1 = g1 / (0.5d+00*l)
54              !> compute B matrix
55          B = [-1.d+00, 1.d+00]
56              !> compute Cauchy strain (l-l_0)/l_0
57          self%E%at(1, 1, iElement) = (l-self%mesh%elements%size(1, gElement))/self%mesh
        %elements%size(1, gElement)
```

```
58              !> compute the stress
59          self%S%at(:, 1, iElement) = E*self%E%at(1, 1, iElement)
60          do iNode=1, self%infos%n_nodes
61              self%Fint_e((iNode-1)*nDofs + 1: iNode*nDofs, iElement) = self%S%at(1, 1,
    iElement)*B(iNode)*self%geometry_data(1, iElement)*e1
62          end do
63      end do
64          !$OMP END DO
65      !$OMP END PARALLEL
66
67  End subroutine linear_elastic_truss_Fint
```

Conclusion

Due to its multi-material architecture, as well as its design freedom, a TFP preform is inherently complex to model. In this thesis, a semi-discrete approach was developed as it offers a good trade-off between modelling accuracy, efficiency and simplicity of development. In order to take into account the possibility of removing the backing material prior to forming, two semi-discrete models are proposed. Both take advantage of the embedded element approach to simplify the modelling of the stitching yarn and its underlying interactions. The latter is either assumed to bond the fibre tows modelled by beam elements to the backing material modelled by 2D elements (Model I) or to the fibre tows of an adjacent layer (Model II). This strategy allows developing two different models from a common base, namely, the explicit discretisation of fibre tows, which was considered as the most natural to take into account the capabilities of TFP preforming. The next step consists in implementing the different features of the models, namely:

- A beam element to model the fibre tows in both models
- A 2D element to numerically investigates Model I
- An embedding constraint to model the stitching yarn in both models

These features are implemented in Femtran. Femtran is an explicit finite element solver written in Fortran, which uses the OOP paradigm to ease the development, maintainability, reusability and readability of the program developed in this thesis. Its architecture allows implementing new finite element behaviours by simply adding new derived types in the code that extend an abstract derived type. In explicit finite element solvers, a new finite element mechanical behaviour requires the computation of internal forces of the element. The subsequent sections deals with the formulation, implementation and numerical validation of the different features of the TFP models.

2.2 Modelling the fibre tows

Introduction

This section deals with the modelling of the fibre tows in the TFP preform models. As mentioned previously in section 2.1, fibre tows can be considered as quasi-inextensible. Although their bending stiffness is low compared to their high tensile stiffness, the bending stiffness has been related to wrinkling defects in conventional textiles forming as mentioned in section 1.2. Therefore, it is taken into account for an accurate prediction of the TFP preform formability.
Consequently, fibre tows are modelled with beam elements to include the different deformation modes and not only the high tensile stiffness. A 2-node shear-flexible beam element, which has been widely studied (Ibrahimbegović et al., 1995; Géradin and Cardona, 2001; Ritto-Corrêa and Camotim, 2002), is formulated hereafter. The major key points are presented and references for further computation details are also given.

2.2.1 Formulation of a beam element

2.2.1.1 Operators' definitions and notations

In the followings:

- $(\bullet')$ is equivalent to $\frac{\mathrm{d}\bullet}{\mathrm{d}S}$ where S is the curvilinear abscissa
- $\tilde{\boldsymbol{v}}$ is a skew symmetric matrix such as $\tilde{\boldsymbol{v}}\vec{\boldsymbol{u}} = \vec{\boldsymbol{v}}\times\vec{\boldsymbol{u}}$. It is defined as $\underset{(3\times3)}{[\tilde{\boldsymbol{v}}]} = \begin{bmatrix} 0 & v_3 & -v_2 \\ -v_3 & 0 & v_1 \\ v_2 & -v_1 & 0 \end{bmatrix}$ where $\underset{(3\times1)}{\vec{\boldsymbol{v}}} = \begin{bmatrix} v_1 & v_2 & v_3 \end{bmatrix}^T$ and $\mathrm{vec}(\tilde{\boldsymbol{v}}) = \vec{\boldsymbol{v}}$

2.2.1.2 Assumptions

This formulation includes two major assumptions:

- The beam cross sections remain plane and do not deform when subjected to elastic deformations
- The strains are small and finite rotations are allowed.

The first assumption assumes no warping of the cross-section, which would be difficult to characterise for a tow made of individual fibres. The small strain assumption is consistent with the quasi-inextensibility of fibre tows, which will be achieved by assigning a high tensile stiffness. The finite rotations allow for large displacements and rotations in the space, which is necessary in forming simulations.

2.2.1.3 Kinematics

The position of a point in the initial and current configurations is defined as:

$$\underset{(3\times1)}{\vec{\boldsymbol{X}}} = S\vec{\boldsymbol{E_1}} + X_2\vec{\boldsymbol{E_2}} + X_3\vec{\boldsymbol{E_3}} \quad \text{(Initial)} \tag{2.9}$$

$$\underset{(3\times1)}{\vec{\boldsymbol{x}}} = \vec{\boldsymbol{\phi_0}}(S) + X_2\vec{\boldsymbol{e_2}} + X_3\vec{\boldsymbol{e_3}} \quad \text{(Current)} \tag{2.10}$$

S is the curvilinear abscissa of the beam axis in the initial configuration and (X_2,X_3) are the coordinates of the planar cross-section. As the cross-section does not deform (no warping), the planar coordinates (X_2,X_3) are unchanged in the deformed configuration. ϕ_0 corresponds to the position of a point located on the neutral axis in the current configuration. $\boldsymbol{E}$ and $\boldsymbol{e}$ define respectively the initial and current cross-section orientations (Fig.2.9):

$$\underset{(3\times3)}{[\boldsymbol{E}]} = \left[\underset{(3\times1)}{\vec{\boldsymbol{E_1}}} \quad \underset{(3\times1)}{\vec{\boldsymbol{E_2}}} \quad \underset{(3\times1)}{\vec{\boldsymbol{E_3}}}\right] \quad \text{(Initial cross-section orientation)} \tag{2.11}$$

$$\underset{(3\times3)}{[\boldsymbol{e}]} = \left[\underset{(3\times1)}{\vec{\boldsymbol{e_1}}} \quad \underset{(3\times1)}{\vec{\boldsymbol{e_2}}} \quad \underset{(3\times1)}{\vec{\boldsymbol{e_3}}}\right] \quad \text{(Current cross-section orientation)} \tag{2.12}$$

$\vec{\boldsymbol{E_1}}$ and $\vec{\boldsymbol{e_1}}$ are the cross-section normal vectors while ($\vec{\boldsymbol{E_2}}$, $\vec{\boldsymbol{E_3}}$) and ($\vec{\boldsymbol{e_2}}$, $\vec{\boldsymbol{e_3}}$) are the in-plane vectors of the cross-section. Since transverse shear is allowed, the tangent vector to the centroid line $\vec{\boldsymbol{g_1}}$ might be different from the cross-section normal $\vec{\boldsymbol{e_1}}$ as illustrated in Fig. 2.9.

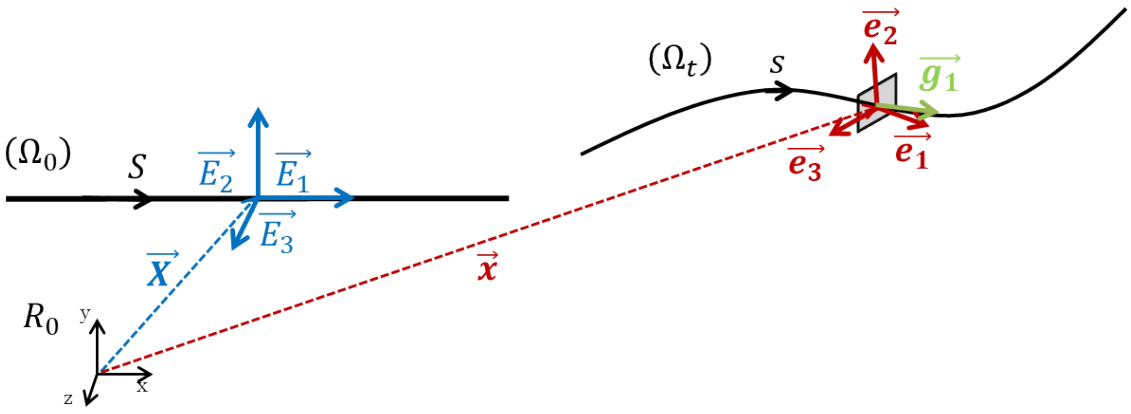

Figure 2.9: Initial and current configurations of a beam

2.2.1.4 Finite rotation parameterization

The current cross-section orientation $\boldsymbol{e}$ is computed by applying the rotation operator $\boldsymbol{R}$ to the initial cross-section orientation $\boldsymbol{E}$ (Eq. 2.13).

$$\boldsymbol{e} = \boldsymbol{R}\boldsymbol{E} \tag{2.13}$$

Several parametrization exist for the rotation operator $\boldsymbol{R}$ such as the Cartesian pseudo-vector or the Quaternions. In this work, the Cartesian pseudo-vector parametrisation is used. It allows defining $\boldsymbol{R}$ as a function of a pseudo-vector $\vec{\boldsymbol{\psi}}$. $\vec{\boldsymbol{\psi}}$ can be written as

$$\underset{(3\times1)}{\vec{\boldsymbol{\psi}}} = \psi\vec{\boldsymbol{n}} \tag{2.14}$$

where ψ is the rotation amplitude and $\vec{\boldsymbol{n}}$ is the rotation axis. Fig. 2.10 illustrates the definition of $\vec{\boldsymbol{\psi}}$.

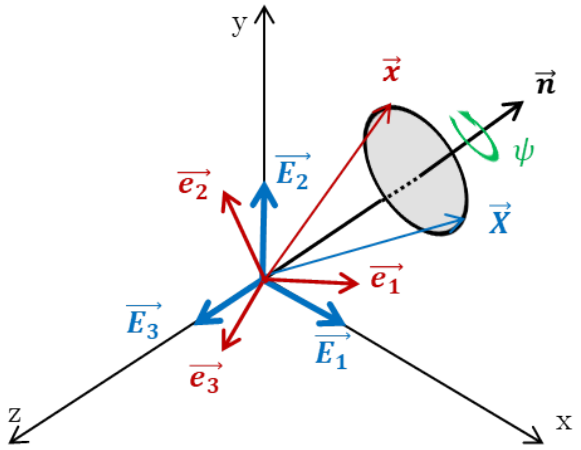

Figure 2.10: Definition of the Cartesian pseudo-vector $\vec{\boldsymbol{\psi}}$

In addition to the rotation operator $\boldsymbol{R}$, the tangent rotation operator $\boldsymbol{T}$ and its directional derivative $\boldsymbol{T}' = D\boldsymbol{T}\left[\frac{\mathrm{d}\vec{\boldsymbol{\psi}}}{\mathrm{d}S}\right]$ are required. These terms come into play when the differentiation with respect to S is applied. $\boldsymbol{R}$, $\boldsymbol{T}$ and $\boldsymbol{T'}$ are computed using the family of trigonometric functions established in Ritto-Corrêa and Camotim (2002) and given hereafter.

Two families of trigonometric functions a_i and b_i are defined according to the following relations:

$$a_1(\psi) = \frac{\sin\psi}{\psi} \qquad a_2(\psi) = \frac{1-\cos\psi}{\psi^2} \qquad a_3(\psi) = \frac{\psi - \sin\psi}{\psi^3} \tag{2.15}$$

$$b_1(\psi) = \frac{\psi\cos\psi - \sin\psi}{\psi^3} \quad b_2(\psi) = \frac{\psi\sin\psi - 2 + 2\cos\psi}{\psi^4} \quad b_3(\psi) = \frac{3\sin\psi - 2\psi - \psi\sin\psi}{\psi^5} \tag{2.16}$$

These function are singular when $\psi = 0$. To deal with this numerical issue, power expansion series of these functions are used when $\psi < 10^{-2}$.

$$a_i(\psi) = \sum_{k=0}^{n} \frac{(-1)^k \psi^{2k}}{(2k+i)!} \qquad b_i(\psi) = \sum_{k=0}^{n} \frac{2(k+1)(-1)^{k+1}\psi^{2k}}{(2k+i+2)!} \tag{2.17}$$

n is equal to 13 for the computation of the power expansion series.

Using the trigonometric functions, the following definitions apply:

$$\underset{(3\times3)}{[\boldsymbol{R}]} = \boldsymbol{I} + a_1\tilde{\boldsymbol{\psi}} + a_2\tilde{\boldsymbol{\psi}}^2 \tag{2.18}$$

$$\underset{(3\times3)}{[\boldsymbol{T}]} = \boldsymbol{I} + a_2\tilde{\boldsymbol{\psi}} + a_3\tilde{\boldsymbol{\psi}}^2 \tag{2.19}$$

$$\underset{(3\times3)}{D\boldsymbol{T}[\vec{\boldsymbol{u}}]} = a_2\tilde{\boldsymbol{u}} + a_3\left(\vec{\boldsymbol{u}}\otimes\vec{\boldsymbol{\psi}} + \vec{\boldsymbol{\psi}}\otimes\vec{\boldsymbol{u}}\right) + b_1\left(\vec{\boldsymbol{\psi}}\cdot\vec{\boldsymbol{u}}\right)\boldsymbol{I} + b_2\left(\vec{\boldsymbol{\psi}}\cdot\vec{\boldsymbol{u}}\right)\tilde{\boldsymbol{\psi}} + b_3\left(\vec{\boldsymbol{\psi}}\cdot\vec{\boldsymbol{u}}\right)\vec{\boldsymbol{\psi}}\otimes\vec{\boldsymbol{\psi}} \tag{2.20}$$

2.2.1.5 Strain and curvature vectors

Strains and curvatures are computed from the displacement gradient $\vec{\boldsymbol{D}}$, more precisely through the difference between the deformation position gradient in the current $\frac{\mathrm{d}\vec{\boldsymbol{x}}}{\mathrm{d}S}$ and initial $\frac{\mathrm{d}\vec{\boldsymbol{X}}}{\mathrm{d}S}$ configurations, brought back to the material frame by applying $\boldsymbol{R}^T$:

$$\begin{aligned}\underset{(3\times1)}{\vec{\boldsymbol{D}}}(S, X_2, X_3) &= \boldsymbol{R}^T\frac{\mathrm{d}\vec{\boldsymbol{x}}}{\mathrm{d}S} - \frac{\mathrm{d}\vec{\boldsymbol{X}}}{\mathrm{d}S} \\ &= \boldsymbol{R}^T\left(\frac{\mathrm{d}\vec{\boldsymbol{\phi_0}}}{\mathrm{d}S} - \vec{\boldsymbol{e_1}}\right) + \boldsymbol{R}^T\frac{\mathrm{d}\boldsymbol{R}}{\mathrm{d}S}\left(X_2\vec{\boldsymbol{e_2}} + X_3\vec{\boldsymbol{e_3}}\right)\end{aligned} \tag{2.21}$$

From the definition of the displacement gradient $\vec{\boldsymbol{D}}$, the strain and curvature vectors in the material frame are identified:

$$\underset{(3\times1)}{\vec{\boldsymbol{\Gamma}}} = \boldsymbol{R}^T\left(\frac{\mathrm{d}\vec{\boldsymbol{\phi_0}}}{\mathrm{d}S} - \vec{\boldsymbol{e_1}}\right) = \begin{bmatrix} E \\ \Gamma_1 \\ \Gamma_2 \end{bmatrix} \qquad \underset{(3\times1)}{\vec{\boldsymbol{K}}} = vec\left(\boldsymbol{R}^T\frac{\mathrm{d}\boldsymbol{R}}{\mathrm{d}S}\right) = \boldsymbol{T}^T\frac{\mathrm{d}\vec{\boldsymbol{\psi}}}{\mathrm{d}S} = \begin{bmatrix} K_T \\ K_1 \\ K_2 \end{bmatrix} \tag{2.22}$$

In Eq. 2.22, E is the longitudinal strain component, Γ_1 and Γ_2 are the transverse shear components. K_T is the torsional strain of the neutral axis whereas K_1 and K_2 are the bending strains along the cross-section axis. These curvatures can also be expressed using the cross matrix expression:

$$\tilde{\boldsymbol{K}} = \boldsymbol{R}^T\frac{\mathrm{d}\boldsymbol{R}}{\mathrm{d}S} \tag{2.23}$$

The spatial counterparts of the strains and curvatures vectors are obtained by applying the rotation operator:

$$\vec{\boldsymbol{\gamma}} = \boldsymbol{R}\vec{\boldsymbol{\Gamma}} \qquad\qquad \vec{\boldsymbol{\kappa}} = \boldsymbol{R}\vec{\boldsymbol{K}} \tag{2.24}$$

2.2.1.6 Equilibrium equations, internal virtual work and strain-curvature variations

Equilibrium equations in the material frame in quasi-static regime are given hereafter for the forces (Eq.2.25) and moments (Eq.2.26):

$$\frac{\mathrm{d}\vec{\boldsymbol{F}}}{\mathrm{d}S} + \tilde{\boldsymbol{K}}\vec{\boldsymbol{F}} + \boldsymbol{R}^T\vec{\boldsymbol{f}} = \vec{\boldsymbol{0}} \tag{2.25}$$

$$\frac{\mathrm{d}\vec{\boldsymbol{M}}}{\mathrm{d}S} + \left(\boldsymbol{R}^T\frac{\mathrm{d}\vec{\boldsymbol{\phi_0}}}{\mathrm{d}S}\right) \times \vec{\boldsymbol{F}} + \tilde{\boldsymbol{K}}\vec{\boldsymbol{M}} + \boldsymbol{R}^T\vec{\boldsymbol{m}} = \vec{\boldsymbol{0}} \tag{2.26}$$

The forces and moments in the material frame are defined according to:

$$\underset{(3\times1)}{\vec{\boldsymbol{F}}} = \begin{bmatrix} N \\ Q_1 \\ Q_2 \end{bmatrix} \qquad \underset{(3\times1)}{\vec{\boldsymbol{M}}} = \begin{bmatrix} M_T \\ M_1 \\ M_2 \end{bmatrix} \tag{2.27}$$

N is the tensile force, Q_1 and Q_2 are the transverse shear forces of the cross-section. M_T is the torsional moment, M_1 and M_2 are the bending moments. $\vec{\boldsymbol{f}}$ and $\vec{\boldsymbol{m}}$ are external distributed forces and moments in the spatial frame brought back to the material frame by applying $\boldsymbol{R}^T$.

Using the weak form of the equilibrium equations in the material frame, the internal virtual work can be expressed as:

$$\delta W_{int} = \int_0^L \vec{\boldsymbol{F}}\delta\vec{\boldsymbol{\Gamma}} + \vec{\boldsymbol{M}}\delta\vec{\boldsymbol{K}}dS \tag{2.28}$$

where L is the initial length of the beam.

To compute the internal forces, the expression of the strain and curvature changes are required to calculate the strain-displacement matrix $\boldsymbol{B}$. These expressions can be derived by differentiating the relationships for the strain and curvature vectors given in Eq.2.22:

$$\underset{(6\times1)}{\begin{bmatrix}\delta\vec{\boldsymbol{\Gamma}}\\ \delta\vec{\boldsymbol{K}}\end{bmatrix}} = \underbrace{\underset{(6\times9)}{\begin{bmatrix}\boldsymbol{R}^T & 0 & \widetilde{\boldsymbol{R}^T\vec{\boldsymbol{\phi}}_{\boldsymbol{0}}{}'}\boldsymbol{T}^T\\ 0 & \boldsymbol{T}^T & \tilde{\boldsymbol{K}}\boldsymbol{T}^T + \boldsymbol{T}'\end{bmatrix}}}_{\boldsymbol{D}} \underset{(9\times1)}{\begin{bmatrix}\delta\vec{\boldsymbol{\phi}}_{\boldsymbol{0}}{}'\\ \delta\vec{\boldsymbol{\psi}}'\\ \delta\vec{\boldsymbol{\psi}}\end{bmatrix}} \tag{2.29}$$

Then, the strain-displacement matrix $\boldsymbol{B}$ is given by:

$$\underset{(6\times n_{dofs})}{[\boldsymbol{B}]} = \underset{(6\times9)}{[\boldsymbol{D}]}\underset{(9\times n_{dofs})}{[\boldsymbol{Q}]} \tag{2.30}$$

where $\boldsymbol{Q}$ is an interpolation matrix that will be detailed in the next section concerning the implementation of the beam element. n_{dofs} is the number of degree of freedom of the beam element.

Finally, the expression of the internal forces vector can be deduced:

$$\underset{(n_{dofs}\times1)}{[\boldsymbol{F_{int}}]} = \int_0^L \boldsymbol{B}^T \begin{bmatrix}\vec{\boldsymbol{F}}\\ \vec{\boldsymbol{M}}\end{bmatrix} dS \tag{2.31}$$

2.2.1.7 Constitutive law

Considering an linear elastic law, the force and moment vectors are related to the strain and curvature vectors by the following equation:

$$\underset{(6\times1)}{\begin{bmatrix}\vec{\boldsymbol{F}}\\ \vec{\boldsymbol{M}}\end{bmatrix}} = \boldsymbol{C}\underset{(6\times1)}{\begin{bmatrix}\vec{\boldsymbol{\Gamma}}\\ \vec{\boldsymbol{K}}\end{bmatrix}} \tag{2.32}$$

As a fibre tow is made of individual fibres, independent section stiffness are used. Moreover, couplings between the deformation modes are neglected. Therefore, the constitutive matrix $\boldsymbol{C}$ is a diagonal matrix given by:

$$\underset{(6\times6)}{[\boldsymbol{C}]} = \begin{bmatrix}C_E & 0 & 0 & 0 & 0 & 0\\ 0 & C_{\Gamma1} & 0 & 0 & 0 & 0\\ 0 & 0 & C_{\Gamma2} & 0 & 0 & 0\\ 0 & 0 & 0 & C_{K1} & 0 & 0\\ 0 & 0 & 0 & 0 & C_{K2} & 0\\ 0 & 0 & 0 & 0 & 0 & C_{K3}\end{bmatrix}$$

C_E is the axial stiffness, $C_{\Gamma 1}$ and $C_{\Gamma 2}$ are the transverse shear stiffness. C_{K1} is the torsional stiffness, C_{K2} and C_{K3} are the flexural stiffness.

Transition

This section described the formulation of a shear-flexible linear beam element. In particular, the Cartesian pseudo-vector representation is used to deal with finite rotations. Since fibre tows cannot be considered as a continuum medium, the relations between the cross-section stiffnesses of the classical beam theory are not considered. Instead, the cross-section stiffnesses are independent and uncoupling between the different deformation modes is assumed. In the following section, the implementation details are given.

2.2.2 Implementation of the beam element

2.2.2.1 Interpolation

The beam element has two nodes and each of them has three displacement degree of freedom (dofs) U_{ij} and three rotation dofs ψ_{ij} where i is the node number and j is the dof number.

$$\vec{\boldsymbol{U_i}} = \begin{bmatrix} U_{i1} & U_{i2} & U_{i3} \end{bmatrix}^T \qquad \vec{\boldsymbol{\psi_i}} = \begin{bmatrix} \psi_{i1} & \psi_{i2} & \psi_{i3} \end{bmatrix}^T \tag{2.33}$$

Consequently, the beam element contains 12 dofs. Linear interpolation functions are used and defined on the parametric domain $\xi \in [-1; 1]$ according to Table 2.2 as well as their derivatives.

Table 2.2: Linear shape functions and their derivatives for the beam element

Node	N_i	$\frac{\mathrm{d}N_i}{\mathrm{d}\xi}$
1	$0.5\,(1-\xi)$	-0.5ξ
2	$0.5\,(1+\xi)$	0.5ξ
Domain definition	$\xi \in [-1; 1]$	

The physical and parametric domains of the beam are illustrated in Fig. 2.11.

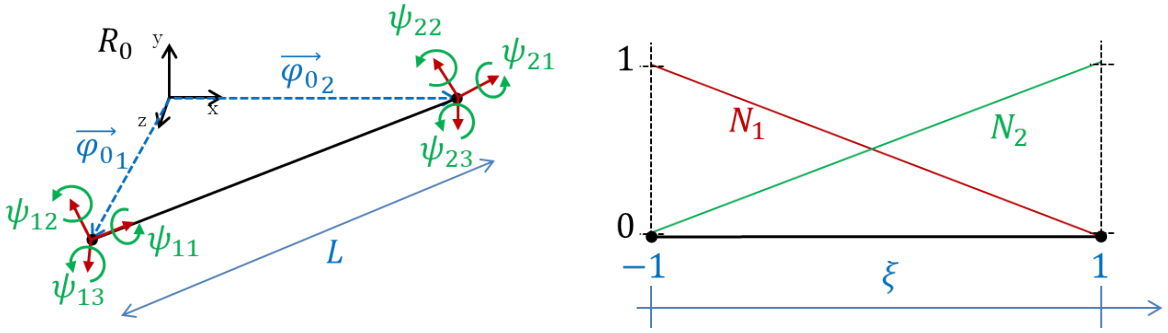

(a) Physical domain **(b)** Parametric domain

Figure 2.11: Definition of the physical (a) and parametric (b) domains of the beam element

The Cartesian derivative of the shape functions is given by:

$$N_i'(\xi) = \frac{1}{J}\frac{\mathrm{d}N_i}{\mathrm{d}\xi} \tag{2.34}$$

where $J = \frac{\mathrm{d}S}{\mathrm{d}\xi}$.

Using the interpolation functions, the current position of a point on the neutral axis of a beam element and its derivative with respect to the curvilinear abscissa S are given by:

$$\begin{aligned} \vec{\boldsymbol{\phi_0}}(\xi) &= N_1(\xi)\vec{\boldsymbol{\phi_{0_1}}} + N_2(\xi)\vec{\boldsymbol{\phi_{0_2}}} \\ \vec{\boldsymbol{\phi_0'}}(\xi) &= N_1'(\xi)\vec{\boldsymbol{\phi_{0_1}}} + N_2'(\xi)\vec{\boldsymbol{\phi_{0_2}}} \end{aligned} \tag{2.35}$$

where $J = \frac{L}{2}$.

Similarly, the Cartesian pseudo-vector $\vec{\boldsymbol{\psi}}$ and its derivative with respect to S are computed from the dofs of the beam elements:

$$\begin{aligned} \vec{\boldsymbol{\psi}}(\xi) &= N_1(\xi)\vec{\boldsymbol{\psi_1}} + N_2(\xi)\vec{\boldsymbol{\psi_2}} \\ \vec{\boldsymbol{\psi'}}(\xi) &= N_1'(\xi)\vec{\boldsymbol{\psi_1}} + N_2'(\xi)\vec{\boldsymbol{\psi_2}} \end{aligned} \tag{2.36}$$

From Eq. 2.35 and 2.36 the relation between the variations of $\left(\vec{\phi_0}', \vec{\psi}', \vec{\psi}\right)$ and the variations of the nodal parameters (dofs) can be expressed using the interpolation shape functions of the beam as well as their derivatives. The interpolation matrix $\boldsymbol{Q}$ is defined as follow:

$$\underset{(9\times1)}{\begin{bmatrix} \delta\vec{\boldsymbol{\phi_0}}' \\ \delta\vec{\boldsymbol{\psi}}' \\ \delta\vec{\boldsymbol{\psi}} \end{bmatrix}} = \underbrace{\begin{bmatrix} N_1'\boldsymbol{I} & \boldsymbol{0} & N_2'\boldsymbol{I} & \boldsymbol{0} \\ \boldsymbol{0} & N_1'\boldsymbol{I} & \boldsymbol{0} & N_2'\boldsymbol{I} \\ \boldsymbol{0} & N_1\boldsymbol{I} & \boldsymbol{0} & N_2\boldsymbol{I} \end{bmatrix}}_{\boldsymbol{Q}\ (9\times12)} \underset{(12\times1)}{\begin{bmatrix} \delta\vec{\boldsymbol{\phi_{0_1}}} \\ \delta\vec{\boldsymbol{\psi_1}} \\ \delta\vec{\boldsymbol{\phi_{0_2}}} \\ \delta\vec{\boldsymbol{\psi_2}} \end{bmatrix}} \tag{2.37}$$

It can be noticed that using the current position of a point on the neutral axis of the beam $\vec{\boldsymbol{\phi_0}}$ or its displacement $\vec{\boldsymbol{U}}$ is equivalent since:

$$\vec{\boldsymbol{\phi_0}} = \vec{\boldsymbol{U}} + \vec{\boldsymbol{X}} \qquad\qquad \vec{\boldsymbol{\phi_0}}' = \vec{\boldsymbol{U}}' \tag{2.38}$$

2.2.2.2 Beam profile and shear locking

Depending on the beam profile, a correction factor k is applied to the transverse shear moduli. k equals 0.89 for a circular profile and $\frac{5}{6}$ for a rectangular one. Therefore, $C_{2_k} = k * C_2$ and $C_{3_k} = k * C_3$.

Using the same interpolation functions for both the displacements and rotations leads to the well-known shear-locking phenomenon. To alleviate this issue, two techniques are used:

- Reduced integration
- The transverse shear moduli are corrected by adding a residual bending rigidity

Taking into account the residual bending rigidity, the transverse shear moduli are given by:

$$\overline{C_{2_k}} = \left(\frac{1}{C_{2_k}} + \frac{L^2}{12C_5}\right)^{-1} \qquad\qquad \overline{C_{3_k}} = \left(\frac{1}{C_{3_k}} + \frac{L^2}{12C_6}\right)^{-1} \tag{2.39}$$

2.2.2.3 Algorithm

The algorithm to compute the internal forces of linear beam element is detailed in Alg.2. In this algorithm $\xi = 0$.

Algorithm 2 Internal forces computation of the linear elastic beam element

1: Compute the covariant vector: $\vec{\boldsymbol{g}} = \sum_{i=1}^{2} \frac{\mathrm{d}N_i(\xi)}{\mathrm{d}\xi} \vec{\boldsymbol{x_i}}$
2: Compute Jacobian: $J = \frac{L}{2}$
3: Compute the derivative of the neutral axis position: $\vec{\boldsymbol{\phi_0}}' = \frac{1}{J}\vec{\boldsymbol{g}}$
4: Compute the Cartesian pseudo-vector: $\vec{\boldsymbol{\psi}} = \sum_{i=1}^{2} N_i(\xi)\vec{\boldsymbol{\psi_i}}$
5: Compute the Cartesian pseudo-vector derivative: $\vec{\boldsymbol{\psi}}' = \sum_{i=1}^{2} N_i'(\xi)\vec{\boldsymbol{\psi_i}}$
6: Compute the rotation operator $\boldsymbol{R}$, the tangent operator $\boldsymbol{T}$ and its directional derivative $D\boldsymbol{T}\left[\vec{\boldsymbol{\psi}}'\right]$ using Eq. 2.18, 2.19 and 2.20.
7: Compute the current cross-section orientation: $e = RE$
8: Compute the strain vector: $\vec{\boldsymbol{\Gamma}} = \boldsymbol{R}^T\left(\vec{\boldsymbol{\psi_0}}' - \vec{\boldsymbol{e_1}}\right)$
9: Compute the curvature vector: $\vec{\boldsymbol{K}} = \boldsymbol{T^T}\vec{\boldsymbol{\psi}}'$
10: Compute the strain-displacement matrix: $\boldsymbol{B = DQ}$
11: Compute the force and moment vectors: $\begin{bmatrix}\vec{\boldsymbol{F}}\\ \vec{\boldsymbol{M}}\end{bmatrix} = C\begin{bmatrix}\vec{\boldsymbol{\Gamma}}\\ \vec{\boldsymbol{K}}\end{bmatrix}$
12: Compute internal forces: $\left[F_{int}\right] = L\boldsymbol{B}^T\begin{bmatrix}\vec{\boldsymbol{F}}\\ \vec{\boldsymbol{M}}\end{bmatrix}$

Transition

This section explained how to implement the linear elastic beam element in the finite element solver. The next step consists in validating the implementation using elementary test cases.

2.2.3 Numerical validation: Elementary and referenced test cases

The numerical validation of the implementation of the linear elastic beam element used to model fibre tows is investigated. First, elementary tests are performed and the results are compared with the B31 element of the commercial code Abaqus. Next, referenced tests are carried out. The beam element is tested using a classical linear elastic constitutive law. Consequently, the cross-section stiffnesses are perfectly defined from the Young's modulus E, the Poisson's ratio ν, the shear moduli G and the geometry of the cross-section.

In the non-referenced elementary tests, the Young's modulus equals 210 GPa, the Poisson's ratio is 0.33 and the density equals 7800N kg/m3. The beam has a circular cross-section of radius 50 mm and a length of 1 m.

2.2.3.1 Elementary tensile test

Objectives This first elementary test case aims at testing the axial behaviour of the beam element.

Table 2.3: Cantilever beam under transverse tip load $F = 100$ N: x-displacement, y-displacement and rotation around z-axis for different number of elements and comparison with Abaqus B31 element

Number of elements	x-displacement (m)		y-displacement (m)		rotation around z-axis	
	Present	B31	Present	B31	Present	B31
1	$-5.272\ 10^{-10}$	$-4.622\ 10^{-10}$	$-3.252\ 10^{-5}$	$-3.047\ 10^{-5}$	$-4.850\ 10^{-5}$	$-4.850\ 10^{-5}$
3	$-6.172\ 10^{-10}$	$-6.110\ 10^{-10}$	$-3.252\ 10^{-5}$	$-3.229\ 10^{-5}$	$-4.850\ 10^{-5}$	$-4.850\ 10^{-5}$
10	$-6.299\ 10^{-10}$	$-6.293\ 10^{-10}$	$-3.252\ 10^{-5}$	$-3.250\ 10^{-5}$	$-4.850\ 10^{-5}$	$-4.850\ 10^{-5}$
Analytic	0		$-3.22\ 10^{-5}$		$-4.85\ 10^{-5}$	

Setup A single element is clamped at one end while an axial point load of 100 N is applied at the other extremities.

Results The loaded-tip displacement equals $6.063\ 10^{-8} m$ for the tested beam element as well as for the B31 element. The analytical value also agrees with this result.

2.2.3.2 Elementary twisting test

Objectives This second elementary test case aims at testing the torsional behaviour of the beam element.

Setup A single element is clamped at one end while a torsional moment of 100 N/m is applied at the other end.

Results The loaded-tip rotation around the neutral axis of the beam equals $1.290\ 10^{-4}$ for the tested beam element as well as for the B31 element. The analytical result also agree with this result.

2.2.3.3 Cantilever beam under transverse tip load

Objectives This third elementary test case aims at testing the transverse behaviour of the beam element when submitted to transverse load. Since a non-following force is applied, transverse shear deformation appears contrary to a pure bending case. While the two previous test cases where limited to small displacements and rotations, this test is performed with two load values, namely 100 N and 10^6 N, to check the behaviour of the beam element when large displacements and finite rotations occur.

Setup A beam is clamped at one end while a transverse point load is applied at the other end. The number of elements as well as the load value are varied.

Results The results for the small displacements case are reported in Table 2.3. Values obtained for the beam element are in good agreement with those of the B31 element and the analytical values. The results for the large displacements and rotations are shown in Table 2.4. The results of the beam element converge to the same values of the B31 element.

2.2.3.4 Cantilever beam tip moment

Objectives This last elementary test case aims at testing the bending behaviour of the beam element when submitted to a moment. Contrary to the previous test case, no transverse shear deformation appear due to the pure bending configuration. As for the previous test, this test is also performed with two load values, namely 100 N/m and $5\ 10^5$ N/m, to check the behaviour of the beam element when large displacements and finite rotations occur.

Table 2.4: Cantilever beam under transverse tip load $F = 10^6$ N: x-displacement, y-displacement and rotation around z-axis for different number of elements and comparison with Abaqus B31 element

Number of elements	x-displacement (m)		y-displacement (m)		rotation around z-axis	
	Present	B31	Present	B31	Present	B31
1	-0.0479	-0.0423	-0.3065	-0.2883	-0.4612	-0.4653
3	-0.0529	-0.0523	-0.2967	-0.2948	-0.4503	-0.4507
10	-0.0537	-0.0537	-0.2959	-0.2956	-0.4493	-0.4493

Table 2.5: Cantilever beam under tip moment $M = 100$ N/m: x-displacement, y-displacement and rotation around z-axis for different number of elements and comparison with Abaqus B31 element

Number of elements	x-displacement (m)		y-displacement (m)		rotation around z-axis	
	Present	B31	Present	B31	Present	B31
1	$-1.176\ 10^{-9}$	$-1.177\ 10^{-9}$	$-4.850\ 10^{-5}$	$-4.850\ 10^{-5}$	$-9.701\ 10^{-5}$	$-9.701\ 10^{-5}$
3	$-1.524\ 10^{-9}$	$-1.524\ 10^{-9}$	$-4.850\ 10^{-5}$	$-4.850\ 10^{-5}$	$-9.701\ 10^{-5}$	$-9.701\ 10^{-5}$
10	$-1.564\ 10^{-9}$	$-1.564\ 10^{-9}$	$-4.850\ 10^{-5}$	$-4.850\ 10^{-5}$	$-9.701\ 10^{-5}$	$-9.701\ 10^{-5}$
Analytic	0		$-4.85\ 10^{-5}$		$-9.70\ 10^{-5}$	

Setup A beam is clamped at one end while a transverse point load is applied at the other end. The number of elements as well as the load value are varied.

Results The results for the small displacement case are reported in Table 2.5 where good agreement with the B31 elements and analytical results is shown. The results for the large displacement and rotations are shown in Table 2.6.

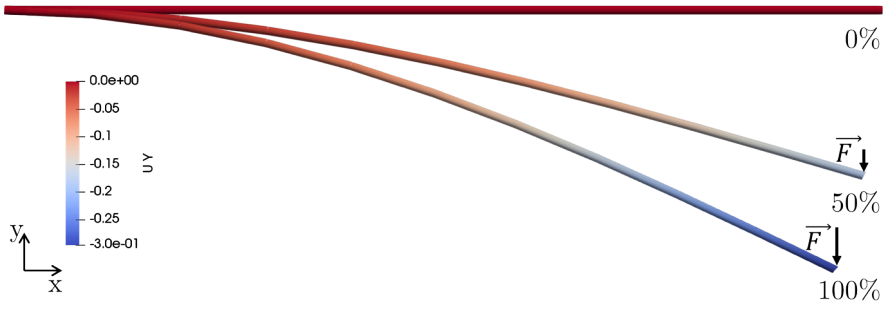

Figure 2.12: Cantilever beam tip moment ($F = 10^6$ N): Different configurations of the beam and displacement field along the y-axis (m)

Table 2.6: Cantilever beam under tip moment $M = 5\ 10^5$ N/m: x-displacement, y-displacement and rotation around z-axis for different number of elements and comparison with Abaqus B31 element

Number of elements	x-displacement (m)		y-displacement (m)		rotation around z-axis	
	Present	B31	Present	B31	Present	B31
1	-0.0292	-0.0292	-0.2401	-0.2402	-0.4850	-0.4850
3	-0.0377	-0.0377	-0.2380	-0.2381	-0.4850	-0.4850
10	-0.0386	-0.0386	-0.2378	-0.2377	-0.4850	-0.4850

Table 2.7: Cantilever beam under two transverse loads: x-displacement, y-displacement and rotation around z-axis for different number of elements and comparison with Géradin and Cardona (2001) and analytical results

Number of elements	x-displacement (m)		y-displacement (m)		rotation around z-axis	
	Present	Ref	Present	Ref	Present	Ref
2	-31.298	-28.986	-69.685	-65.862	-1.076	-1.100
4	-30.872	-30.258	-67.310	-66.627	-1.048	-1.056
8	-30.877	-30.621	-67.210	-66.874	-1.047	-1.046
Analytic	-30.75		-66.96		-	

2.2.3.5 Referenced test: cantilever beam under two transverse loads

Objectives This first referenced test case aims at testing the bending and transverse behaviour of the beam element when submitted to two transverse point loads.

Setup A beam is clamped at one end while two transverse point loadings are applied as illustrated in Fig. 2.13. The material parameters have no specified units and does not correspond to a known material. In particular, the Poisson's ratio is negative and equals -0.931. The Young's modulus equals 1570796 and the density ($\rho = 0.01$) is chosen such as a reasonable critical time step is obtained while the kinetic energy is low compared to the internal one. The beam has a circular cross-section of radius 0.252 and a total length of 102.75. The first transverse force is applied at a distance $L_1 = 52.03$ with a magnitude of 0.85 while the second is applied at the tip with the magnitude of 1.35. The number of elements is varied.

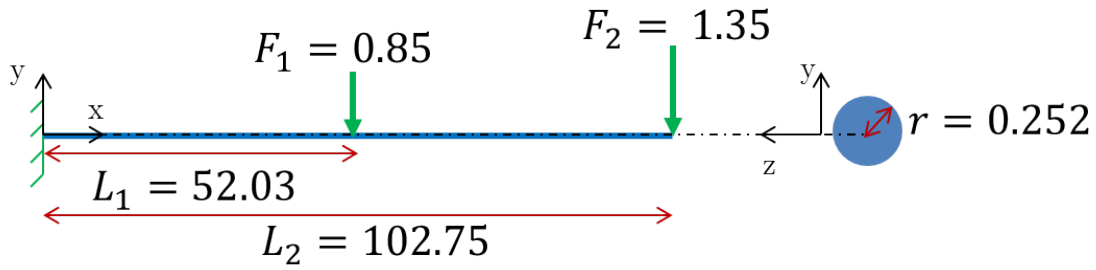

Figure 2.13: Cantilever beam under two transverse loads: initial configuration and boundary conditions

Results The results are summarized in Table 2.7 and compared with those by Géradin and Cardona (2001) as well as the analytical solution. The beam element behaviour is in good agreement with both the reference's results and the analytical ones.

2.2.3.6 Referenced test: roll-up of a beam under tip moment

Objectives This second referenced test case aims at testing the pure bending behaviour of the beam element when submitted to a tip moment. It is similar to the elementary test case 2.2.3.4 but it features higher rotation and is documented in the literature.

Setup A beam is clamped at one end while a moment is applied at the other end. As the previous test, the material parameters are given without specified units. The Young's modulus equals 79577, the Poisson's ratio is null and the density equals 10. The beam has a circular cross-section of radius 0.2 and a length of 10. 10 elements are used and two loading scenario

Table 2.8: Roll-up of a beam under tip moment ($M = 2.5\pi$): x-displacement and y-displacement comparisons with Ibrahimbegović et al. (1995) and Ritto-Corrêa and Camotim (2002)

Number of elements	x-displacement (m)		y-displacement (m)	
	Present	Ref	Present	Ref
10	-0.9945	-0.9945	3.7302	3.7302

are considered. In the first one a moment of 2.5π is applied while in the second one a moment of 20π is applied such as the beam finally forms a circle.

Results The results are summarized in Table 2.8. The beam element behaviour agrees perfectly with the one described in Ibrahimbegović et al. (1995); Ritto-Corrêa and Camotim (2002) in the first scenario. In the second scenario, the loaded tip of the beam finally coincides with the clamped one which gives the beam a circle shape. The final position of the loaded tip is $(5.75716\ 10^{-5}, 1.38638\ 10^{-6})$ in the xy-plane. Fig. 2.14 shows different configurations of the beam for the second scenario.

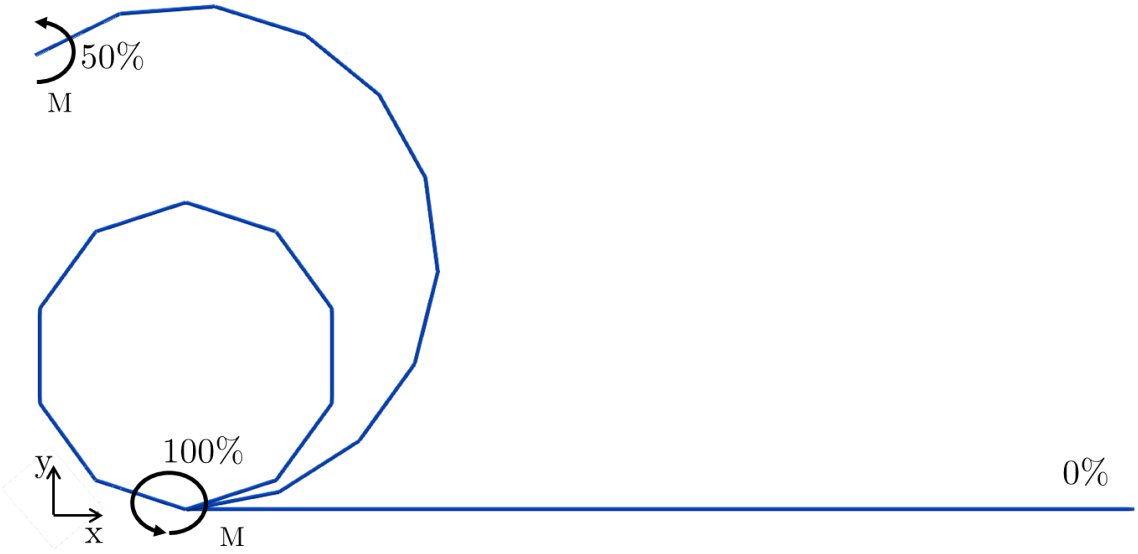

Figure 2.14: Roll-up of a beam under tip moment ($M = 20\pi$): different configurations of the beam

2.2.3.7 Referenced test: roll-up of a beam under tip moment and perturbation force

Objectives This third referenced test case is similar to the first scenario of the previous test case. However, a perturbation force, namely an out-of-plane point load, is applied to test the behaviour of the beam in a 3D loading case.

Setup The material parameters and geometry are those of test case 2.2.3.6 with an additional point load applied at the free end along the z-axis. The load magnitude is 0.0625, which is relatively small but sufficient to create a 3D configuration.

Results The results are reported in Table 2.9. The beam element behaviour agrees well with the one described in Ibrahimbegović et al. (1995); Ritto-Corrêa and Camotim (2002).

Table 2.9: Roll-up of a beam under tip moment ($M = 2.5\pi$) and perturbation force: displacement components' comparisons with Ritto-Corrêa and Camotim (2002) (Ref1) and Ibrahimbegović et al. (1995) (Ref2)

Number of element	x-displacement			y-displacement			z-displacement		
	Present	Ref1	Ref2	Present	Ref1	Ref2	Present	Ref1	Ref2
10	-0.99644	-0.99618	-0.99619	3.72913	3.72853	3.72855	0.19170	0.19523	0.19507

Table 2.10: Cantilever bend of Bathe and Bolourchi: comparison of tip displacement components with references

	Present	Bathe and Bolourchi	Simo and Vu-Quoc	Géradin and Cardona	Ibrahimbegović et al.	Ritto-Corrêa and Camotim
x-displacement	-13.57	-13.4	-13.49	-13.74	-13.668	-13.668
y-displacement	-23.53	-23.5	-23.48	-23.67	-23.697	-23.696
z-displacement	53.52	53.4	53.37	53.50	53.498	53.498

2.2.3.8 Referenced test: cantilever bend by Bathe and Bolourchi (1979)

Objectives This last referenced test case is another 3D test case that checks the ability of the beam element to represent initially in-plane curved configurations.

Setup The beam lies in the xy-plane following a circle arc of radius 100. The length of the beam is such as a 45° cantilever bend is formed as illustrated in Fig 2.15. The Young's modulus is 10^7, the Poisson's ratio is null and the density is 100. The beam has a rectangular cross-section of side-length one and is meshed with eight equal-length elements. A point load of 600 is applied to the free end in the z-direction.

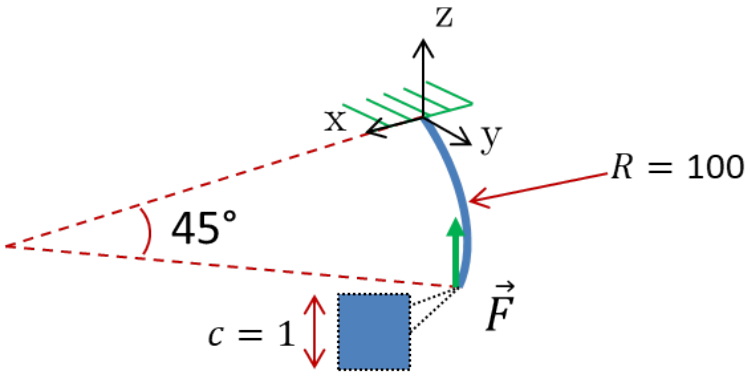

Figure 2.15: Cantilever bend of Bathe and Bolourchi: initial configuration and boundary conditions

Results The results are summarized in Table 2.10. The beam element behaviour is in good agreement with the one reported in the literature by Bathe et al. Fig. 2.16 shows different configurations of the beam.

Conclusion

A linear elastic beam element has been formulated and successfully implemented in the finite element solver. It allows for small strains and finite rotations which is necessary in forming simulation. Elementary and referenced test cases were performed to numerically validate the implementation of this finite element. Constant and independent cross-section stiffnesses will be used to model fibre tows with this beam element since fibre tows are made of individual fibres.

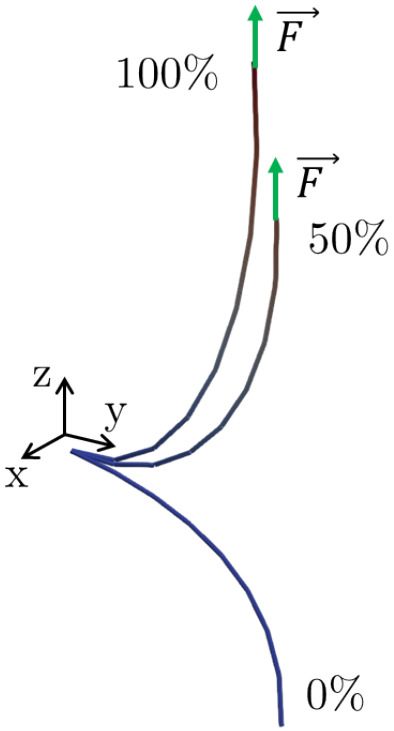

Figure 2.16: Cantilever bend of Bathe and Bolourchi: different configurations of the beam

2.3 Backing material model

Introduction

Model I requires the modelling of the backing material using 2D elements. Any 2D linear finite element formulation can be used depending on the backing material to be modelled. For instance, the finite element developed by Hamila et al. (2009) could be used to model a woven fabric. In order to perform numerical elementary tests of Model I without considering a specific backing material, a 2D hyperelastic membrane is formulated and implemented in the finite element solver. This element allows for large deformations and has isotropic properties. For the sake of clarity and brevity of the demonstration, an incompressible Neohookean material, which is among the simplest hyperelastic materials, is used. Consequently, only the major points of the formulation are detailed and some elementary test cases are addressed.

2.3.1 Formulation of an incompressible Neohookean membrane

2.3.1.1 Assumptions

The membrane is supposed to be incompressible and plane-stress condition applies. Consequently all the tensorial quantities are reduced to two dimensional tensors to simplify the demonstration. Only the transverse component C_{33} of the right Cauchy-Green strain tensor will be additionally required and computed from the plane-stress condition.

2.3.1.2 Kinematics

The transformation between the initial and current configuration is described by the plane transformation gradient $\boldsymbol{F}$:

$$\underset{(2\times2)}{[\boldsymbol{F}]} = \frac{\mathrm{d}\vec{\boldsymbol{x}^{\boldsymbol{e}}}}{\mathrm{d}\vec{\boldsymbol{X}^{\boldsymbol{e}}}} \tag{2.40}$$

where $\underset{(2\times1)}{\vec{\boldsymbol{X}^{\boldsymbol{e}}}}$ and $\underset{(2\times1)}{\vec{\boldsymbol{x}^{\boldsymbol{e}}}}$ are respectively the planar coordinates in the initial (Ω_0) and current (Ω_t) configuration of a point in the membrane defined by a local basis.

2.3.1.3 Strain measure and energy

The planar right Cauchy-green tensor is defined as:

$$\underset{(2\times2)}{[\boldsymbol{C}]} = \boldsymbol{F}^T\boldsymbol{F} \tag{2.41}$$

The incompressibility condition imposing the Jacobian J equals 1 where $J = \det \boldsymbol{F_{3D}}$ (where $\boldsymbol{F_{3D}}$ is the three dimensional transformation gradient) leads to an analytic expression for the transverse component of C_{33} of the three dimensional right Cauchy-Green tensor:

$$C_{33} = \frac{1}{C_{11}C_{22} - C_{12}^2} \tag{2.42}$$

The strain energy of an incompressible neohookean material is defined as:

$$W(\boldsymbol{C}) = \frac{\mu}{2}(I_1 - 3) \tag{2.43}$$

where I_1 is the first main invariant: $I_1 = tr(\boldsymbol{C})$ and μ is a material parameter.

2.3.1.4 Stress tensors

The second Piola-Kirchhoff stress tensor $\boldsymbol{S}$ is computed from the strain energy for a nearly-incompressible hyperelastic material by:

$$\underset{(2\times2)}{[\boldsymbol{S}]} = 2\frac{\mathrm{d}W(\boldsymbol{C})}{\mathrm{d}\boldsymbol{C}} + \rho J\boldsymbol{C}^{-1} \tag{2.44}$$

In this expression, J is the determinant of the transformation gradient $\boldsymbol{F}$ as defined in the previous section and equals 1 in the incompressible case. p is a penalty factor resulting from the incompressibility condition and can be computed from the plane-stress condition imposing $S_{33} = 0$. Using Eq. 2.44 and the plane-stress, it comes:

$$p = -\mu C_{33} \tag{2.45}$$

The derivative of the deformation energy according to the right Cauchy-green tensor is defined as:

$$\underset{(2\times2)}{\left[\frac{\mathrm{d}W(\boldsymbol{C})}{\mathrm{d}\boldsymbol{C}}\right]} = \frac{\mu}{2}\boldsymbol{I} \tag{2.46}$$

Consequently, the second Piola-Kirchhoff stress tensor is computed from:

$$\boldsymbol{S} = \mu\left(\boldsymbol{I} - C_{33}\boldsymbol{C}^{-1}\right) \tag{2.47}$$

The Cauchy stress tensor $\boldsymbol{\sigma}$ is obtained by the transformation of $\boldsymbol{S}$:

$$\underset{(2\times2)}{[\boldsymbol{\sigma}]} = \frac{1}{J}\boldsymbol{F}\boldsymbol{S}\boldsymbol{F}^{\boldsymbol{T}} \tag{2.48}$$

Table 2.11: Linear shape functions and derivatives of the triangle element

Node	N_i	$\frac{\partial N_i}{\partial \xi}$	$\frac{\partial N_i}{\partial \eta}$
1	ξ	1	0
2	η	0	1
3	$1-\xi-\eta$	-1	-1
Domain definition	$(\xi,\eta) \in [0;1] \times [0;1]$		

2.3.1.5 Internal forces

Finally the internal forces vector is derived from the weak form of the equilibrium equation:

$$\underset{(n_{dofs}\times 1)}{\left[F_{int}\right]} = \int_A \boldsymbol{B}^T \boldsymbol{\sigma} ds \tag{2.49}$$

where A is the current area of the 2D element and $\boldsymbol{B}$ is the strain-displacement matrix computed using the Cartesian derivatives of the 2D element shape functions as detailed in the implementation section.

Transition

This section gave the major points of the formulation of an incompressible Neohookean membrane. The next section will discuss its implementation in the finite element solver. In particular, the interpolation order and the computation of the strain-displacement matrix are detailed.

2.3.2 Implementation of the incompressible Neohookean membrane

This section discusses the implementation of an incompressible Neohookean membrane element. Linear triangle and quadrangle element are implemented.

2.3.2.1 Interpolation

Triangle and quadrangle elements possess 3 displacement degrees of freedom per node:

$$\underset{(3\times 1)}{\vec{\boldsymbol{U}}_{\boldsymbol{i}}} = \begin{bmatrix} U_{i_1} & U_{i_2} & U_{i_3} \end{bmatrix}^T$$

where i is the node number.

A point $\vec{\boldsymbol{x}}$ in the element is defined according to the coordinates of the element's nodes $\vec{\boldsymbol{x}}_{\boldsymbol{i}}$ and the element shape functions N_i evaluated at the natural coordinates (ξ,η) of $\vec{\boldsymbol{x}}$:

$$\vec{\boldsymbol{x}} = \sum_{i=1}^{n_{nodes}} N_i \vec{\boldsymbol{x}}_{\boldsymbol{i}} \tag{2.50}$$

The linear shape functions defined in the parametric domain (ξ,η) are given for the triangle in Table 2.11 and for the quadrangle in Table 2.12.

2.3.2.2 Local basis

The covariant basis $\boldsymbol{G}$ of the element is defined as:

$$\underset{(3\times 2)}{[\boldsymbol{G}]} = \begin{bmatrix} \underset{(3\times 1)}{\vec{\boldsymbol{g}}_{\boldsymbol{1}}} & \underset{(3\times 1)}{\vec{\boldsymbol{g}}_{\boldsymbol{2}}} \end{bmatrix} \tag{2.51}$$

Table 2.12: Linear shape functions and derivatives of the quadrangle element

Node	N_i	$\frac{\partial N_i}{\partial \xi}$	$\frac{\partial N_i}{\partial \eta}$
1	$0.25\,(1-\xi)\,(1-\eta)$	$0.25\,(\eta-1)$	$0.25\,(\xi-1)$
2	$0.25\,(1+\xi)\,(1-\eta)$	$0.25\,(1-\eta)$	$0.25\,(-1-\xi)$
3	$0.25\,(1+\xi)\,(1+\eta)$	$0.25\,(1+\eta)$	$0.25\,(1+\xi)$
4	$0.25\,(1-\xi)\,(1+\eta)$	$0.25\,(-1-\eta)$	$0.25\,(1-\xi)$
Domain definition	$(\xi,\eta) \in [-1;1] \times [-1;1]$		

where the covariant vector $\vec{\boldsymbol{g_j}} = \sum_{j=1}^{2} \frac{\partial N_i}{\partial \chi_j} \vec{\boldsymbol{x_i}}$ with $\chi_1 = \xi$ and $\chi_2 = \eta$.

Next, a local orthonormal base $\boldsymbol{e}$ is required to compute the planar coordinates of the element and can be defined from the vectors constituting the covariant base:

$$\vec{\boldsymbol{e_1}} = 0.5\frac{\vec{\boldsymbol{g_1}} + \vec{\boldsymbol{g_2}}}{\|\vec{\boldsymbol{g_1}}\|\|\vec{\boldsymbol{g_2}}\|} \quad \vec{\boldsymbol{e_3}} = \frac{\vec{\boldsymbol{g_1}} \times \vec{\boldsymbol{g_2}}}{\|\vec{\boldsymbol{g_1}}\|\|\vec{\boldsymbol{g_2}}\|} \quad \vec{\boldsymbol{e_2}} = \vec{\boldsymbol{e_3}} \times \vec{\boldsymbol{e_1}} \tag{2.52}$$

The planar coordinates of the element's nodes, named x_i^e are obtained by projecting the node coordinates $\vec{\boldsymbol{x_i}}$ is the plane defined by $(\vec{\boldsymbol{e_1}}, \vec{\boldsymbol{e_2}})$:

$$\underset{(2\times1)}{\vec{\boldsymbol{x_i^e}}} = \underset{(2\times3)}{\begin{bmatrix} \vec{\boldsymbol{e_1}}^T \\ \vec{\boldsymbol{e_2}}^T \end{bmatrix}} \underset{(3\times1)}{\vec{\boldsymbol{x_i}}} \tag{2.53}$$

2.3.2.3 Strain-displacement matrix

Then, the Jacobian $\boldsymbol{J}$ of the transformation from the parametric to the physical domain is given by:

$$\underset{(2\times1)}{\begin{bmatrix} dx \\ dy \end{bmatrix}} = \underbrace{\underset{(2\times2)}{\begin{bmatrix} \frac{\partial x}{\partial \xi} & \frac{\partial y}{\partial \xi} \\ \frac{\partial x}{\partial \eta} & \frac{\partial y}{\partial \eta} \end{bmatrix}}}_{\boldsymbol{J}} \underset{(2\times1)}{\begin{bmatrix} d\xi \\ d\eta \end{bmatrix}} \tag{2.54}$$

where $\vec{\boldsymbol{x^e}} = \begin{bmatrix} x \\ y \end{bmatrix} = \sum_{i=1}^{n_{nodes}} N_i(\xi,\eta)\vec{\boldsymbol{x_i^e}}$.

Therefore, the Cartesian derivatives of the shape functions are defined as:

$$\underset{(2\times1)}{\begin{bmatrix} \frac{\partial N_i}{\partial x} \\ \frac{\partial N_i}{\partial y} \end{bmatrix}} = \boldsymbol{J^{-1}} \underset{(2\times1)}{\begin{bmatrix} \frac{\partial N_i}{\partial \xi} \\ \frac{\partial N_i}{\partial \eta} \end{bmatrix}} \tag{2.55}$$

Finally, the strain-displacement matrix is defined from the Cartesian derivatives of the shape functions as given by:

$$\underset{((3\times3)\times n_{nodes})}{[\boldsymbol{B}]} = \begin{bmatrix} B_1 & \dots & B_{n_{nodes}} \end{bmatrix} \tag{2.56}$$

where $\boldsymbol{B_i}$ is defined as:

$$\underset{(3\times3)}{[\boldsymbol{B_i}]} = \begin{bmatrix} \frac{\partial N_i}{\partial x}\vec{\boldsymbol{e_1}} \\ \frac{\partial N_i}{\partial y}\vec{\boldsymbol{e_2}} \\ \frac{\partial N_i}{\partial x}\vec{\boldsymbol{e_1}} + \frac{\partial N_i}{\partial x}\vec{\boldsymbol{e_2}} \end{bmatrix} \tag{2.57}$$

Table 2.13: Gauss point definition for the linear triangle element

Gauss point	ξ	η	w_g
1	$\frac{1}{3}$	$\frac{1}{3}$	$\frac{1}{2}$

Table 2.14: Gauss point definition for the linear quadrangle element

Gauss point	ξ	η	w_g
1	$-\frac{1}{\sqrt{3}}$	$-\frac{1}{\sqrt{3}}$	1
2	$\frac{1}{\sqrt{3}}$	$-\frac{1}{\sqrt{3}}$	1
3	$\frac{1}{\sqrt{3}}$	$\frac{1}{\sqrt{3}}$	1
4	$-\frac{1}{\sqrt{3}}$	$\frac{1}{\sqrt{3}}$	1

2.3.2.4 Integration

The internal forces are integrated over the element using a Gauss point quadrature. Tables 2.13 and 2.14 define the position of the Gauss points as well as their weight for the triangle and quadrangle elements.

2.3.2.5 Algorithm

The algorithm to compute the internal forces of the Neohookean linear membrane element is detailed in Alg.3.

Algorithm 3 Internal forces computation of the Neohookean linear membrane

Initialize $\left[\boldsymbol{F_{int}}\right] = 0$
for `each Gauss point` **do**
    Compute the covariant vectors $\vec{\boldsymbol{g_1}}$ and $\vec{\boldsymbol{g_2}}$ defined in Eq. 2.51
    Compute the local base $\boldsymbol{e}$ defined in Eq. 2.52
    Compute the planar coordinates $\vec{\boldsymbol{x_i^e}}$ of the element' nodes using Eq. 2.53
    Compute the Jacobian $\boldsymbol{J}$ using: $J_{jk} = \sum_{i=1}^{n_{nodes}} \frac{\partial N_i}{\partial \chi_j} x_{ik}^e$ where x_{ik}^e is the k^{th} component of $\vec{\boldsymbol{x_i^e}}$ and $\chi_1 = \xi, \chi_2 = \eta$
    Compute $\det(\boldsymbol{J})$
    Compute the Cartesian shape functions using Eq. 2.55
    Set $\boldsymbol{B}$ from Eq. 2.56 and 2.57
    Compute the planar transformation gradient $\boldsymbol{F}$ defined in Eq.2.40
    Compute the planar right Cauchy-Green tensor $\boldsymbol{C}$ using Eq. 2.3.1.3
    Compute the transverse component C_{33} from Eq. 2.42
    Compute $\det(\boldsymbol{F_{3D}}) = \sqrt{C_{33}}\det(\boldsymbol{F})$
    Update membrane thickness: $t = \sqrt{C_{33}} t_0$ where t_0 is the initial thickness
    Compute invariant $I_1 = \mathrm{tr}(C) + C_{33}$
    Compute Piola-Kirchhoff tensor $\boldsymbol{S}$ defined in Eq. 2.44
    Compute Stress tensor σ using Eq. 2.48
    Compute internal forces: $\left[\boldsymbol{F_{int}}\right] = \left[\boldsymbol{F_{int}}\right] + w_g \boldsymbol{B}^T \boldsymbol{\sigma} \det(\boldsymbol{J}) t$ where w_g is the weight of the current Gauss point.

Transition

This section gave the needed materials to implement linear triangle and quadrangle elements with an incompressible Neohookean behaviour. Numerical validation of the implementation is carried out in the next section.

2.3.3 Numerical validation: Elementary test cases

In the following elementary test cases, the material parameters does not correspond to a known material. The density of 0.01 is chosen such as the kinetic energy remains small to ensure quasi-static analysis. In all test, μ equals 100 MPa. Besides, the analysed tensorial quantities are the second Piola-Kirchhoff stress tensor and the Green-Lagrange strain tensor defined by:

$$E_{GL} = \frac{1}{2}(C - I) \tag{2.58}$$

2.3.3.1 Biaxial tensile test

Objectives This first elementary test case aims at testing the behaviour of the element when submitted to biaxial tension. The imposed kinematic should result in zero shear deformation.

Setup The bottom edge of a single element is fixed along y-direction and the left edge is fixed along y-direction. The right edge or node is translated in the x-direction with a value of Δ_1 while the top edge or node is translated in the y-direction with a value of Δ_2. Fig. 2.17 illustrates the initial and final configurations. The transformation gradient $\boldsymbol{F}$ describing this kinematic is given by:

$$\underset{(2\times2)}{[\boldsymbol{F}]} = \begin{bmatrix} 1+\frac{\Delta_1}{L_1} & 0 \\ 0 & 1+\frac{\Delta_2}{L_2} \end{bmatrix}$$

According to the definition of the planar right Cauchy-Green strain tensor (Eq. 2.3.1.3):

$$\underset{(2\times2)}{[\boldsymbol{C}]} = \begin{bmatrix} \left(1+\frac{\Delta_1}{L_1}\right)^2 & 0 \\ 0 & \left(1+\frac{\Delta_2}{L_2}\right)^2 \end{bmatrix}$$

And $C_{33} = \frac{1}{\left(1+\frac{\Delta_1}{L_1}\right)^2\left(1+\frac{\Delta_2}{L_2}\right)^2}$ using Eq. 2.42.

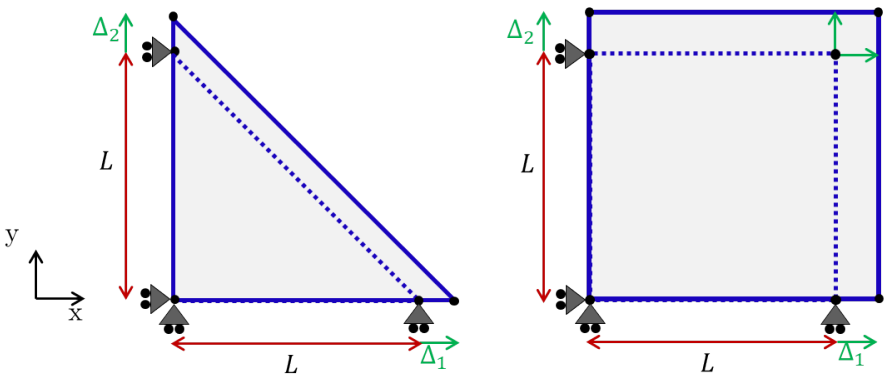

Figure 2.17: Biaxial tension test of an incompressible Neohookean membrane (initial configuration (dotted line), final configuration (solid line)

The lengths L_1 and L_2 equal 1 mm. Two scenarios are analysed. The first one where both displacements are equal ($\Delta_1 = \Delta_2 = 0.1$ mm) and a second where $\Delta_1 = 2\Delta_2$ with $\Delta_2 = 0.1$ mm

Table 2.15: Equibiaxial tensile test of an incompressible Neohookean membrane: values of the Green-Lagrange strain tensor and Second Piola-Kirchhoff stress tensor

Components	Green-Lagrange strain tensor				Second Piola-Kirchoff stress tensor (MPa)		
	E_{11}	E_{22}	E_{33}	E_{12}	S_{11}	S_{22}	S_{12}
Triangle	0.105	0.105	-0.158493	0	61.4457	61.4457	0
Quadrangle	0.105	0.105	-0.158493	0	61.4457	61.4457	0
Analytic	0.105	0.105	-0.158493	0	61.4457	61.4457	0

Table 2.16: Biaxial tensile test of an incompressible Neohookean membrane: values of the Green-Lagrange strain tensor and Second Piola-Kirchhoff stress tensor

Components	Green-Lagrange strain tensor				Second Piola-Kirchoff stress tensor (MPa)		
	E_{11}	E_{22}	E_{33}	E_{12}	S_{11}	S_{22}	S_{12}
Triangle	0.22	0.105	-0.213039	0	77.126	72.7781	0
Quadrangle	0.22	0.105	-0.213039	0	77.126	72.7781	0
Analytic	0.22	0.105	-0.213039	0	77.126	72.7781	0

Results The values of the Green-Lagrange strain tensors and those of the second Piola-Kirchhoff stress tensors as well as the analytic values are given in Table 2.15 for the first scenario and in Table 2.16 for the second. The numerical results are in good agreement with the analytic ones for both scenarios.

2.3.3.2 Simple shear test

Objectives This second elementary test case aims at testing the behaviour of the element when submitted to simple shear. The imposed kinematics should result in zero through-the-thickness deformation.

Setup As depicted in Fig. 2.18, the bottom edge of a single element is clamped while the top edge (quadrangle) or the top point (triangle) is translated in the x-direction by the value Δ. The bottom and top edges have an initial length of L_1 while the side edges have a length of L_2. The plane transformation gradient associated with this kinematic is defined as:

$$\underset{(2\times2)}{[\boldsymbol{F}]} = \begin{bmatrix} 1 & \frac{\Delta}{L_2} \\ 0 & 1 \end{bmatrix}$$

According to the definition of the plane right Cauchy-Green strain tensor (Eq. 2.3.1.3):

$$\underset{(2\times2)}{[\boldsymbol{C}]} = \begin{bmatrix} 1 & \frac{\Delta}{L_2} \\ 0 & 1 + \left(\frac{\Delta}{L_2}\right)^2 \end{bmatrix}$$

And $C_{33} = 1$ using Eq. 2.42.

The lengths L_1 and L_2 are equal to 1 mm. A displacement $\Delta = 0.1$ mm is imposed.

Results The values of the Green-Lagrange strain tensors and those of the second Piola-Kirchhoff stress tensors are given in Table 2.17 as well as the analytic values. The numerical results are in good agreement with the analytic ones.

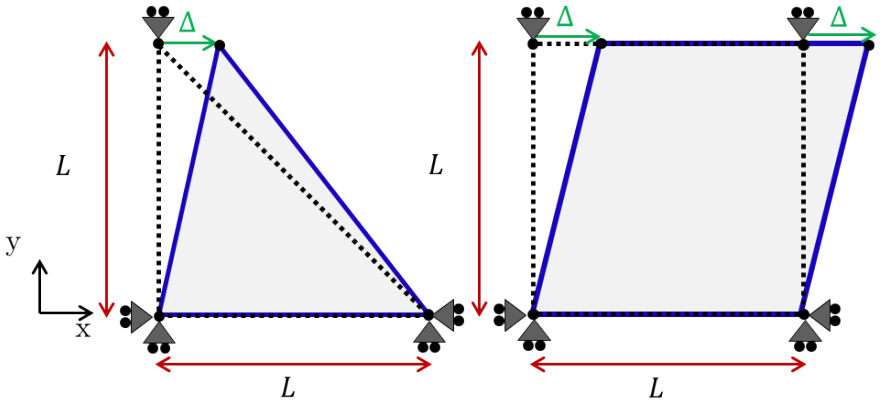

Figure 2.18: Simple shear of an incompressible Neohookean membrane (initial configuration (dotted line), final configuration (solid line)

Table 2.17: Simple shear of an incompressible Neohookean membrane: values of the Green-Lagrange strain tensor and Second Piola-Kirchhoff stress tensor

Components	Green-Lagrange strain tensor				Second Piola-Kirchoff stress tensor (MPa)		
	E_{11}	E_{22}	E_{33}	E_{12}	S_{11}	S_{22}	S_{12}
Triangle	0	0.005	$\approx 10^{-16}$	0.05	-1	$\approx -10^{-15}$	10
Quadrangle	$\approx -10^{-15}$	0.005	$\approx 10^{-15}$	0.05	-1	$\approx -10^{-14}$	10
Analytic	0	0.005	0	0.05	-1	0	10

2.3.3.3 Pure shear test

Objectives This third elementary test case aims at testing the behaviour of the element when submitted to pure shear. The imposed kinematic should result in zero shear deformation.

Setup As illustrated in Fig. 2.19, the bottom and top edges (or point) of a single element are fixed in the y-direction while the right edge (quadrangle) or right point (triangle) is translated in the x-direction by a value of Δ. The left edge is clamped in the x-direction. The edges have an initial length of L. The plane transformation gradient associated with this kinematics is defined as:

$$\underset{(2\times2)}{[\boldsymbol{F}]} = \begin{bmatrix} \frac{1+\Delta}{L} & 0 \\ 0 & 1 \end{bmatrix}$$

According to the definition of the planar right Cauchy-Green strain tensor (Eq. 2.3.1.3):

$$\underset{(2\times2)}{[\boldsymbol{C}]} = \begin{bmatrix} \left(\frac{1+\Delta}{L}\right)^2 & 0 \\ 0 & 1 \end{bmatrix}$$

And $C_{33} = C_{11}^{-1}$ using Eq. 2.42.

The length L equals 1 mm. A displacement $\Delta = 0.001$ mm is imposed.

Results The values of the Green-Lagrange strain tensors are given in Table 2.18 as well as the analytic values. The numerical results are in good agreement with the analytic ones.

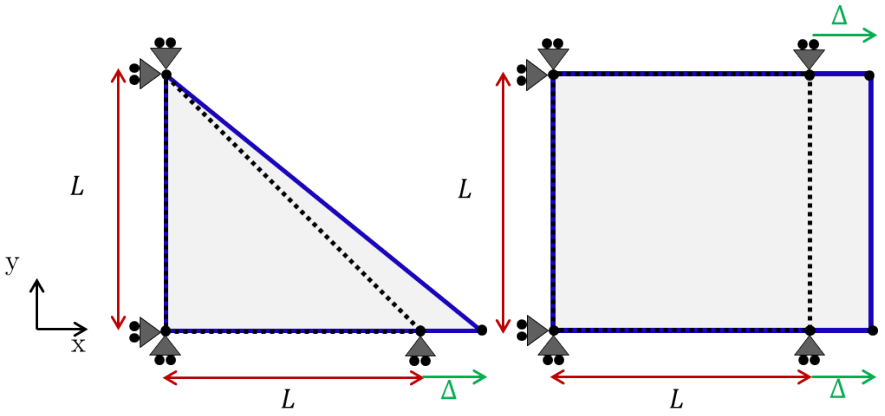

Figure 2.19: Pure shear of an incompressible Neohookean membrane (initial configuration (dotted line), final configuration (solid line)

Table 2.18: Pure shear of an incompressible Neohookean membrane: values of the Green-Lagrange strain tensor

Components	Green-Lagrange strain tensor			
	E_{11}	E_{22}	E_{33}	E_{12}
Triangle	$1.0005\ 10^{-3}$	0	$-9.98502\ 10^{-4}$	0
Quadrangle	$1.0005\ 10^{-3}$	$\approx -10^{-17}$	$-9.98502\ 10^{-4}$	$\approx 10^{-18}$
Analytic	$1.0005\ 10^{-3}$	0	$-9.98502\ 10^{-4}$	0

Conclusion

This section presented the formulation and implementation details of an incompressible Neohookean membrane chosen to model the backing material. This membrane will be used to perform elementary test cases on Model I in the next section. Obviously, more complex and specific mechanical behaviours could be implemented depending on the nature of backing material. The simplicity of the implemented hyperelastic behaviour allows for representing isotropic material with large deformations if necessary.

2.4 Modelling the stitching yarn as an embedding constraint

Introduction

As stated in section 2.1.2, the stitching yarn is supposed to act as a bond either between the fibre tows and the backing material (Model I) or between fibre tows of adjacent layers (Model II). To avoid an explicit and time consuming representation of the stitching yarn as well as the contact interactions with their surroundings, an implicit modelling based on the embedded element approach, which has been introduced in section 2.1.3, is used. This section begins with presenting the general formulation of the embedded element approach. In particular, the kinematic constraints applied to the embedded elements from the host element and the transfer of the internal forces from the embedded elements to the host one are explained. Next, the embedded element approach is successively applied to Model I and Model II. Finally, some elementary test cases are addressed to validate the implementation of the TFP preform models.

2.4.1 General formulation and implementation

2.4.1.1 Kinematic constraint

The embed of a node into the host element is achieved by computing the position of the embedded node from the position of the nodes of the host element as:

$$\vec{\boldsymbol{x^e}} = \sum_{\alpha} N^h_\alpha(\chi_e)\, \vec{\boldsymbol{x^h_\alpha}}$$

Consequently, the displacement dofs $\vec{\boldsymbol{U^e_k}}$ of the k^{th} node of an embedded element is computed from the displacement dofs $\vec{\boldsymbol{U^h_\alpha}}$ of the nodes of its host element:

$$\vec{\boldsymbol{U^e_k}} = \sum_{\alpha} N^h_\alpha(\chi_e)\, \vec{\boldsymbol{U^h_\alpha}} \tag{2.59}$$

However, beam elements have also rotation dofs. Therefore, there is two options to embed a beam element. The first one consists in embedding both displacement and rotational dofs. This means that, similarly to the displacement dofs, the rotation dofs of a beam's node k are computed using:

$$\vec{\boldsymbol{\psi^e_k}} = \sum_{\alpha} N^h_\alpha(\chi_e)\, \vec{\boldsymbol{\psi^h_\alpha}} \tag{2.60}$$

where $\vec{\boldsymbol{\psi^h_\alpha}}$ are the rotation dofs of the α^{th} host node. With this option, the host element either requires rotation dofs (using a shell formulation for instance) or they have to be computed from geometric considerations as done by Markou (2011) where beams are embedded in 3D solid elements. The embed of the rotation dofs implies a full transfer of the torques of the embedded elements to the host element as if they were welded. However, as stated in section 2.1.2, in the TFP preform models, there is a hinge connection between the embedded and host elements to allow rotation at the fibre tows' intersections. Moreover, the resistance to rotation due to friction and deformation of the stitching yarn is taken into account using a linear elastic torsional spring. Consequently, the second option, which only constraints the displacement dofs of the embedded beam from those of the host element, is chosen here.

Harrison (2016), which embedded beams on the edges of membrane elements to model woven fabrics, already noticed that the embed of the rotation dofs lead to an excessive and non-physical in-plane shear stiffness.

2.4.1.2 Transfer of the internal forces to the host element

Since the embedded elements are kinematically constrained by the host element, the embedded dofs $\boldsymbol{q^e}$ are dependent on the dofs of the host element $\boldsymbol{q^h}$. As a consequence, the internal forces of an embedded element are transferred to the host element. Therefore, the internal forces of a host element $\boldsymbol{F^h_{int}}$ are composed of the internal forces $\boldsymbol{F^{hb}_{int}}$ resulting from the host element behaviour and the internal forces $\boldsymbol{F^{he}_{int}}$ due to the embedded element (Eq. 2.61):

$$\boldsymbol{F^h_{int}} = \boldsymbol{F^{hb}_{int}} + \boldsymbol{F^{he}_{int}} \tag{2.61}$$

The contribution $\boldsymbol{F^{he}_{int}}$ is easily computed from the internal forces of the embedded elements. The kinematic constraint implies:

$$\underset{(n^e_d \times 1)}{[\boldsymbol{q^e}]} = \underset{(n^e_d \times n^h_d)}{[\boldsymbol{N^e_h}]} \underset{(n^h_d \times 1)}{\left[\boldsymbol{q^h}\right]} \tag{2.62}$$

where n_d^e is the number of embedded dofs of the embedded element and n_d^h is the number of host dofs. $\boldsymbol{N_h^e}$ is the matrix of shape functions of the host element evaluated at the embedded nodes so that Eq. 2.62 is a generalization of Eq. 2.59 to all the embedded dofs of the embedded element.

Then, the variation of deformation of the embedded element $\boldsymbol{\epsilon^e}$ is related to the variation of the degrees of freedom by:

$$\delta\boldsymbol{\epsilon^e} = \boldsymbol{B^e}\delta\boldsymbol{q^e} \tag{2.63}$$

where $\boldsymbol{B^e}$ is the strain-displacement matrix of the embedded element.

Introducing Eq. 2.62 into Eq. 2.63 gives:

$$\delta\boldsymbol{\epsilon^e} = \underbrace{\boldsymbol{B^e}\boldsymbol{N_h^e}}_{\boldsymbol{B_h^e}}\delta\boldsymbol{q^h} \tag{2.64}$$

where $\boldsymbol{B_h^e}$ is the strain-displacement matrix that relates the variation of deformation of the embedded element to the variation of the host dofs.

Therefore the contribution of the embedded element to the internal forces of the host element is defined as:

$$\underset{(n_d^h\times 1)}{\left[\boldsymbol{F_{int}^{he}}\right]} = \int_\omega \boldsymbol{B_h^{eT}}\boldsymbol{\sigma^e}d\omega \tag{2.65}$$

where $\boldsymbol{\sigma^e}$ is the stress tensor of the embedded element.

Eq. 2.65 can also be written at the α^{th} node of the host element as:

$$\boldsymbol{F_{int_\alpha}^{he}} = \sum_k N_\alpha(\chi_k)\boldsymbol{F_{int_k}^e} \tag{2.66}$$

where $\boldsymbol{F_{int_k}^e}$ is the internal forces of the k^{th} node of the embedded element.

Model I Fig. 2.20 illustrates the transfer of the internal forces from one 1D embedded element to a 2D host element. The red solid arrows correspond to the internal forces of the embedded nodes that are transferred to the host element's nodes. The green arrows correspond to the contribution from the embedded nodes and adds up to the internal forces of the host element's nodes (light blue arrows) to form the total internal forces at the host nodes (dark blue arrows).

Model II Fig. 2.21 illustrates the transfer of the internal forces from one embedded node to a 1D host element.

2.4.1.3 Mass contribution of embedded elements

The embedding constraint also involves a transfer of the mass of the embedded elements to the host element. Regarding the computation of the mass matrix, the contribution of an embedded element to a host element is computed according to Eq.2.67 established in Taylor et al. (2005).

$$M_{\alpha\beta}^{he} = \sum_{kl} N_\alpha(\chi_k)M_{kl}^e N_\beta(\chi_l) \tag{2.67}$$

In Eq. 2.67, Greek subscript refers to the nodes of the host element, whereas Latine superscript refers to the nodes of the embedded element. As explicit time integration is performed in the present study, a lumped mass matrix is used. Although lumping the mass matrix in the presence of embedded elements is not straightforward, it is done by summing the columns of the mass matrix (sum over the β index). In the case of quasi-static analyses, this approximation is supposed to have minor effects on the results (Taylor et al., 2005).

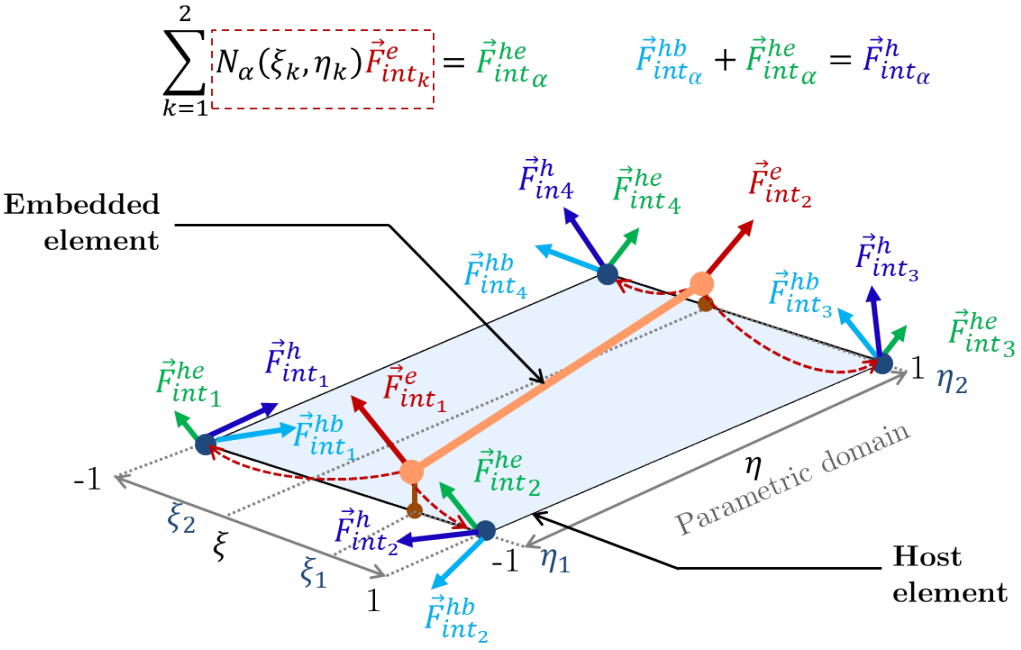

Figure 2.20: Transfer of internal forces in Model I

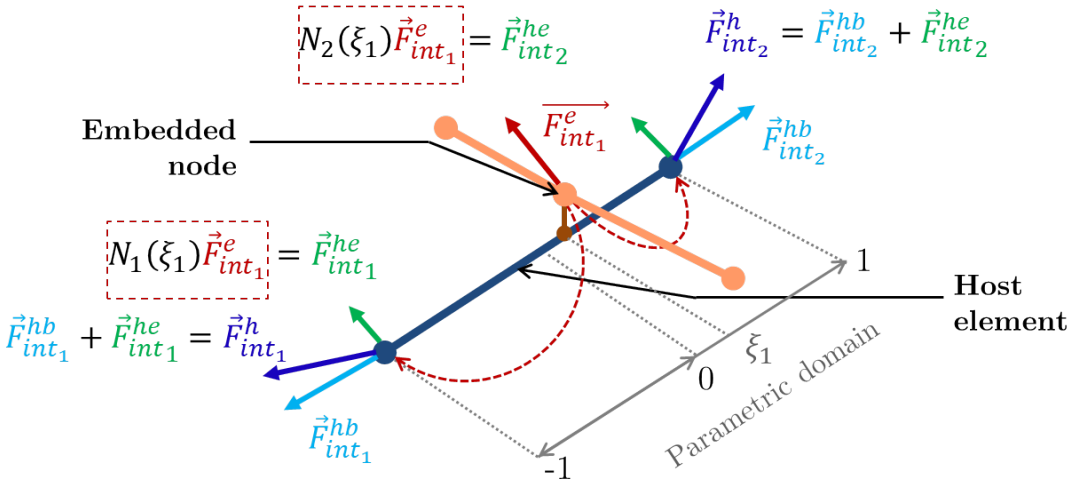

Figure 2.21: Transfer of internal forces in Model II

Model II For Model II, the mass contribution of an embedded node to a host element reduces to:

$$M^{he}_{\alpha\beta} = N_\alpha(\chi_k) M^e N_\beta(\chi_k) \tag{2.68}$$

where M^e is the mass of the embedded node.

2.4.1.4 Integration into Femtran

The standard workflow in Femtran was presented in Fig. 2.8. Fig 2.22 shows the workflow of Femtran where embedding constraints are included. The green boxes describe the additional steps to take into account embedding constraints. First, the transfer of mass from the embedded dofs to the host dofs occurs after the computation of mass is achieved for all elements and assemble into a vector at the dof level. Once the kinematic variables of the host elements are computed in the time integration step, the kinematic constraint of the embed is applied. Finally,

after computing the internal forces of all the elements and assembling the internal forces into a vector at the dof level, the internal forces of the embedded dofs are transferred to the host dofs.

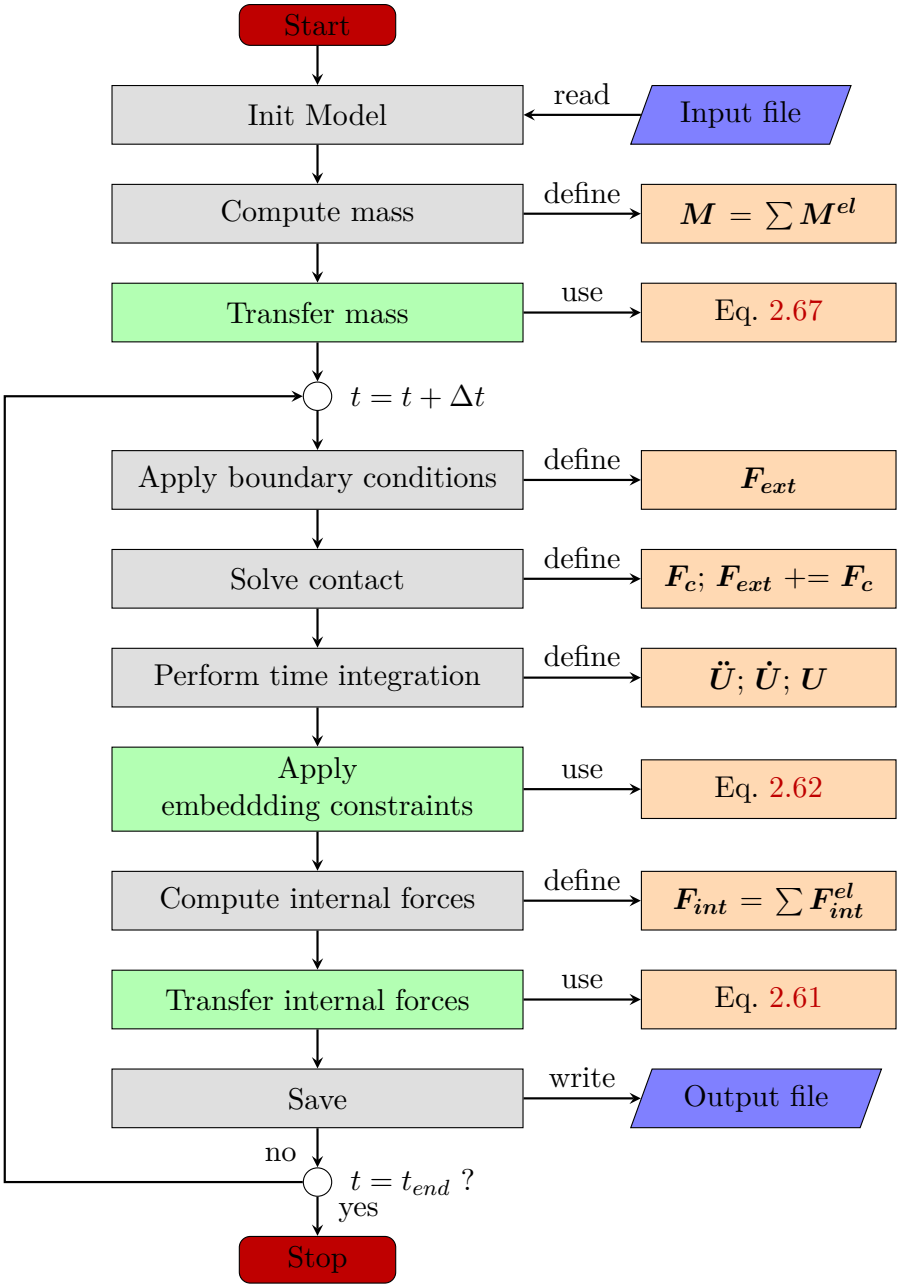

Figure 2.22: Femtran workflow under embedding constraints

Transition

This section described the implicit modelling of the stitching yarn assumed to act as a hinge between the fibre tows and the backing material (Model I) or between the fibre tows of adjacent layers (Model II). The embedded element approach allows modelling this bond. Only the displacement degrees of freedom are embedded since the rotation between fibre tows of different layers is allowed. The resistance to this rotation is taken into account through linear elastic torsional springs placed at the intersections between fibre tows of adjacent layers. The kinematic constraint resulting from the embedding element approach implies a transfer of the mass and internal forces from the embedded

elements to the host elements. The next section explains how to generate the TFP models.

2.4.2 Generation of TFP preform models

The embedding constraint requires knowing the natural coordinates of the finite element nodes embedded into the host elements. The natural coordinates are computed using the procedure described in section 2.1.3.1. Each model is generated from the trajectories of the fibre tows which allows a fairly good representation of the preform design. The design process of the TFP preforms will be presented in the next chapter. In the following, a fibre tow trajectory is simply represented as a 2D array where each line corresponds to the plane coordinates of a point describing the trajectory.

2.4.2.1 Meshing of Model I: 1D elements embedded in 2D elements

Model I is based on the embedding of 1D elements into 2D elements. It requires identifying for each node of the embedded elements, its host element. Moreover, 1D embedded elements cannot cross over the boundaries of the 2D host elements as shown in Fig 2.23. Consequently, nodes are required at the intersections between a fibre tow trajectory and the boundaries of the 2D elements of the backing material. Identifying the host element of each embedded node as well as the intersections with the boundaries of 2D elements can be extremely time consuming if a basic search algorithm is used. The simplest algorithm would, for each embedded node, iterate through each host element, compute the natural coordinates and check if the natural coordinates are in the parametric domain of the element. To optimize the generation of the model, a specific algorithm has been developed and will be detailed hereafter. It basically consists in identifying the host element of the first point of a fibre tow trajectory and then pass to the next points by using the topology information of the host element such as its neighbours.

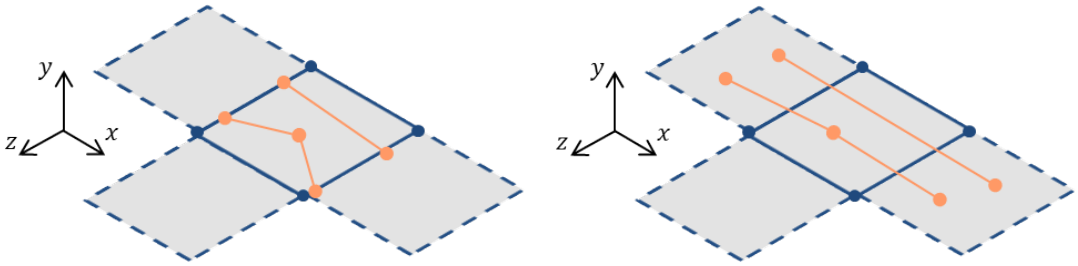

(a) Correct mesh **(b)** Incorrect mesh

Figure 2.23: Meshing of 1D embedded elements in 2D host elements

Overview of the model generation process The generation of the model of a TFP preform with backing material is represented in Fig 2.24. First, the geometry of the backing material is meshed using 2D elements. Then, knowing the points describing the trajectories of the fibre tows, the later are meshed by adding crossing points at the intersections with the boundaries of the host elements. At the end of this step, the mesh of fibre tows contains the original points that discretize the fibre path with additional crossing points at the intersections with the backing material element boundaries. The mesh quality of the fibre tows can be improved by removing some points. Points on host element boundaries cannot be removed.

Principle of the algorithm The principle of the algorithm is illustrated in Fig. 2.25.
Fig. 2.25 (a) represents a portion of the TFP preform design with some numbered backing

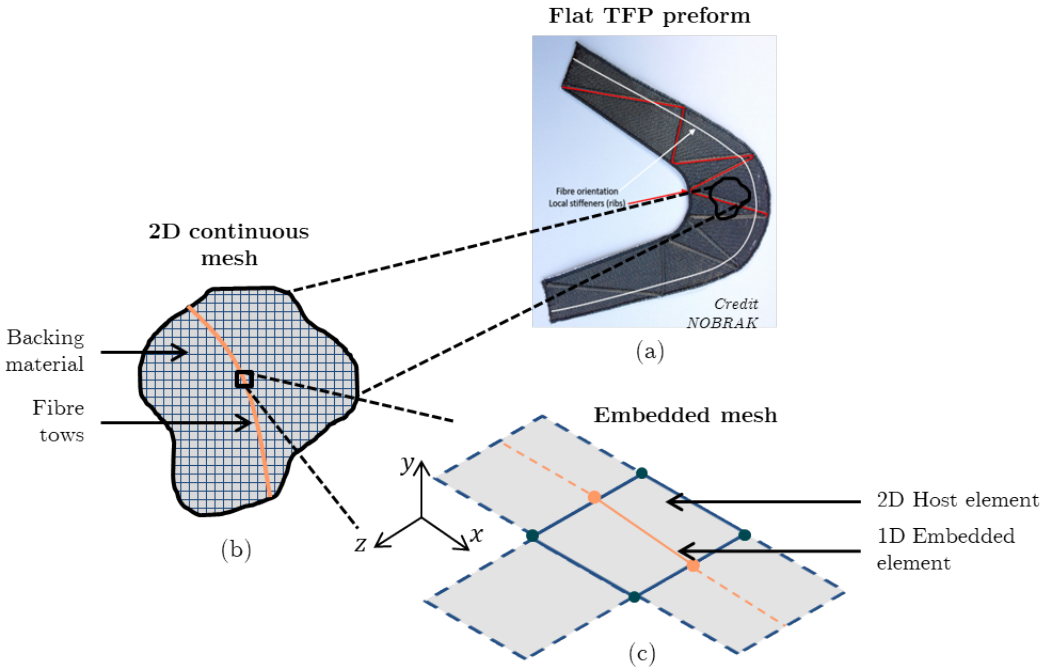

Figure 2.24: Overview of the meshing procedure of Model I: (a) TFP preform design, (b) 2D mesh of the backing material, (c) mesh of the 1D embedded elements

material elements and the path of one fibre tow. **Step 1** (Fig. 2.25 (b)) consists in identifying the host element of the first point of the trajectory by iterating through all the backing material elements, computing the natural coordinates of the first point and checking if it lies in the parametric domain of the inspected element. In Fig. 2.25 (b), the pair $(2;1)$, where the first argument of the pair is the element number and the second is the point number along the fibre path, is appended in a list as well as the natural coordinates of the point in its host element. This pair gives information about the current host element and point along the fibre path. The next step (**Step 2**) is to find the host element associated to the next points by using the backing material mesh topology. To this end, if the next point is not in the current host element, the crossing between the segment formed by the current point and the next one (blue points in Fig. 2.25 (c)) and the boundaries of the current host element is searched. The current host element and the intersection point (green point in Fig. 2.25 (c)) are appended in the list as a new pair $(2;2)$. If the intersection point is located on an edge of the current host element, then the new current element is the neighbour sharing this edge. However, if the intersection point is located on a node, the new current element is identified by considering a dummy point located on the segment defined by the current point (those of the intersection) and the next point along the path. This dummy point is chosen really close to the current point and its natural coordinates are computed for each neighbour element sharing the node until finding the neighbour element containing this dummy point. Then, if the next point is in the new current element as illustrated in Fig. 2.25 (d)), this new pair $(5;3)$ is appended. Otherwise, **Step 2** is repeated until the host element of the next trajectory's point is identified. The workflow of the algorithm is detailed in Fig. 2.26.

Mesh quality At the end of the meshing process, some nodes representing the fibre tows can be removed if they lie strictly inside an element and are placed along a straight line. Very small elements might be generated depending on the backing material mesh topology and the fibre path. When possible, meshing the backing material according to the direction of the fibre tows considerably increases the element size of the fibre tows.

Algorithm 4 Find first fibre tow trajectory's point

Define: $isIn \leftarrow \boldsymbol{false}$
while not $isIn$ **do**
    Define the parametric domain of the current element: D_χ
    Compute the natural coordinates $\vec{\boldsymbol{\chi}}$ of the first point in the current element using Alg. 1
    if $\vec{\boldsymbol{\chi}} \in D_\chi$ **then**
        $isIn \leftarrow \boldsymbol{true}$
    else
        get next element
Return: current element and $\vec{\boldsymbol{\chi}}$

Algorithm 5 Identify new current host element

Inputs The crossing point $\vec{\boldsymbol{x}}_{int}$ between fibre path and the host element boundaries, the next point along the fibre path $\vec{\boldsymbol{x}}_{next}$

Outputs The new current element among the current neighbours

if $\vec{\boldsymbol{x}}_{int}$ on an edge **then**
    Return: Neighbour element sharing this edge
else
    Compute: $\vec{\boldsymbol{x_d}} \leftarrow \vec{\boldsymbol{x}}_{int} + t\frac{\vec{\boldsymbol{x}}_{next}-\vec{\boldsymbol{x}}_{int}}{\|\vec{\boldsymbol{x}}_{next}-\vec{\boldsymbol{x}}_{int}\|}$ where t has a small value
    Define: $isIn \leftarrow \boldsymbol{false}$
    while not $isIn$ **do**
        Define the parametric domain of the current neighbour element: D_χ
        Compute the natural coordinates $\vec{\boldsymbol{\chi}}$ of $\vec{\boldsymbol{x_d}}$ in the current element using Alg. 1
        if $\vec{\boldsymbol{\chi}} \in D_\chi$ **then**
            $isIn \leftarrow \boldsymbol{true}$
        else
            get next neighbour element
Return: neighbour element

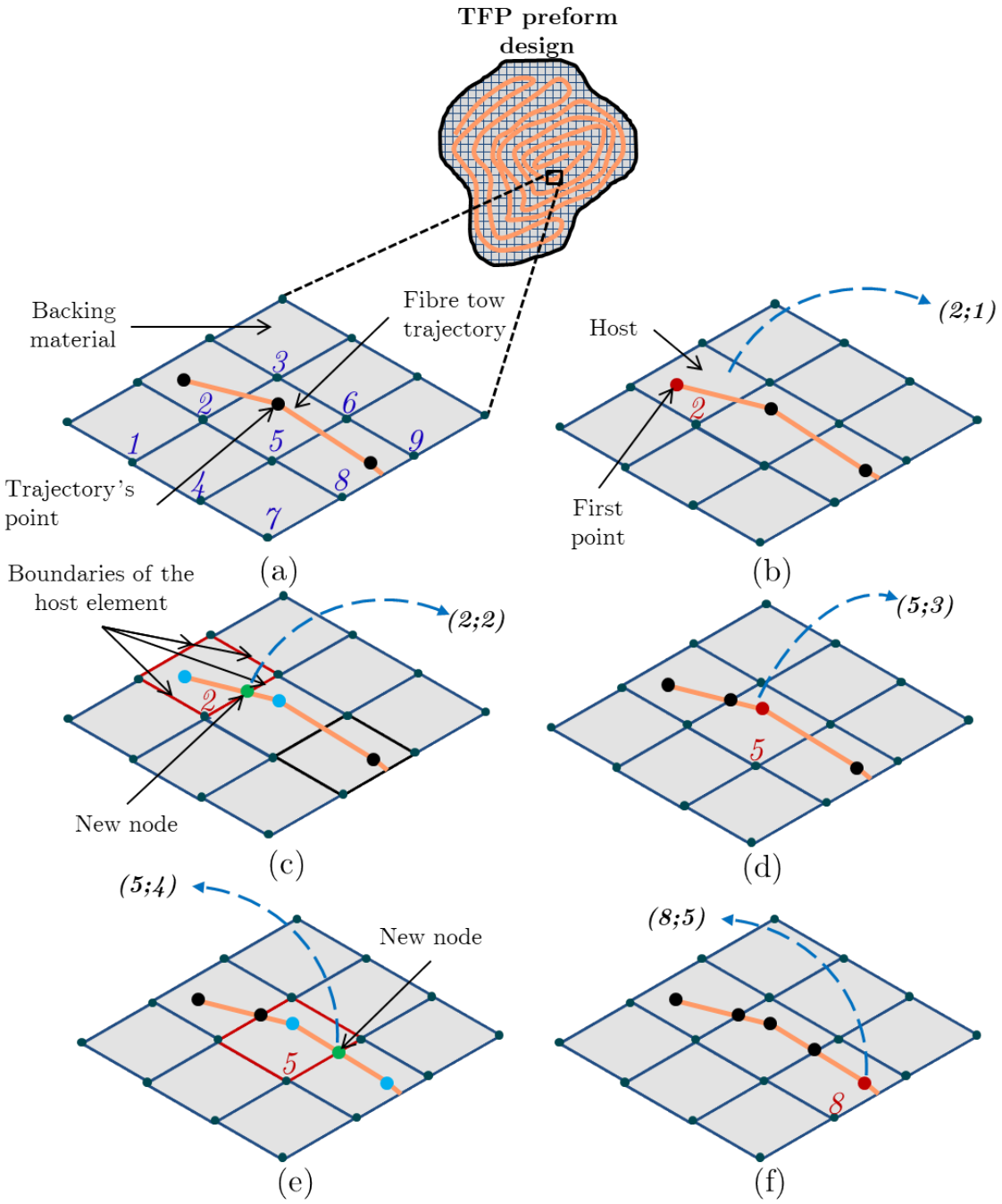

Figure 2.25: Meshing principle of Model I

2.4.2.2 Meshing of Model II: nodes embedded in 1D elements

The generation of Model II is easier. The first deposited layer is meshed and the second deposited layer is mesh independently. Next, segment-to-segment intersection is performed between both meshes. The crossing points are added as nodes in the second layer mesh. If the distance between the appended nodes and their neighbours is smaller than half the minimal element size of the initial mesh, the neighbour nodes are removed. This process is repeated with the subsequent layers. The segment-to-segment intersection is a brute force algorithm looping over each segment of each mesh. Using the sweep-line algorithm might considerably decrease the time to create the model when large TFP preforms or high fibre tow density preforms are modelled.

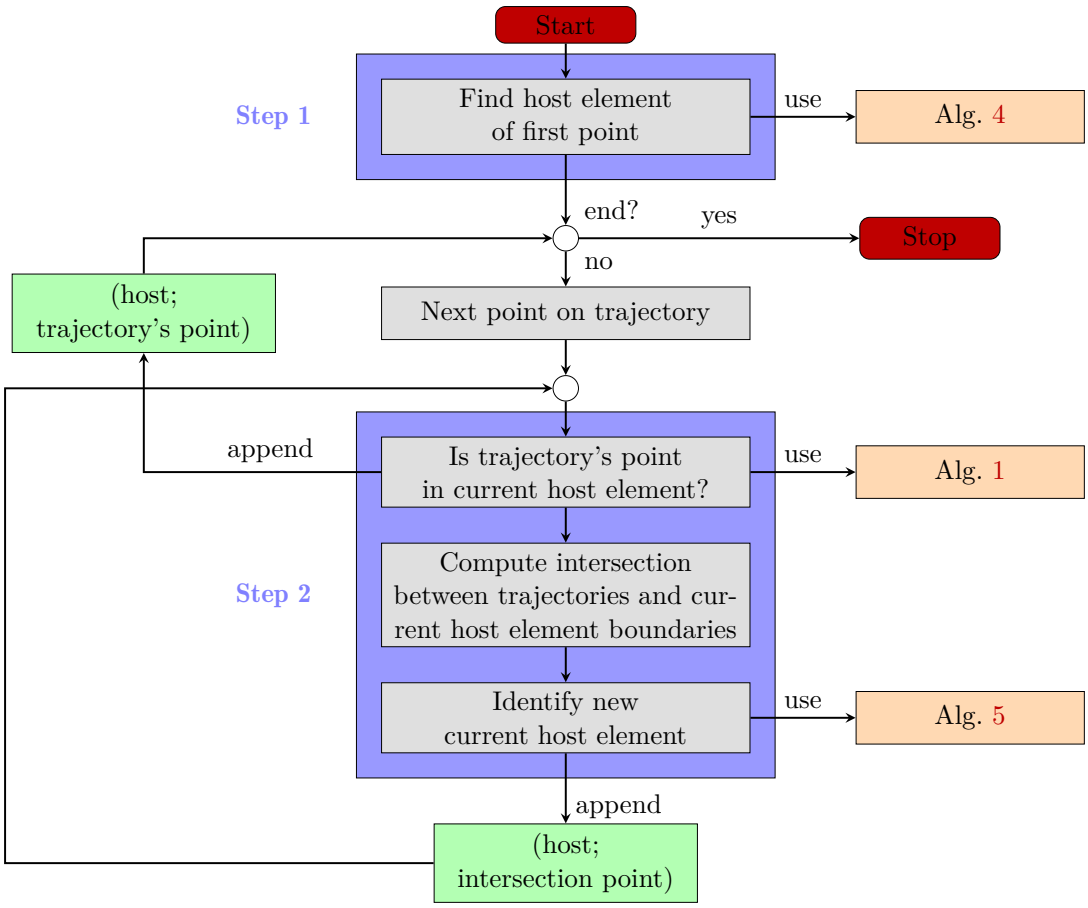

Figure 2.26: Model I meshing algorithm workflow

Transition

This section described the generation of the TFP preform models. Model I required the development of a specific algorithm to meet the constraint of the embedded element approach, namely, nodes are required at the intersections between the fibre path and the boundaries of the backing material elements. Generation of Model II only requires additional nodes at the intersections between adjacent layers. The algorithm that allows to compute the crossing points could be improved. In the next section, numerical elementary tests are achieved to check the implementation of the embedded element approach for both models.

2.4.3 Numerical validation: Elementary test cases

The aim of this section is to test the implementation of the embedding constraint for both models. In particular, the kinematic constraint and the transfer of internal forces is checked. Since only the displacement degrees of freedom of the beam are embedded, the embedding constraint should be equivalent to a perfect hinge connection between the beam and membrane elements or between the beams of adjacent layers. Simple configurations are considered to facilitate the analysis of the results even if the models can handle complex fibre path. Moreover, in the first elementary tests, the resistance to rotation due to friction and deformation of the stitching yarn at the crossings of fibre tows is not considered. The linear elastic torsional springs are taken into account in the last elementary tests. The material parameters of the beam elements used for all the tests are given in Table 3.1.

Table 2.19: Beams' material parameters for the following elementary test cases

Material parameters	C_E	C_{Γ_1}	C_{Γ_2}	C_{K_1}	C_{K_2}	C_{K_3}
Value	1.423 10^7	$\frac{C_E}{2}$	$\frac{C_E}{2}$	10^2	10^1	10^2
Unit	N	N	N	N.mm^2	N.mm^2	N.mm^2

2.4.3.1 Biaxial tension of a reinforced membrane (Model I)

Objectives This first elementary test case aims at testing the behaviour of a reinforced membrane element when subjected to biaxial tension. Displacements of the embedded beams are checked as well as the total internal forces of the reinforced membrane that should contain the beam's contribution.

Setup The bottom edge of a single 2D element is fixed along the y-direction and the left edge is fixed along y-direction. The right edge or node is translated along the x-direction with a value of Δ while the top edge or node is translated along the y-direction with a value of Δ too. A first beam is embedded, aligned with the x-direction and placed in the 2D element center. A second beam is embedded in the orthogonal direction and crosses the first beam at its center. Fig. 2.27 illustrates the initial and expected final configurations.

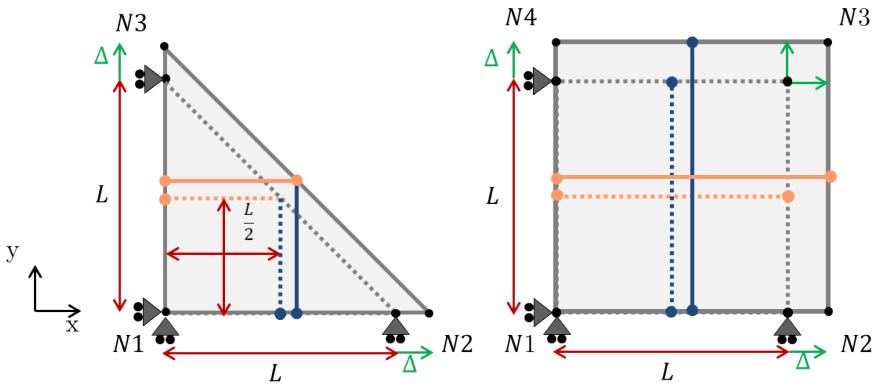

Figure 2.27: Biaxial tension of an incompressible Neohookean membrane reinforced with 2 orthogonal beam elements (initial configuration (dotted line), final configuration (solid line))

For the membrane, the coefficient $\mu = 1000$ MPa and the density equals 0.5. The length L is 1 mm. A displacement $\Delta = 10^{-3}$ mm is imposed in both directions.

Results The in-plane displacement field of the beam matches well those of the membrane element, which validates the kinematic constraint as shown in Fig. 2.28. Table 2.20 and 2.21 show the values of the in-plane internal forces at the beam nodes ($\vec{\boldsymbol{F}}^e_{int_i}$) as well as those resulting from the membrane behaviour at membrane nodes ($\vec{\boldsymbol{F}}^{hb}_{int_i}$) and the total internal forces at the membrane node ($\vec{\boldsymbol{F}}^h_{int_i}$). Therefore, the transfer of internal forces expressed in Eq. 2.61 is validated too.

Table 2.20: Biaxial tension reinforced triangle: checking of internal forces transfer

Internal forces	$F^1_{int_1}$	$F^1_{int_2}$	$F^2_{int_1}$	$F^2_{int_2}$	$F^{hb}_{int_1}$	$F^{hb}_{int_2}$	$F^{hb}_{int_3}$	$F^h_{int_1}$	$F^h_{int_2}$	$F^h_{int_3}$
F_x	-1423.53	1423.53	0	0	-0.49	0.49	0	-712.26	712.26	0
F_y	0	0	-1423.53	1423.53	-0.49	0	0.49	-712.26	0	712.26

Table 2.21: Biaxial tension reinforced quadrangle: checking of internal forces transfer

Internal forces	$F^1_{int_1}$	$F^1_{int_2}$	$F^2_{int_1}$	$F^2_{int_2}$	$F^{hb}_{int_1}$	$F^{hb}_{int_2}$	$F^{hb}_{int_3}$	$F^{hb}_{int_4}$	$F^{h}_{int_1}$	$F^{h}_{int_2}$	$F^{h}_{int_3}$	$F^{h}_{int_4}$
F_x	−1423.53	1423.53	0	0	−0.49	0.49	0.49	−0.49	−712.26	712.26	712.26	−712.26
F_y	0	0	−712.26	1423.53	−0.49	−0.49	0.49	0.49	−712.26	−712.26	712.26	712.26

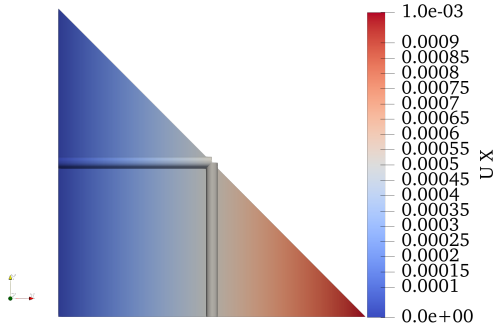

(a) Triangle

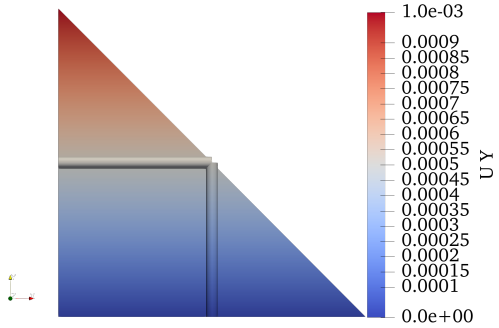

(b) Triangle

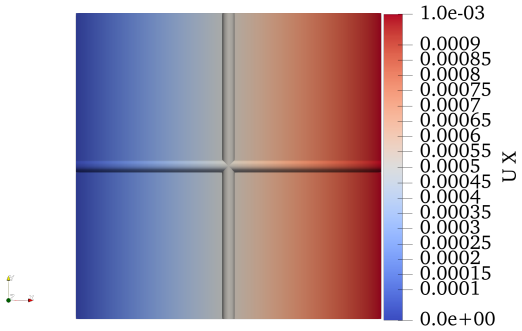

(c) Quadrangle

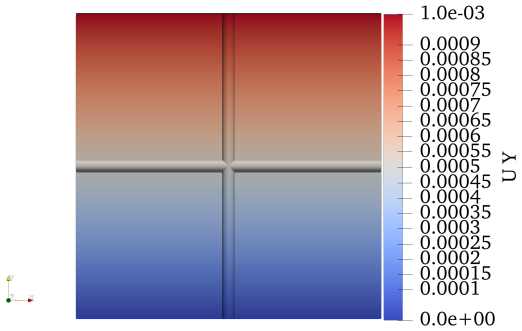

(d) Quadrangle

Figure 2.28: Checking the kinematic constraint: displacement along x-direction (left) and y-direction (right)

2.4.3.2 Biaxial tension of two orthogonal beams (Model II)

Objectives This second elementary test case aims at validating the embedding constraint in Model II. The consistency of the displacements of the embedded and host beams is checked.

Setup A horizontal beam made of two elements is embedded in a vertical beam made of one element The node (N_{e2}) of the horizontal beam at the intersection with the other beam is embedded. The bottom node (N_{h1}) is fixed along the y-direction and the left node (N_{e1}) is fixed along the x-direction. The right (N_{e3}) and top (N_{h2}) nodes are translated in the beams' axis direction with a value of Δ. Fig. 2.29 illustrates the initial and expected final configurations. The length L is 1 mm. A displacement $\Delta = 10^{-3}$ mm is imposed in both directions.

Results The in-plane displacement field of the beam is consistent with the boundary conditions. The displacement applied to the vertical host beam leads to a vertical translation of the horizontal beam due to the embed of the node at the intersection. Similarly, the displacement applied to the horizontal beam leads to a horizontal translation of the host beam due to the transfer of the internal forces from the embedded node.

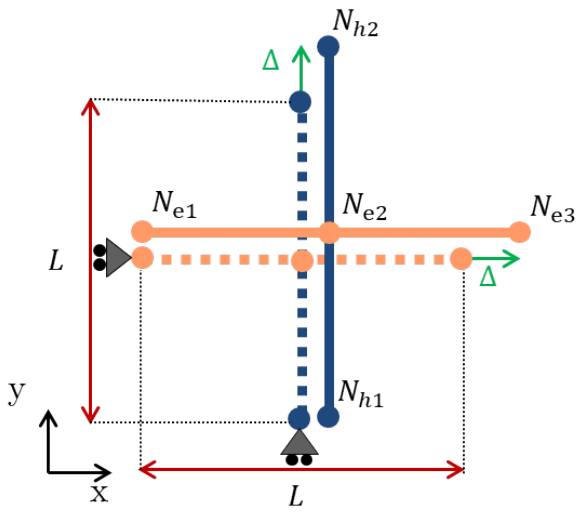

Figure 2.29: Biaxial tension of two orthogonal beams (initial configuration (dotted line), final configuration (solid line)

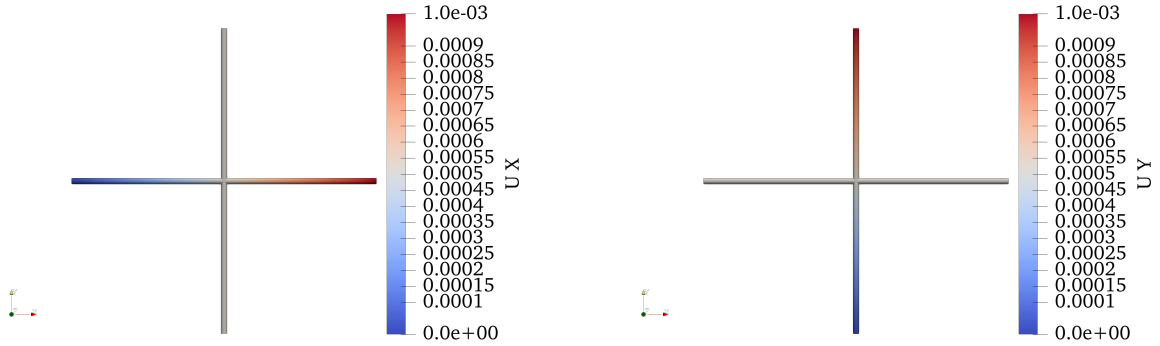

(a) **(b)**

Figure 2.30: Checking the kinematic constraint: displacement along x-direction (a) and y-direction (b)

2.4.3.3 Pure shear-like behaviour of a reinforced membrane (Model I)

Objectives This third elementary test case aims at testing the perfect hinge connection resulting from the embed of the displacement degrees of freedom in Model I. The boundary conditions should result in a pure shear-like behaviour, which means that the stiff embedded beams freely rotate on the membrane. It should modify the kinematics observed in the pure shear test of the membrane (2.3.3.3) and create a state of shear with through-the-thickness deformation due to its incompressibility.

Setup The embedded beams have the same configuration as in Test 2.4.3.1. The first node of the membrane is clamped while a displacement is applied on both directions on the third node. The length L is 1 mm and the displacement Δ equals 0.3 mm in both directions. Fig. 2.31 illustrates the initial and final expected configurations. For the membrane, the coefficient $\mu =$ 100 MPa and the density equals 0.5.

Results Table 2.22 shows the Green-Lagrange strain tensor components. The in-plane deformation along the beam directions (E_{11} and E_{22}) are negligible and the membrane deforms via shear (E_{12}) and through-the-thickness (E_{33}) as expected. For the beam elements, E_{11}

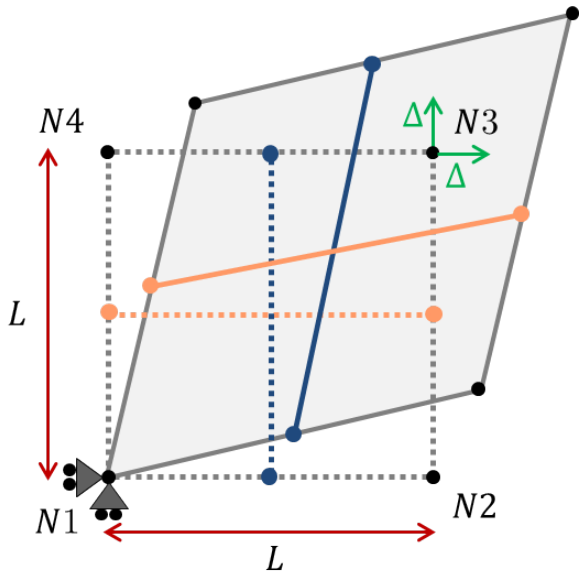

Figure 2.31: Pure shear-like behaviour of a membrane reinforced with two orthogonal beams (initial configuration (dotted line), final configuration (solid line))

corresponds to the longitudinal component E of the strains vector defined in section 2.2.1.5. Therefore, the results validate the free rotation of the embedded beams. Fig. 2.32 shows a comparison of the results when the rotational degrees of freedom are embedded. The observed kinematic is very different. The beams are welded and the rotation is not free, which leads to the longitudinal deformation as shown in Table 2.23. This very stiff behaviour, which is unrealistic to model the crossing of fibre tows, was observed by Harrison (2016).

Table 2.22: Pure shear-like behaviour of a reinforced membrane: strain tensor components

Elements	E_{11}	E_{22}	E_{33}	E_{12}
Horizontal beam	10^{-6}	0	0	0
Vertical beam	10^{-6}	0	0	0
Membrane	10^{-6}	10^{-6}	0.45	0.34

Table 2.23: Pure shear-like behaviour of a reinforced membrane with embedded rotational dofs: strain tensor components

Elements	E_{11}	E_{22}	E_{33}	E_{12}
Horizontal beam	0.1	0	0	0
Vertical beam	0.1	0	0	0
Membrane	0.12	0.12	-0.13	0.2

2.4.3.4 Initial orthogonal beams' rotation (Model II)

Objectives This fourth elementary test case aims at validating the perfect hinge connection resulting from the embed of the displacement degrees of freedom in Model II. Negligible internal forces (due to inertia forces) are expected to validate the free rotation between the connected beams.

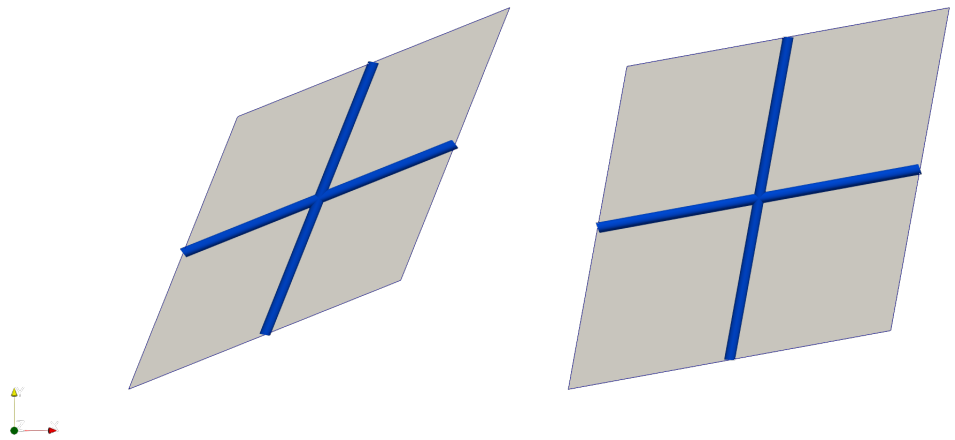

Figure 2.32: Checking free rotation of embedded beams: embed of displacement dofs (left), full embedding (right)

Setup The configuration of the orthogonal beams is the same as in Test 2.4.3.2. However, the bottom node is free and the top node is translated along the x-direction while being free to move along the y-direction as shown in Fig. 2.33. The length L equals 1 mm and the imposed displacement Δ is 0.3 mm.

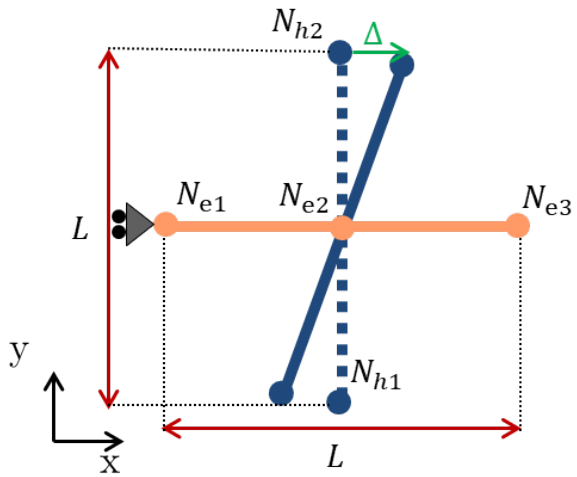

Figure 2.33: Free rotation between beams at their intersection (initial configuration (dotted line), final configuration (solid line))

Results The in-plane displacement field of the beams is consistent with the boundary conditions. The horizontal displacement applied to the top node of the host beam leads to a rotation around the intersection where the embedding constraint applies. The longitudinal deformation of the beam elements is around 10^{-12} and therefore negligible as expected.

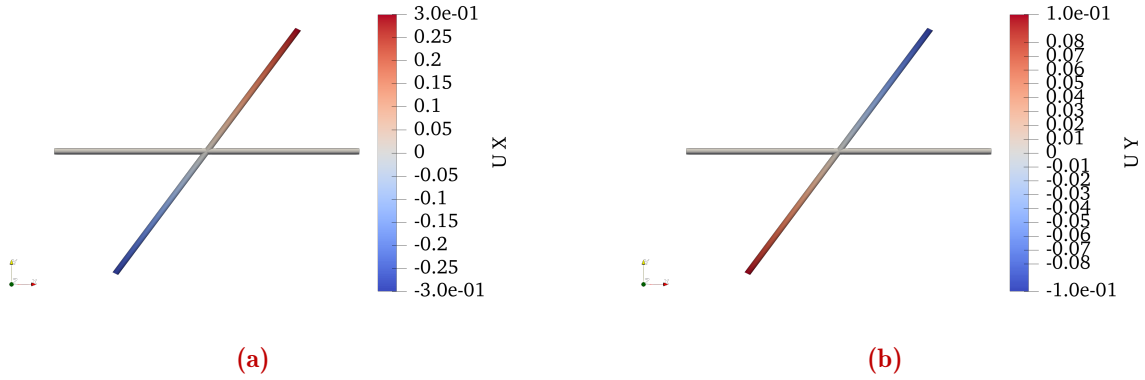

(a) **(b)**

Figure 2.34: Checking the perfect hinge connection: displacement along x-direction (a) and y-direction (b)

2.4.3.5 Effect of torsional spring in Model I

Objectives This elementary test case aims at validating the implementation of the linear elastic torsional spring in Model I. This spring is added at the intersections between the beam elements of adjacent layers to take into account the resistance to rotation due to the friction and stitching yarn deformation. Combined together, the embedding constraint and the torsional spring model the hinge connection with resistance to rotation in the local plane define by the intersected beams.

Setup The configuration of the orthogonal beams is the same as in Test 2.4.3.4. However, displacement on the third node is replaced by a point load of 100 N. A linear elastic torsional spring with a stiffness of 20 N.mm^{-1} is added at the intersection between the embedded beams. Fig. 2.35 shows the initial and final expected configurations.

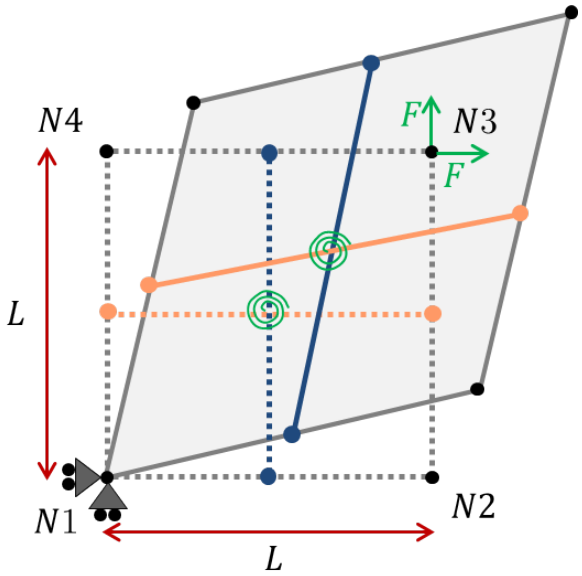

Figure 2.35: Constrained rotation between beams at intersection in Model I (initial configuration (dotted line), final configuration (solid line))

Results Fig. 2.36 superimposed the final shape and rotation with (blue color) and without (orange color) the linear elastic torsional spring. Due to the torsional spring, the rotation angle

is lower than those without the torsional spring, which is consistent.

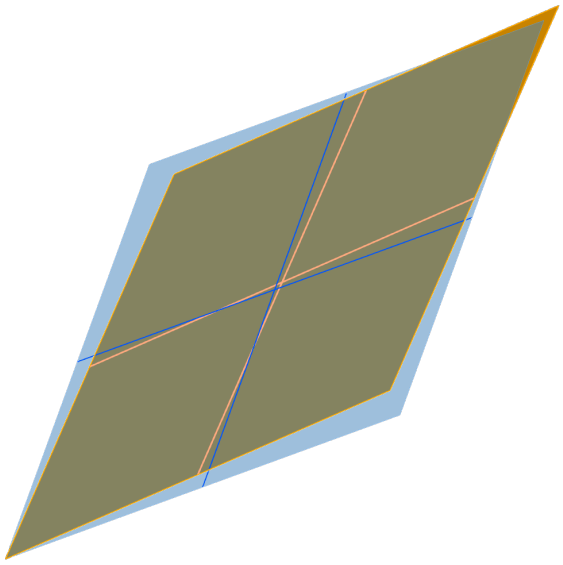

Figure 2.36: Constrained (blue color) vs unconstrained (orange color) rotation between embedded beams at intersection (Model I)

2.4.3.6 Effect of torsional spring in Model II

Objectives This elementary test case aims at validating the implementation of the linear elastic torsional spring in Model II.

Setup The configuration of the orthogonal beams is the same as in Test 2.33. However, the displacement on the top node is replaced by a punctual force of 0.5 N. A linear elastic torsional spring with a stiffness of 0.1 N.mm^{-1} is added at the intersection between the beams. Fig. 2.35 shows the initial and expected final configurations.

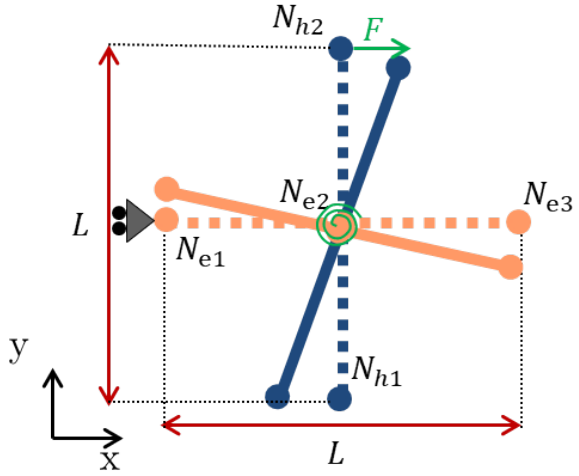

Figure 2.37: Constrained rotation between beams at intersection in Model II (initial configuration (dotted line), final configuration (solid line))

Results Fig. 2.38 shows the results with (dark colors) and without (light colors) the linear elastic torsional spring. Due to the torsional spring, the horizontal beam rotates too since the

left node is free to move along the y-direction. Since the left node is constrained along the x-direction, the beams also slightly translate. Without the torsional spring, the vertical beam rotates while the horizontal beam stays in place. This result validates the implementation of the resistance to rotation through a linear elastic torsional spring.

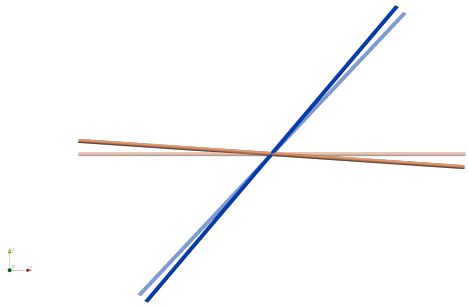

Figure 2.38: Constrained (dark colors) vs unconstrained (light colors) rotation between beams at their intersection (Model II)

Conclusion

This section gave the formulation and explained the implementation of the embedding constraint in both models. The kinematic constraint is limited to the displacement dofs of the embedded elements since the embed of the rotation dofs leads to very stiff and unrealistic behaviour of crossing fibre tows. As a result of the kinematic constraint, the internal forces of the embedded elements are transferred to the host elements. With this formulation, the stitching yarn is modelled as perfect hinges between the backing material and the fibre tows (Model I) or between crossing fibre tows of adjacent layers (Model II). To take into account the resistance to rotation due to friction and the deformation of the stitching yarn, linear elastic torsional spring are added at the intersections between the fibre tows of adjacent layers. Finally, elementary test cases validated the implementation of the proposed models.

Chapter conclusion

This chapter presented the modelling strategy adopted to address the forming of TFP preforms. The TFP technology can be used to locally reinforce another conventional textile or as a whole preforming tool where the backing material is removed prior to forming. The geometrical complexity of TFP preforms' makes the semi-discrete approach more suitable as a first step. Therefore, two semi-discrete models are considered to take into account the possibility to retain or remove the backing material prior to forming. Predicting the orientations of fibre tows in the final part as well as manufacturing defects are the main objectives of the numerical model. With this philosophy in mind, fibre tows are modelled explicitly using beam elements to take into account the design freedom offered by the TFP. The proposed models are based on the strong assumption which considers the stitching yarn to act as a hinge connection between the backing material and the fibre tows in Model I or between the fibre tows of adjacent layers in Model II. This hypothesis allows modelling implicitly the stitching yarn using an embedded element approach where only the displacement degrees of freedom are embedded. A beam element with independent cross-section stiffnesses is formulated to model the fibre tows. Since no specific backing material is consider in this work, an incompressible Neohookean membrane is implemented to investigate numerically Model I. The embedding constraint to model the stitching yarn is implemented for both models. In Model I, the beam elements of fibre tows are embedded in the 2D elements of the backing material while in Model II the element nodes of fibre tows of a layer are embedded in beam elements of fibre tows of the previous layer. Moreover, torsional linear elastic springs are added at fibre tows intersections to take into account the resistance to rotation due to friction and deformation of the stitching yarn. Elementary test cases were successfully performed separately on the beam element and the incompressible Neohookean membrane and finally on the embedding constraints.

Full-scale validation of the proposed modelling strategy is the next step in the development of the numerical forming tool for TFP preforms. In the next chapter, experimental forming of high doubly-curved parts is carried out as well as their numerical simulation.

Bibliography

Allwood, R. J. and Bajarwan, A. A. (1989). A new method for modelling reinforcement and bond in finite element analyses of reinforced concrete. *International Journal for Numerical Methods in Engineering*, 28(4):833–844.

Bathe, K.-J. and Bolourchi, S. (1979). Large displacement analysis of three-dimensional beam structures. *International Journal for Numerical Methods in Engineering*, 14(7):961–986.

Bel, S., Hamila, N., Boisse, P., and Dumont, F. (2012). Finite element model for NCF composite reinforcement preforming: Importance of inter-ply sliding. *Composites Part A: Applied Science and Manufacturing*, 43(12):2269–2277.

Carpenter, N. J., Taylor, R. L., and Katona, M. G. (1991). Lagrange constraints for transient finite element surface contact. *International Journal for Numerical Methods in Engineering*, 32(1):103–128.

Creech, G. and Pickett, A. K. (2006). Meso-modelling of Non-Crimp Fabric composites for coupled drape and failure analysis. *Journal of Materials Science*, 41(20):6725–6736.

Cunha, V. M., Barros, J. A., and Sena-Cruz, J. M. (2012). A finite element model with discrete embedded elements for fibre reinforced composites. *Computers & Structures*, 94-95:22–33.

De Luycker, E., Morestin, F., Boisse, P., and Marsal, D. (2009). Simulation of 3D interlock composite preforming. *Composite Structures*, 88(4):615–623.

d'Agostino, M., Giorgio, I., Greco, L., Madeo, A., and Boisse, P. (2015). Continuum and discrete models for structures including (quasi-) inextensible elasticae with a view to the design and modeling of composite reinforcements. *International Journal of Solids and Structures*, 59:1–17.

Géradin, M. and Cardona, A. (2001). *Flexible Multibody Dynamics: A Finite Element Approach*. Wiley–Blackwell, New York.

Hamila, N., Boisse, P., Sabourin, F., and Brunet, M. (2009). A semi-discrete shell finite element for textile composite reinforcement forming simulation. *International Journal for Numerical Methods in Engineering*, 79(12):1443–1466.

Harrison, P. (2016). Modelling the forming mechanics of engineering fabrics using a mutually constrained pantographic beam and membrane mesh. *Composites Part A: Applied Science and Manufacturing*, 81:145–157.

Ibrahimbegović, A., Frey, F., and Kožar, I. (1995). Computational aspects of vector-like parametrization of three-dimensional finite rotations. *International Journal for Numerical Methods in Engineering*, 38(21):3653–3673.

Markou, G. (2011). Detailed Three-Dimensional Nonlinear Hybrid Simulation for the Analysis of Large-Scale Reinforced Concrete Structures. page 310.

Markou, G. and Papadrakakis, M. (2012). An efficient generation method of embedded reinforcement in hexahedral elements for reinforced concrete simulations. *Advances in Engineering Software*, 45(1):175–187.

Ritto-Corrêa, M. and Camotim, D. (2002). On the differentiation of the Rodrigues formula and its significance for the vector-like parameterization of Reissner-Simo beam theory: Diferrentiation of Rodrigues formula. *International Journal for Numerical Methods in Engineering*, 55(9):1005–1032.

Simo, J. and Vu-Quoc, L. (1986). A three-dimensional finite-strain rod model. part II: Computational aspects. *Computer Methods in Applied Mechanics and Engineering*, 58(1):79–116.

Spickenheuer, A., Scheffler, C., Bittrich, L., Haase, R., Weise, D., Garray, D., and Heinrich, G. (2018). Tailored Fiber Placement in Thermoplastic Composites. *Technologies for Lightweight Structures (TLS)*, Vol 1:Chemnitz–.

Taylor, R. L., Oñate, E., and Ubach, P.-A. (2005). Finite Element Analysis of Membrane Structures. In Oñate, E. and Kröplin, B., editors, *Textile Composites and Inflatable Structures*, volume 3, pages 47–68. Springer-Verlag, Berlin/Heidelberg.

Chapter 3

Full-scale validation of the TFP preform modelling strategy: application to the forming of high curved orthotropic parts

Abstract

This third chapter of the thesis aims at validating the numerical modelling approach presented in the previous chapter (Chapter 2). To this end, experimental work has been carried out about TFP preform forming to allow full-scale comparison with forming simulations. Moreover, the following work highlights the ability of 2-layer TFP preforms to be formed on highly curved parts with orthotropic final orientations. Obtaining orthotropic composite parts from an initially flat preform represents a challenge in the manufacturing of optimized 3D shell-like composite structures by forming. Section 3.1 is an introduction providing the objectives of this validation study, justifying the choice of the formed geometries as well as presenting the TFP preform manufacturing process and the materials used. The next two sections follow the same structure. They start by presenting the experimental forming on a particular geometry and ends up with the numerical simulation of the forming. In both sections, the specific TFP preform design conducting to final orthotropic composites is explained and comparison between experimental and numerical results is displayed. Section 3.2 presents the forming validation on a hemispheric part, which is considered as a basic test case in conventional textile forming. Only qualitative analysis is given for this example. Then, Section 3.3 investigates TFP preform forming on a tetrahedral part, which has a direct industrial application since it corresponds to corner brackets. Due to the difficulty in finding a suitable backing material able to overcome large deformation, the two forming validations are performed with Model II, meaning that the backing material is removed prior to forming. A simulation with Model I is performed in the last section but no experimental work has been performed. Consequently, this chapter focuses on one application of the TFP technology, namely, its use as a whole preforming tool.

Contents

3.1 Introduction

Introduction

This section is a short introduction of the experimental work achieved in this thesis about forming of TFP preforms. It begins by presenting the objectives of the forming experiments. In particular, the choice of the targeted 3D shapes is argued before presenting the TFP preform manufacturing process and the materials used.

3.1.1 Objectives of the forming experiments

Only few works on the manufacturing of 3D parts using TFP preforms were reported in the literature (Fial et al., 2018; Rihaczek et al., 2020; Takezawa et al., 2021). In these works, 3D part manufacturing was achieved by folding (Fial et al., 2018; Rihaczek et al., 2020) or layer by layer forming (Takezawa et al., 2021) with cuts in the backing material as presented in Section 1.4.2.

The following experiments aim at demonstrating the ability of 2-layer TFP preforms to be formed on doubly-curved shapes without defects and designed to provide orthotropic properties to the final part. It is worth noting that obtaining orthotropic properties on doubly-curved shapes cannot be achieved using conventional bi-axial textiles. Therefore, the forming of TFP preforms will show great interest in improving the mechanical properties of structural parts.

These forming experiments aim to demonstrate the formability of TFP preforms and the advantage of the combination of the TFP technology and the forming to obtain peculiar fibre orientations in the final part. However, they are limited to dry forming and this work does not address the impregnation and consolidation steps.

Moreover, determining the flat TFP pattern leading to the targeted 3D orientations is not the objective of this thesis. Consequently, the studied shapes have to allow an analytical or at least intuitive flattening of the 3D orientations.

3.1.2 Choice of the targeted part geometries

The ability of 2-layer TFP preforms to be formed on doubly-curved shapes has been shown using both hemispheric and tetrahedral punches.

On one hand, the hemisphere is a highly-curved shape with axial symmetry. It is a well-known shape extensively used as bench mark for conventional textiles (De Luycker et al., 2009; Lin et al., 2007; Bel et al., 2012; Labanieh et al., 2018; Guzman-Maldonado et al., 2019; Sun et al., 2022). Although the hemisphere has double curvatures, conventional textiles can be formed without defects quite easily since the maximal shear angle reached is close to 45°. Therefore, this shape was deemed appropriate for as a first forming test. However, in this work the TFP preforms are designed to obtain orthotropic orientations in the final configuration, which maximizes the angle between the layers. Therefore, an improvement of the mechanical properties is expected compared to conventional textiles.

On the other hand, the tetrahedral shape, which is also a doubly-curved shape, corresponds to angle brackets. Therefore, it shows a great interest in industries using complex parts. Forming such a shape is possible using conventional textiles such as woven fabrics or interlocks but requires a specific design of the blank-holders and a control of the pressure applied on them to avoid defects such as wrinkles (Allaoui et al., 2011; Capelle et al., 2014; Allaoui et al., 2014). However, if wrinkles can be prevented in the functional area of corner brackets, they cannot be avoided in the surrounding regions (Allaoui et al., 2011). Moreover, high shear angles are inevitable and weaken the part in those regions. Consequently, forming of 2-layer

TFP preforms with orthotropic orientations in the final tetrahedral part using basic blank-holders will demonstrate significant improvements of the manufacturing process and the final mechanical properties of the part.

3.1.3 TFP preform deformation mechanisms

As described in Section 1.4, a TFP preform is made of fibre tows placed on a backing material and remained in place thanks to a zig-zag stitching (Fig.1.26). NCF might be the conventional textile having the closest architecture from TFP preforms, since they are made of several UD plies stitched together with a through-thickness stitching yarn as presented in Section 1.1.2. TFP preform can be approximatively considered as a generalisation of NCF to multi-directional plies with the difference that an additional backing material is necessary for the stitching. Besides, this backing material can remain during forming, either for constituting polymer matrix or because TFP is used to locally reinforce a conventional textiles for instance.

During forming, TFP preforms might show the same deformation mechanisms as those already listed for conventional textiles in Section 1.2.1 and illustrated in Fig. 1.9. In addition to these deformation mechanisms, interactions of the backing material with both the fibre tows and the stitching yarn occur. The overall behaviour of TFP preforms will strongly depends on the individual properties of the fibre tows, the backing material and the stitching yarn, as well as the way they interact with each other. Moreover, the stitching parameters presented in Section 1.4.1 strongly influences the behaviour of the TFP preform. The shorter the stitch length, the higher the friction between fibre tows and the backing material and the stiffer the preform. On one hand, the influence of the stitching parameters over the whole preform behaviour allows varying the stitching parameters inside the preform to overcome forming issues. On the other hand, it increases the modelling complexity of these tailored preforms. Consequently, the mechanical behaviour of TFP preforms is inherently complex.

3.1.4 TFP preform manufacturing and materials

3.1.4.1 Preform design

The design of the TFP preforms used in the forming experiment was computed with Python scripts that generate the stitch coordinates. In a script, a list of TFP segments is defined. Each TFP segment possesses basic geometric entities such as a line, a polyline, a circle arc and a spirale as well as a stitching rule. This stitching rule prescribes the stitching length along the curvilinear abscissa of the geometric entity of the TFP segment. Stitching rules such as no-stitching, constant stitching length or linear stitching length can be defined for the TFP segment. When defining a constant length stitching rule, either the stitching length or the total number of stitches is given as input. The list of TFP segment has to be contiguous, which means that the end of a TFP segment in the list has to be connected to the neighbouring TFP segment. This list of contiguous TFP segments forms a TFP path. Fig. 3.1 illustrates the TFP design process. If two layers are designed and a cut is required between the layers, then two different TFP paths have to be defined. Otherwise, a single TFP path is sufficient. The stitching width is defined in the TFP machine controller and therefore is constant in the input file.

Once the TFP paths have been defined, virtual stitching is performed which generates the 2D coordinates of the stitching points stored in an array. Then, an open source Python library "pyembroidery" writes a "DST" file that can be opened in the commercial software EPC-WIN of the TFP machine to check the design and convert the data to the format used by the TFP machine. This method allows the TFP preform drawing to be set up and the stitch coordinates to be accessed to create the corresponding digital model.

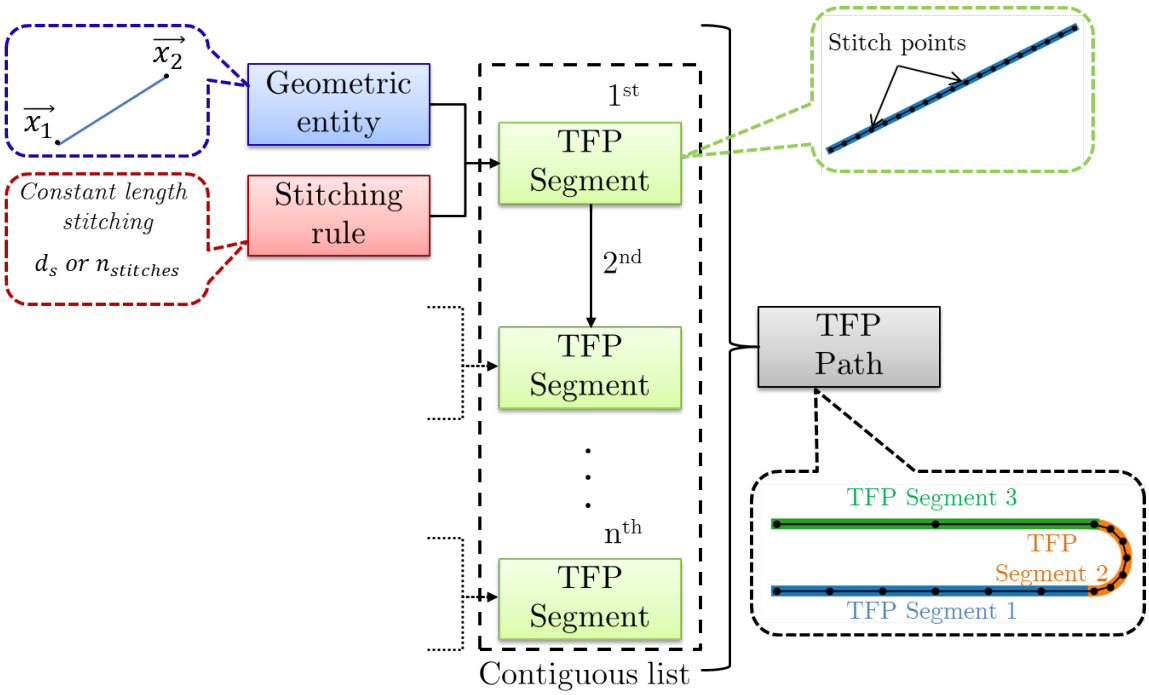

Figure 3.1: TFP preform design process

3.1.4.2 Manufacturing

The TFP preforms used in these experiments have been manufactured at IRT Jules Verne using the TFP ZSK © CMCW 0200-900D-2500 embroidery machine shown in Fig 3.2. A control system for the tension of the upper stitching yarn has been added and the tension of the lower stitching yarn is set via the bobbin's mechanism. The stitching width is set via the machine controller as well as the stitching speed.

Figure 3.2: TFP machine used at IRT Jules Verne (TFP ZSK © CMCW 0200-900D-2500)

3.1.4.3 Materials

Both forming experiments, which are performed at room temperature, required high deformation of the TFP preforms. Rotation between the dry fibre tows of the different layers, known as in-plane shear for conventional textiles, is the main deformation mode during forming. It is therefore difficult to find a backing material able to deform accordingly without creating defects. Consequently, in both forming experiments, the backing material has been removed prior to forming. Even after removing the backing material, the stitching yarn still ensures a strong cohesion between the layers. To this end, a PVA water soluble film was used as backing material. After manufacturing, the TFP preforms were washed and then dried in an oven at a temperature of 60°. The 2690 tex PET/E-glass continuous tow (from P-D- Glasseiden GMBH, Oschatz, Germany) was stitched onto the PVA film (Gunold® Solvy film 80, Stecker) using a 24 tex PET stitching yarn (Serafil fine, Amman). The stitching length and width were set to 2.5mm and the stitching tension to 5 g for both TFP preform designs. The stitching length is smaller in U-turns and highly curved paths.

The material properties of the fibre tow has not been measured. The material parameters required in the finite element model for the beam elements have been estimated. Their values are shown in Table 3.1. In particular, the tensile stiffness (C_E) is estimated from the tensile modulus of a E-glass fibre (72.5 GPa). The transverse shear stiffnesses (C_{Γ_1} and C_{Γ_2}) are taken as half the tensile stiffness. The torsional and bending stiffnesses have non-zero but low values compared to the tensile stiffness. A circular cross-section of diameter 2.5 mm is used.

Table 3.1: Beams' material parameters for the forming simulation

Material parameters	C_E	C_{Γ_1}	C_{Γ_2}	C_{K_1}	C_{K_2}	C_{K_3}
Value	$1.423\ 10^7$	$\frac{C_E}{2}$	$\frac{C_E}{2}$	10^2	10^1	10^1
Unit	N	N	N	N.mm^2	N.mm^2	N.mm^2

Conclusion

These forming experiments aim at demonstrating that this hybrid solution (flat TFP preform + forming) is an attractive process to manufacture doubly-curved parts with orthotropic final orientations. Due to the difficulty in finding a suitable backing material allowing large deformations and valuable in the final part, a water soluble film is used during stitching before being removed prior to forming. Consequently, this experimental work investigates the use of the TFP technology as a whole preforming tool. Using the TFP technology as a mean to locally reinforce a conventional textile is not carried out experimentally.

3.2 TFP preform forming on a hemispheric shape with orthotropic final orientations

Introduction

This section deals with the dry forming of a hemispheric part from a flat TFP preform without backing material. The main objective of the hemisphere forming is to obtain one layer aligned with the parallel of latitudes (parallel layer) and a second layer aligned with the meridian of longitudes (meridian layer) as illustrated in Fig 3.3. Such configuration provides orthotropic mechanical properties to the part and has been numerically studied in Muscat et al. (2017) to manufacture fibre reinforced composite pressure vessel heads subject to external pressure. First, the determination of the design of the TFP preform to obtain orthotropic final orientations is explained. Next, the forming device is presented before analysing and discussing the results. Then, the finite element model is presented before showing the simulation's results and compare them with the experimental ones.

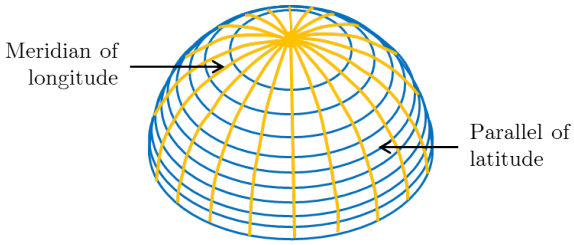

Figure 3.3: Targeted orientations for the forming of a hemispheric part

3.2.1 Experimental forming

3.2.1.1 TFP preform design: analytic flattening

The determination of the flat configuration of the TFP preform from the targeted 3D orientations is based on the inextensibility of the fibre tows and the no-sliding condition between the fibre tows of the two layers. Due to the axial symmetry of the hemisphere and those of the targeted 3D orientations, the flat configuration can be determined analytically. For brevity and clarity, an intuitive demonstration is illustrated in the following. For a strict mathematical demonstration, the reader is referred to Sholl et al. (2021).

Fig. 3.4 (a) shows the hemispheric geometry and a projection plane whose normal is aligned with the hemisphere's revolution axis. The projection of the hemisphere's basis is drawn as a circle of radius r_h on the plane. Three parallels of latitude are drawn in Fig. 3.4 (b). The curvilinear distance along the meridians between the consecutive parallels is the same and named l_c. This configuration allows a better understanding of what follows while not limiting the case studied. Because of the quasi-inextensibility of the fibre tows, the flattening of these parallels results in circles whose radius is equal to the orthogonal distance between the parallels and the axis of the hemisphere. The in-plane distance between the resulting consecutive circles decreases from the projected centre of the hemisphere to the outer diameter. As a consequence of the non-slip assumption between the tows, the parallel tows constrain the shape of meridian tows in their flat configuration. The meridian-aligned tows begin from the projected centre of the hemisphere and end at a distance of r_h. Since there is the same portion of meridian l_c between consecutive concentric circles representing the flattened parallels of latitude, the meridian tows are curved in the plane Fig. 3.4 (c). The curvilinear abscissa along the flattened meridian curve shown in

Fig. 3.4 (d) has the following expression in polar coordinates of the projection plane:

$$s(r) = r_h * \arcsin \frac{r}{r_h} \tag{3.1}$$

The general expression of the curvilinear abscissa in a polar coordinates system is given by:

$$s(r) = \int_0^a \sqrt{r(\theta)^2 + \left(\frac{dr(\theta)}{d\theta}\right)^2} d\theta \tag{3.2}$$

Introducing Eq.3.1 into Eq.3.2, and differentiating with respect to θ and taking the square of the expression leads to the following ordinary differential equation:

$$r(\theta)^2 + \left(\frac{dr(\theta)}{d\theta}\right)^2 \left(1 - \frac{1}{1 - \frac{r(\theta)^2}{r_h^2}}\right) = 0 \tag{3.3}$$

The solution of Eq.3.3 yields the expression of the flattened meridian:

$$r(\theta) = r_h * \sin\theta \tag{3.4}$$

3.2.1.2 Final preform design

The fibre tows of the meridian layer converge towards the center of the hemisphere. To avoid overlapping, the length of some of these fibre tows is shortened. Fig. 3.5 illustrates the manufactured flat TFP preform. The outward extension of the meridian fibre tows is needed for the clamping system as explained in the next section. Instead of circles, a spiral is used for the parallel layer to avoid cutting operations and loosing the fibre continuity.

3.2.1.3 Forming device

The forming device shown in Fig 3.6 is composed of a hemispheric punch of radius 100 mm and a blank-holder made of two parts. The pins located at the outer edge of the bottom part of the blank-holder are used to constrain the meridian layer from sliding inwards. Extending the fibre tows of the meridian layer to the outer edge of the blank-holder has been chosen to simplify the design. However, the constraint applied to the meridian layer could be achieved differently to minimize material wastage. To prescribe the hemispheric punch motion, a simplistic mechanism was used based on a lift table. The TFP preform was clamped in the blank-holder that was fixed on a frame and placed above the punch located on the middle of the lift table. The punch was then moved upward using the lift table while a picture was taken every 2 mm from the top.

3.2.1.4 Results

The result of the hemisphere forming is shown in Fig. 3.7. Only qualitative analysis is given for this example. The orientations of the layers are very close to the targeted ones. During the forming, the TFP preform rotates along the hemisphere axis as illustrated by the red circular arrow in Fig 3.7 (c). In fact, due to the inextensibility of the fibre tows, the fibre tows of the meridian layer have to realign with the meridians of longitudes.

3.2.1.5 Discussion

The difference with the targeted orientations might be attributed to the manufacturing process which generates a slight error on the curvature of the initial configuration, since the stitching leads to a discretization of the true path. Moreover, the slight undulation of the fibre tows, as

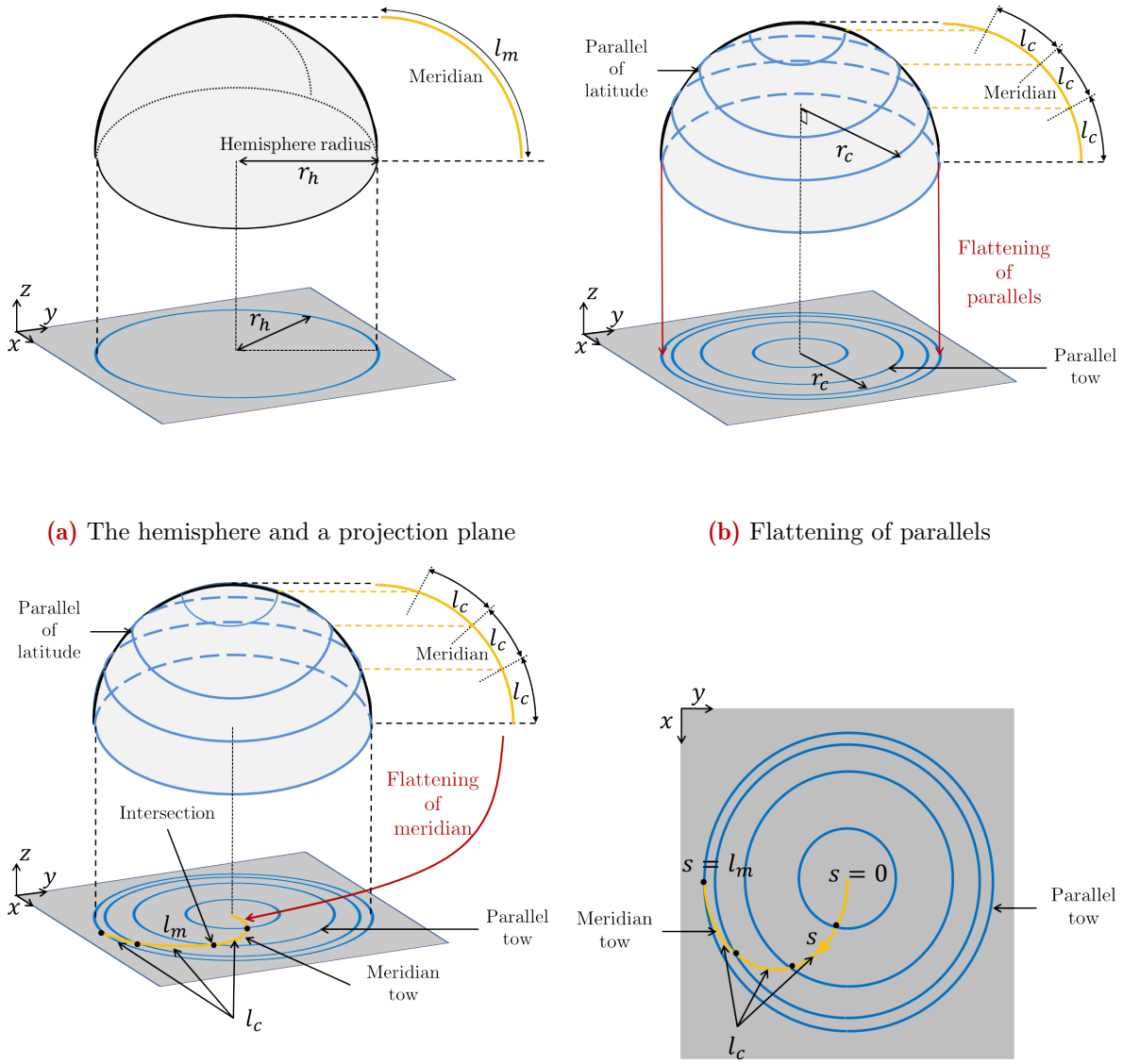

(a) The hemisphere and a projection plane

(b) Flattening of parallels

(c) Flattening of meridians

(d) Flat pattern

Figure 3.4: Analytic flattening process

observed in Uhlig et al. (2016), which is due to the stitching pattern, might lead to an extra length of deposited material along the path, which can explain why the realignment is not perfectly achieved. Although the flat TFP pattern can be improved to increase the density of fibres and obtain a better realignment, this forming example demonstrates the ability to form a hemispheric part with orthotropic properties from a flat TFP preform.

Transition

The experimental results of the hemispherical shape forming are promising. Obtaining orthotropic final orientations from flat preforms with this geometry is a real challenge impossible to address using conventional textiles. The forming simulation of this shape is presented in the next section.

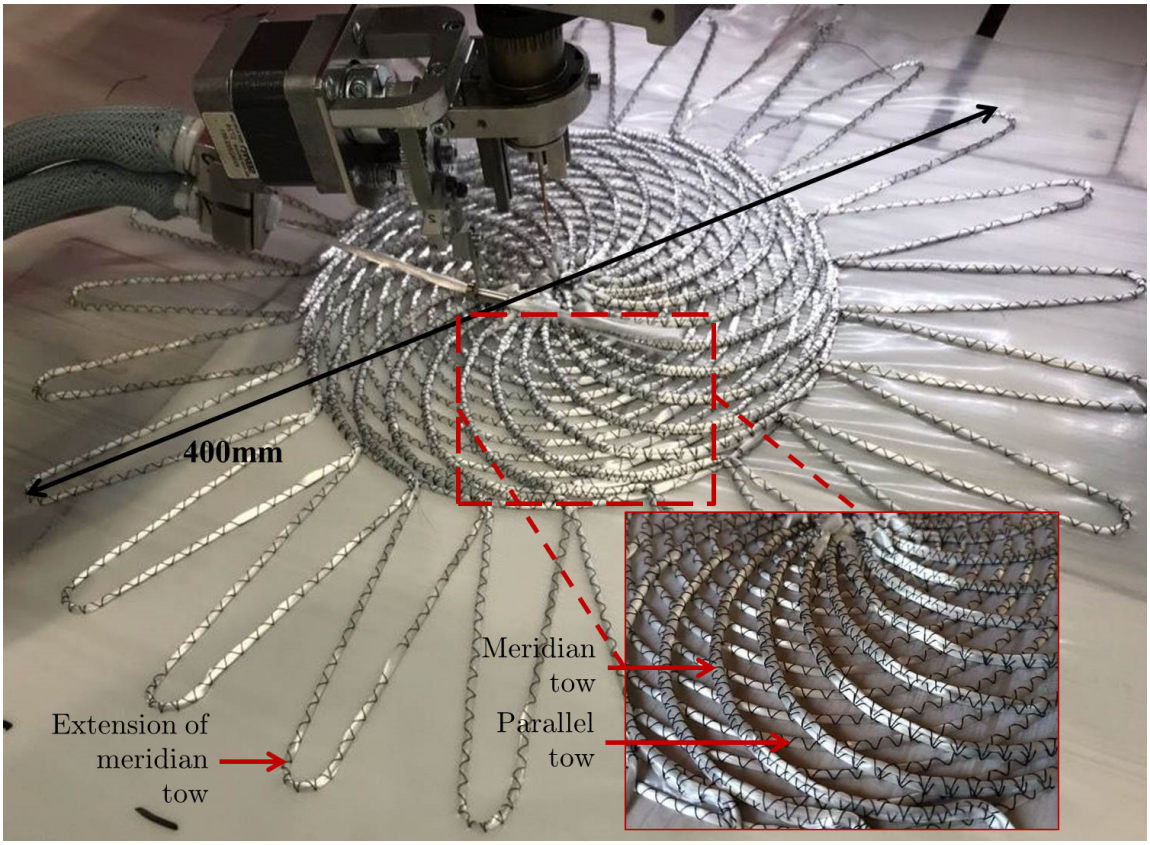

Figure 3.5: Manufactured TFP preform

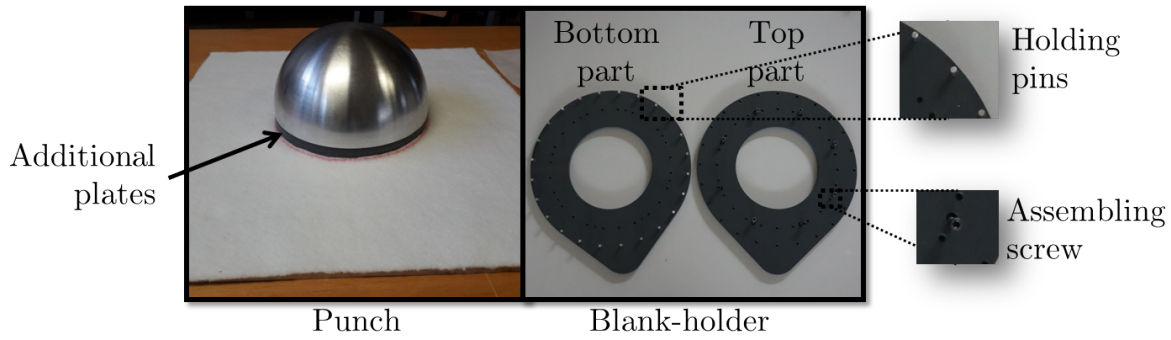

Figure 3.6: Forming device for the hemisphere forming

3.2.2 Forming simulation

3.2.2.1 Finite element model

General settings

Model II (without backing material) is used for this forming study because the backing material would have to undergo a very large deformation to allow the realignment of the tows along the targeted orientations. The material parameters of the beam elements are given in Table 3.1. Due to the low fibre density, the resistance to rotation between crossing beams of the meridian and parallel layers was neglected. Since only qualitative analysis have been carried out experimentally, the choice of material parameters is supposed to have a minor impact on the observed kinematics. If quantitative measurements were achieved, the punch force would strongly depends on the material parameters for instance. Since fibre tows are quasi-inextensible, a

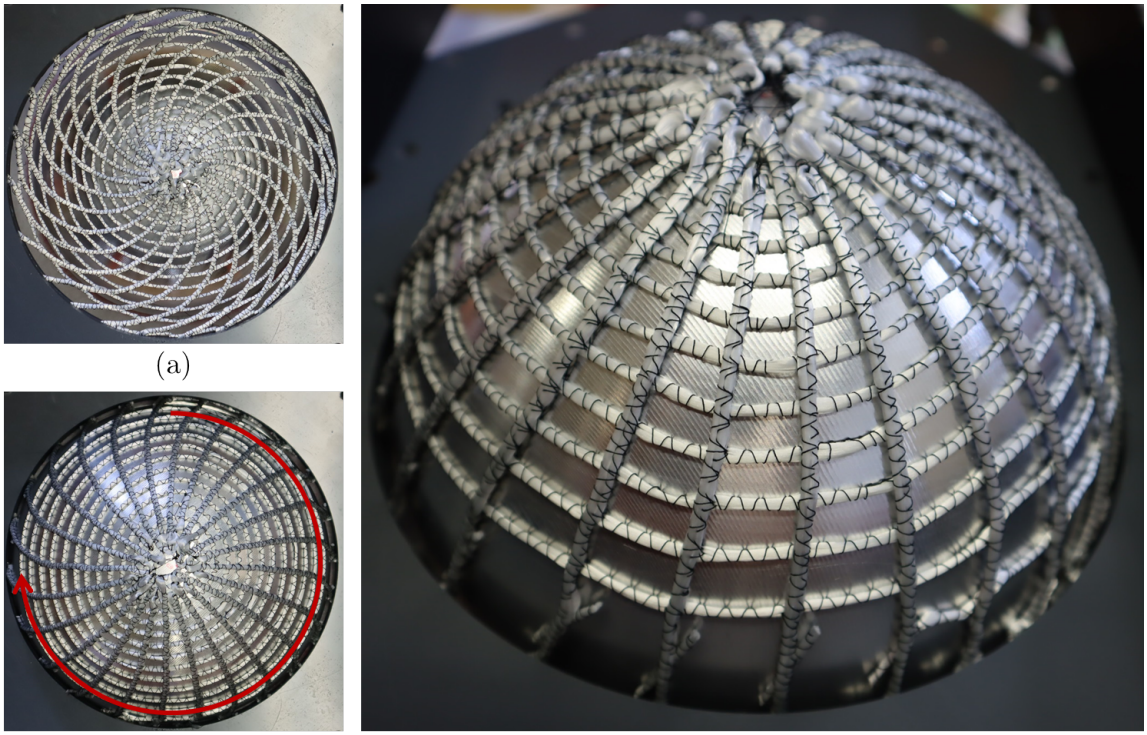

Figure 3.7: Forming of a TFP preform on a hemisphere: (a) initial configuration and (b) final configuration (from top view), (c) final configuration from side view

negligible longitudinal deformation of the beam elements in the simulation will demonstrate the model consistency. The friction coefficient between the punch and the preform was set to 0.2. The simulation time period is 100 s meaning that the punch has a velocity of 1 mm/s. This velocity allows to respect the quasi-static condition which imposes a low kinetic energy compared to the internal one. In the meanwhile, this velocity minimizes the required time for the simulation to run. A time step of 10^{-4} s is used to ensure the convergence of the contact algorithm with a minimal number of iterations.

Mesh and boundary conditions

The beam elements have an approximate size of 2.5 mm. The parallel and meridian layers are meshed independently. Next, the intersections between the beam elements of the two layers are computed. Nodes are added at these intersections in the meridian layer that is embedded in the parallel layer. Adjacent nodes to the newly added ones, which are closer than half the initial element length, are removed to obtain a better mesh quality. Fig. 3.8 shows the mesh of the TFP preform. The blue nodes represent the parallel layer while the green ones correspond to the meridian layer. The red nodes are the meridian layer's nodes that are embedded in the parallel layer. The extensions of the meridian layer present in the TFP preform of the experimental work are not represented. The clamping system is simplified in the simulation by fixing the yellow nodes (ends of meridian fibre tows) to avoid representing the blank-holders. The parallel layer is made of 3127 nodes and the meridian layer contains 1650 nodes.

3.2.2.2 Results and comparison with experimental forming

The simulation runs in approximately 1 hour using four cores of an Intel(R) Core(TM) i7-8750H CPU 2.20GHz processor. Fig. 3.9 shows the experimental and simulation results side by side.

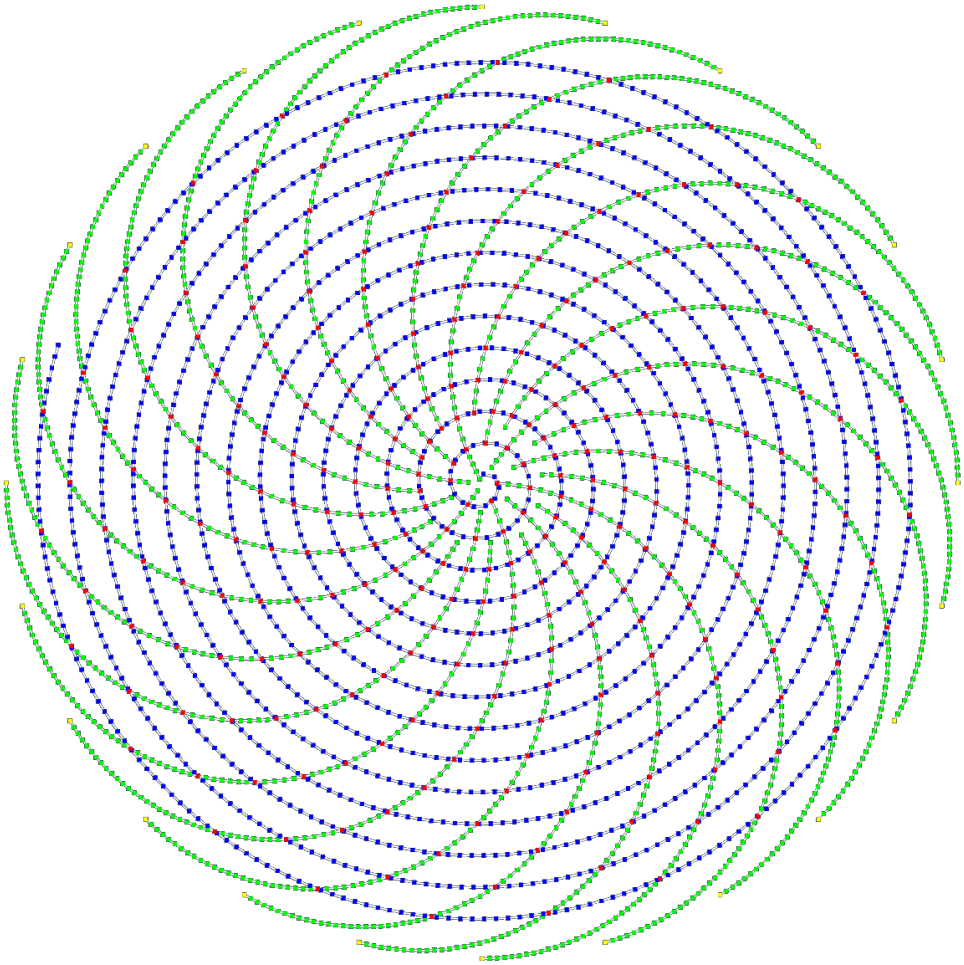

Figure 3.8: Mesh of the TFP preform for the hemispheric shape forming

The simulation result matches the experimental one. Both results show some discrepancies from the targeted orientations but are very encouraging. The longitudinal deformation of the beam elements E is lower than 10^{-3}. Therefore, the kinematics of forming is consistent with the quasi-inextensibility of the fibre tows and validates the flat TFP preform design.

Fig. 3.10 shows different configurations of the TFP preform during the forming simulation from top and side views. The clockwise rotation of the TFP preform as observed experimentally can be noticed. This specific kinematics was observed by Sholl et al. (2021). They embedded cotton fibres in a thin elastomer membrane to reinforce and control the deformation of soft-bodies.

3.2.2.3 Discussion on the orthotropic hemispheric part forming validation

The experimental and simulation results are in a good agreement and close to the targeted fibre orientations. The forming of a hemispheric part is a basic test case for biaxial conventional textiles where the fibre orientations are initially orthotropic. However, this study goes beyond the validation of the numerical model by demonstrating the ability of 2-layer TFP preforms to form an orthotropic final part. Therefore, these results are as important for the validation of the numerical model and for highlighting the strength of TFP preform forming.

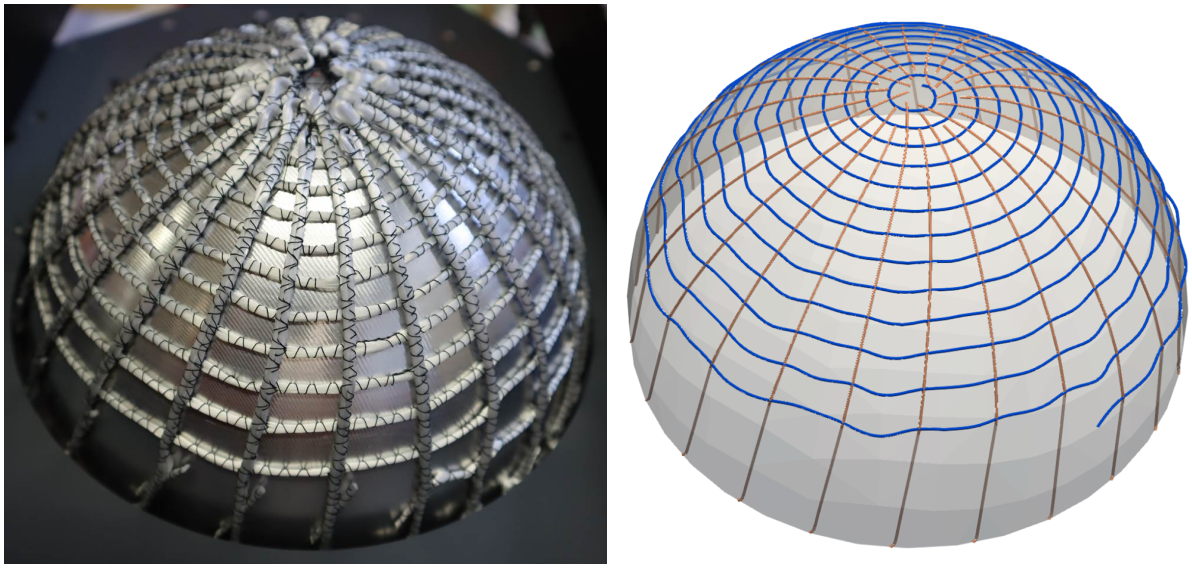

(a) Experimental **(b)** Simulation

Figure 3.9: Qualitative comparison of the experimental and simulation results for the hemispheric shape forming

Since the numerical model does not take into account lateral contact between adjacent fibre tows, the fibre tows density was chosen accordingly. Obviously, the fibre tow density can be increased and beam contact interactions could be incorporated in the numerical model if needed. Carrying out quantitative measurements in this experimental work would be a possible improvement. However, this shape was used only as a first basic test case to observe the feasibility of complex TFP preform design's forming.

Conclusion

This section showed a first example of how the hybridisation of the TFP technology and forming can be used to form orthotropic parts. The forming on a hemispherical shape demonstrated the ability of 2-layer TFP preforms to be formed on a simple part with double curvature. The axial symmetry and constant Gaussian curvature of this shape made it a basic test case in conventional textiles forming. However, using a specific TFP preform design made it even more attractive to investigate the realignment of initially in-plane curved fibre tows. Even if the results do not exactly match the targeted orientations, they are very close. Improvement of the preform design to take into account the discrepancies introduced by the TFP preform manufacturing process might give the expected result. Nevertheless, the numerical model gave result in agreement with the experimental ones.

Further full-scale validations are required to confirm these observations. That is why the next section, which follows the same structure as this one, focuses on another shape which has a direct industrial application. Moreover, additional efforts were undertaken to conduct quantitative measurements of the experimental forming.

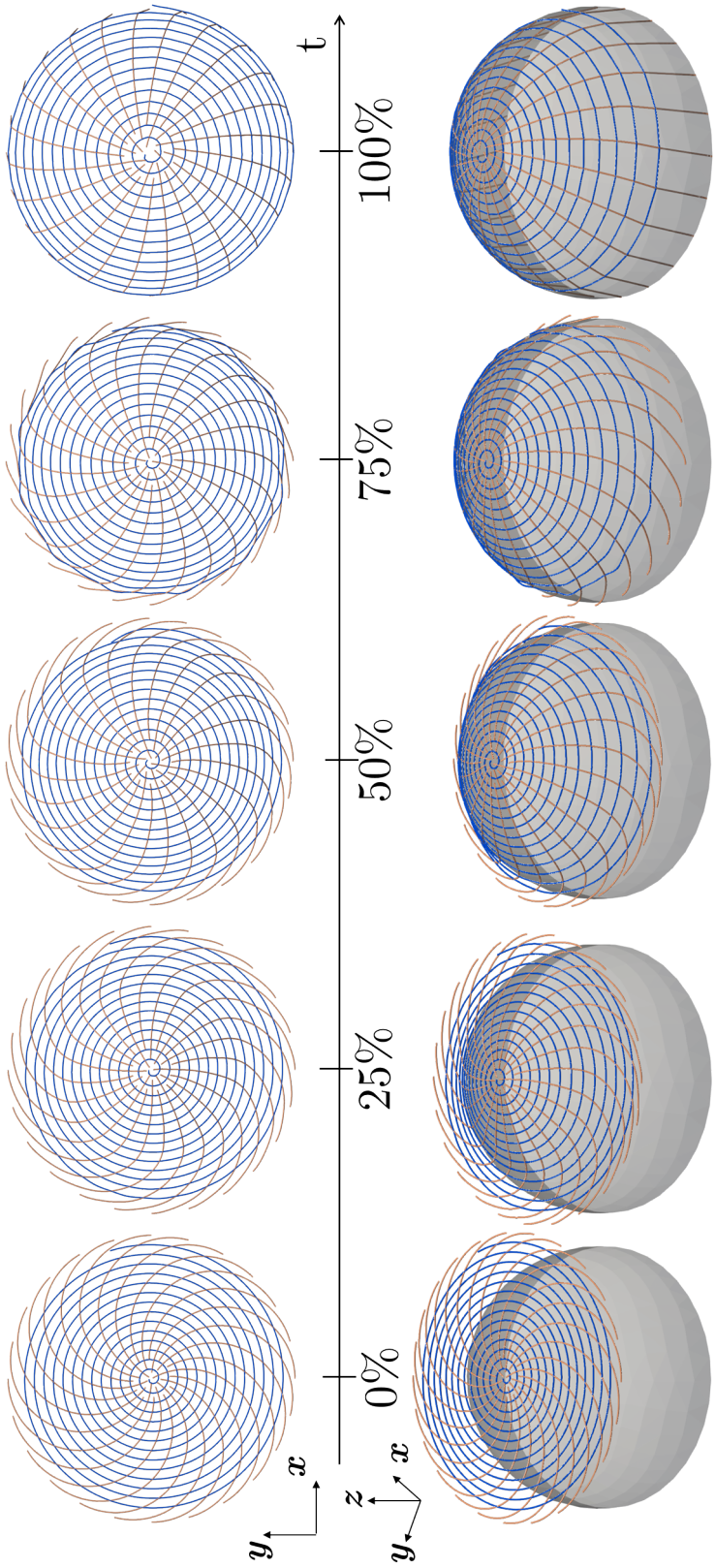

Figure 3.10: Successive configurations of the TFP preform during the hemispheric shape forming simulation: top (top) and side views (bottom)

3.3 TFP preform forming on a tetrahedral shape with orthotropic final orientations

Introduction

This section deals with the dry forming of a tetrahedral part from a flat TFP preform without backing material. The forming on a tetrahedral shape of TFP preforms aims at demonstrating the ability to obtain final orthotropic orientations in the whole part without defect using a simple forming set-up. The 2D displacement field (orthogonal to the punch displacement) and the final angles between the layers on one face of the formed part have been measured for quantitative analysis of the results. This section begins with the determination of the TFP preform design allowing obtaining orthotropic final orientations and the presentation of the forming setup. Methods for quantitative analysis are described before explaining and discussing the experimental results. Finally, the finite element model is presented before showing the simulation's results and compare them with the experimental ones.

3.3.1 Experimental forming

3.3.1.1 TFP preform design

Fig 3.11 shows an example of structural part having a triple vertex and the desired orthotropic fibre orientations. Some fibres are parallel to the corner's edges while other are orthogonal to them. As shown in Fig 3.12 (a), the angle between the edges of a face of the tetrahedral shape is equal to 90°. Their projection in the plane, whose normal is parallel to the tetrahedral shape axis, yields the angle of 120° (Fig 3.12 (b)). Consequently, placing fibres parallel to the edges for each face leads to a TFP pattern shown in Fig 3.12 (c) whose fibre orientation will have to rotate by 30° during forming. Fig 3.12 (d) and (e) illustrate a possible combination of two layers to obtain the flat pattern depicted in Fig 3.12 (c). Therefore, this design should lead to the targeted 3D orientation via the 30° in-plane shear of the flat TFP preform. Layer 1 is obtained from a spiral equation with points placed every 60° to get a hexagonal shape. The number of fibre tows from the center to the outer edge is equal to 50. Layer 2 is built by offsetting the curve linking the edges of a face for each face with 50 fibre tows. In Fig. 3.12 (d) and (e), the number of tows have been divided by a factor of two for the sake of clarity.

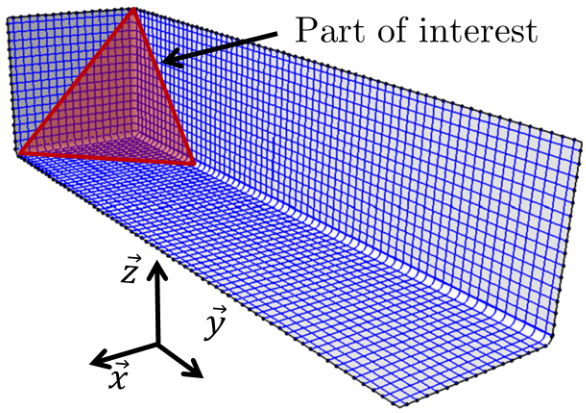

Figure 3.11: Example of orthotropic design for a structural part with a triple point

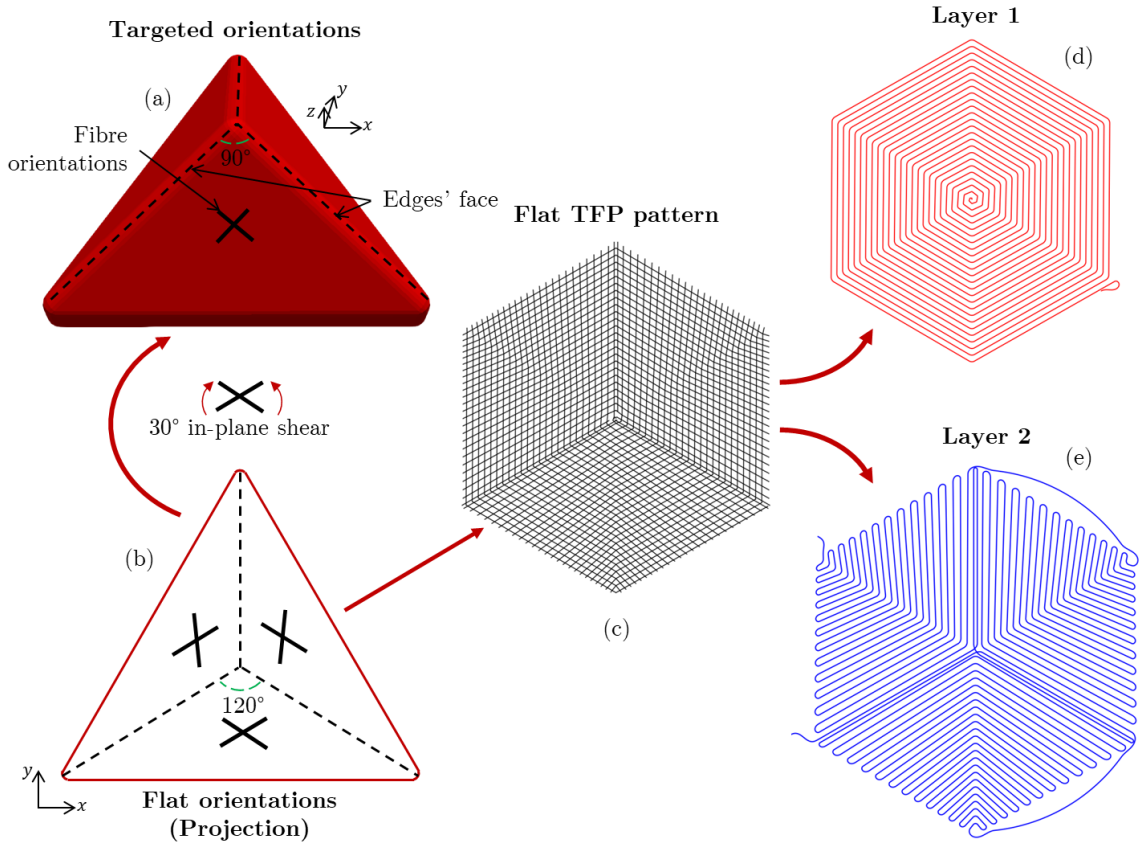

Figure 3.12: Design of the TFP preform for the tetrahedral forming: (a) targeted 3D orientations, (b) projection of the 3D orientations along the axis of the tetahedral shape, (c) flat TFP pattern, (d) first TFP layer and (e) second TFP layer

3.3.1.2 Forming device

The forming device, which is shown in Fig 3.13, is composed of a tetrahedral punch mounted on an universal tensile machine (AG-Xplus by Shimadzu). Two square PMMA plates (550 mm × 550 mm × 10 mm) were used as blank-holder. One plate is fixed on a metallic frame and the other one is laid down directly onto the preform. A pin system constraints the movable plate of the blank-holder in the plane. No external pressure is applied on the movable plate, only its dead weight is distributed on the TFP preform over the contact surface. The punch is composed of a tetrahedral part, 120 mm high with a 20 mm thick base. The punch motion controlled by the tensile machine has a stroke of 140 mm with a velocity of 15 mm/min. The velocity of the punch was chosen according to the capacity of the camera to take a picture every 5 secondes minimum.

3.3.1.3 Optical measurements and post-processing

Quantitative measurements were carried out by post-processing images taken from a single camera positioned along the axis of the punch displacement. Pictures are taken every 2 mm of punch displacement and allows visualizing the 2D displacement field orthogonal to the punch direction. An EOS Canon Mark II camera was used with a constant focal length of 15 mm and initially positioned at 52 mm from the TFP preform. At the end of the experiment, a picture was taken after placing the camera according to the normal of one of the face of the tetrahedral punch. This picture allows measuring the final angles between the two layers on a face.

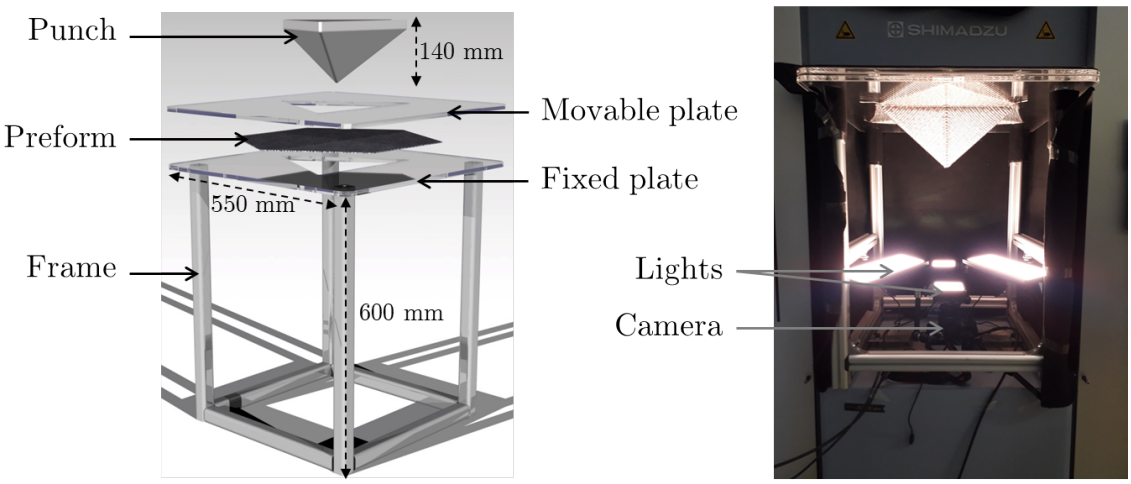

Figure 3.13: Tetrahedral forming device: CAO of the forming device (left) and real setup with lights and a camera (right)

Measurements of the 2D displacement field

The objective is to measure the 2D displacement field of the TFP preform. Measuring the displacement field of preforms during open-die forming has been performed in previous studies on conventional textiles (Lomov et al., 2008). 3D image correlation is a popular technique to measure 3D displacement fields. To measure a 2D displacement field, the marker tacking method is efficient and easy to process. It consists in placing markers on the preform whose detection and identification can be automatized using image post-processing tools. In this experiment, red-ink markers were manually drawn onto the preform as shown in Fig 3.14. Then, a Python script based on an open-source image-processing library OpenCV, was developed to detect and identify the red markers from a frame to another.

Figure 3.14: TFP preform with red ink markers drawn manually

Choice of the tracking method: optical flow algorithm Several methods are available to track markers on successive frames. One of them consists in finding for each marker of the i^{th} frame, the closest marker on the $(i+1)^{th}$ frame. The Euclidean distance is used to identify the markers. This method is efficient and robust when the markers' displacement is small enough between successive frames but implies to detect the markers in each frame. The reader is refereed to Hautefeuille et al. (2019) for an example of application of this method to the measurement of squeeze flow in a woven fabric during consolidation. Another method, which is the one used in this work, consists in computing the optical flow between successive frames.

Definition of optical flow Optical flow is based on the per-pixel motion computation between successive frames. It allows computing the relative displacement of objects in front of a camera. Dense optical flow consists in computing the motion of each pixel while sparse optical flow only track a set of predefined pixels. Therefore, sparse optical flow can be used to track markers.

This method is based on the pixel intensity, which is defined as a function of time t and of the coordinates (x, y) of the pixel in the image: $I(x, y, t)$. The theory of optical flow assumes that intensity changes are negligible between two successive frames. Therefore, the following equation holds:

$$I(x, y, t) = I(x + \delta x, y + \delta y, t + \delta t) \tag{3.5}$$

Using a first order Taylor-series expansion gives:

$$I_x u + I_y v = -I_t \tag{3.6}$$

where $I_x = \frac{\partial I}{\partial x}$, $I_y = \frac{\partial I}{\partial y}$, $I_t = \frac{\partial I}{\partial t}$, $u = \frac{\partial x}{\partial t}$ and $v = \frac{\partial y}{\partial t}$. The two unknowns u and v give the pixel motion and have to be solved.

Sparse optical flow with Lucas-Kanade method u and v cannot be solved from Eq. 3.6 only. Therefore, additional information is necessary to identify the pixel motion. Lucas-Kanade method assumes the local motion constancy, which means that neighbouring pixels have similar motion. Therefore, by applying equation Eq. 3.6 to neighbouring pixels, which have the same motion (same u and v), an over-determined system is obtained which is solved using the least squares method. The advantage of using this method is that the home-made marker detection algorithm is only used on the first frame where the TFP preform is flat. There is no need for developing a robust marker detection algorithm able to detect all the markers in every frame. Therefore, the difficult part of the work is performed with a time-tested and well-implemented method of OpenCV.

Flowchart of the algorithm The post-processing was achieved using a Python script and the open-source image-processing library OpenCV. Fig 3.15 presents the flowchart of the algorithm for computing the 2D displacement field. The initialization of the post-processing consists in identifying the markers on the first image (frame 0). From the identified markers, the pixel located at the center of each marker is stored in the array p_0 which is given as input of a sparse optical flow algorithm and corresponds to the set of pixel to be tracked. For post-visualisation of the result, a mesh is built from the triangulation of p_0. Then, the function "calcOpticalFlowPyrLK" from OpenCV, based on Lucas-Kanade method, is used. The array p_1 represents the position of the pixel p_0 in the i^{th} frame given as second input of the sparse optical flow algorithm. Then, the increment of displacement dU is simply computed as the difference between the previous (p_0) and the new position (p_1). At the end of each iteration, p_1 becomes the new p_0.

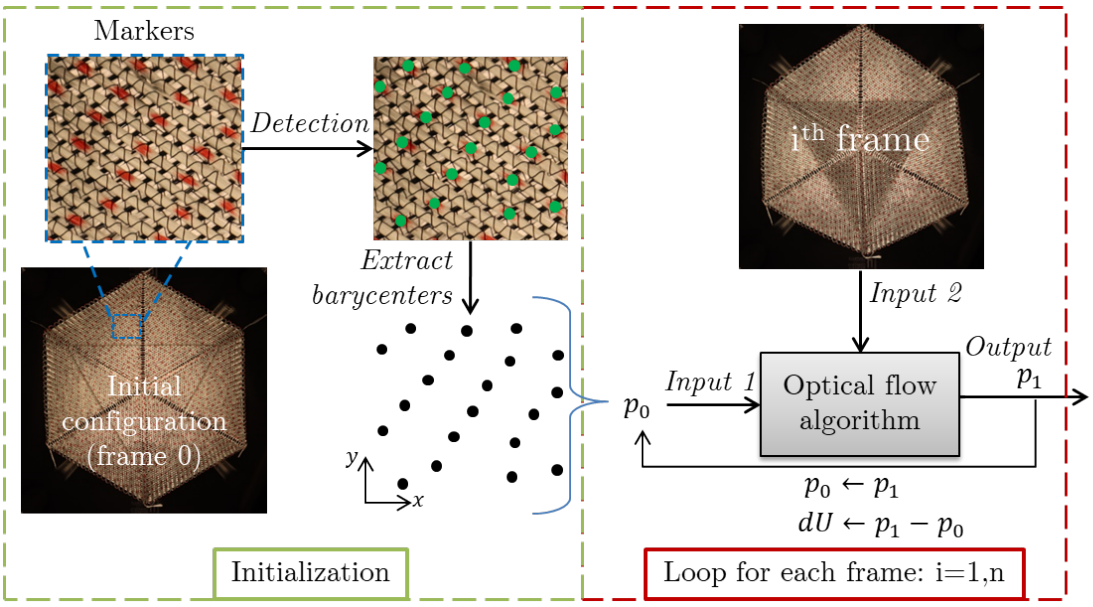

Figure 3.15: Flowchart of the post-processing for the computation of the 2D displacement field

Measurements of inter-layer angles

An image of one face of the tetrahedral shape is taken at the end of the experiment. The camera is positioned such as the face is parallel to the camera. From this image, the fibre tows of the two layers are drawn as polylines in an open-source software named Inkscape as shown in Fig. 3.16. Next, the fibre tows' trajectories are saved as a svg file before being extracted using a Python script. In this script each fibre tows corresponds to a list of points defining a polyline. The script iterates over each fibre tows of a layer, and searches the intersection points with the fibre tows of the other layer. At each intersection point, the tangents of the intersecting fibre tows are computed as well as the angle, which defines the inter-layer angle. Finally, a mesh is generated from a 2D Delaunay triangulation of the intersection points with the inter-layer angles stored at the nodes for visualisation of the inter-layer angle field.

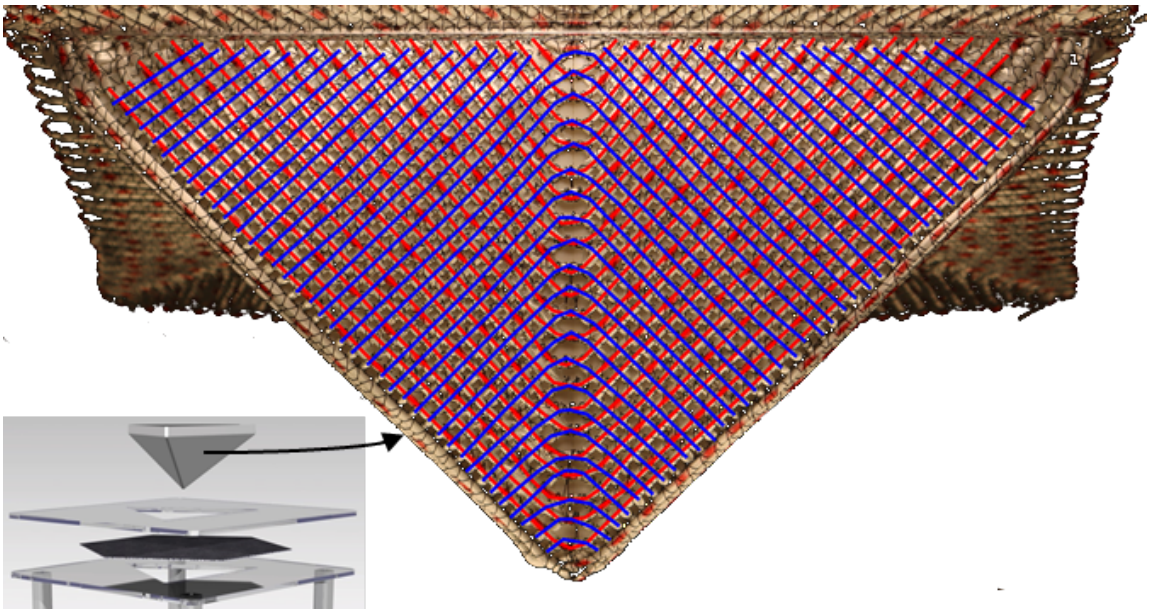

Figure 3.16: Fibre tows drawn in Inskape: first layer (blue), second layer (red)

3.3.1.4 Results

Visual aspects

The final configuration of the TFP preform is shown in Fig 3.17. Neither wrinkle nor major fibre tow slippage were observed in the formed part. The singularity observed in the middle of each face where the angle between layers is 0° can be eliminated by modifying the flat TFP pattern. This possibility has been noticed too late to be taken into account in this work.

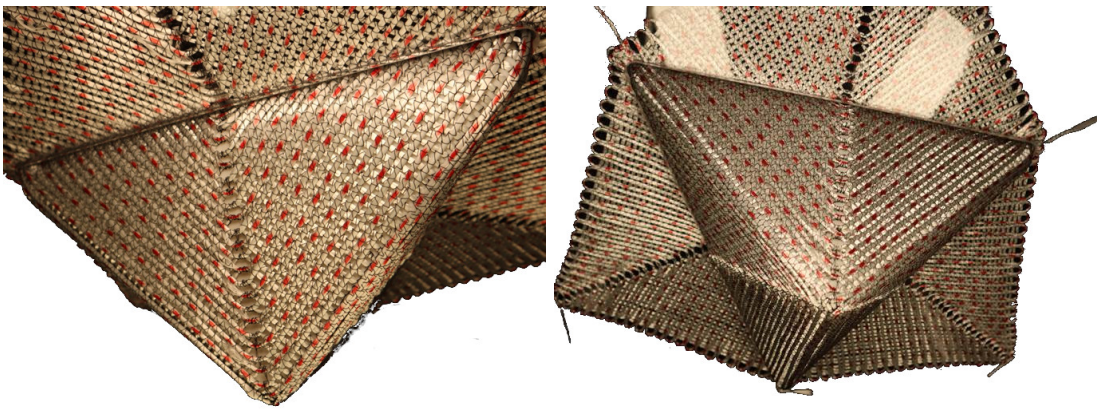

(a) (b)

Figure 3.17: Final configuration of tetrahedral forming

Final angle between layers on a face

The angles between the layers on one face has been computed and are shown in Fig 3.18 (a). Fig 3.18 (b) shows that the distribution of the angles are distributed around 90°. Considering a normal distribution of the angles, a mean angle of 90.72° with a standard deviation of 4.31° is obtained.

2D displacement field

The result of the post-processing of the marker tracking giving the 2D displacement field is shown in Fig. 3.19 (b). The bottom part of the TFP preform slightly left the camera window during the experiment. Consequently, the markers that are not present during the whole experiment were not treated.

Punch force vs displacement curves

The punch force vs displacement is plotted in Fig. 3.20. A strong non-linear behaviour is noticed. The force increases quite slowly until reaching the height of the tetrahedral shape (0 to 120 mm). Then the force increases rapidly due to the contact of the TFP preform with the punch base (120 to 140 mm). The maximal effort required during forming is about 150 N which is quite low. Moreover the movable part of the blank-holder stayed in place, meaning that the self-weight of the plate was sufficient.

3.3.1.5 Discussion

The tetrahedral part was formed without defects using a TFP preform and a minimal blank-holder setup. The design of the TFP preform allows obtaining nearly orthotropic properties where angles are 90.72°±4.31 on the whole part except on the center of each face. However, it has been noticed afterwards that a different deposition strategy can eliminate these defects

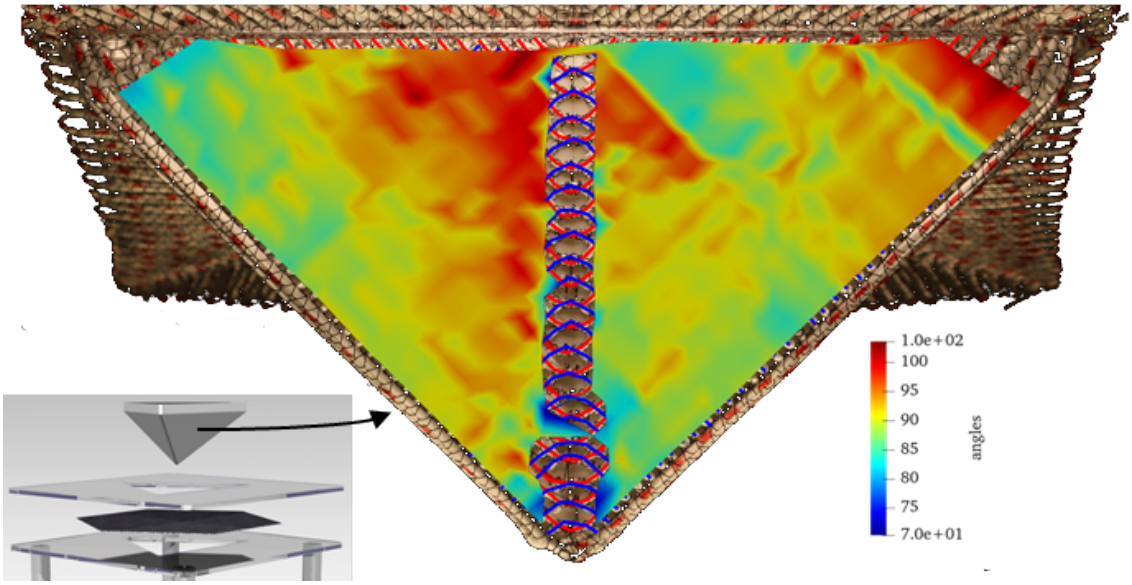

(a)

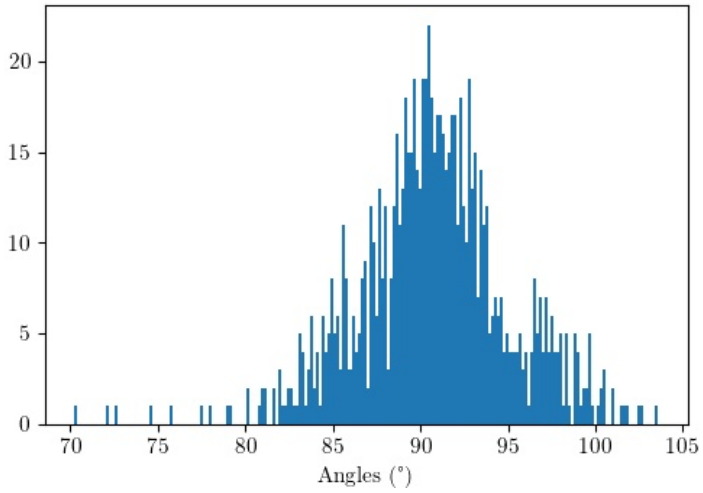

(b)

Figure 3.18: Angles between layers: (a) mesh build from triangulation of intersection points displaying the angles and (b) distribution of the angles

of orientation. Only 30° shear angle is necessary for the TFP preform to accommodate the tetrahedral shape, which is quite low compared to forming of conventional textiles where shear angle can reach 60°. Pressure control blank-holders are required to form this part without defects with conventional textiles. In this study, only a minimal forming set-up is sufficient. For this shape, measuring the 2D displacement field using markers gave satisfactory results. 3D image correlation can be used for more complex parts.

Transition

The experimental results of the tetrahedral shape forming with orthotropic final orientations are unparalleled. Obtaining orthotropic final orientations from flat preforms with this geometry is a real challenge that is impossible to address using conventional textiles. The forming simulation of this shape is presented in the next section.

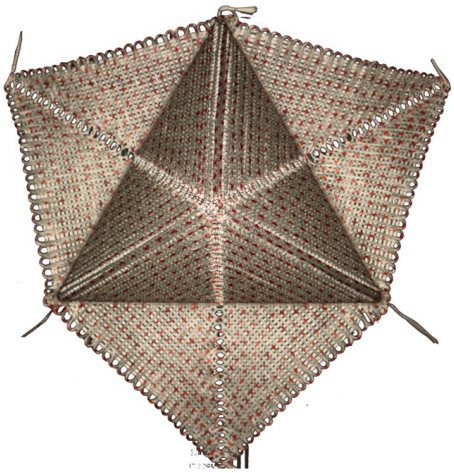

(a) Final configuration of the tetrahedral forming

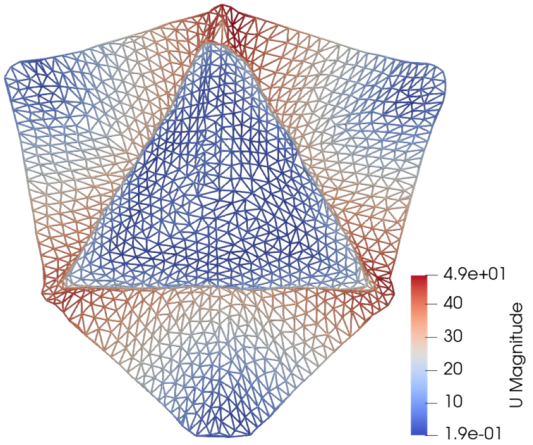

(b) Mesh build from triangulation of the red markers displaying the magnitude of the 2D displacement field (mm)

Figure 3.19

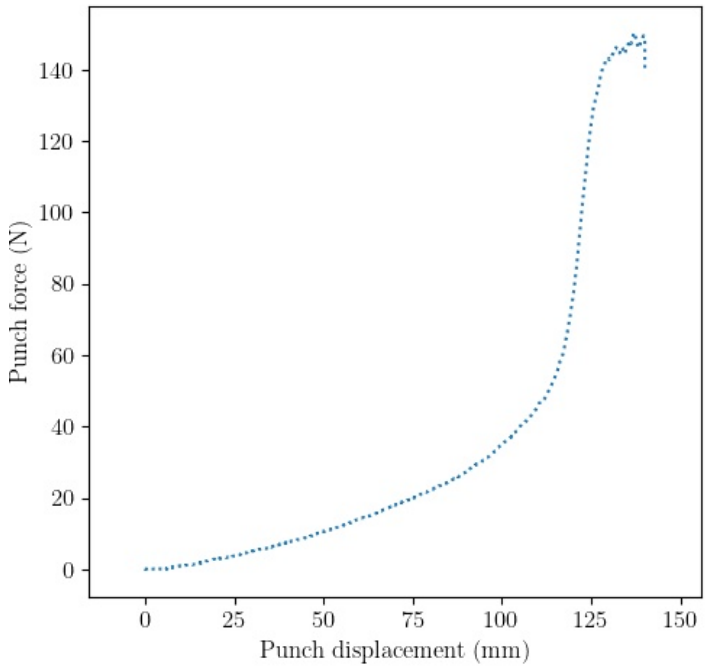

Figure 3.20: Force-displacement curve of the tetrahedral punch

3.3.2 Forming simulation

3.3.2.1 Finite element model

General settings

Model II (without backing material) is also used for this forming simulation because the backing material would have to undergo a large anisotropic shear deformation (around 30°). The material parameters of the beam elements are the same as those of the hemispheric shape forming given in Table 3.1. The stiffness of the torsional springs at intersection between beams of layer

1 and layer 2 equals 1 N/mm. When smaller torsional spring stiffnesses are used, excessive in-plane shear leading to lateral penetration between beams appears. The friction coefficient between the fibre tows and the forming tools is equal to 0.2, even though it might be different since the blank-holders are made of PMMA and the punch of PLA. The simulation time period is 140 s meaning that the punch has a velocity of 1 mm/s. As previously mentionned, this velocity allows to respect the quasi-static condition while it minimizes the required time for the simulation to run. A time step of 10^{-4} s is also used to ensure the convergence of the contact algorithm is a minimal number of iterations.

Mesh and boundary conditions

Layer 1 is first meshed with an element size of 2.5 mm. Then, layer 2 is meshed with the same element size and nodes are appended at intersections with the first layer. These additional nodes are embedded in the corresponding host elements of layer 1. The adjacent nodes of the nodes located at the intersections are deleted if the element size is lower than half the initially prescribed size. The total number of beam elements is 22190. Fig 3.21 shows the TFP preform mesh. A displacement of 140 mm is imposed to the punch. Regarding the blank-holder, the fixed part is clamped and the movable part can only move along the punch axis.

3.3.2.2 Results and comparison with experimental forming

The simulation runs in 12 hours using four cores of an Intel(R) Core(TM) i7-8750H CPU 2.20GHz processor.

Preform contour In Fig. 3.22, the final configuration of the simulation is superimposed on the experimental result. The predicted contour matches well the experimental one. In the TFP path of the simulation, the curved paths connecting the straight ones have been removed for simplicity. It might contribute to the slight differences observed between the contours. Fig. 3.23 shows both simulation and experimental results.

Inter-layer angles Fig. 3.24 shows the final angles between the two layers on a face of the tetrahedral shape. As for the experimental results, the angles are computed at the intersection points of the fibre tows between layers. A 2D mesh is built from a triangulation of these points to displayed a continuous field. The angles are very close to 90° at every position on the face except in the center due to the layer deposition strategy as mentioned in the experimental section.

Finally, Fig. 3.25 shows the configuration of the TFP preform at different times from top and side views. The blue surface corresponds to a 2D mesh built from the triangulation of the meshes' nodes for a better visibility.

3.3.2.3 Discussion on the orthotropic tetrahedral part forming validation

The experimental and simulation results are in very good agreement and close to the targeted fibre orientations. The numerical model (Model II) gives reliable results for this shape, which supports the validity of the proposed modelling strategy. The computation time is acceptable and could be reduced by implementing the given model in highly parallel finite element codes. Even if a better layer deposition strategy is possible to eliminate the singularity at the center of the faces of the tetrahedron, this modification is supposed to have no effect on the overall forming behaviour of the TFP preform.
For this shape and this TFP preform design, the forming kinematics results in an increase of the inter-layer angles from 60° to 90°. Consequently, the distance between adjacent fibre tows

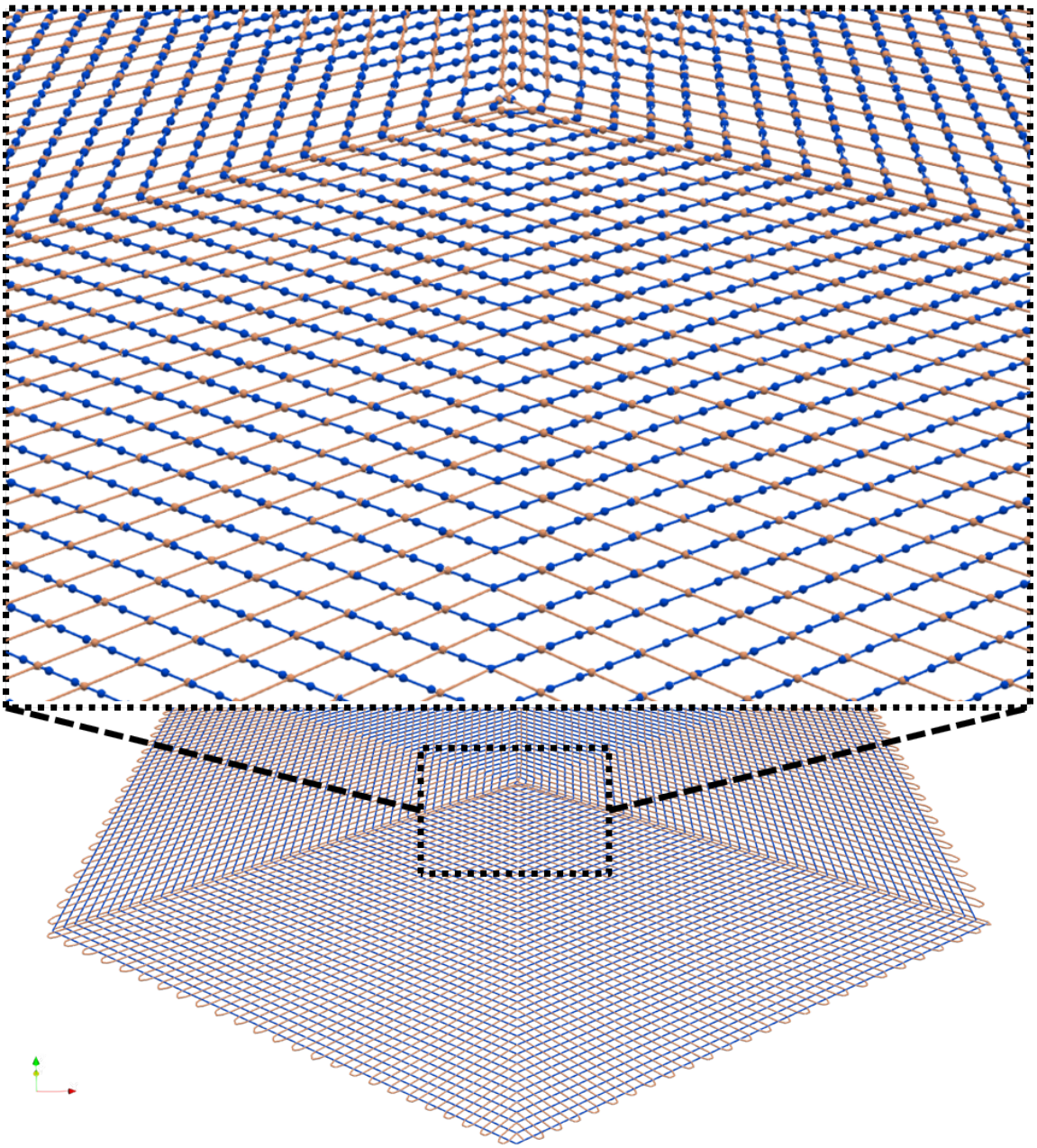

Figure 3.21: Tetrahedral shape forming: Mesh of the TFP preform

within a layer increases during the forming. Therefore, neglecting the lateral contact between fibre tows of a same layer is valid.

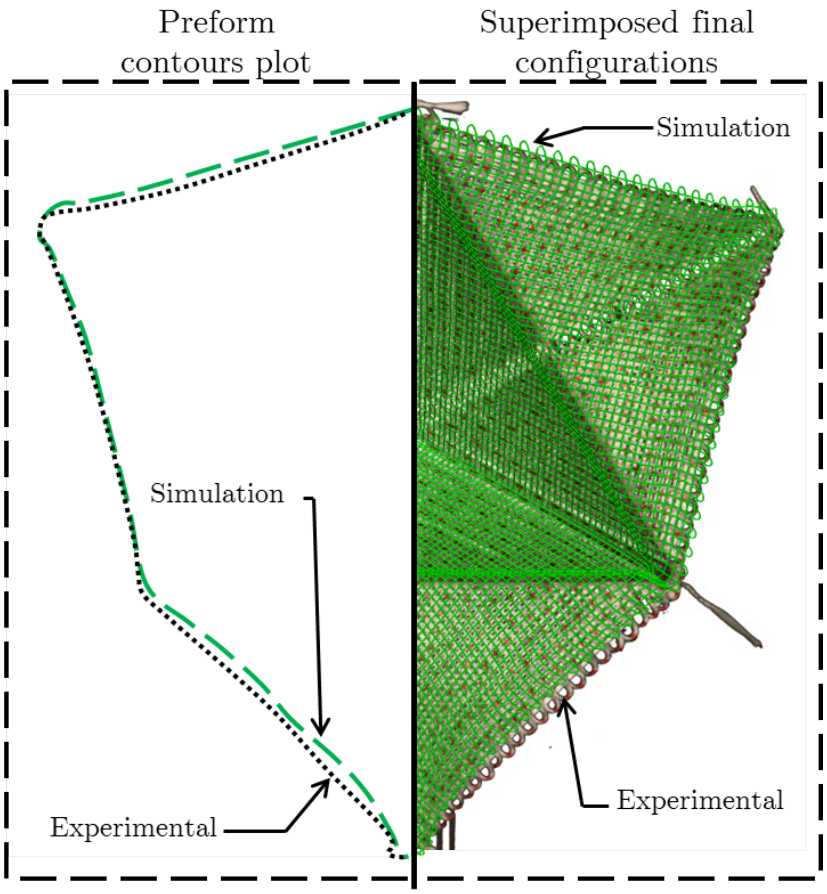

Figure 3.22: Experimental preform contour (dotted line) and simulation (dashed line) (left) and superposition of final configurations of experimental (picture) and simulation (green wireframe mesh) (right)

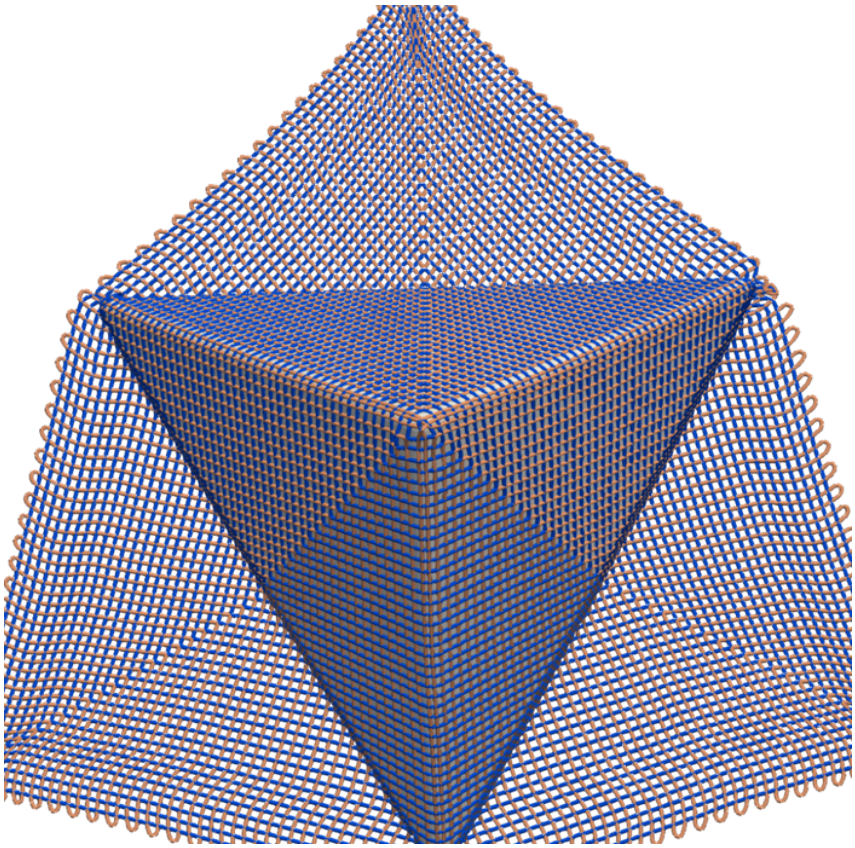

(a) Simulation

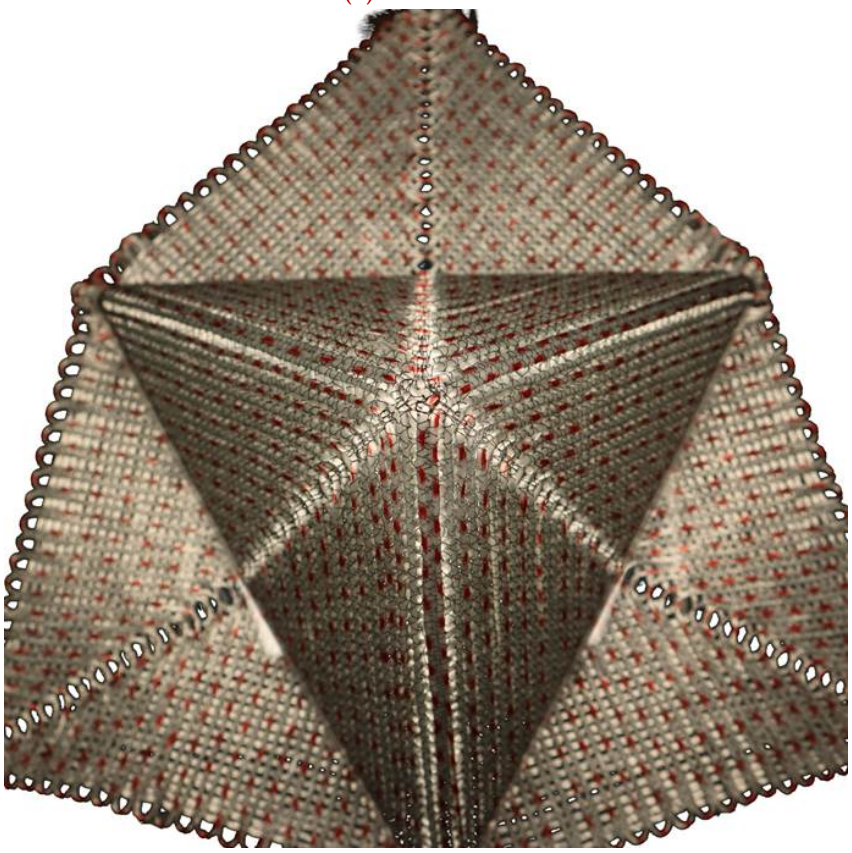

(b) Experimental

Figure 3.23: Qualitative comparison of the results

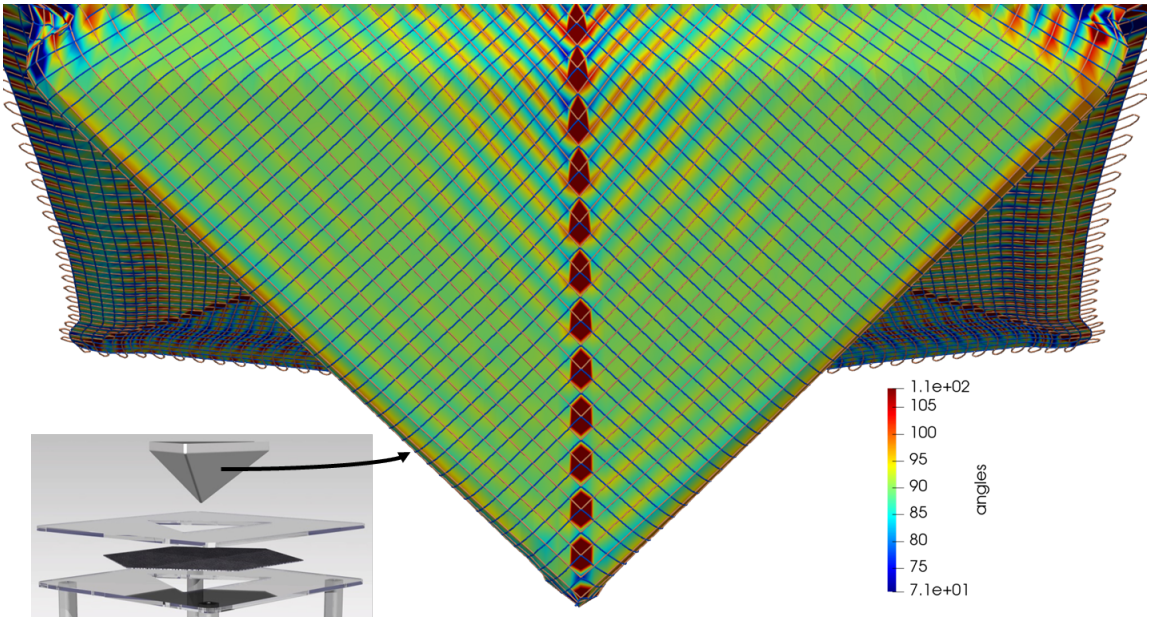

Figure 3.24: Angles between layers: mesh built from triangulation of intersection points and displaying the angles

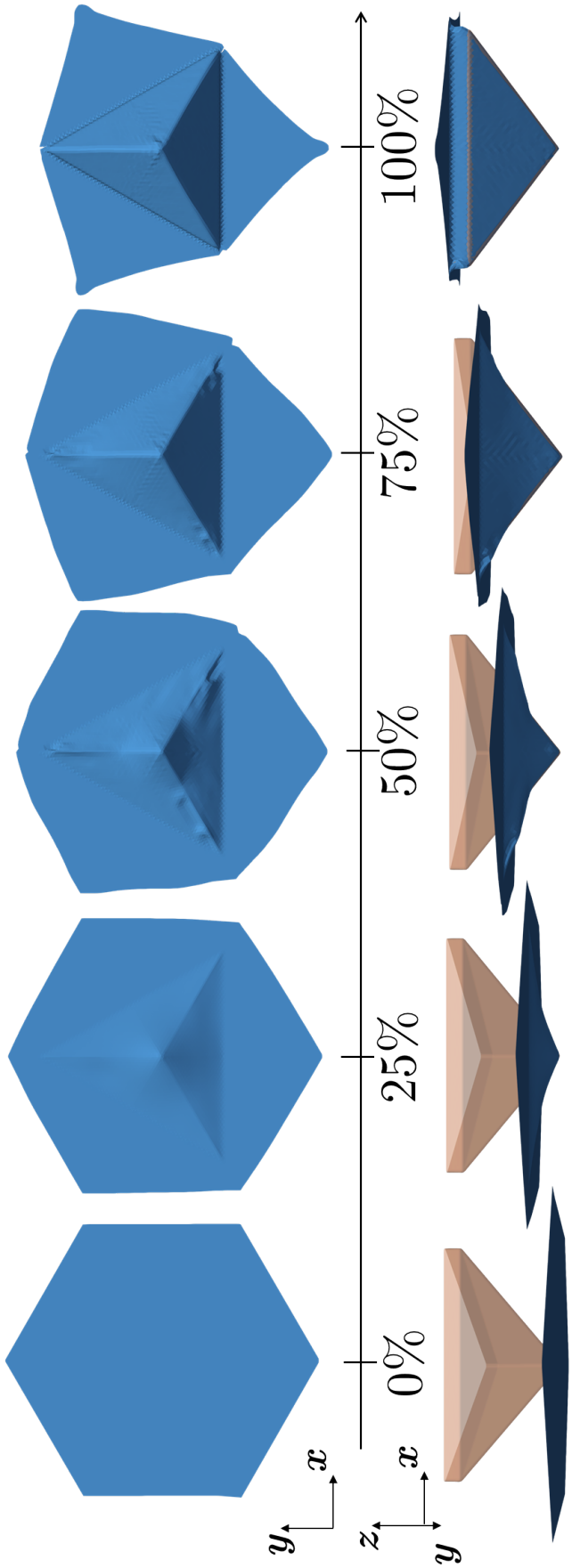

Figure 3.25: Top and side views of the tetrahedral shape forming simulation at different instants

Conclusion

This section addressed a second example of TFP preform forming. Quantitative measurements were undertaken to analyse the experimental results. The optical measurements, namely, the 2D displacement fields and the inter-layer angles on a face of the shape, allowed to compare the simulation results with the experimental ones. The comparison validates the accuracy of Model I to simulate the forming of TFP preform without backing material. As the case of the hemisphere, this study goes beyond the validation of the numerical model (Model II) by evidencing the ability of 2-layer TFP preforms to form a challenging orthotropic final part. Therefore, these results are as important for the validation of the numerical model as for highlighting the potential of TFP preform forming. While the forming of a hemispheric part is generally viewed as a basic test case, the tetrahedral part has a direct industrial application. Therefore, forming such a part without defects, using a minimalist blank-holder set-up and with orthotropic final configuration represents important progress in the field of fibrous reinforcement forming.

Due to the difficulty in finding a suitable backing material which has to be tolerant to stitching, able to overcome large deformation and be valuable in the final part, this study validates Model II only. In the next section, the use of Model I to model locally TFP-reinforced convention textiles is investigating by simulating a bias extension test on a woven fabric with a central hole.

3.4 Discussion on the proposed models and perspectives

Introduction

This last section discusses the validity of the proposed strategies. First, to complete the previous study focused on Model II, the application of Model I to model TFP-reinforced conventional textile is addressed though the simulation of a specific bias extension test. Next, the advantages of the proposed modelling strategy are highlighted before listing the missing features. Finally, one of the possible improvements is chosen and will be developed in the last chapter.

3.4.1 Using Model I to model locally TFP-reinforced conventional textiles

The previous sections focused on the application of the TFP technology to design and manufacture flat preforms to be formed on highly double-curved shapes with orthotropic final orientations. In this previous study, the TFP technology was considered as a whole preforming tool and Model II was shown to be suitable to model TFP preforms without backing material. The next step is to investigate the use of Model I to model conventional textiles reinforced with continuous tows deposited using TFP. This work is based on numerical simulations only.

3.4.1.1 Local reinforcement of conventional textiles

Due to the intrinsic unidirectional orientation of layers, drilling operations used to create holes in composite laminates made of conventional textiles result in stress concentrations around these singularities. As shown in section 1.4.2, TFP is particularly attractive to remove stress concentration around geometric singularities in 2D laminates. Notched laminate plates can be manufacture entirely by TFP or TFP can be associated with another conventional textile to save manufacturing time and benefit from well-approved composite materials. However, in case of the manufacturing of 3D shell-like composite structures using forming, high deformation of

the conventional textile is necessary to accommodate complex geometries. As mentioned in section 1.2.1, biaxial textiles such as woven fabrics mainly deform via in-plane shearing due to the inextensibility of fibres. Adding continuous and curvilinear fibre tows on biaxial textiles using TFP might affect their initial behaviour and potentially create defects. Therefore, Model I can be of interest to predict the effect of the local TFP reinforcement over the forming behaviour of the reinforced preform.

3.4.1.2 Simulation of a bias extension test on a TFP-reinforced conventional textile with a central hole

Choice of the simulation test To study the effect of adding TFP reinforcement on another conventional textile, the simulation of a bias extension test has been preferred over a forming simulation. This choice is justified by the fact that the bias extension test is a well-defined method to characterize the in-plane shear behaviour of conventional textiles as described in section 1.2.3. Therefore, this test will show the modification of the in-plane shear behaviour of the conventional textile due to the TFP reinforcement. To this end, a rectangular sample with a hole at its center is considered. A continuous fibre tows is deposited on the circumference of the hole. The initial configuration is illustrated in Fig.3.26.

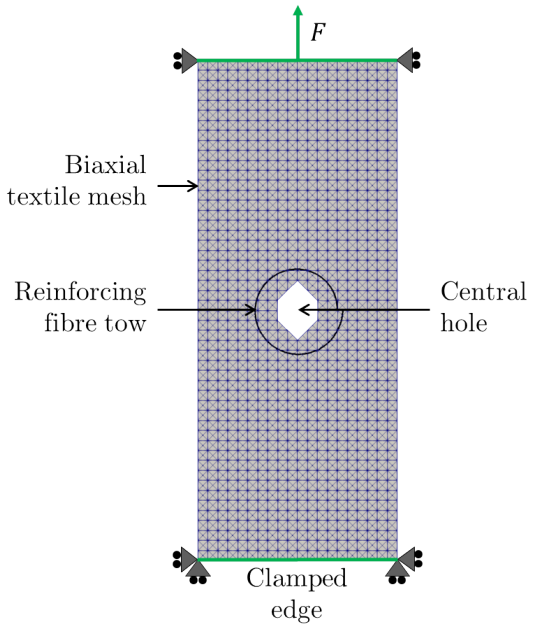

Figure 3.26: Initial configuration of the bias extension test sample with a centred hole and an additional continuous fibre tows

Conventional textile model Modelling the behaviour of conventional textiles is an area of work as evidenced in section 1.2.2. To avoid developing or implementing a new mechanical behaviour in the finite element solver, the finite element developed by Hamila et al. (2009), which allows modelling biaxial fabrics and that is already available in the code, is used. The 3-node semi-discrete element is based on the description of an unit cell. The internal virtual work δW_{int} is defined as the sum of the independent contributions of the tensile δW_t, in-plane shear δW_s and bending δW_b behaviours:

$$\delta W_{int} = \delta W_t + \delta W_s + \delta W_b \tag{3.7}$$

Table 3.2: Material parameters for the model by Guzman-Maldonado et al. (2019)

Material parameters	Tension		In-plane shear moment		
	C_1	C_2	K_1	K_2	K_3
Value	1000	1000	0.37697	-0.41628	2.42827
Unit	N/yarn	N/yarn	N.mm	N.mm	N.mm

The tensile and bending behaviour are assumed linear:

$$T_{ii} = C_i \epsilon_{ii} \tag{3.8}$$

$$M_{ii} = B_i \chi_{ii} \tag{3.9}$$

where T_{ii} and ϵ_{ii} are respectively the tensile stiffness and the longitudinal strain in the i^{th} fibre direction. M_{ii} and χ_{ii} are respectively the bending moment and the curvature in the i^{th} fibre direction.

The in-plane shear moment is non-linear and modelled using a five order polynomial law:

$$M_\gamma = K_1\gamma + K_2\gamma^3 + K_3\gamma^5 \tag{3.10}$$

where γ is the shear angle.

For simplicity the out-of-plane bending rigidity is neglected in the simulation of the bias-extension test.

The material parameters required in the biaxial textile model are those given in Guzman-Maldonado et al. (2019) for a plain weave reinforcement and shown in Table 3.2.

Simulation without hole and without reinforcement First, simulations without hole and with hole but without reinforcement are performed. The shear angle field in the final configurations is shown in Fig. 3.27. As expected, three zones of constant shear are present. When comparing the simulations, the effect of the hole on the shear angle seems negligible.

Simulation with reinforcement A simulation is performed with an additional fibre tow deposited along the circumference of the hole. Model I is used for the simulation. To simplify the analysis of the simulation, the fibre tow is modelled with a 1D linear elastic truss rather than the beam element presented in section 2.2. This simplification allows focusing on the effect of the quasi-inextensibility of the additional fibre tow without considering its bending behaviour which is negligible and essentially required to model wrinkles. The tensile stiffness of the truss elements has the same value than those used in the previous simulation for the beam element ($C_E = 1.423\ 10^7\ N$). The result is shown in Fig. 3.28. The shear angle field is highly affected by the presence of the reinforcing fibre tow. Due to its quasi-inextensibility and the assumption of non-slip between the conventional textile and the fibre tow, a third fibre direction is added that locks the shear deformation of the conventional textile around the reinforcement. If real, this very stiff behaviour might compromise the formability of the TFP-reinforced conventional textile by introducing defects such as wrinkles. On one hand, if this simulation is unrealistic, it would mean that the no-slip assumption which assumes the stitching yarn to act as a hinge connection is incorrect. On the other hand, if this very stiff behaviour is real, then it would be necessary to allow for slippage by choosing appropriate stitching parameters. In both cases, fibre tow slippage is required.

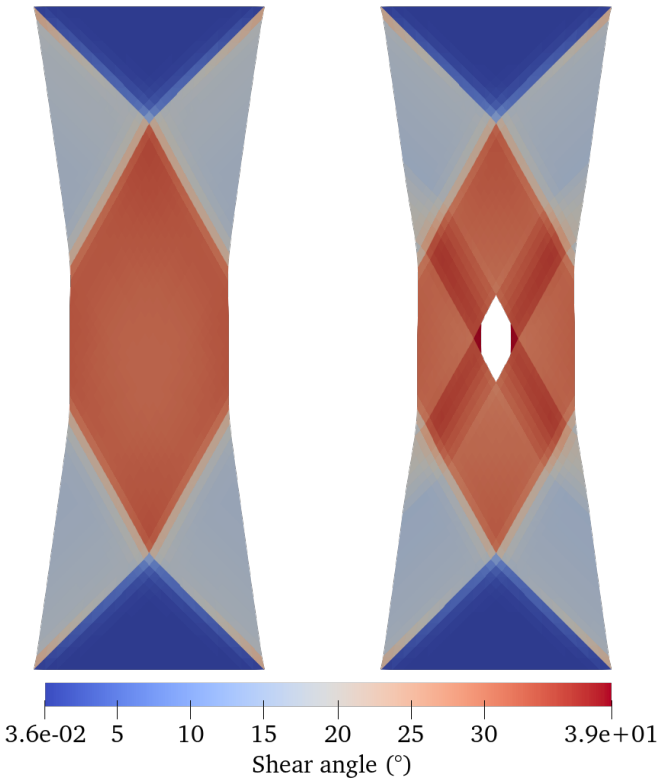

Figure 3.27: Final configurations of the bias extension test sample without (left) and with (right) hole

3.4.1.3 Discussion on Model I

In the previous sections of this chapter, the two forming cases were carried out successfully and the assumption of no-slip between the fibre tows of adjacent layers was verified experimentally. In case of Model I, the simulation of the reinforcement of the hole in a biaxial textile using TFP shows a very stiff behaviour. As mentioned in section 1.4.2.3, Fial et al. (2018) showed that the stitching parameters can be adjusted to allow slippage between the fibre tows and the backing material. Since no-slip can lead to a very stiff behaviour, the formability of TFP-reinforced conventional textile would benefit from allowing slippage.

3.4.2 Advantages of the proposed modelling strategy

3.4.2.1 Two models for two applications

This work considers two applications of the TFP technology, namely, its use as a preforming tool or as a mean to locally reinforce another conventional textile. The TFP preform models proposed herein have been developed to take into account the aforementioned versatility of the TFP technology.

Model II can be used to model the forming of 2-layer TFP preforms without backing material on doubly-curved shapes. It was demonstrated that this model helps the mechanical designer in finding the appropriate flat TFP pattern to obtain the desired final orientations. In particular, Model II was used to evidence the ability of forming orthotropic parts using a specific design of the flat TFP preforms. Forming experiments on hemispheric and tetrahedral shapes validated Model II.

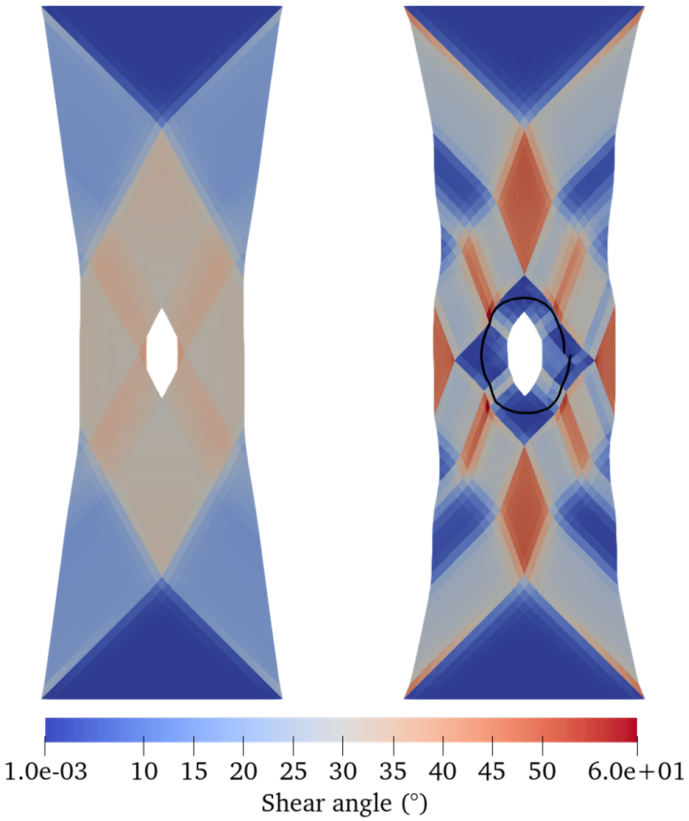

Figure 3.28: Final configurations of the bias extension test sample with (right) and without (left) reinforcement

Model I can be used to model TFP-reinforced conventional textiles. However, as mentioned previously, the no-slip assumption leads to a very stiff behaviour which is either unreal or not desired. Moreover, experimental work would be required to confirm the observed behaviour.

3.4.2.2 A common basis based on a natural description

Even if two distinct models have been developed, the proposed modelling strategy offers a common basis to both models. First, the fibre tows are modelled explicitly using beam elements. Secondly, the stitching yarn is modelled implicitly using the embedded element approach. This approach aims at tracking the fibre orientations while the modelling of other features such as the stitching yarn are simplified. In particular, it simplifies the frictional contact interactions between the constituents of the TFP preform. Moreover, this is a natural and direct approach to take into account all the capabilities of the TFP technology.

3.4.2.3 Simplified characterisation procedures

The semi-discrete models split the behaviour of the TFP preform constituents into well-defined contributions that can be characterized separately. This work did not address the experimental characterisation procedures. However, the material parameters required in the model can be identified from the characterisation of the TFP preform constituents alone, which considerably simplified the procedure. For example, the tensile stiffness of the beam element can be identified from a tensile test of a fibre tow while its bending properties can be measured using the cantilever beam method. The characterisation of the backing material will depend on the 2D finite element formulation used. Test at the preform scale, such as the bias extension test, can be used to determine the stiffness of the linear elastic torsional spring.

3.4.3 Possible improvement of the models

3.4.3.1 Interaction between adjacent fibre tows

In both models, the contacts between the fibre tows within a layer have been neglected. For conventional textiles, the existence of a unit cell in the fibrous reinforcement allows taking into account the lateral compaction of fibre tows in the constitutive law as in the previously used model by Hamila et al. (2009). In the forming experiments, the fibre tows density was chosen such as this interaction does not occur. However, for higher fibre density TFP preforms and for different TFP preform designs, the modelling of this contribution can be required. Frictional contact between adjacent beam elements can be explicitly added in the models.

3.4.3.2 Beam element with deformable cross-section

The beam element assumes no-warping and no transverse deformation of the cross-section. Instead, a beam element based on a 3D constitutive law could be used for a better description of the deformation of the fibre tows.

3.4.3.3 Non-linear torsional spring

The stitching yarn is implicitly model as a hinge connection. For the sake of simplicity, the resistance to rotation of crossing fibre tows is taken into account using a linear elastic torsional spring. This resistance is due to the friction between crossing fibre tows as well as the longitudinal deformation of the stitching yarn. Therefore, using a non-linear torsional spring would better reflect these complex underlying interactions. Carrying out bias extension test on TFP-made samples would provide information about the real behaviour.

3.4.3.4 Fibre tow slippage

One of the most important improvement of the modelling strategy is the modelling of fibre tow slippage. As shown in the previous section, the stiff behaviour of Model I would considerably benefit from the fibre tow slippage. Even if fibre tow slippage was not observed in the forming experiments based on Model II, taking it into account in the current models without changing their initial features is a desirable improvement. In particular, conserving the embedded element approach while modelling slippage would be an important enhancement since it would not require to model the contact interactions explicitly. Moreover, as in Fial et al. (2018), taking advantage of the fibre tow slippage, which is considered as a defect in conventional textile, to improve the formability of preforms reinforced with TFP would be very attractive.

Conclusion

This last section started by giving an insight into the application of Model I. From simulations of a bias extension test, it appears that the continuous tow reinforcing a conventional textile leads to a very stiff behaviour that is neither realistic nor desired. In both cases, it seems necessary to relax the non-slip assumption in the model. Next, the advantages of the proposed modelling strategy were highlighted as well as possible improvements. Among the latter, including fibre tow slippage in the models would represent a major step towards turning a defect in conventional textiles into an advantage in TFP preforms.

Chapter conclusion

This chapter presented the experimental work on forming 2-layer TFP preforms without backing material. Forming experiments on hemispheric and tetrahedral shapes were carried out and demonstrated the ability of 2-layer TFP preforms to be formed on doubly curved parts. Moreover, for this particular shapes, this work investigated the determination of the flat TFP design leading to orthotropic fibre orientations in the final part. While the hemispheric shape was used as a basic test case, the tetrahedral shape has a direct industrial application as it corresponds to corner bracket. In this sense, additional effort were undertaken to measure quantitative data as a 2D displacement field and the final inter-layer angles on one face of the tetrahedron. In both cases, the results are close to the targeted orientations. These forming experiments were used as validation test cases of Model II. The simulation results are in agreement with the experimental ones for both shapes. It should be noticed that the simulations were performed prior to the experimental forming, as if the numerical tool was used by a mechanical designer. To improve the analysis of the hemispherical forming results, the optical methods used for the tetrahedron could be applied. In particular, this would allow the rotation of the fibre tows around the hemisphere axis to be measured. Concerning the shapes studied, they allowed analytical flattening of the targeted 3D orientations. For more complex shapes, developing a numerical flattening tool might be required. As mentioned in section 1.4.3.2, the development of a numerical forming tool for TFP preforms was seen as a first step in the development of the full numerical chain of design and manufacturing processes.

The validity of Model I, which is used to model TFP-reinforced conventional textile, was only addressed via simulations of a bias extension test. The very stiff behaviour due to the non-slip assumption compromises the formability of these preforms. Consequently, allowing and controlling fibre tow slippage is a major step to improve Model I. Even if fibre tow slippage was not experimentally observed in case of Model II, adding this feature in both models would be beneficial. Including fibre tow slippage in the models without modifying their initial features is the challenge addressed in the next chapter.

Bibliography

Allaoui, S., Boisse, P., Chatel, S., Hamila, N., Hivet, G., Soulat, D., and Vidal-Salle, E. (2011). Experimental and numerical analyses of textile reinforcement forming of a tetrahedral shape. *Composites Part A: Applied Science and Manufacturing*, 42(6):612–622.

Allaoui, S., Hivet, G., Soulat, D., Wendling, A., Ouagne, P., and Chatel, S. (2014). Experimental preforming of highly double curved shapes with a case corner using an interlock reinforcement. *International Journal of Material Forming*, 7(2):155–165.

Bel, S., Hamila, N., Boisse, P., and Dumont, F. (2012). Finite element model for NCF composite reinforcement preforming: Importance of inter-ply sliding. *Composites Part A: Applied Science and Manufacturing*, 43(12):2269–2277.

Capelle, E., Ouagne, P., Soulat, D., and Duriatti, D. (2014). Complex shape forming of flax woven fabrics: Design of specific blank-holder shapes to prevent defects. *Composites Part B: Engineering*, 62:29–36.

De Luycker, E., Morestin, F., Boisse, P., and Marsal, D. (2009). Simulation of 3D interlock composite preforming. *Composite Structures*, 88(4):615–623.

Fial, J., Harr, M., Böhler, P., and Middendorf, P. (2018). Automated wet compression moulding of load-path optimised TFP preforms with low cycle times. *IOP Conference Series: Materials Science and Engineering*, 406:012018.

Guzman-Maldonado, E., Wang, P., Hamila, N., and Boisse, P. (2019). Experimental and numerical analysis of wrinkling during forming of multi-layered textile composites. *Composite Structures*, 208:213–223.

Hamila, N., Boisse, P., Sabourin, F., and Brunet, M. (2009). A semi-discrete shell finite element for textile composite reinforcement forming simulation. *International Journal for Numerical Methods in Engineering*, 79(12):1443–1466.

Hautefeuille, A., Comas-Cardona, S., and Binetruy, C. (2019). Mechanical signature and full-field measurement of flow-induced large in-plane deformation of fibrous reinforcements in composite processing. *Composites Part A: Applied Science and Manufacturing*, 118:213–222.

Labanieh, A. R., Garnier, C., Ouagne, P., Dalverny, O., and Soulat, D. (2018). Intra-ply yarn sliding defect in hemisphere preforming of a woven preform. *Composites Part A: Applied Science and Manufacturing*, 107:432–446.

Lin, H., Wang, J., Long, A. C., Clifford, M. J., and Harrison, P. (2007). Predictive modelling for optimization of textile composite forming. *Composites Science and Technology*, 67(15):3242–3252.

Lomov, S., Boisse, P., Deluycker, E., Morestin, F., Vanclooster, K., Vandepitte, D., Verpoest, I., and Willems, A. (2008). Full-field strain measurements in textile deformability studies. *Composites Part A: Applied Science and Manufacturing*, 39(8):1232–1244.

Muscat, M., Camilleri, D., and Ellul, B. (2017). Fibre Reinforced Composite Pressure Vessel Heads Subject to External Pressure. In *Volume 3A: Design and Analysis*, Waikoloa, Hawaii, USA. American Society of Mechanical Engineers.

Rihaczek, G., Klammer, M., Başnak, O., Petrš, J., Grisin, B., Dahy, H., Carosella, S., and Middendorf, P. (2020). Curved Foldable Tailored Fiber Reinforcements for Moldless Customized Bio-Composite Structures. Proof of Concept: Biomimetic NFRP Stools. *Polymers*, 12(9):2000.

Sholl, N., Moss, A., Krieg, M., and Mohseni, K. (2021). Controlling the deformation space of soft membranes using fiber reinforcement. *The International Journal of Robotics Research*, 40(1).

Sun, X., Belnoue, J. P.-H., Thompson, A., Said, B. E., and Hallett, S. R. (2022). Dry Textile Forming Simulations: A Benchmarking Exercise. *Frontiers in Materials*, 9:831820.

Takezawa, M., Otoguro, Y., Matsuo, K., Shibutani, T., Sakurai, A., and Maekawa, T. (2021). Fabrication of doubly-curved CFRP shell structures with control over fiber directions. *Computer-Aided Design*, 136:103028.

Uhlig, K., Tosch, M., Bittrich, L., Leipprand, A., Dey, S., Spickenheuer, A., and Heinrich, G. (2016). Meso-scaled finite element analysis of fiber reinforced plastics made by Tailored Fiber Placement. *Composite Structures*, 143:53–62.

Chapter 4

Towards controlling fibre tow slippage to increase the formability of TFP preforms

Abstract

The validation of the TFP preform models addressed in the previous chapter showed the limitation of the no-slip assumption for Model I. This chapter aims at improving the modelling strategy without modifying its initial ingredients. Therefore, the models are still based on the embedded element approach which simplifies the modelling of the stitching yarn as well as the underlying contact interactions. The challenge lies in finding a method to include fibre tows slippage while maintaining the kinematic constraints imposed to the embedded elements or nodes. Section 4.1 recalls the motivations of modelling fibre tow slippage in TFP preforms. It also gives an overview of the modelling of fibre slippage in conventional textiles and describes the method required to include fibre tow slippage in the TFP preform models without affecting its initial features. Next, it briefly introduces the Arbitrary Lagrangian-Eulerian (ALE) description in continuum mechanics. Finally, the formulation of a 1D element allowing material flow is given, based on existing works achieved in the field of pulley-cable system modelling. Section 4.3 presents the characterisation method to determine the model of the friction law to be implemented in the 1D ALE element. A parametric study based on pull-out experiments is carried out to determine the material parameters of the proposed analytical friction model. Finally, section 4.4 addresses the application of the 1D ALE element in the TFP preform models. In particular, an update of the bias extension test simulated in section 3.4.1 with the Model I is performed. Next, its application to Model II as well as the possible enhancement of the 1D ALE element are presented. Finally, the application of the 1D ALE element to the modelling of conventional textiles is addressed. In particular, the modelling of fibre tow slippage in woven fabrics and a simplified approach to model the tufting yarn of tufted preforms are proposed.

Contents

4.1 Turning slippage defects in conventional textile into an additional degree of design freedom in TFP preforms

Introduction

This section begins with explaining the reasons why controlling fibre tow slippage in TFP preforms will be a major improvement to form complex TFP preforms. Next, it shows some modelling strategy developed to take into account this forming defect in conventional textiles before presenting how fibre tow slippage can be included in the TFP preforms models without changing their initial ingredients. Then, a concise introduction to the Arbitrary Lagrangian-Eulerian (ALE) description gives the necessary background to understand the existing models allowing to describe material flow in 1D elements. Finally, among the possible models, the formulation of the one which best fits the framework of an explicit solver is detailed before implementing and testing this 1D ALE element with elementary test cases.
Therefore, the objectives of this section are:

- Examine existing modelling approaches taking into account fibre slippage
- Chose a method to add material flow in the TFP preform models without changing their initial ingredients
- Give the necessary background to understand the formulation of 1D ALE finite elements

4.1.1 Introduction

4.1.1.1 Motivations

Fibre slippage is a well-known manufacturing defect which can occur during the forming of conventional textiles due to excessive tension in the fibre directions. However, in case of TFP

preforms, the fibre tow slippage could be used as an additional degree of freedom to form complex shapes with specific targeted orientations. As mentioned in section 1.4.2.3, Fial et al. (2018) used fibre tow slippage in TFP preform to form a complex corner-like shape by folding rather than forming, which reduces unformability issues while increasing the final part properties (Fig.1.43).

Fibre tow slippage can be used to simplify the flat TFP pattern. For example, in the hemispheric shape forming addressed in section 3.2, the flat TFP pattern design was obtained by considering the no-slip assumption between the fibre tows. This strong hypothesis led to a TFP pattern where the fibre tows of the meridian layer have a initial high curvature and end tangent to the parallel layer. This initial configuration leads to high rotation of the TFP preform during forming driven by the realignment of the meridian fibre tows with the meridians of longitude of the hemisphere. If the fibre tows of the meridian layer could slip over the parallel layer, the initial curvature of the meridian fibre tows could be reduced, which would improve the filling of the TFP preform.

Moreover, as shown in section 3.4.1, the no-slip assumption between the fibre tows and the backing material leads to a very stiff behaviour which considerably modifies the initial behaviour of the backing material. Therefore, in case of TFP-reinforced biaxial textiles, absence of slippage in the TFP reinforcement can result in the unformability of the preform due to the presence of more than two inextensible directions.

Consequently, controlling fibre tow slippage in TFP preforms will allow to improve the formability of complex preforms on complex shapes and will increase the design freedom. The next section is a brief review of the modelling of fibre slippage in conventional textiles.

4.1.1.2 Fibre slippage in conventional textiles and its modelling

The success of forming complex composite parts is mainly driven by the ability of the fibrous reinforcement to accommodate the final shape. When conventional textiles cannot fit into the mould, defects occur. Wrinkles, fibre breakage or large fibre slippage are the main defects encountered during manufacturing of complex parts. Wrinkling in conventional textile has been widely investigated by the scientific community using both numerical simulations and experiments (Hamila et al., 2009; Allaoui et al., 2011, 2014; Chen et al., 2015; Sjölander et al., 2016; Labanieh et al., 2018). The dependency between the size or occurence of wrinkles and the mechanical properties of the dry textile has also been studied (Boisse et al., 2011). One solution to prevent defects relies on the use of a system of independent pressure-control blank-holders (Allaoui et al., 2011, 2014; Capelle et al., 2014; Labanieh et al., 2018). Fibre slippage also known as inter-ply sliding or intra-ply sliding in conventional depends on the punch geometry, the process parameters as well as the initial preform orientation with respect to the punch geometry and the interactions between the plies for multi-layer preforms. A major difficulty in avoiding defects is to understand the coupling between defects. For example, the induced tensile forces resulting from the use of blank holders can lead to fibre slippage. Fibre slippage tends to decrease the bending stiffness which in turn can facilitate the onset of wrinkles. Understanding fibre slippage is a crucial step for the prediction of the forming behaviour of conventional but is very challenging to model. Fibre slippage in NCF or woven fabrics relies on the same mesoscopic interactions, namely the friction between the fibres. However, in NCF the resistance to fibre slippage is due to the friction between the stitched layers and depends on the type of stitching whereas in woven fabrics, the weave pattern plays a crucial role. Some modelling approaches developed to study fibre slippage in NCF and woven fabrics are presented hereafter as an introduction.

NCF models Creech and Pickett (2006) modelled NCF using a discrete model where rows of solid elements represent the yarns to take into account the inter-ply and intra-ply sliding using contact friction interaction between the rows. Bar element modelling the stitching interconnect the rows of solid elements as shown in Fig. 4.1 (a).
Bel et al. (2012) modelled inter-ply sliding in NCF using shell elements for each layer and used trusses with anisotropic contact interactions to represent the stitch linking the layers Fig. 4.1 (b). This modelling strategy showed good agreement with the experimental forming on a hemisphere geometry (Fig 4.2).
While the model by Creech and Pickett (2006) takes into account inter-ply and intra-ply slippages, the one by Bel et al. (2012) is limited to inter-ply slippage.

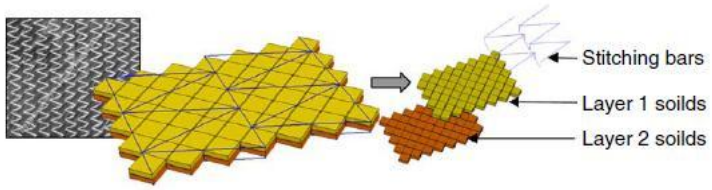

(a) NCF model by Creech and Pickett (2006)

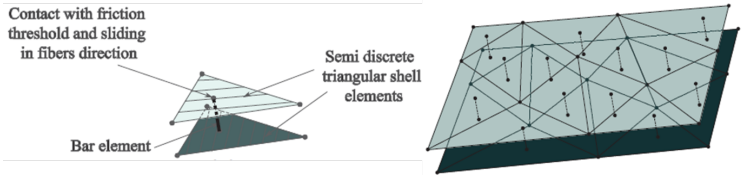

(b) NCF model by Bel et al. (2012)

Figure 4.1: Example of models for NCF taking into account fibre slippage

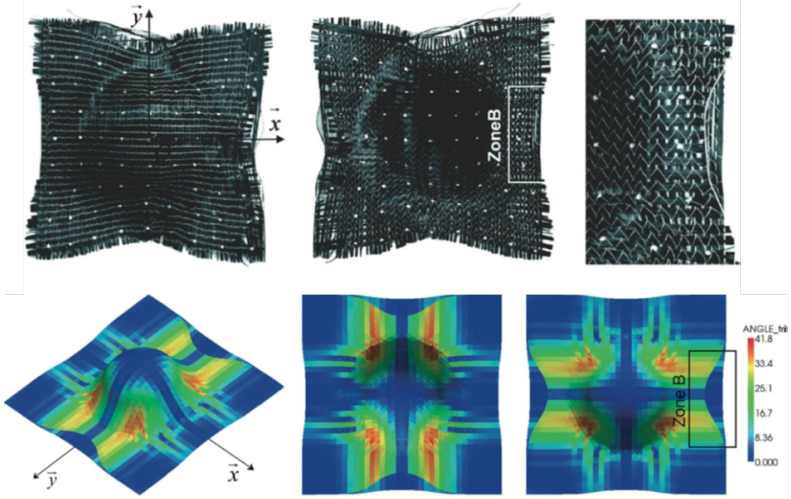

Figure 4.2: Simulation result of a hemispheric shape forming by Bel et al. (2012)

Woven fabric models In woven fabrics intra-ply slippage is referenced as a loss of cohesion of the woven fibre network. Gatouillat et al. (2013) modelled this loss of cohesion using a meso-modelling approach. This model is based on a coarse description of a plain weave unit cell where the fibre tows are straight and represented using 2D shell elements rather than 3D solid elements. Isotropic Coulomb frictional contact is used to model the interactions between the yarns constituting the unit cell. To validate the model, forming using a hemispherical punch has been addressed (Fig 4.3).

Figure 4.3: Simulation result of a hemispheric shape forming by Gatouillat et al. (2013)

The previous modelling approaches relies either on discrete models or a combination of macro-modelling with some discrete fabric features. Moreover, they are based on a Lagrangian description which implies explicitly modelling the contact interactions to take into account fibre slippage. The originality of the model presented in Parsons et al. (2010, 2013) is the use of a continuum approach which takes into account the fibre slippage in woven fabric. However, this model has not been used to study the forming process but was used in impact simulations. In this model, a woven fabric is represented by a regular mesh of 2D elements where the nodes correspond to the crossover points. Each node (crossover point) is associated with an internal unit cell of the fabric depicted in Fig. 4.4 (a). This unit cell is made of two sets of two trusses representing the warp and weft fibre tows and additional "locking" trusses connecting the fibre tows to model the shear resistance and lateral fibre tow contact. In the unit cell a fibre tow is represented by two trusses connected by a spring element to account for out-of-plane bending stiffness. The fibre tows are also connected by a "cross-over spring" to model the resistance to in-plane shear. Additional degrees of freedom quantify the change in crimp amplitude and are used to compute the friction forces between the two fibre tows at the crossover point. Forces computed for each unit cell are then homogenized through the boundaries of the continuum (see Fig. 4.4 (b) for a schematic view of the modelling approach).

To take into account the fibre slippage, the mesh nodes have additional degrees of freedom (one per fibre tow family) which quantify the displacement of a material point on a fibre tow with respect to the crossover point and are denoted as slip displacements. Each additional degree of freedom is driven by the gradient of tension in the portion of fibre tow it is associated with and the friction forces resulting from the interactions with the other family. The originality of this model comes from the use of an ALE description that considerably simplifies the modelling of the contact interactions between the weft and warp fibre tows in woven fabrics. This attractive description allows modelling material flow through a moving mesh. Its application to include fibre tow slippage in the TFP preform models is discussed in the next section.

4.1.1.3 Including fibre tow slippage in the TFP preform models

Including fibre tow slippage in the proposed TFP preform models without changing the initial ingredients is challenging. The method used by Parsons et al. (2013), which considers additional

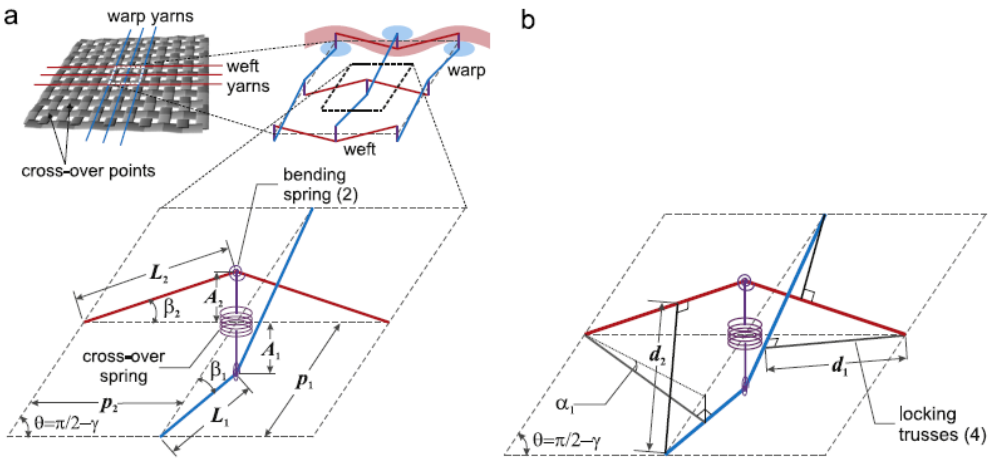

(a) Unit cell description

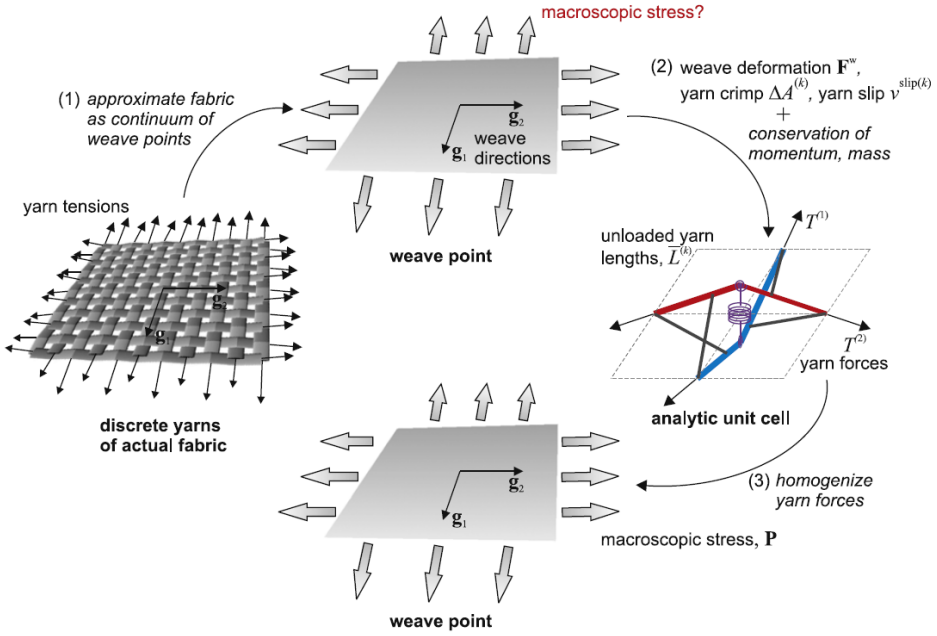

(b) Homogenisation process

Figure 4.4: Woven fabric model including fibre tow slippage by Parsons et al. (2013)

slip displacement degrees of freedom, is very attractive. However, it was applied to a 2D continuum representation of fibrous reinforcement whereas the TFP preform models are based on the explicit discretisation of the fibre tows using 1D elements. Consequently, it is necessary to investigate the application of this method to model the material flow in 1D elements rather than in 2D elements.

Fig. 4.5 illustrates the targeted TFP preform models. In these new models, all the initial features of the TFP models remain. In this figure, a material point described by its curvilinear coordinates S_i is considered on the initial configuration of the i^{th} fibre tow. Then, after slippage, this material point moved to the curvilinear abscissa s_i. The fibre tow slippage or material flow within the 1D elements is defined by the difference between these two curvilinear abscissa:

$$U^i_{slip} = s_i - S_i \tag{4.1}$$

where U^i_{slip} is the slip displacement on the i^{th} material point, which is a scalar quantity.

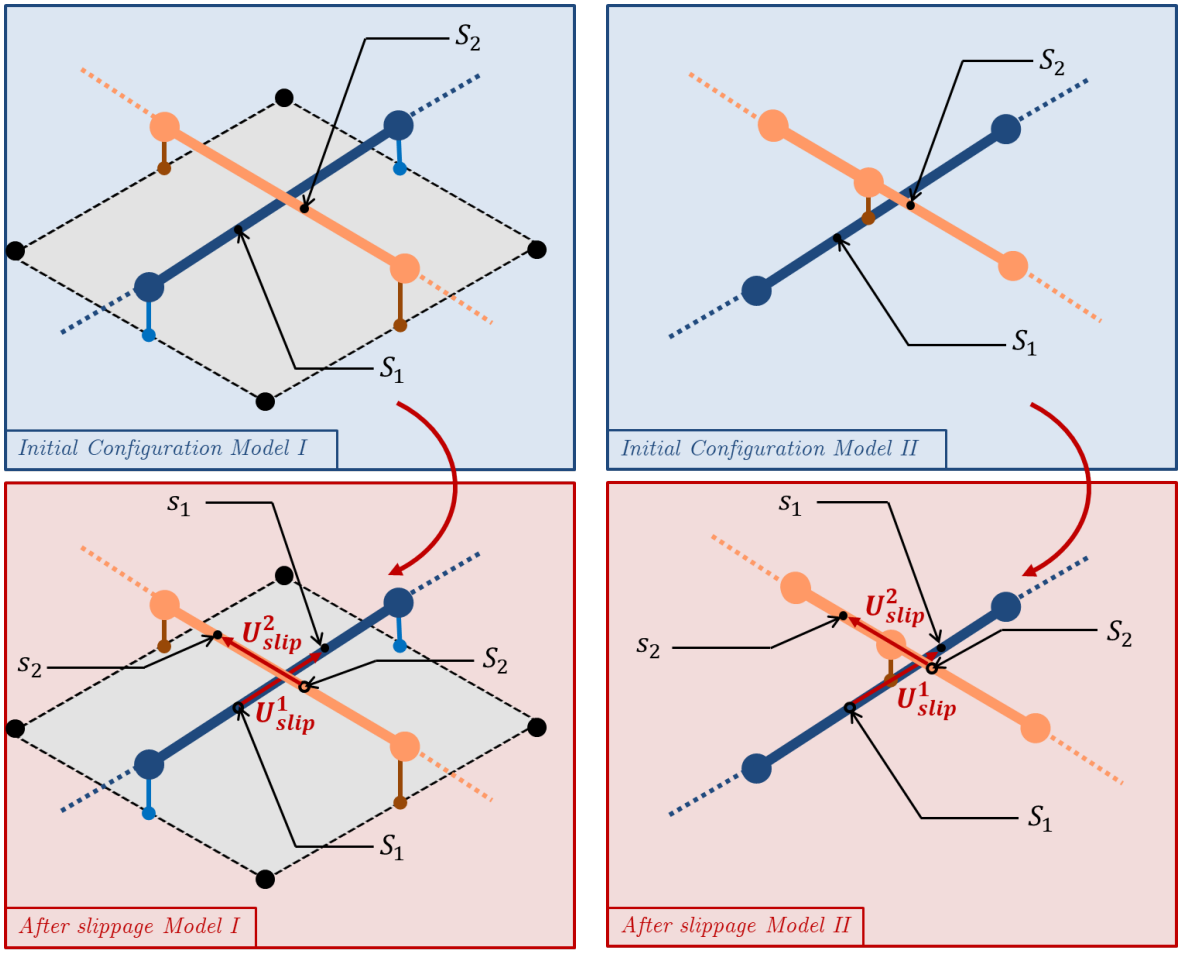

(a) Model I **(b)** Model II

Figure 4.5: Representation of fibre tow slippage in the TFP models

Transition

Taking into account the fibre tow slippage in the TFP preform models without modifying the initial ingredients requires to quantify the slip displacement of the fibre tows. Therefore, in the new models, material flow within the 1D elements representing the fibre tows has to be modelled. The ALE description is a suitable framework to model relative motion between a moving mesh and the matter it contains. The next section aims at giving the necessary background to understand the ALE description and the formulation of material flow in 1D elements.

4.1.2 A brief introduction to the Arbitrary-Eulerian description in continuum mechanics

This section introduces the basics of the Arbitrary Lagrangian Eulerian (ALE) framework in continuum mechanics. Donea and Huerta (2003); Belytschko et al. (2013) can be referred for a clear understanding of the underlying descriptions.

4.1.2.1 Origins

In composite forming modelling, the finite elements method is a well-established approach. Most of the models developed rely on a Lagrangian description of the continuum or of the discrete

features constituting fabrics. This is the standard approach when dealing with solid mechanics as opposed to the Eulerian description mainly used in fluid mechanics. The Lagrangian description which enforces no relative movement between the spatial discretization (mesh) and the material points of the continuum suffers from a lack of accuracy when very large deformations occur. Burdensome adaptive remeshing techniques are required to overcome this defect. The Eulerian description is able to track large movement of material points through a fixed spatial discretization but it complicates the treatment of moving boundaries and interfaces. Consequently, both approaches have their own field of application. However, a more general frame referenced as ALE description has been developed to take advantage of both latter descriptions while minimizing their drawbacks. In this description, the spatial discretization of the domain is neither attached to the matter, nor fixed in space.

4.1.2.2 ALE reference configuration

In practice, the Lagrangian and Eulerian descriptions differ from the reference configuration used to describe the equations of motion and the independent variables used. The motion and deformation of a body is generally described using two configurations, namely, an initial configuration referred as (Ω_0) corresponding to a time variable $t = 0$ and a current configuration (Ω) corresponding to an instant t. A point $\vec{\boldsymbol{X}}$ in (Ω_0) is generally referred as a material point which does not vary in time. This point corresponds to a point $\vec{\boldsymbol{x}}$ in (Ω) referred as a spatial point. A one-to-one mapping ϕ exists between the reference and current configurations:

$$\vec{\boldsymbol{x}} = \boldsymbol{\phi}\left(\vec{\boldsymbol{X}}, t\right) \tag{4.2}$$

This mapping describes the body motion. In the Lagrangian description, (Ω_0) is the reference configuration. A finite element node in a Lagrangian mesh is associated to the same material point during the body motion and deformation. In the Eulerian description, a fixed spatial domain (Ω) is the reference configuration and the equations of motion track information at the material points which are flowing through it. Therefore, in an Eulerian mesh, a node is not associated to a unique material point. In the ALE mesh, the mesh moves independently from the material points and this motion must be carefully chosen to avoid severe distortion of the elements and allow tracking the moving material boundaries or solid/fluid interfaces for example.
Consequently, another configuration $(\bar{\Omega})$, named referential configuration or ALE domain, must be introduced to track the mesh motion independently from the material motion. Since the mesh is generally created in this configuration it is also defined as the computational domain. A point $\vec{\boldsymbol{\chi}}$ defined in $(\bar{\Omega})$ is related to a material point $\vec{\boldsymbol{X}}$ in (Ω_0) through the mapping $\boldsymbol{\psi}$ and to a spatial point $\vec{\boldsymbol{x}}$ in (Ω) through $\bar{\boldsymbol{\phi}}$. The mapping $\boldsymbol{\phi}$ is still defined between (Ω_0) and (Ω) and corresponds to the material motion.

In fact, the material motion can be decomposed into two steps, a first step where matter to mesh motion occurs and second step where the mesh is fixed to the material and deforms accordingly. The first step is described by $\boldsymbol{\psi}$ whereas the second step corresponds to $\bar{\boldsymbol{\phi}}$. The ALE description simply reduces to a Lagrangian description when $\boldsymbol{\psi} = \boldsymbol{I}$, and reduces to the Eulerian description when $\bar{\boldsymbol{\phi}} = \boldsymbol{I}$. Therefore, $\boldsymbol{\phi}$ can be seen as a composition of an Eulerian motion $\boldsymbol{\psi}$ and a Lagrangian motion $\bar{\boldsymbol{\phi}}$. Expressions of the kinematic variables in the different continuum descriptions are given in Table. 4.1. The relations between these three mapping functions are illustrated in Fig. 4.6.

4.1.2.3 Illustrative example in one dimension

Before introducing some existing models to account for material flow in 1D elements, the mappings between the different configurations of the ALE framework are explained in an one di-

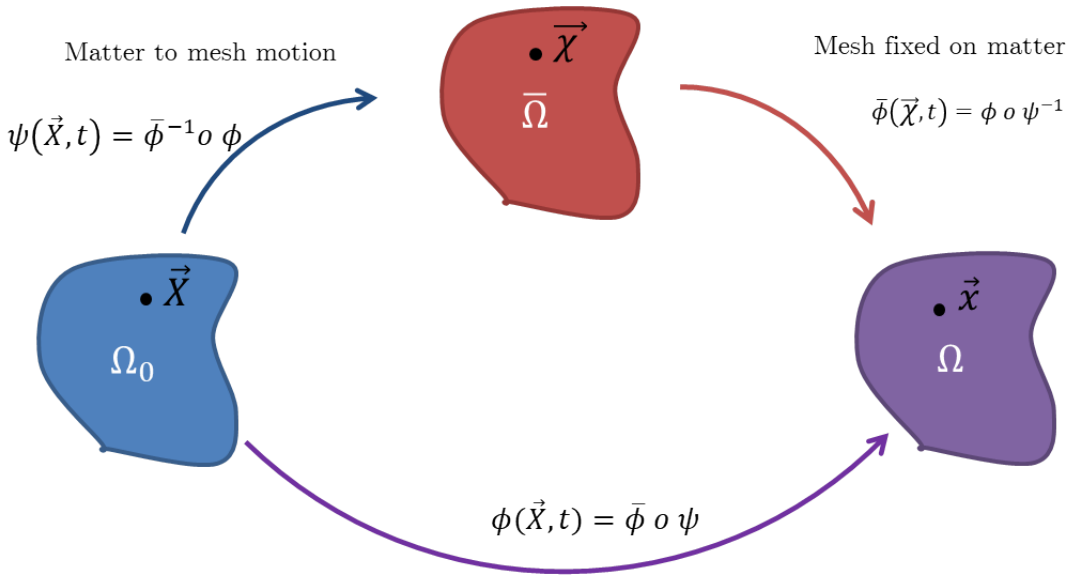

Figure 4.6: Relations between the mapping functions in an ALE framework

Table 4.1: Motion and displacement definitions for the different descriptions: ALE, Lagrangian, Eulerian

Description		ALE	Lagrangian	Eulerian
Motion	Material	$\vec{\boldsymbol{x}} = \boldsymbol{\phi}\left(\vec{\boldsymbol{X}}, t\right)$	$\vec{\boldsymbol{x}} = \boldsymbol{\phi}\left(\vec{\boldsymbol{X}}, t\right)$	$\vec{\boldsymbol{x}} = \boldsymbol{\phi}\left(\vec{\boldsymbol{X}}, t\right)$
	Mesh	$\vec{\boldsymbol{x}} = \bar{\boldsymbol{\phi}}\left(\vec{\boldsymbol{\chi}}, t\right)$	$\vec{\boldsymbol{x}} = \boldsymbol{\phi}\left(\vec{\boldsymbol{X}}, t\right)$	$\vec{\boldsymbol{x}} = \boldsymbol{I}\left(\vec{\boldsymbol{x}}\right)$
Displacement	Material	$\vec{\boldsymbol{u}} = \vec{\boldsymbol{x}} - \vec{\boldsymbol{X}}$	$\vec{\boldsymbol{u}} = \vec{\boldsymbol{x}} - \vec{\boldsymbol{X}}$	$\vec{\boldsymbol{u}} = \vec{\boldsymbol{x}} - \vec{\boldsymbol{X}}$
	Mesh	$\vec{\boldsymbol{v}} = \vec{\boldsymbol{x}} - \vec{\boldsymbol{\chi}}$	$\vec{\boldsymbol{v}} = \vec{\boldsymbol{u}}$	$\vec{\boldsymbol{v}} = \vec{\boldsymbol{0}}$

mensional domain. Fig. 4.7 (a) shows the initial configuration where one element of length L defined by two nodes (black dots) is represented. In this element, a material point X is defined as well as its parametric coordinates S in the element.
The referential configuration is represented in Fig. 4.7 (b). The referential point χ corresponding to the material point X has moved through the mesh. Consequently, the parametric coordinates $\bar{S}$ of χ is different from S while the length $\bar{L}$ equals L since the mesh does not deform in the Eulerian step.
In the current configuration presented in Fig. 4.7 (c), the spatial point x of parametric coordinates s has moved from χ in the physical domain but still coincides with χ in the parametric domain which means that s equals $\bar{S}$. In other words, between $(\bar{\Omega})$ and Ω (Lagrangian step), the mesh deforms with the material and the length l is different from $\bar{L}$.

Transition

Taking into account fibre tow slippage in the TFP preform models without modifying its initial ingredients requires modelling material flow in the 1D elements representing the fibre tows. The ALE description allows independent displacement of the material points and the mesh. The next section describes some models which were developed in the field of pulley-cable systems to simplify the contact interactions.

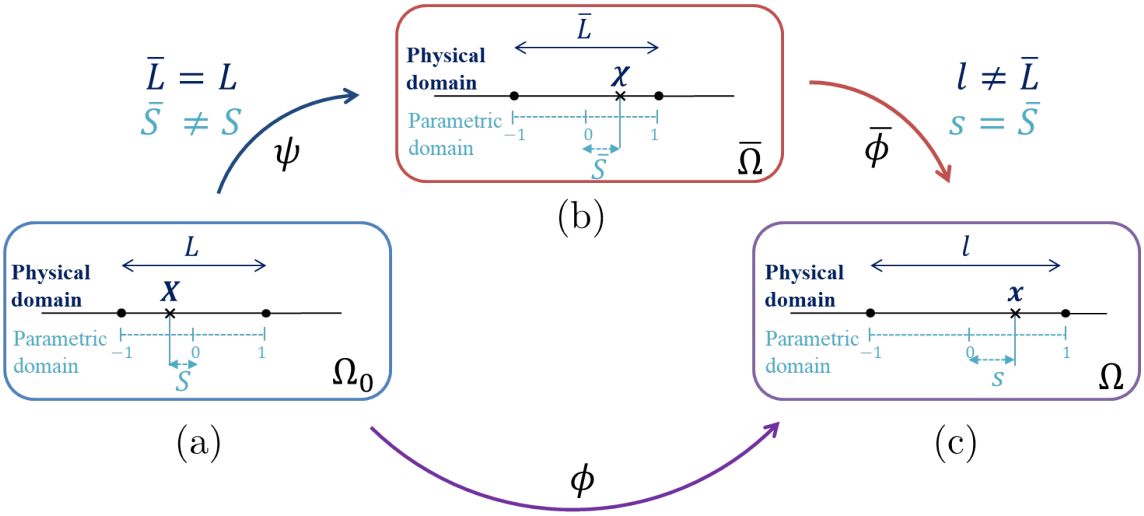

Figure 4.7: Decomposition of the motion of a material point in an one dimensional ALE framework

4.1.3 Modelling material flow in 1D elements

4.1.3.1 From pulley-cable system to TFP preform models

The section aims at finding the formulation of a 1D element which allows the matter to flow through it. Modelling of the interactions between pulleys and cables has been widely addressed (Aufaure, 1993, 2000; Zhou et al., 2004; Ju and Choo, 2005; Peng et al., 2017; Coulibaly et al., 2018; Liu et al., 2018; Du et al., 2019; Zhang et al., 2019; Kan et al., 2019, 2021). The main problem is to judiciously model the cable-pulley system to avoid modelling all the contact points between the cable and the pulley. Fig. 4.8 (a) shows the representation of a cable lying on a pulley. Using the Lagrangian description to model this system requires discretizing separately the pulley and the cable. In this case, all the cable elements are prone to interact with the pulley elements. Consequently, a fine discretisation of the cable is required (Fig. 4.8 (b)). Moreover, a very fine mesh is generally needed to avoid spurious numerical oscillations in the contact algorithm due to the lack in the representation of the real geometries. The model illustrated in Fig. 4.8 (c) considerably simplifies the representation of the system. The portion of cable in contact with the pulley shares the same nodes than the pulley. The shared mesh is made of cable-pulley elements. When the cable slides, the material particles of the cable flow through the cable-pulley elements which are fixed. This modelling allows a high reduction of the element number and removes the spurious numerical oscillations of a contact algorithm. When the size of the pulley is small, only one node is needed to model it (Fig. 4.8 (d)).

The representation of the system using cable-pulley elements is very attractive. Fig. 4.9 shows two modelling approaches to include fibre tow slippage in Model I. In the Lagrangian approach (Fig. 4.9 (a)), the embedding constraint is no longer possible and a very fine discretisation of the fibre tows is required. Moreover, a contact law allowing slippage along the fibre tow axis is needed as developed by Bel et al. (2012) to model slippage of the stitching yarn in NCF. Therefore, this modelling approach requires higher computational effort and important changes in the initial model. The mixed embedded element - ALE approach illustrated in Fig. 4.9 (b) is still based on the embedded element approach and takes into account the fibre tow slippage through material flow as for the cable-pulley system. The red dots represent the position of a single material point due to material flow in the 1D element. The fibre tow discretisation is the same than without including fibre tow slippage. In the following, three cable-pulley models are briefly presented. Their advantages and drawbacks are reported and the one which is best

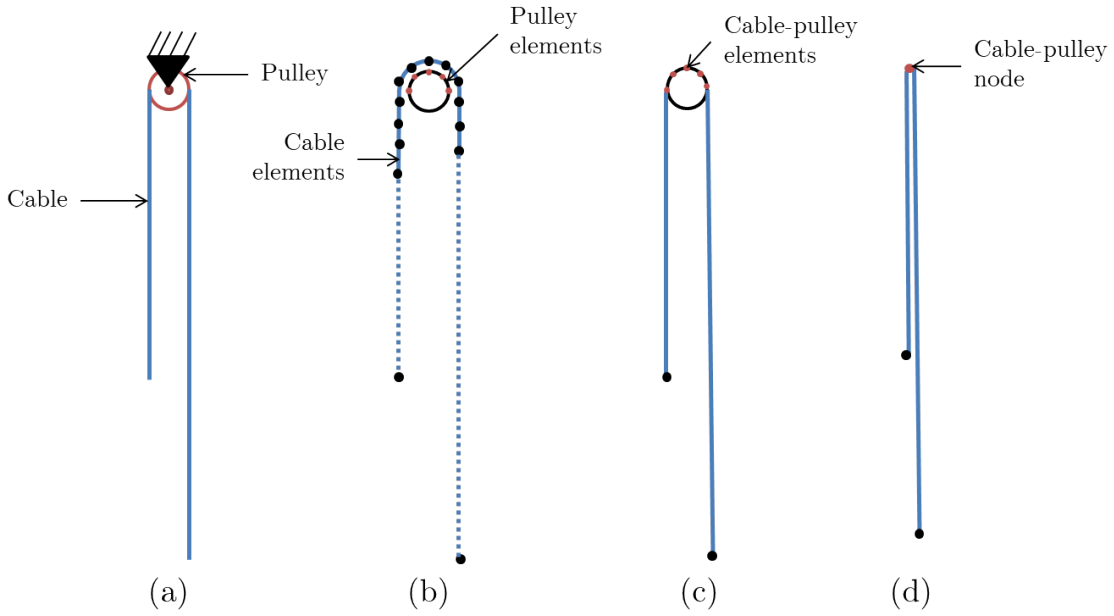

Figure 4.8: Representation of a cable-pulley system: real system (a), Lagrangian mesh (b), ALE mesh (c), ALE mesh with for a small pulley (d)

suited to fit into an explicit solver is chosen.

4.1.3.2 Multi-sliding nodes

One of the first modelling strategies developed is to consider a cable-pulley element composed of 3 nodes (Aufaure, 1993, 2000; Zhou et al., 2004; Zhang et al., 2019). Two Lagrangian nodes (N1, N2) represent the cable ends and an ALE node in between (N3) models the pulley as depicted in Fig. 4.10 (a). The cable is assumed to be flexible, does not resist to compression and its cross-section remains the same (small strains assumption). For a frictionless pulley, the internal forces at the nodes are computed knowing that the tension in the segments N1-N3 and N3-N2 must be equal. The derivation of the internal forces for explicit integration scheme or the stiffness matrix for implicit scheme is then straightforward (see Aufaure (2000) for implicit scheme and Zhou et al. (2004) for an explicit one). For this kind of modelling, a cable-pulley system with several pulleys is modelled using a series of 3-nodes cable-pulley elements as shown in Fig. 4.10 (b). The main issue with this modelling is the need to remesh when the cable flow is such that one of the Lagrangian node of a cable-pulley element will pass through an ALE node (Fig. 4.10 (c)). Another disadvantage is the frictionless pulley assumption which does not allow an accurate modelling of the cable-pulley interaction. Zhang et al. (2019) extended the work of Zhou et al. (2004) to account for pulley with friction.

To encompass the remeshing procedure Ju and Choo (2005); Coulibaly et al. (2018); Kan et al. (2021) use a multi-sliding nodes approach where several ALE nodes (representing pulleys for instance) can be cumulated along a cable without Lagrangian cable node in between every other ALE node (Fig. 4.11). The ALE nodes are named sliding nodes in these models.

They used different approaches to solve the system of equations resulting from this model and the remainder of this section elaborates further on the methods used by Coulibaly et al. (2018) and Kan et al. (2021).
The model is driven by two systems of equations. The first one is the classical moment equilibrium and the second one is the conservation of mass. To model material flow through the sliding nodes, the quantity of material exchanged on both side of such a node must be computed. The

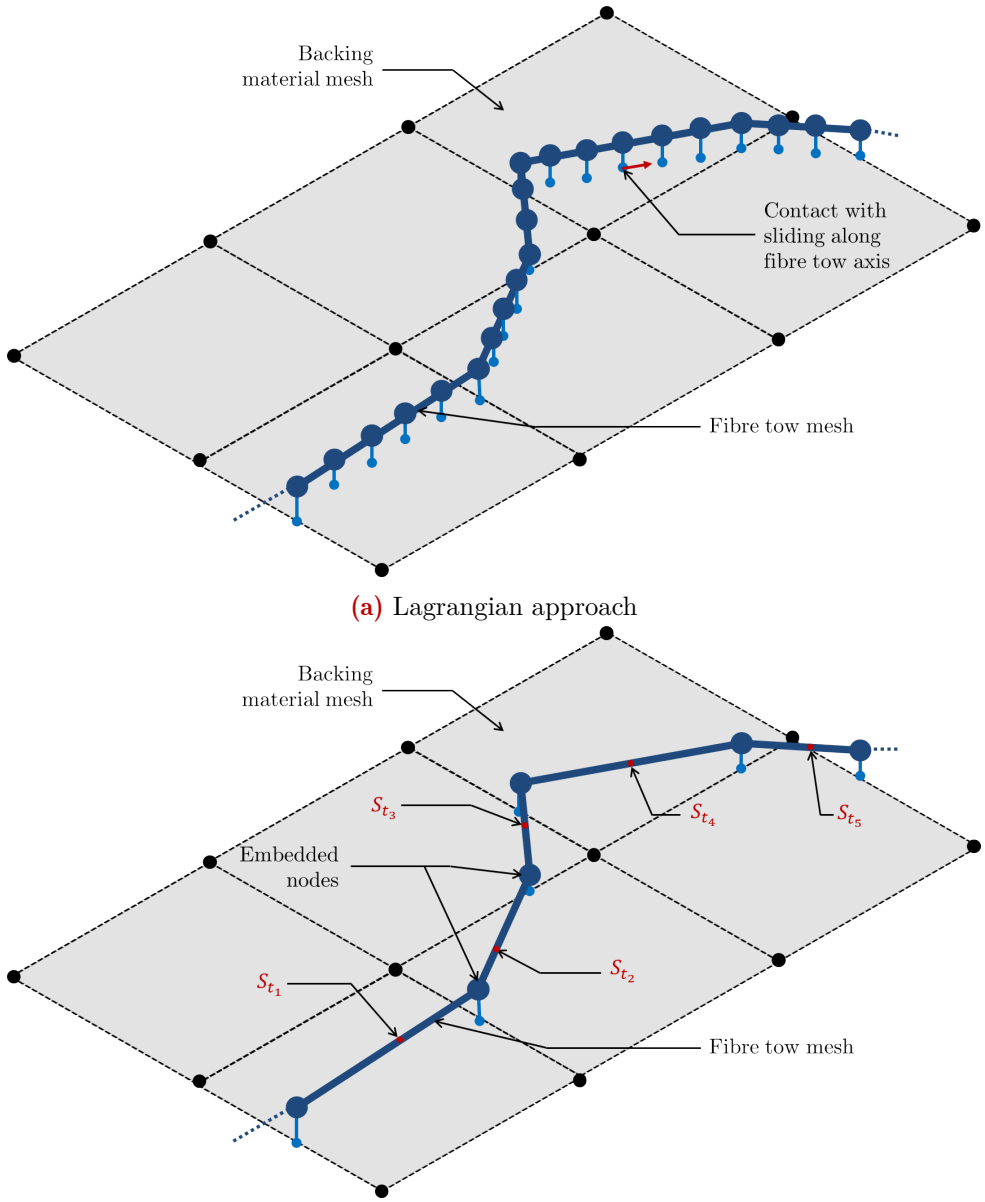

(a) Lagrangian approach

(b) Mixed embedded element-ALE approach

Figure 4.9: Modelling approaches to include fibre tow slippage in Model I

material flow at a sliding node is driven by an equilibrium between the tension in the adjacent elements and the friction force at the sliding node. This friction force can be due to a pulley or another sliding component along the cable but pulleys will be considered here for simplicity. Fig. 4.12 illustrates the different configurations for one sliding node.

In Coulibaly et al. (2018), since an explicit time integration scheme is used, at each time step, the current configuration (Ω) is known. To compute the strain and stress in the elements, the material flow δL has to be computed to determine the ALE configuration ($\bar{\Omega}$). The strategy used consists in a prediction-correction method. The unstretched lengths $\bar{L}_i$ describe the referential configuration in the ALE reference domain and constitute the unknowns. The mass conservation equation yields:

$$\sum_i L_i = \sum_i \bar{L}_i \tag{4.3}$$

where L_i is the initial unstretched length of the i^{th} element.

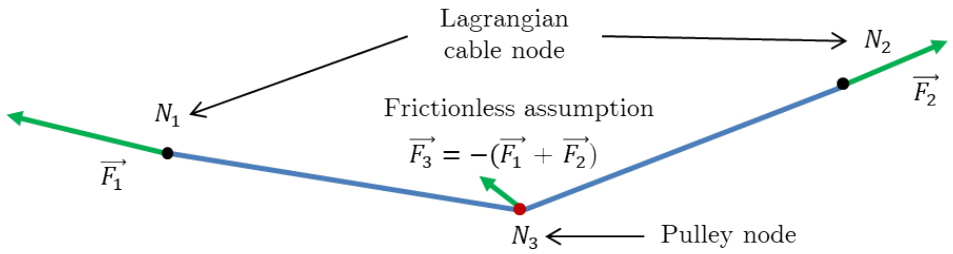

(a) A 3-node cable-pulley element

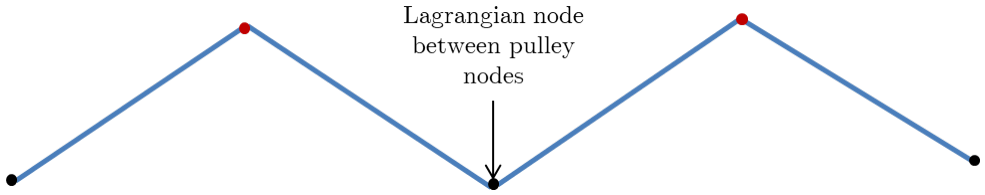

(b) Assembly of 3-node cable-pulley elements

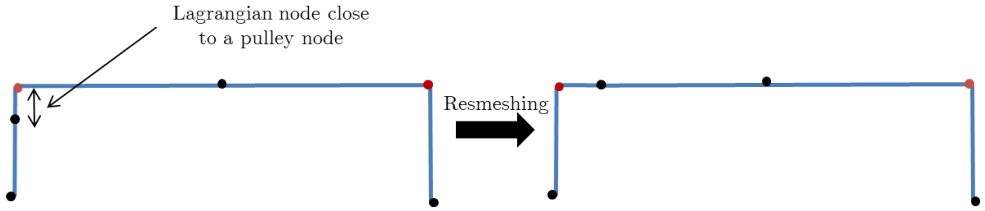

(c) Lagrangian node close to a sliding node implies remeshing

Figure 4.10: A modelling approach of cable-pulley element

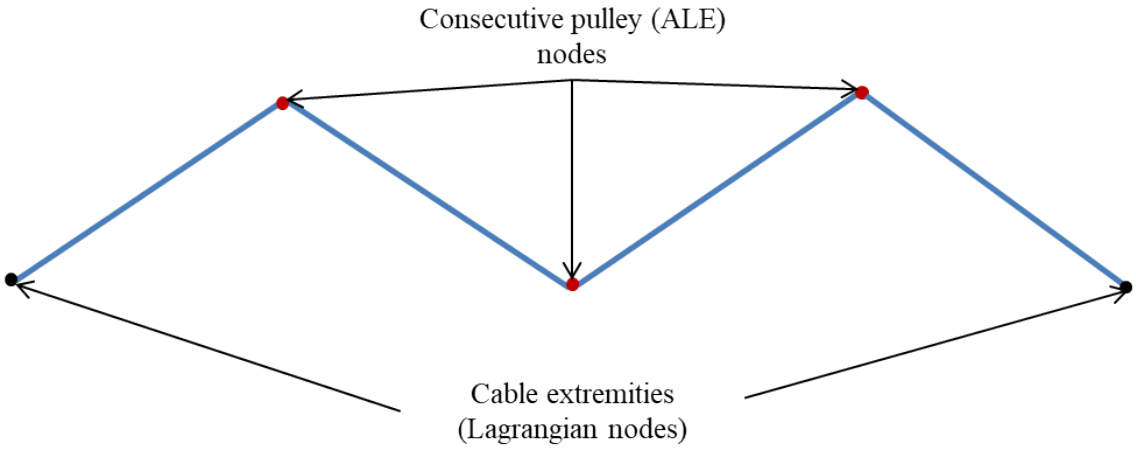

Figure 4.11: Representation of the multi-sliding nodes model

Moreover, for each sliding node a friction law yields an equation linking the element tension on both sides. For a pulley at sliding node i:

$$T_{i+1} = \lambda T_i \tag{4.4}$$

where T_i is the tension in the i^{th} element and λ is the friction coefficient. If a multi-sliding nodes composed of N elements is considered, the system of equations consists in $N-1$ equations from the friction law (Eq. 4.4) at the $N-1$ sliding nodes and an additional equation which is the conservation of mass (Eq. 4.3). Therefore, the N unknown unstretched lenghts $\bar{L}_i$ can be solved. In case of one sliding node on a linear elastic cable element, the system of equations is:

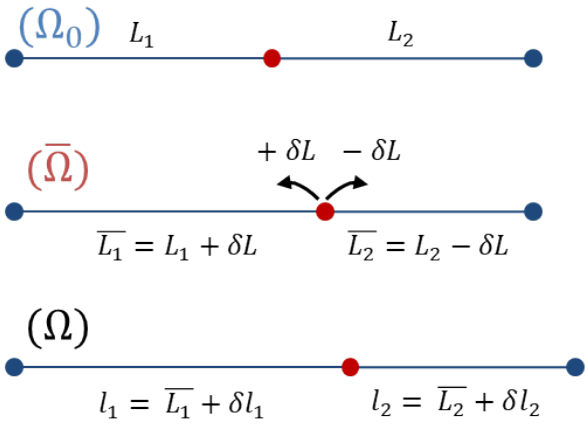

Figure 4.12: Configurations of the multi-sliding nodes model with one sliding node

$$L_1 + L_2 = \bar{L_1} + \bar{L_2} \quad \text{(Mass conservation)} \tag{4.5}$$

$$T_1 = \lambda T_2 \quad \text{(Pulley friction law at sliding node)} \tag{4.6}$$

Using the Cauchy strain definition yields:

$$T_i = E\epsilon_i = E\frac{l_i - \bar{L}_i}{\bar{L}_i} \tag{4.7}$$

Where E is the tensile modulus of the cable material. $\bar{L}_i$ can be expressed according to the tension T_i using Eq. 4.7.

For one sliding node, the exchange of matter δL can be computed analytically. In the general case, a Newton-Raphson method is used at each time step to solve for the tension equilibria and the mass conservation. It is a prediction-correction method in the extent that the first guess tensions are computed by considering no slip at the sliding nodes. In other words, the previous ALE configuration is used as a first guess. The advantage of this method is the strict respect of the mass conservation when a small convergence criterion is used. However, since it requires the computation of the unstretched lengths from the tension, the constitutive law must be inverted and consequently this function must be bijective disabling the use of softening material. Besides the elements cannot resist longitudinal compression which is appropriate for a cable but not necessarily for a fibre tow.

4.1.3.3 In implicit framework

Ju and Choo (2005); Kan et al. (2021) used a different approach. Their finite element solver was based on an implicit framework. To be consistent with this framework, they formulated the equations of mass conservation and friction at sliding nodes as an additional functional to be minimized with the functional resulting from the principle of virtual work to solve for the displacements. The difference between both resides in the fact that Ju and Choo (2005) used the small strain assumption which considerably reduces the effort for the differentiation of this additional functional. Since the friction law for a pulley involves non-smooth inequalities, a special treatment must be applied to obtain a differentiable functional. Kan et al. (2021) used the nonlinear complementary approach based on Kuhn-Tucker complementary theory and the modified Fischer-Burmeister complementarity function to solve this issue. They firstly used a linear complementary approach in Kan et al. (2019) but the linear method was limited to

Table 4.2: Comparison of different modelling approaches to take into account material flow in 1D elements

Methods	Prediction-correction Coulibaly et al. (2018)	Complementary approach Kan et al. (2021)	Additional dofs Peng et al. (2017); Liu et al. (2018)
Integration scheme	Explicit	Implicit	Explicit
ALE configuration	Unknown	Unknown	Known
Current configuration	Known	Unknown	Known
Implementation	Displacement dofs are time integrated while material flow is determined using N-R iterations	Displacement dofs and material flow are determined simultaneously using N-R iterations	Displacement dofs and material flow are time integrated
Advantages	Mass conservation is strictly respected	Mass conservation is strictly respected Can be implemented in a standard implicit framework	Implementation is easy and allows material flow at every nodes even extremities
Drawbacks	Costly N-R iterations at each time increment Material behaviour restrictions	Cumbersome procedure to determine the functional terms of material flow	Mass conservation accuracy depends on time step

explicit dynamic analysis. This is why they extended their work with a nonlinear complementary approach. In fact this method considers the material flow at a sliding node as an additional degree of freedom. The use of additional degrees of freedom to compute the material flow is similar to the work by Parsons et al. (2013) but in an implicit framework with 1D elements.

4.1.3.4 Comparisons of the existing approaches

The functional established in Kan et al. (2021) could be used to take into account material flow in the TFP preform models. However, minimizing the functional at every time step is non-consistent with the explicit solver paradigm where the degrees of freedom are integrated over time. The same applies for the model by Coulibaly et al. (2018) which requires an iterative algorithm to converge at each time increment.
Nevertheless, Peng et al. (2017); Liu et al. (2018); Du et al. (2019) developed a 1D element with additional degrees of freedom talking into account the material flow at both element boundaries. They expressed the internal forces conjugated to the material flow degree of freedom. Peng et al. (2017); Liu et al. (2018) used the curvilinear coordinates as additional degree of freedom to describe the material flow and Du et al. (2019) directly used the material flow as an additional degree of freedom. The advantages and drawbacks of the mentioned modelling approach are reported in Table 4.2.

Conclusion

This section introduced the issue of fibre tow slippage in fibrous reinforcements. This deformation mode, which is a manufacturing defect in conventional textiles, can be turned into an additional degree of freedom in TFP preforms. To exploit and control fibre tow slippage in TFP preforms, its modelling is required. To add this feature in the TFP preform models while keeping their initial ingredients, the modelling approaches developed for conventional textiles are not suitable. However, existing models, initially developed for cable-pulley systems, allow modelling material flow in 1D elements. Among these modelling approaches, the formulation of the ALE truss element by Peng et al. (2017) as well as the formulation of the ALE beam by Liu et al. (2018) are very attractive. In some circumstances, the bending stiffness of reinforcing fibre tows might be neglected. Therefore, to enhance the TFP preform models, both formulations are detailed, implemented and numerically tested in the next section.

4.2 Modelling fibre tow slippage in TFP preforms: formulation of ALE truss and beam elements

Introduction

This section addresses the formulation of an ALE 2-node truss element (Peng et al., 2017) and those of an ALE 2-node shear-flexible beam element (Liu et al., 2018). In particular, the shear-flexible ALE beam element is an extension of the Lagrangian beam element presented in section 2.2. Both formulations, which have the same outline, are given in parallel. The differences rely on the presence of additional terms due to the rotation degrees of freedom of the beam and also on the chosen strain measure. Next, some numerical validation test cases are addressed to check the implementation in the finite element solver Femtran. To this end, referenced test cases from cable-pulley systems are achieved with the ALE truss element. Since, only one reference was found for the ALE beam, only elementary test cases based on those in section 2.2 are addressed for this element.
Therefore, the objectives of this section are:

- Describe the formulations of the ALE truss and beam elements
- Implement them in the finite element solver and address their numerical validation

4.2.1 Formulation of the ALE 1D elements

4.2.1.1 Kinematics

Both linear elements contains 3 displacement (positional) dofs per node. Due to the presence of material flow in the 1D element, the curvilinear coordinates of a material point are no longer fixed in time. Therefore, the 1D elements have an additional degree of freedom per node corresponding to the curvilinear coordinates. The beam possesses 3 additional rotation dofs. The dofs of the truss ($\boldsymbol{q_T}$) and those of the beam ($\boldsymbol{q_B}$) are defined as:

$$\underset{(8\times1)}{\left[\boldsymbol{q_T}\right]} = \begin{bmatrix} \underset{(3\times1)}{\vec{\boldsymbol{r}}_1} \\ s_1 \\ \underset{(3\times1)}{\vec{\boldsymbol{r}}_2} \\ s_2 \end{bmatrix} \qquad \underset{(14\times1)}{\left[\boldsymbol{q_B}\right]} = \begin{bmatrix} \underset{(3\times1)}{\vec{\boldsymbol{r}}_1} \\ \underset{(3\times1)}{\vec{\boldsymbol{\psi}}_1} \\ s_1 \\ \underset{(3\times1)}{\vec{\boldsymbol{r}}_2} \\ \underset{(3\times1)}{\vec{\boldsymbol{\psi}}_2} \\ s_2 \end{bmatrix} \tag{4.8}$$

where $\vec{\boldsymbol{r_i}}$ is the current position of the i^{th} node. It corresponds to $\vec{\boldsymbol{\phi_{0i}}}$ in section 2.2, which was used to describe the beam node position on the neutral axis. s_i is the curvilinear coordinates of the i^{th} node. Fig. 4.13 depicts the dofs of the ALE elements.

The linear shape functions defined in section 2.2 are used:

$$N_1(\xi) = \frac{1}{2}(1-\xi) \qquad N_2(\xi) = \frac{1}{2}(1+\xi) \tag{4.9}$$

The parametric coordinates ξ is related to the curvilinear abscissa s by:

$$\xi(s) = \frac{2s - s_1 - s_2}{s_2 - s_1} \tag{4.10}$$

Since the shape functions depends on the curvilinear coordinates s_i, they are time-varying.

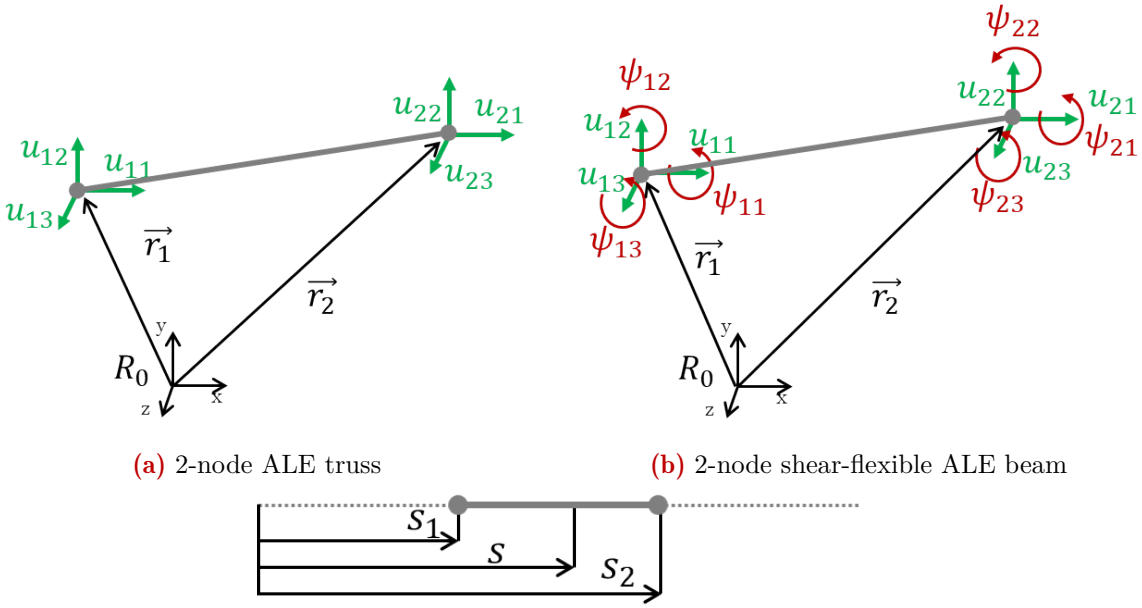

(a) 2-node ALE truss

(b) 2-node shear-flexible ALE beam

(c) Definition of the curvilinear abscissa

Figure 4.13: Description of the dofs of the 1D ALE elements

Using the shape functions, the position of a point in the 1D elements $\vec{r}$ is given by:

$$\vec{r}_T = \underbrace{\begin{bmatrix} N_1 \boldsymbol{I}_{3\times3} & \boldsymbol{0}_{3\times1} & N_2 \boldsymbol{I}_{3\times3} & \boldsymbol{0}_{3\times1} \end{bmatrix}}_{\boldsymbol{N}_{r_T}} \boldsymbol{q_T} \quad \text{(for a truss)} \tag{4.11}$$

$$\vec{r}_B = \underbrace{\begin{bmatrix} N_1 \boldsymbol{I}_{3\times3} & \boldsymbol{0}_{3\times3} & \boldsymbol{0}_{3\times1} & N_2 \boldsymbol{I}_{3\times3} & \boldsymbol{0}_{3\times3} & \boldsymbol{0}_{3\times1} \end{bmatrix}}_{\boldsymbol{N}_{r_B}} \boldsymbol{q_B} \quad \text{(for a beam)} \tag{4.12}$$

where $\boldsymbol{I}_{3\times3}$ and $\boldsymbol{0}_{3\times3}$ ($\boldsymbol{0}_{3\times1}$) are respectively the identify and zero matrices (or vector).

For the beam element its cross-section is still defined by:

$$\vec{\psi} = \underbrace{\begin{bmatrix} \boldsymbol{0}_{3\times3} & N_1 \boldsymbol{I}_{3\times3} & \boldsymbol{0}_{3\times1} & \boldsymbol{0}_{3\times3} & N_2 \boldsymbol{I}_{3\times3} & \boldsymbol{0}_{3\times1} \end{bmatrix}}_{\boldsymbol{N}_{\psi}} \boldsymbol{q_B} \tag{4.13}$$

4.2.1.2 Strains

The longitudinal deformation of the truss is defined using the Green-Lagrange strain:

$$\epsilon = \frac{1}{2}\left(\vec{\boldsymbol{r_T}}'^T \vec{\boldsymbol{r_T}}' - 1\right) \tag{4.14}$$

The strain and curvature measures for the beam are those defined in Eq. 2.22 and recalled hereafter:

$$\underset{(3\times1)}{\vec{\boldsymbol{\Gamma}}} = \boldsymbol{R}^T\left(\vec{\boldsymbol{r_B}}' - \vec{\boldsymbol{e_1}}\right) \qquad \underset{(3\times1)}{\vec{\boldsymbol{K}}} = \boldsymbol{T}^T \vec{\boldsymbol{\psi}}' \tag{4.15}$$

4.2.1.3 Strain variations and strain-displacement matrix

The differentiation of the strain measures gives the strain-displacement matrix which is needed to compute the internal forces at the dofs from the stress in the element.

The differentiation of the longitudinal strain of the truss gives:

$$\delta\epsilon = \vec{\boldsymbol{r_T}}'\delta\left(\vec{\boldsymbol{r_T}}'\right) \tag{4.16}$$

and those of the strains and curvatures of the beam yields:

$$\delta\vec{\boldsymbol{\Gamma}} = \boldsymbol{R}^T\delta\vec{\boldsymbol{r_B}}' - \widetilde{\boldsymbol{R}^T\vec{\boldsymbol{r_B}}'}\boldsymbol{T}^T\delta\vec{\boldsymbol{\psi}} \qquad \delta\vec{\boldsymbol{K}} = \boldsymbol{T}\delta\left(\vec{\boldsymbol{\psi}}'\right) + \left(\tilde{\boldsymbol{K}}\boldsymbol{T} + \boldsymbol{T'}\right)\delta\vec{\boldsymbol{\psi}} \tag{4.17}$$

as defined in Eq. 2.29.

However, the terms $\delta\vec{\boldsymbol{r_T}}'$, $\delta\vec{\boldsymbol{r_B}}'$ and $\delta\vec{\boldsymbol{\psi}}'$, which only depend on the positional and rotation dofs in the Lagrangian description, also depend on the curvilinear abscissa dofs in the ALE description. Therefore, the variations will be perfectly defined once the terms $\delta\vec{\boldsymbol{r_T}}'$, $\delta\vec{\boldsymbol{r_B}}'$ and $\delta\vec{\boldsymbol{\psi}}'$ will be expressed using the shape functions (or their derivatives) and all the dofs.

For the term $\delta\vec{\boldsymbol{r_T}}'$:

$$\delta\vec{\boldsymbol{r_T}}' = \delta\boldsymbol{N}_{\boldsymbol{r_T}}\boldsymbol{q_T} + \boldsymbol{N}_{\boldsymbol{r_T}}\delta\boldsymbol{q_T} \tag{4.18}$$

where:

$$\delta\boldsymbol{N}_{\boldsymbol{r_T}} = \frac{\partial\boldsymbol{N}_{\boldsymbol{r_T}}}{\partial\boldsymbol{q_T}}\delta\boldsymbol{q_T} \tag{4.19}$$

$$= \frac{\partial\boldsymbol{N}_{\boldsymbol{r_T}}}{\partial\vec{\boldsymbol{r}}_1}\delta\vec{\boldsymbol{r}}_1 + \frac{\partial\boldsymbol{N}_{\boldsymbol{r_T}}}{\partial s_1}\delta s_1 + \frac{\partial\boldsymbol{N}_{\boldsymbol{r_T}}}{\partial\vec{\boldsymbol{r}}_2}\delta\vec{\boldsymbol{r}}_2 + \frac{\partial\boldsymbol{N}_{\boldsymbol{r_T}}}{\partial s_2}\delta s_2 \tag{4.20}$$

which gives:

$$\delta\vec{\boldsymbol{r_T}}' = \begin{bmatrix} N_1'\boldsymbol{I}_{3\times3} & -\frac{\vec{r}_2-\vec{r}_1}{(s_2-s1)^2} & N_2'\boldsymbol{I}_{3\times3} & \frac{\vec{r}_2-\vec{r}_1}{(s_2-s1)^2}\end{bmatrix}\delta\boldsymbol{q_T} \tag{4.21}$$

The same procedure is applied for the term $\delta\vec{\boldsymbol{r_B}}'$, which yields:

$$\delta\vec{\boldsymbol{r_B}}' = \begin{bmatrix} N_1'\boldsymbol{I}_{3\times3} & \boldsymbol{0}_{3\times3} & -\frac{\vec{r}_2-\vec{r}_1}{(s_2-s1)^2} & N_2'\boldsymbol{I}_{3\times3} & \boldsymbol{0}_{3\times3} & \frac{\vec{r}_2-\vec{r}_1}{(s_2-s1)^2}\end{bmatrix}\delta\boldsymbol{q_B} \tag{4.22}$$

Replacing $\vec{\boldsymbol{r}}$ with $\vec{\boldsymbol{\psi}}$ gives:

$$\delta\vec{\boldsymbol{\psi}}' = \begin{bmatrix} \boldsymbol{0}_{3\times3} & N_1'\boldsymbol{I}_{3\times3} & -\frac{\vec{\psi}_2-\vec{\psi}_1}{(s_2-s1)^2} & \boldsymbol{0}_{3\times3} & N_2'\boldsymbol{I}_{3\times3} & \frac{\vec{\psi}_2-\vec{\psi}_1}{(s_2-s1)^2}\end{bmatrix}\delta\boldsymbol{q_B} \tag{4.23}$$

Therefore, the strain-displacement matrix of the ALE truss, linking the variation of strain with the variation of the dofs ($\epsilon = \boldsymbol{B_T}\boldsymbol{q_T}$), is:

$$\underset{(1\times8)}{[\boldsymbol{B_T}]} = \begin{bmatrix} -\frac{\vec{r}_2-\vec{r}_1}{(s_2-s_1)^2} & -\frac{\|\vec{r}_2-\vec{r}_1\|^2}{(s_2-s_1)^3} & \frac{\vec{r}_2-\vec{r}_1}{(s_2-s_1)^2} & \frac{\|\vec{r}_2-\vec{r}_1\|^2}{(s_2-s_1)^3}\end{bmatrix} \tag{4.24}$$

For those of the beam element, only the interpolation matrix $\boldsymbol{Q}$ defined in Eq. 2.37 is modified as:

$$\underset{(9\times1)}{\begin{bmatrix}\delta\vec{\boldsymbol{r_B}}' \\ \delta\vec{\boldsymbol{\psi}}' \\ \delta\vec{\boldsymbol{\psi}}\end{bmatrix}} = \underbrace{\begin{bmatrix} N_1'\boldsymbol{I}_{3\times3} & \boldsymbol{0}_{3\times3} & -\frac{\vec{r}_2-\vec{r}_1}{(s_2-s_1)^2} & N_2'\boldsymbol{I}_{3\times3} & \boldsymbol{0}_{3\times3} & \frac{\vec{r}_2-\vec{r}_1}{(s_2-s_1)^2} \\ \boldsymbol{0}_{3\times3} & N_1'\boldsymbol{I}_{3\times3} & -\frac{\vec{\psi}_2-\vec{\psi}_1}{(s_2-s_1)^2} & \boldsymbol{0}_{3\times3} & N_2'\boldsymbol{I}_{3\times3} & \frac{\vec{\psi}_2-\vec{\psi}_1}{(s_2-s_1)^2} \\ \boldsymbol{0}_{3\times1} & \boldsymbol{0}_{3\times3} & N_1\boldsymbol{I}_{3\times3} & \boldsymbol{0}_{3\times3} & N_2\boldsymbol{I}_{3\times3} & \boldsymbol{0}_{3\times1}\end{bmatrix}}_{\boldsymbol{Q}\ (9\times14)} \underset{(14\times1)}{\begin{bmatrix}\delta\vec{\boldsymbol{r}}_1 \\ \delta\vec{\boldsymbol{\psi}}_1 \\ \delta s_1 \\ \delta\vec{\boldsymbol{r}}_2 \\ \delta\vec{\boldsymbol{\psi}}_2 \\ \delta s_2\end{bmatrix}} \tag{4.25}$$

with $\boldsymbol{B_B} = \boldsymbol{DQ}$ where D is defined in Eq. 2.29.

4.2.1.4 Constitutive law

A linear elastic truss is considered. Consequently, the Cauchy stress is defined as:

$$\sigma = E\epsilon \tag{4.26}$$

where E is the Young's modulus of the truss material.

The constitutive law of the ALE beam is defined in section 2.2.1.7.

4.2.1.5 Internal forces

For both elements, the internal forces are defined as:

$$\underset{(8\times1)}{[\boldsymbol{F_{int_T}}]} = \int_0^{\bar{L}} \boldsymbol{B_T^T}\sigma ds \qquad \underset{(14\times1)}{[\boldsymbol{F_{int_B}}]} = \int_0^{\bar{L}} \boldsymbol{B_B^T} \begin{bmatrix} \vec{\boldsymbol{F}} \\ \vec{\boldsymbol{M}} \end{bmatrix} ds \tag{4.27}$$

where $\bar{L}$ is the current unstretched length of the element defined through the mass conservation:

$$\bar{L} = s_2 - s_1 \tag{4.28}$$

4.2.1.6 Additional inertia forces

Since the curvilinear abscissa are time-varying, the mass of the element varies too. This mass variation implies additional inertia forces which are detailed in Peng et al. (2017) and Liu et al. (2018). In particular, the equation of dynamics becomes:

$$\boldsymbol{M\ddot{U}} + \boldsymbol{\dot{M}\dot{U}} - \boldsymbol{mU} + \boldsymbol{C\dot{U}} + \boldsymbol{F_{int}} = \boldsymbol{F_{ext}} \tag{4.29}$$

where $\boldsymbol{\dot{M}\dot{U}} - \boldsymbol{mU}$ corresponds to the additional inertia forces. In this work, since TFP preform forming is achieved under the quasi-static assumption, these inertia forces are neglected and the equation of dynamics reduces to Eq. 2.8.

4.2.1.7 Material flow and friction forces

Finally, for better post-processing of the results, the curvilinear abscissa dofs can be replaced by material flow dofs U_s (without modification of the previous developments), which represent the displacement of matter through the mesh. It is defined by:

$$U_s = s - S \tag{4.30}$$

where s is the current curvilinear abscissa and S is the initial curvilinear abscissa (This is equivalent to using displacements or positions as dofs). This allows a direct visualisation of the material flow in the mesh.

The material flow can be subjected to external forces arising from friction between cable and pulley for instance. In case of a pulley-cable system, at the pulley node, the Capstan equation applies:

$$\begin{cases} T_2 = e^{-\mu\theta}T_1 & \text{if } V_s > 0 \\ e^{-\mu\theta} < \frac{T_2}{T_1} < e^{\mu\theta} & \text{if } V_s = 0 \\ T_2 = e^{\mu\theta}T_1 & \text{if } V_s < 0 \end{cases} \tag{4.31}$$

where T_i is the tension in the adjacent elements of the pulley node, μ is the friction coefficient and θ the angle defined in Fig. 4.14. V_s is the velocity of the material through the mesh.

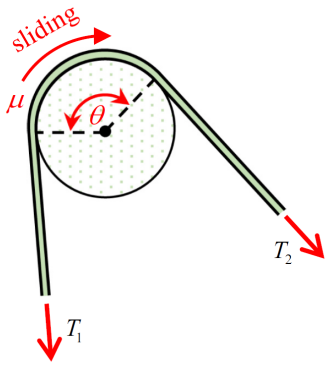

Figure 4.14: Friction law at a pulley node (from Kan et al. (2021))

The advantage of the explicit formulation is the flexibility concerning the implementation of friction laws. In Kan et al. (2021), the implicit formulation requires a specific method leading to cumbersome computations to take into account the step-like friction law of a pulley. Therefore, other friction laws such as static or dynamic Coulomb friction laws can be easily implemented with the chosen formulations.

Transition

This section introduced the formulation of an ALE truss and an ALE beam element which will be used to take into account fibre tow slippage in the TFP preform models. However, before addressing some numerical elementary test cases and integrating these finite elements in the TFP preform models, the degeneration of the proposed 1D ALE element into Eulerian and Lagrangian elements is presented. This allows a better understanding of both the modelling and the boundary conditions which will be used in the numerical validation.

4.2.2 Boundary conditions and degeneration of the 1D ALE elements into Eulerian and Lagrangian elements

4.2.2.1 Example of rigid body motions

Before presenting elementary test cases, boundary conditions have to be explained. Since the element has material flow dofs at both nodes, it allows more boundary conditions than the 3-node cable-pulley element by Aufaure (2000) or the multi-sliding node element by Coulibaly et al. (2018). In this element the material flow, also named slip displacement, can be prescribed at both nodes.

Eulerian degeneration In the Eulerian case, the nodes of a single element are fixed in space (U_{ij} are zeros) and a slip displacement c is applied on node 2 (Fig. 4.15 (a)). In this particular case, since the mesh is fixed in space and the material flows through it, the nodes can be seen as Eulerian nodes. If no external forces limit the slip displacement, then no deformation will appear since both $\bar{L}$ and l are kept constant (U_{s_1} will equal U_{s_2}). If an external force limits the flow at one node, then U_{s_1} will be different from U_{s_2} and consequently $\bar{L}$ will change implying longitudinal deformation of the element.

Lagrangian degeneration Now, if the slip displacement are set to zero and a spatial displacement is imposed on node 2 while node 1 is free (Fig. 4.15 (b)), the element will simply translate and the nodes can be seen as Lagrangian since they are attached to the material. If node 1

is now fixed, by applying a spatial displacement on node 2, deformation will occur due to the modification of l while $\bar{L}$ is kept constant due to zero material flow.

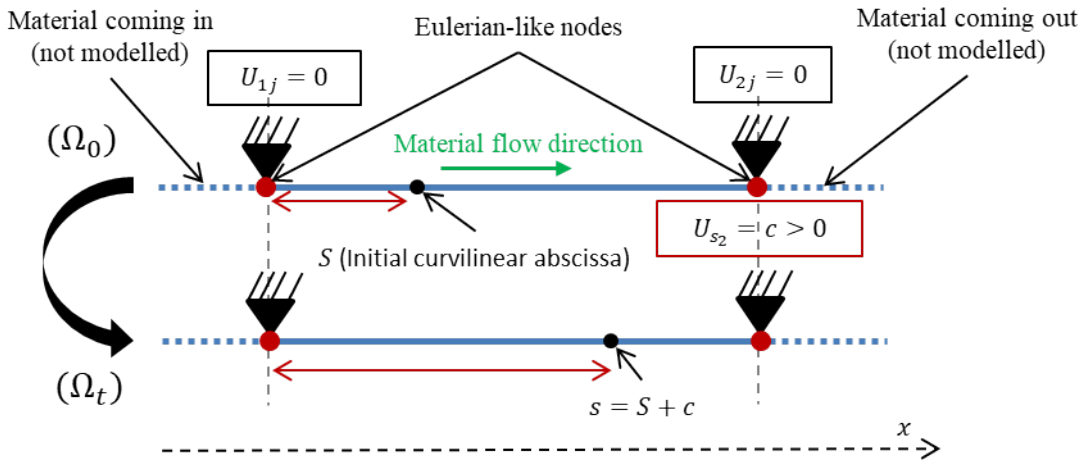

(a) Eulerian rigid body translation

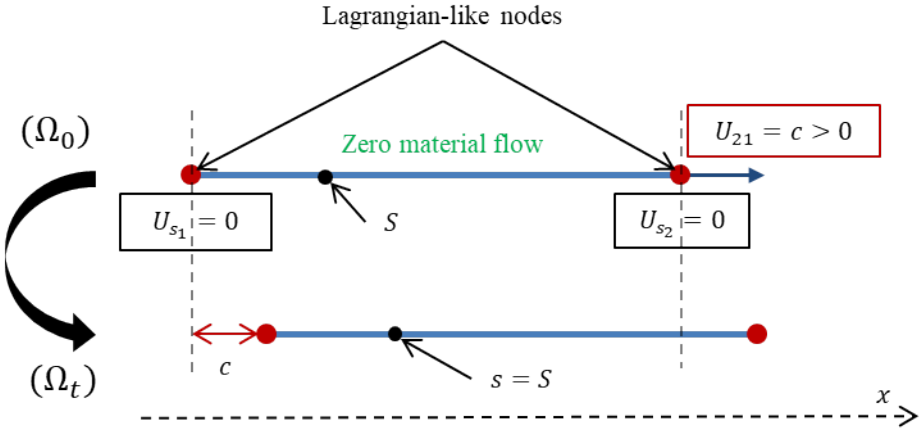

(b) Lagrangian rigid body translation

Figure 4.15: Example of rigid body motions for the Eulerian and Lagrangian degenerated cases

These rigid body motions illustrate the degeneration of the ALE element to either an Eulerian or Lagrangian element. More generally, in models using 1D ALE elements, depending on the boundary conditions, some nodes will behave like Eulerian nodes, some other as Lagrangian nodes and others as ALE nodes.

4.2.2.2 Simplification

By using slip displacement degrees of freedom, a lot of flexibility is offered. For instance, extremities of fibre tows, which do not need to be modelled explicitly, can be simplified to allow the matter to flow in or out as illustrated in Fig. 4.16 in case of Model I.

Transition

This section gave an insight into the modelling possibilities and flexibility offered by the 1D ALE elements. Before integrating them into the TFP preform models, a numerical validation is addressed in the next section.

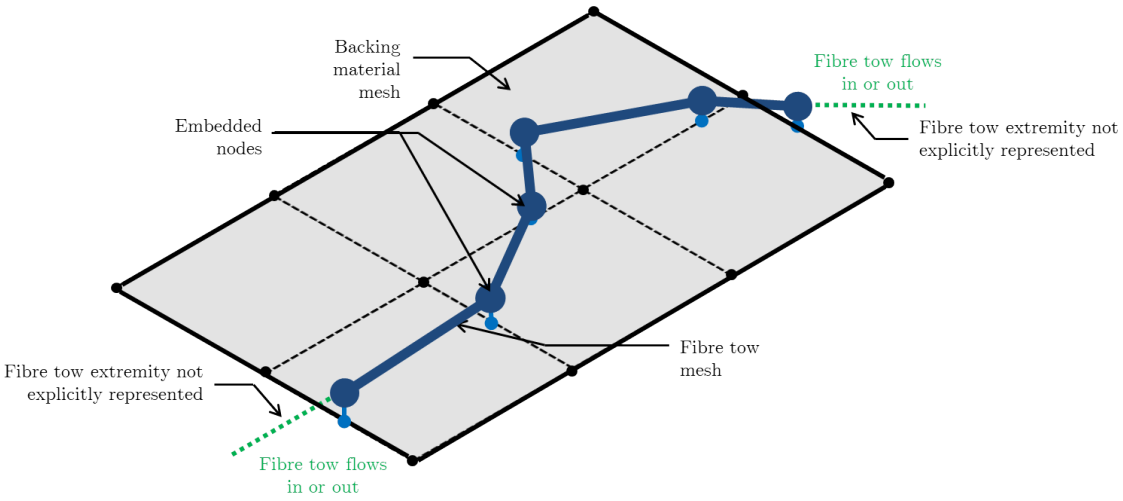

Figure 4.16: Simplifying the representation of the fibre tow extremities in Model I

4.2.3 Numerical validation of the ALE truss

Most of the 1D ALE element formulations found in the literature are based on a truss element used in cable-pulley systems. Consequently, there are numerous validation test cases for the truss element which are addressed in the following. In particular, the objectives of this validation test cases is to check the consistency of the material flow and the absence of deformation when the matter in the elements is not subjected to any constraint.

4.2.3.1 Cable with a fixed pulleys

Objectives This first test aims at showing the kinematics of a cable anchored at one end and pulled at the other end. In this test, the material flow direction should not change and the pulley node should behave as an Eulerian node. Cases with and without friction are analysed.

Set-up A cable is lying on a pulley. The left end is anchored while a point load is applied on the other end. The left part of the cable is horizontal while the right part is vertical. Fig. 4.17 shows the configuration of the cable (left) and its finite element model (right). Both parts of the cable have same length (L =1 m) and a point load of 100 N is applied along the y-direction. The cable has a tensile modulus of 100 GPa. In the friction case, the coefficient μ of the pulley is such that the tension in the vertical part of the cable equals twice those of the horizontal part.

Results Fig. 4.18 shows the mesh and slip displacements for the frictionless case. The mesh displacement of the horizontal part of the cable is null since both nodes are fixed while the 3$^{\text{rd}}$ node has a vertical displacement of 2 10^{-2} mm. The slip displacement of the pulley node equals half the mesh displacement of the loaded node. Both elements have the same longitudinal deformation ($\epsilon = 10^{-3}$) which means that the cable freely slips in the pulley node.
In case of friction, the vertical part has a deformation of 10^{-3} while the horizontal part has a deformation of $\epsilon = 5\ 10^{-4}$. Therefore, the tension ratio between the vertical and horizontal parts equals 2, which agrees with the selected friction coefficient of the pulley. Moreover the displacement of the loaded node is smaller (1.5 10^{-2} mm) than the frictionless case which is consistent with the dissipation of energy due to friction from the pulley.

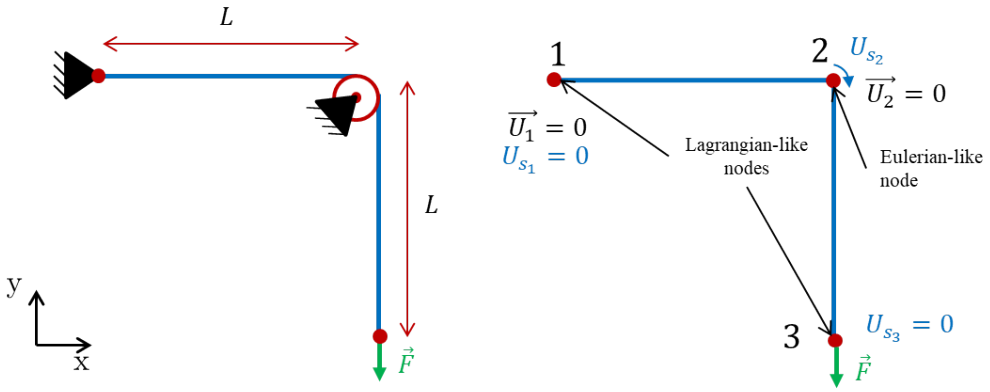

Figure 4.17: Pulling anchored rope with a pulley: rope configuration (left) and finite element model (right)

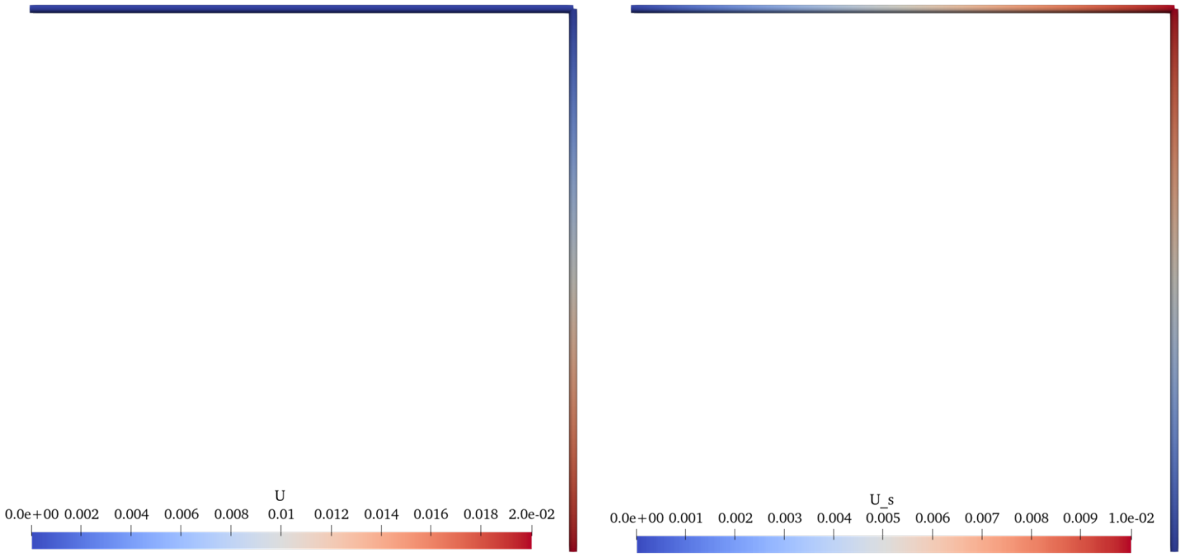

(a) Mesh displacement (mm)

(b) Slip displacement (mm)

Figure 4.18: Pulling anchored rope with a pulley: frictionless case

4.2.3.2 Pulley oscillating on a cable

Objectives This second test case aims at showing the kinematics of a pulley oscillating on a cable due to gravity. Without friction, the pulley is supposed to oscillate continuously without loss of energy while in case of a friction pulley, its movement is supposed to be damped until it stops. In particular, the material flow direction will change.

Set-up The positions of the cable ends are fixed while a pulley is placed in a non equilibrium position such that oscillations start due to gravity as shown in Fig. 4.19. The distance d equals 1 m, h is 0.15 m and v is 0.3 m. The cable has a tensile modulus of 100 GPa. In the friction case, μ =0.05.

Results As shown in Fig. 4.20, in the frictionless case, the pulley is oscillating without energy loss. Moreover the deformation of the elements oscillates around 10^{-6}, which is negligible. With friction, the pulley movement is damped as expected (Fig. 4.21)

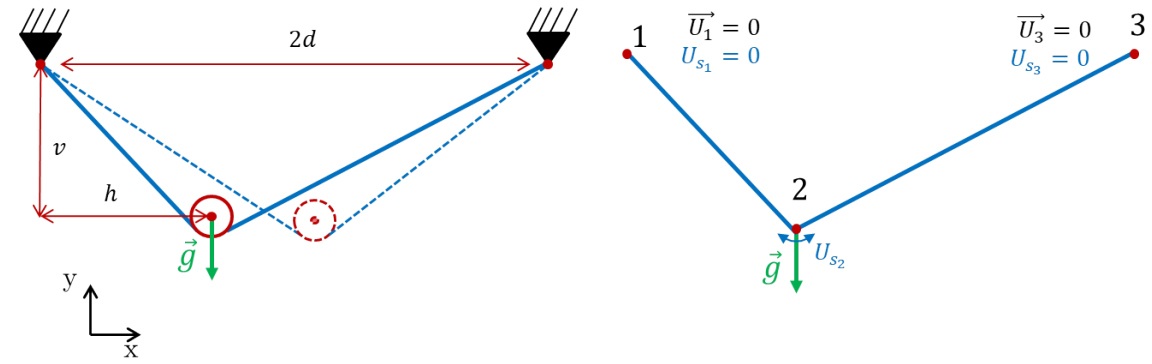

Figure 4.19: Oscillating pulley: initial (solid line) and intermediary (dash line) system configurations (left) and finite element model (right)

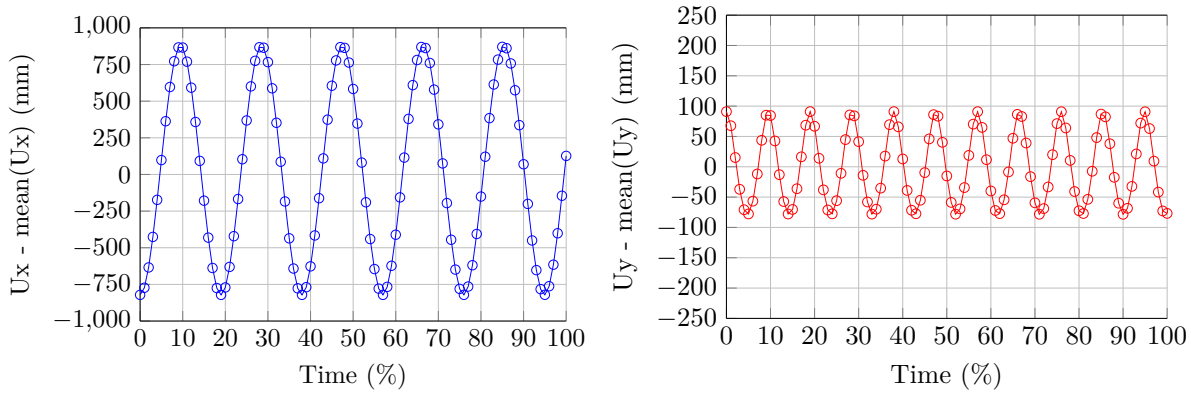

(a) Centered x-displacement (mm) **(b)** Centered y-displacement (mm)

Figure 4.20: Frictionless oscillating pulley: displacements

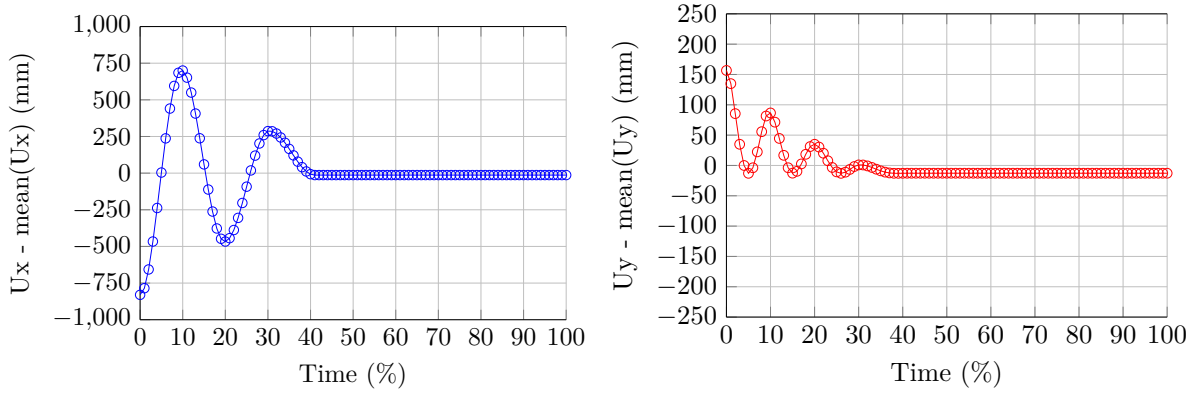

(a) Centered x-displacement (mm) **(b)** Centered y-displacement (mm)

Figure 4.21: Oscillating pulley with friction: displacements

4.2.3.3 Cable passing through two fixed pulleys

Objectives In the previous test, material flow occurred in one node only. In this third test, which is discussed in Kan et al. (2019), two pulleys are considered. Moreover, loading and unloading steps are successively applied to check that the different possible status of a pulley are modelled accurately.

Set-up A cable is anchored at one end and passes through two fixed pulleys as illustrated in Fig. 4.22. The lengths L_1 and L_3 equal 1 m and L_2 is 0.4 m. A point load of 30 kN is applied to the other end along the x-direction. The loading step is followed by unloading. The cable has a tensile modulus of 115 GPa and the friction coefficient of the pulleys μ is 0.05.

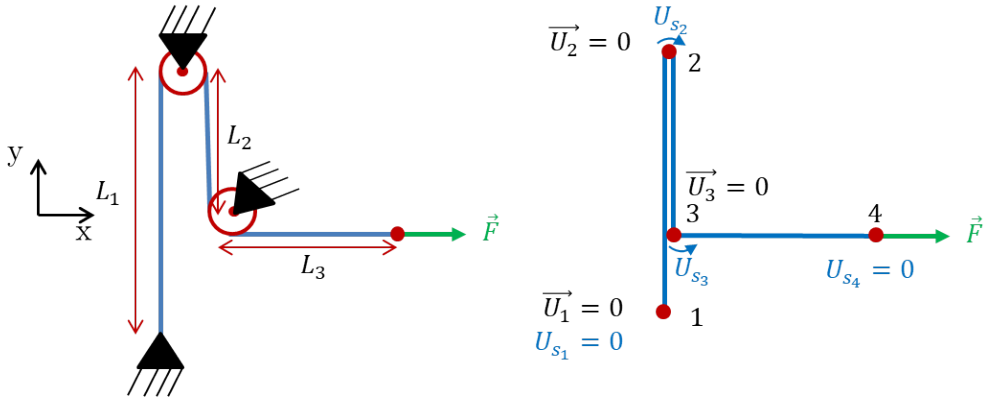

Figure 4.22: Cable with two fixed pulleys: system configuration (left) and finite element model (right)

Results The results are shown in Fig. 4.23. During the loading step, the tension in the element 2 is smaller than that of element 3 and the tension in element 1 is smaller than that of element 2 as a result of the friction at the pulleys (Fig. 4.23 (a)). When the unloading step starts, the two pulleys stick. Therefore, only the tension in element 3 decreases. Then, once the tension ratio between element 2 and element 3 overcomes the thresholds, slip starts again at the second pulley. The same applies to the first pulley with an additional delay. When slip occurs in both pulleys during the unloading step, the tension ratios are inverted compared to the loading step. In Fig. 4.23 (b), the different states of the pulleys, as expressed in Eq. 4.31, are plotted. The sticky state can be observed directly on the slip displacement curves (Fig. 4.23 (c)).

4.2.3.4 Ten pulleys system with loaded cable end (ALE truss)

Objectives This referenced test is similar to the first test, except that ten pulleys are involved and that the results will be compared with those by Kan et al. (2021).

Set-up A cable passes through ten pulleys as depicted in Fig. 4.24. The curved arrows show the positive direction of slip displacement. The pulleys are fixed in space. The left end is fixed while a vertical displacement of -0.01 m is applied to the other end along the y-direction. The length of each segment is 1 m and the cable has a tensile stiffness of 10^8 N.

Results The slip displacements at the pulleys reported in Table 4.3 show very good agreement with the referenced results.

Table 4.3: Ten pulleys system with loaded cable end: comparison of the slip displacements

Slip displacement	U_{s_2}	U_{s_3}	U_{s_4}	U_{s_5}	U_{s_6}	U_{s_7}	U_{s_8}	U_{s_9}	$U_{s_{10}}$	$U_{s_{11}}$
Present study	$4.941\ 10^{-6}$	$1.474\ 10^{-5}$	$3.433\ 10^{-5}$	$7.351\ 10^{-5}$	$1.518\ 10^{-4}$	$3.085\ 10^{-4}$	$6.211\ 10^{-4}$	$1.246\ 10^{-3}$	$2.497\ 10^{-3}$	$4.997\ 10^{-3}$
Kan et al. (2021)	$4.877\ 10^{-6}$	$1.463\ 10^{-5}$	$3.414\ 10^{-5}$	$7.315\ 10^{-5}$	$1.512\ 10^{-4}$	$3.072\ 10^{-4}$	$6.192\ 10^{-4}$	$1.243\ 10^{-3}$	$2.490\ 10^{-3}$	$4.981\ 10^{-3}$

4.2.3.5 Ten pulleys system with symmetric boundary conditions

Objectives This referenced test aims at checking the symmetry of the slip displacement in case of symmetric boundary conditions.

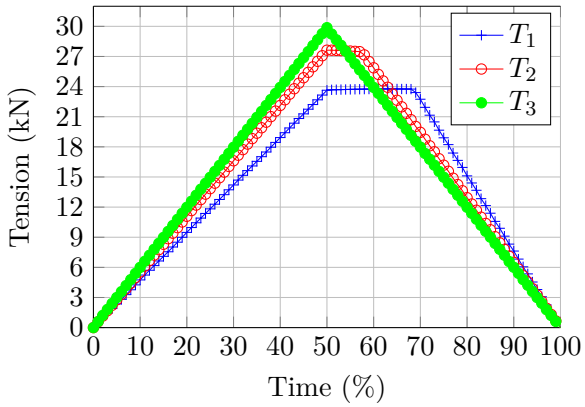

(a) Tension in elements (kN)

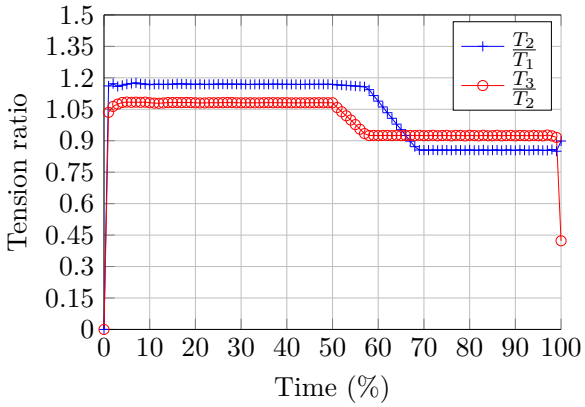

(b) Tension ratio between adjacent elements

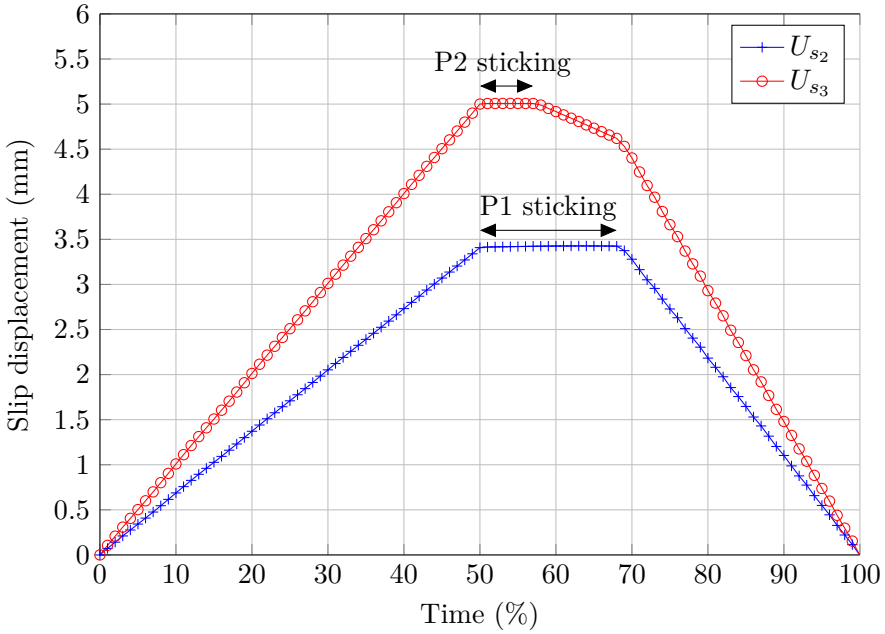

(c) Slip displacement in pulleys P1 and P2

Figure 4.23: Cable with two fixed pulleys

Set-up This configuration is similar to the previous test (Fig. 4.25). However, both cable ends are fixed and the 6^{th} and 7^{th} pulleys are displaced along the y-direction with a value of 0.01 m.

Results The slip displacements at the pulleys reported in Table 4.4 show very good agreement with the referenced results and the symmetry is obtained.

4.2.3.6 Static coulomb friction

Objectives The last test for the ALE truss aims at showing that other friction laws can be implemented. For instance, the static Coulomb friction law is tested.

Set-up The left end of a horizontal cable is free while a displacement of 10 mm is applied to the right end along the x-direction. A smooth S-shape curve is used to imposed the displacement rather than a ramp. The cable is meshed using 2 elements and a static Coulomb friction law is applied at the middle node. The cable has a length of 1 m and a tensile modulus of 100 GPa. A virtual normal force is applied on the middle node such that slip occurs when the tensile

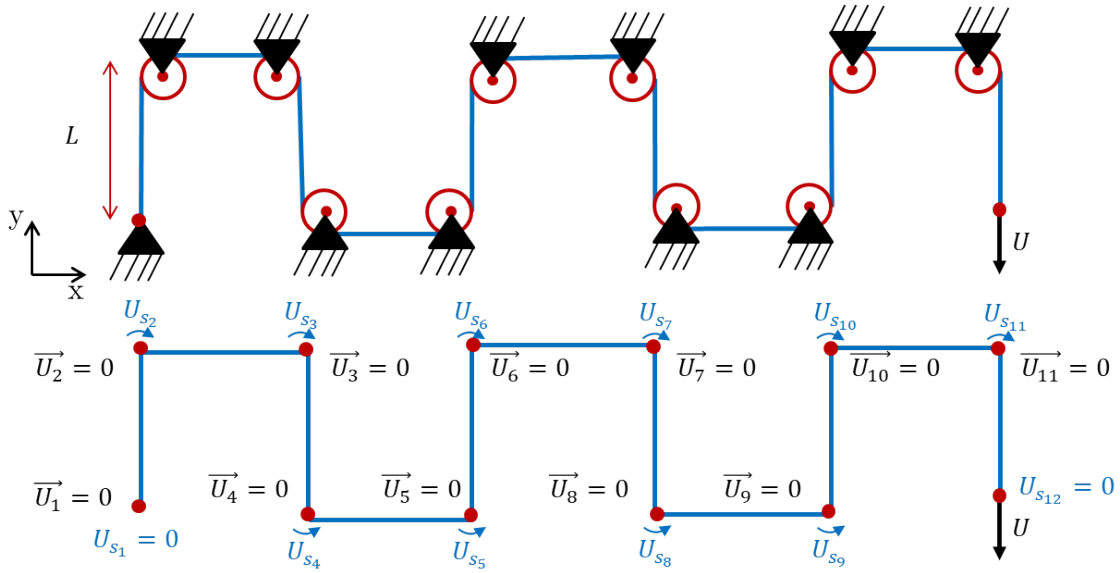

Figure 4.24: Ten pulleys system with loaded cable end: system configuration (top) and finite element model (bottom)

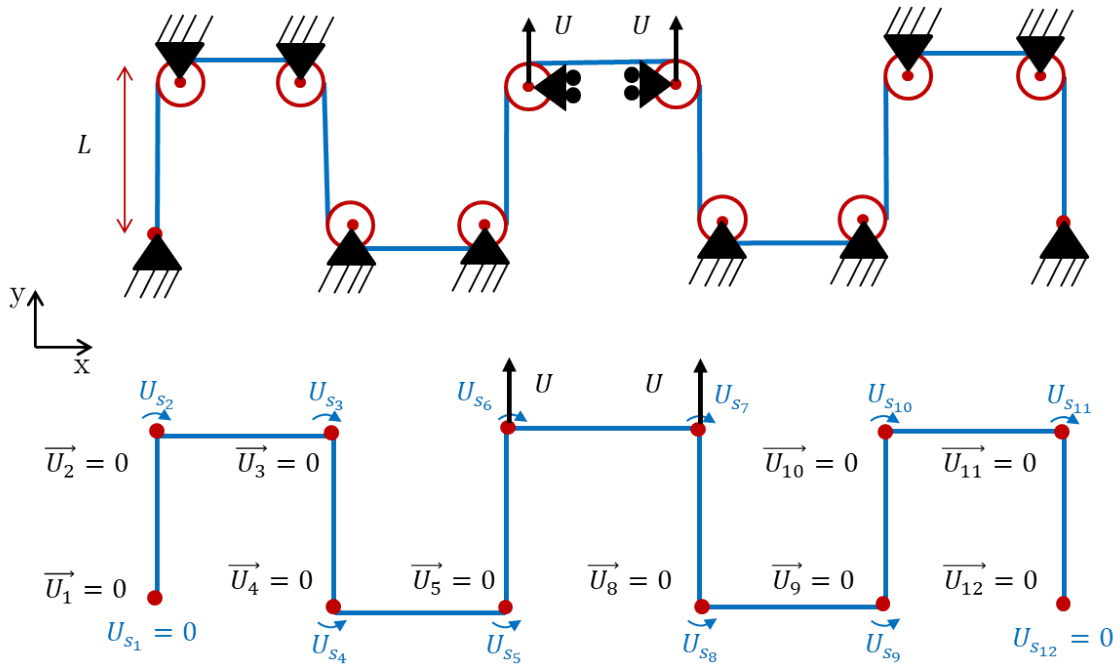

Figure 4.25: Ten pulleys system with symmetric boundary conditions: system configuration (top) and finite element model (bottom)

stiffness of the right element reaches 200 N.

Results The results are shown in Fig. 4.27. The tension of the second element increases progressively due to the displacement of the right end until reaching the friction threshold of the middle node (200 N) (Fig. 4.27 (a)). Then, the cable starts slipping in the middle node. Due to the deformation of the second element, a difference is observed between the displacement of the left (U_{3x}) and right (U_{3x}) end. The slip displacement U_{s_2} and the left end displacement U_{1x} are equal, which is consistent.

Table 4.4: Ten pulleys system pulling cable end: comparison of the slip displacements

Slip displacement	U_{s_2}	U_{s_3}	U_{s_4}	U_{s_5}	U_{s_6}	U_{s_7}	U_{s_8}	U_{s_9}	$U_{s_{10}}$	$U_{s_{11}}$
Present study	$2.857\ 10^{-4}$	$8.571\ 10^{-4}$	$1.999\ 10^{-3}$	$4.285\ 10^{-3}$	$-1.142\ 10^{-3}$	$1.142\ 10^{-3}$	$-4.285\ 10^{-3}$	$-1.999\ 10^{-3}$	$-8.571\ 10^{-4}$	$-2.857\ 10^{-4}$
Kan et al. (2021)	$2.852\ 10^{-4}$	$8.554\ 10^{-4}$	$1.995\ 10^{-3}$	$4.272\ 10^{-3}$	$-1.138\ 10^{-3}$	$1.138\ 10^{-3}$	$-4.272\ 10^{-3}$	$-1.995\ 10^{-3}$	$-8.554\ 10^{-4}$	$-2.852\ 10^{-4}$

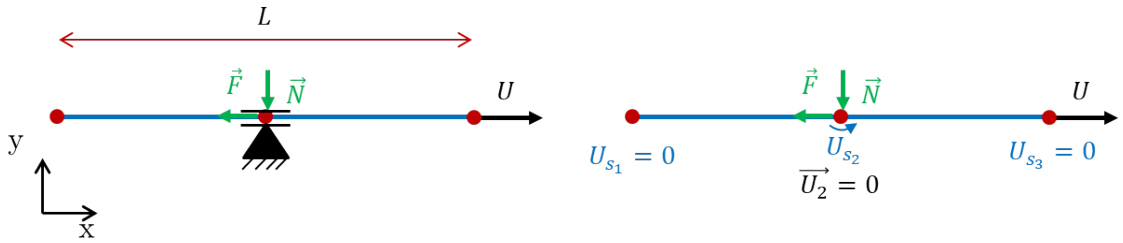

Figure 4.26: Static coulomb friction: system configuration (left) and finite element model (right)

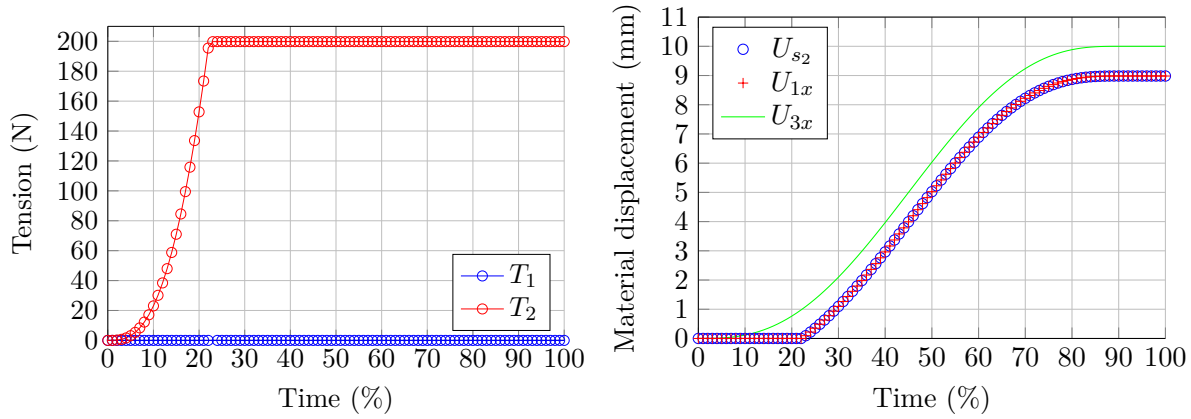

(a) Tension in elements

(b) Slip displacement at the middle node and displacement of the cable ends

Figure 4.27: Static coulomb friction

Transition

This section addressed the numerical validation of the ALE truss. Since this element was developed in the field of pulley-cable system, the Capstan friction law was mainly used in the numerical test. However, other friction law can be implemented such as the static Coulomb friction law. The next section addressed some elementary numerical tests to validate the implementation of the ALE beam element.

4.2.4 Numerical validation of the ALE beam

For the ALE beam, only one reference (Liu et al., 2018) was found. Moreover, they used this element to model beams running through tubes in drilling engineering and developed specific validation test cases which are not really appropriate for the TFP preform models. Consequently, only elementary test cases are addressed for the ALE beam element.

4.2.4.1 Twisting followed by translation

Objectives The first test aims at checking that the state of the cross-section in the beam is not influenced by a translation implying a slip displacement.

Set-up A two-step loading is applied on a horizontal beam represented using two elements (Fig. 4.28). In the first step, the rotation along the axis of the beam is fixed at the left end of the beam while a twisting moment is applied at the other end. This step will create a linear field of twisting angle along the beam. In the second step, the beam is translated by applying a displacement of 0.25 m along the x-direction to its right end. A slip displacement occurs in the middle node, which is fixed in space (acts as a slider).

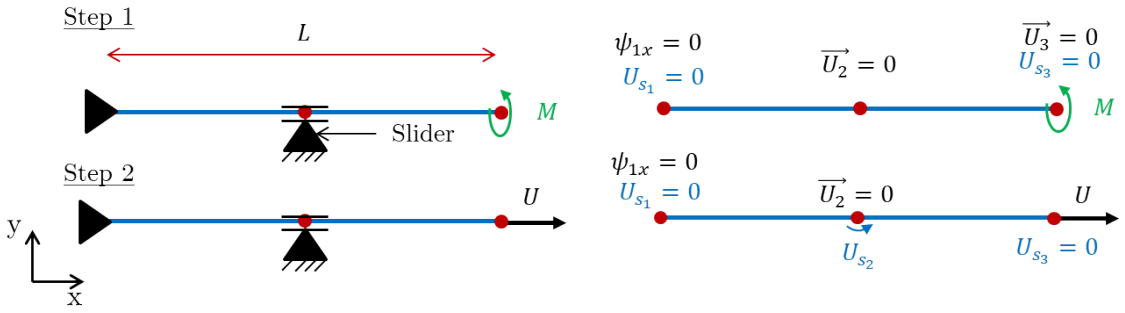

Figure 4.28: Twisting and translation: system configuration (left) and finite element model (right)

Results The results are shown in Fig. 4.29. During the first step, the twisting angle of the middle node equal half the value at the loaded node, which is consistent. Then, during the translation step, due to the slip displacement, the twisting angle of the middle node decreases until reaching the fourth of the left beam end value since the middle node is now located at 25% of the beam length (Fig. 4.29 (a)). Fig. 4.30 shows the twisting angle field at the end of the two steps. This field stays constant during the slip displacement as expected. Fig. 4.29 (b) shows that there is no deformation in the beam since the material displacement of the nodes are equal.

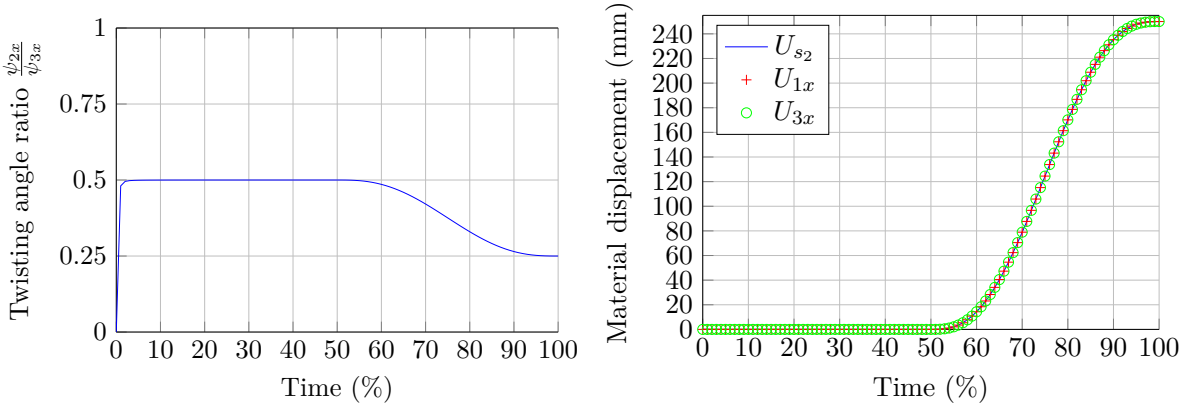

(a) Twisting angle ratio

(b) Material displacement of the beam nodes

Figure 4.29: Twisting and translation

4.2.4.2 Cantilever beam under transverse tip load

Objectives This test is similar to Test 2.2.3.3 for the Lagrangian beam. The difference is that the middle nodes are ALE nodes whose positions along the x-direction are fixed. This constraint is supposed to lead to a material flow in the mesh to reproduce the kinematics observed for the Lagrangian beam.

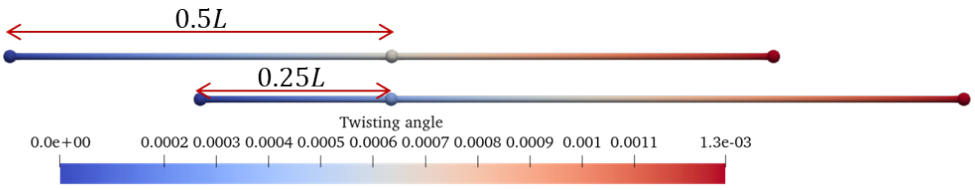

Figure 4.30: Twisting angle: configuration at the end of step 1 (top) and step 2 (bottom)

Set-up Fig. 4.31 shows the initial configuration. The parameters are identical to those of Test 2.2.3.3. The beam is meshed with 10 elements. Therefore, nodes 2 to 9 are ALE nodes whose x-coordinates are fixed. Small and large displacements are considered too using loading values of 100 N and 10^6 N respectively.

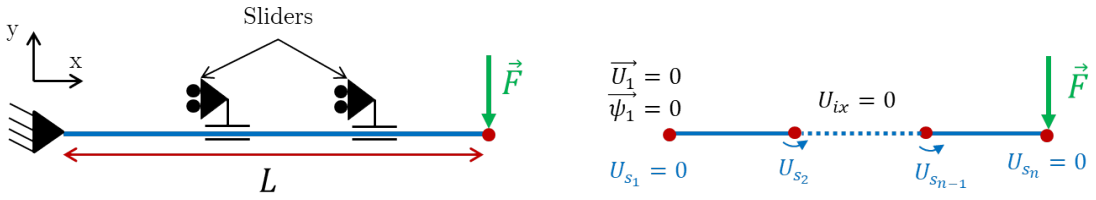

Figure 4.31: Cantilever beam under transverse tip load: system configuration (left) and finite element model (right)

Results Fig. 4.32 shows different configurations of the large displacement case as well as the slip displacement. The tip displacements and rotation are reported and compared with the Lagrangian beam in Table 4.5. The values agree well for the small displacement case and slightly differ in the large displacement case. Therefore, the flow of material generated by fixing the x-coordinates of the middle nodes allows recovering the kinematics of the Lagrangian beam.

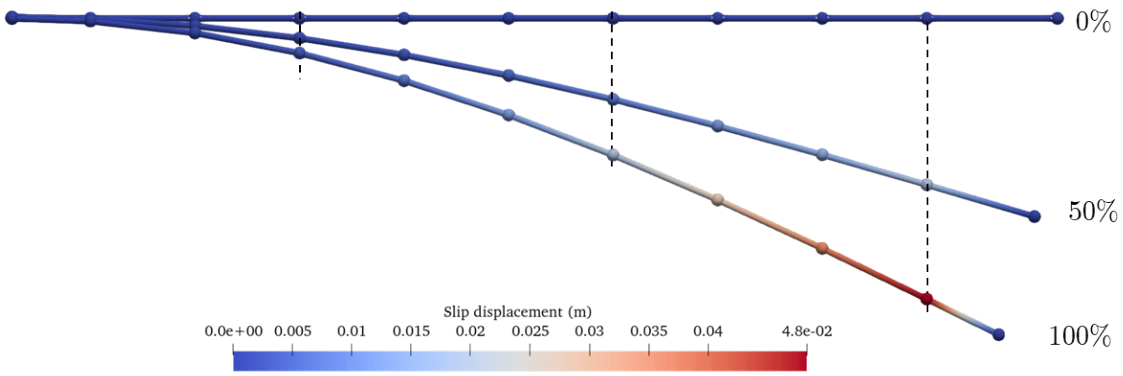

Figure 4.32: Cantilever beam under transverse tip load: different configurations for the large displacement case and slip displacement

4.2.4.3 Cantilever beam under tip moment

Objectives This test is similar to Test 2.2.3.4 for the Lagrangian beam. As the previous test, the difference lies in the fact that the middle nodes are ALE nodes whose positions along the x-direction are fixed. Similarly, this constraint is supposed to lead to a material flow in the mesh to reproduce the kinematics observed for the Lagrangian beam.

Table 4.5: Cantilever beam under transverse tip load: comparison of tip displacements and rotation with the Lagrangian beam

Loading case	$F = 100$ N			$F = 10^6$ N		
Tip values	U_x	U_y	ψ_z	U_x	U_y	ψ_z
ALE beam	$-6.314\ 10^{-10}$	$-3.251\ 10^{-5}$	$-4.850\ 10{-}5$	-0.0562	-0.302	-0.458
Lagrangian beam	$-6.299\ 10^{-10}$	$-3.252\ 10^{-5}$	$-4.850\ 10{-}5$	-0.0537	-0.296	-0.449

Set-up Fig. 4.33 shows the initial configuration. The parameters are identical to those of Test 2.2.3.4. The beam is meshed with 10 elements. Therefore, nodes 2 to 9 are ALE nodes whose x-coordinates are fixed. Small and large displacements are considered too using loading values of 100 N and 5 10^5 N respectively.

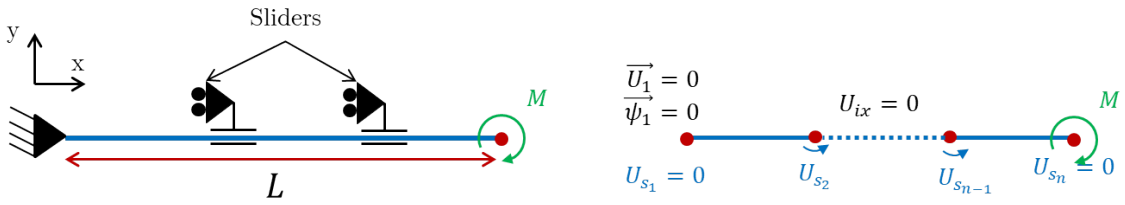

Figure 4.33: Cantilever beam under tip moment: system configuration (left) and finite element model (right)

Results Fig. 4.34 shows different configurations of the large displacement case as well as the slip displacement. The tip displacements and rotation are reported and compared with the Lagrangian beam in Table 4.6. The values agree well for both cases. Moreover, for this pure bending test, the longitudinal deformation of the beam elements is negligible (10^{-12}), which is consistent. Therefore, as the previous test, the flow of material generated by fixing the x-coordinates of the middle nodes allows recovering the kinematics of the Lagrangian beam.

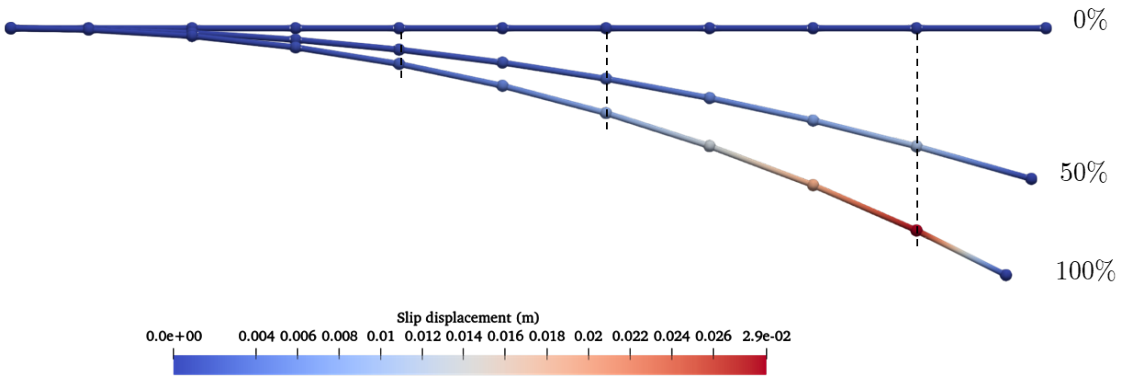

Figure 4.34: Cantilever beam under tip moment: different configurations for the large displacement case and slip displacement

Table 4.6: Cantilever beam under tip moment: comparison of tip displacements and rotation with the Lagrangian beam

Loading case	$F = 100$ N			$F = 5\ 10^5$ N		
Tip values	U_x	U_y	ψ_z	U_x	U_y	ψ_z
ALE beam	$-1.564\ 10^{-9}$	$-4.850\ 10^{-5}$	$-9.701\ 10{-}5$	-0.0386	-0.2378	-0.4850
Lagrangian beam	$-1.564\ 10^{-9}$	$-4.850\ 10^{-5}$	$-9.701\ 10{-}5$	-0.0386	-0.2378	-0.4850

Conclusion

This section presented the formulation of two 1D ALE elements, namely a 2-node elastic truss and a 2-node shear flexible linear elastic beam. These elements can model material flow, which will allow modelling fibre tow slippage in the enhanced TFP preform models. Numerical tests were addressed for these two elements and validated their formulation and implementation in the explicit finite element solver. Even if a beam element is used in the TFP preform models to represent the fibre tows, an ALE truss is also considered for cases where the bending contribution of the fibre tows might be negligible.
Fibre tow slippage in fibrous reinforcements is subjected to complex contact interactions. The friction law, which constraints the material flow in the ALE elements of the enhanced TFP preform models, is unknown. Consequently, carrying out the characterisation of fibre tow slippage in TFP preforms is required. The next section addresses the characterisation of the friction law when fibre tows slip over the backing material.

4.3 Characterisation of the fibre tow slippage in TFP preforms based on pull-out experiments

Introduction

This section deals with the characterization of the friction behaviour between the fibre tows and the two other constituents of TFP preforms, namely the stitching yarn and the backing material. Experimental and numerical studies of the friction forces implied during fibre slippage in conventional textiles have already been carried out. The pull-out test is a well-established method to characterize the friction behaviour. In this work, a literature review was made on the pull-out test used for woven fabrics. Next, the pull-out device developed for the characterisation of the friction behaviour of the fibre tows in TFP preforms with backing material is presented. The design and manufacturing of the TFP samples are detailed. A developed image processing tool allows a real-time checking of the camera settings before proceeding with the pull-out test. Finally, the parametric study, which has been carried out to analyse the influence of the stitching parameters, allows formulating an analytical friction law to model fibre tow slippage in TFP preforms with backing material.
Therefore, the objectives of this section are:

- Characterize the friction forces applied to the fibre tows when slippage occurs due to tow-tow, tow-backing material and tow-stitching yarn interactions
- Identify and propose an analytical friction model to be implemented in the finite element solver for the ALE elements

4.3.1 A short review of the pull-out experiments for conventional textiles

This section is an overview of the experimental studies concerning the pull-out method for analysing fibre tow friction in fibrous reinforcements. Pull-out is a more general method but this overview focuses on those which focus on the friction behaviour in dry conventional textiles.

4.3.1.1 Studied friction interactions

Analysing the required force to extract a single fibre tow from conventional textiles has been widely addressed to study the fibre slippage properties. Several friction interactions are involved when forming conventional textiles. Some works investigated tools-textile, textile-textile and tow-tow friction behaviours (Allaoui et al., 2012; Najjar et al., 2014; Mulvihill et al., 2017). For instance Tourlonias and Bueno (2016) and Tourlonias et al. (2019) studied the influence of the tow-to-tow angle on the frictional response and showed that a difference exists essentially when tows are almost parallel. Pull-out experiments are used to investigate the friction between the fibre tows in textiles. In composite forming, fibre tow slippage is a defect to be predicted in order to be avoided. However, in ballistic impact field, fibre tow slippage is a dissipation phenomenon which has to be understood for improving the textile energy-absorption property and enhancing ballistic armors for example (King et al., 2005; Parsons et al., 2010, 2013; Bai et al., 2018). This is the reason why many pull-out studies concern Kevlar® woven fabrics (Dong and Sun, 2009; Zhu et al., 2011b; López-Gálvez et al., 2016; Bai et al., 2018).

4.3.1.2 Standard device

For woven fabric, the experimental procedure mainly consists in clamping the opposite edges of a rectangular sample of textile in either the warp or weft direction and then extracts a single fibre tow in the other direction (Fig. 4.35). In woven fabrics, the pull-out force is strongly dependent on the sample length and the transverse load applied (Zhu et al., 2011a; Bai et al., 2018) but also on the number of yarn being pulled-out (Bilisik and Korkmaz, 2011). The number of contacts for the yarn being pulled out increases with the sample length. A higher transverse load reduces the crimp amplitude by compressing the tows on each other, which can increase significantly the contact areas and normal force at the crossover points. Since pull-out force increases with the transverse tension, this parameter can be used to increase the fabric cohesion. The pull-out force vs slip displacement response strongly depends on the pull-out setup as illustrated in Fig. 4.36.

In a recent study Salem et al. (2020) shows the dependence of the pull-out force on the woven fabric shear angle by out-of-plane pull-out of a single fibre tow in in-plane sheared woven fabrics. The woven fabric was clamped within a special picture frame system designed to avoid in-plane bending. They firstly measured the tow-tow friction coefficient for several tow-tow angles using tribological friction tests to analyse their out-of-plane pull-out experiments. They showed that shear angles increase the fabric cohesion but only for high shear angles (higher than 15° for plain weave and 30° for twill 2×2 weave).

4.3.1.3 Existing study for TFP

In a TFP preform, tow-to-backing material, tow-to-stitching yarn and tow-to-tow interactions contribute to the friction behaviour. In Bohler et al. (2015), single fibre tow pull-out of a TFP sample was performed. They study the effect of the stitching parameters on the pull-out force. A higher stitch length, stitch width and stitching yarn tension fraction leads to a higher pull-out force. The stitching yarn tension fraction corresponds to the tension ratio between the upper and lower stitching yarns. However, as shown in Fig. 4.37 the force-displacement curves they obtained are difficult to interpret.

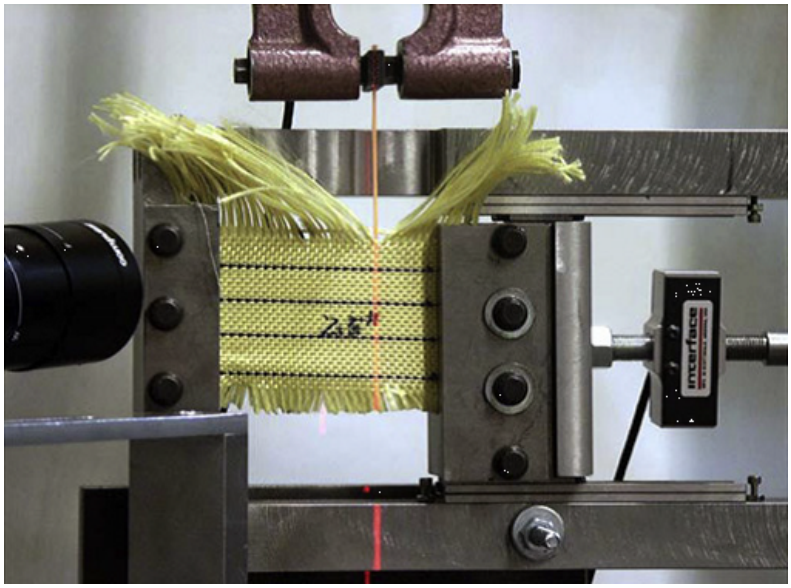

Figure 4.35: Example of single fibre tow pull-out device by Zhu et al. (2011b)

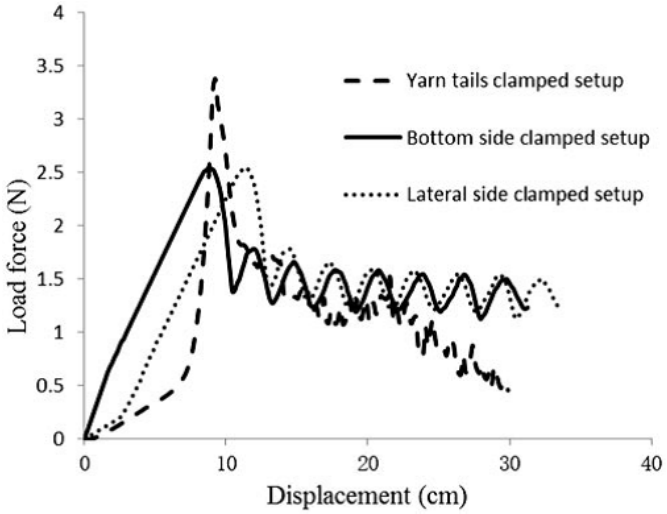

Figure 4.36: Pull-out force vs displacement curve obtained for several pull-out devices by Zhou et al. (2019)

As mentioned in the beginning of this chapter the fibre tow slippage in TFP preform can be used to allow a new forming mode in the preform. Fial et al. (2018) manufactured a light-weight structure using a new forming process. Instead of deforming the backing material, the process is based on backing material folding and fibre tow slippage. Some fibre tows slip to span the cut regions of the base material during the wet compression moulding (Fig. 1.43). They used the previously cited study by Bohler et al. (2015) to determine the stitching parameters to be used in the region where fibre tow slippage is needed and regions where tows must remain fixed on the backing material.

Transition

The pull-out method has been widely use to characterize fibre tow slippage in conventional textiles. The boundary conditions applied on the sample, its geometry and the number of extracted fibre tows strongly affect the results. Consequently, all these set-up parameters

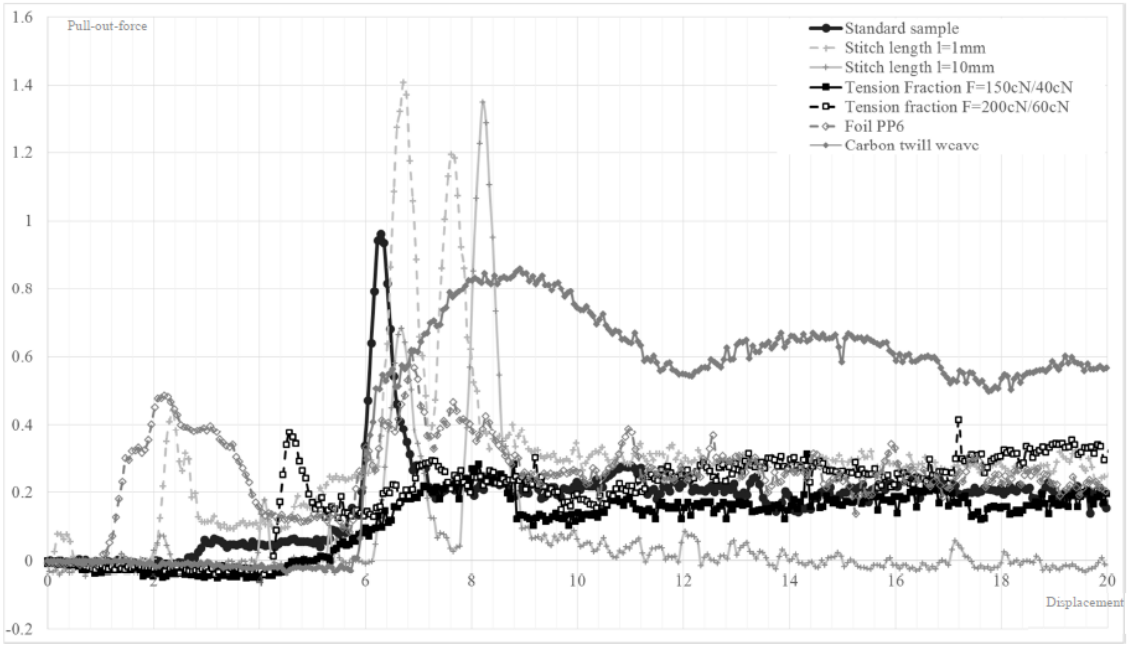

Figure 4.37: Pull-out force (N) vs displacement (mm) with parameter variation by Bohler et al. (2015)

have to be considered in the design of the pull-out experiment to characterize fibre tow slippage in TFP preforms. The next section present the experimental principle adopted in this work which is different from the device used by Bohler et al. (2015) for TFP.

4.3.2 Design of the pull-out experiment

A TFP preform is composed of three constituents, namely, the fibre tows, the backing material and the stitching yarn, which ensures the preform cohesion as mentioned in section 1.4. Fibre tow slippage in TFP preforms can be turned into an additional degree of freedom as demonstrated by Fial et al. (2018) and can be used to develop new forming processes. Bohler et al. (2015) argued about the dependence of the fibre tow slippage on the stitching parameters and used pull-out tests to investigate this dependency. In the following, the objective of the pull-out experiment and its design are presented. Then, the design and manufacturing of the TFP sample is described before presenting the experimental methods adopted to quantity the fibre tow slippage and the associated friction force.

4.3.2.1 Experiment setup and configurations

Device design The device used to perform pull-out tests on TFP samples is quite similar to the one used for woven fabrics where no transverse tension is applied as in Bilisik and Korkmaz (2011). The set-up used and shown in Fig. 4.38 is an updated version of the pull-out device developed by Hautefeuille et al. (2019). It is mounted on an INSTRON 5584 tensile test machine and a load cell of capacity 1 kN. The tests are performed with a velocity of 10 mm/min.

The stitching parameters , which have been depicted in Fig. 1.31, constraint the fibre tow geometry. In particular, as mentioned in section 1.4.1.3, the zig-zag pattern generates in-plane and out-of-plane waviness due to the local line contact between the stitching yarn and the fibre tows. These wavinesses affect the mechanical performances of the final product since they

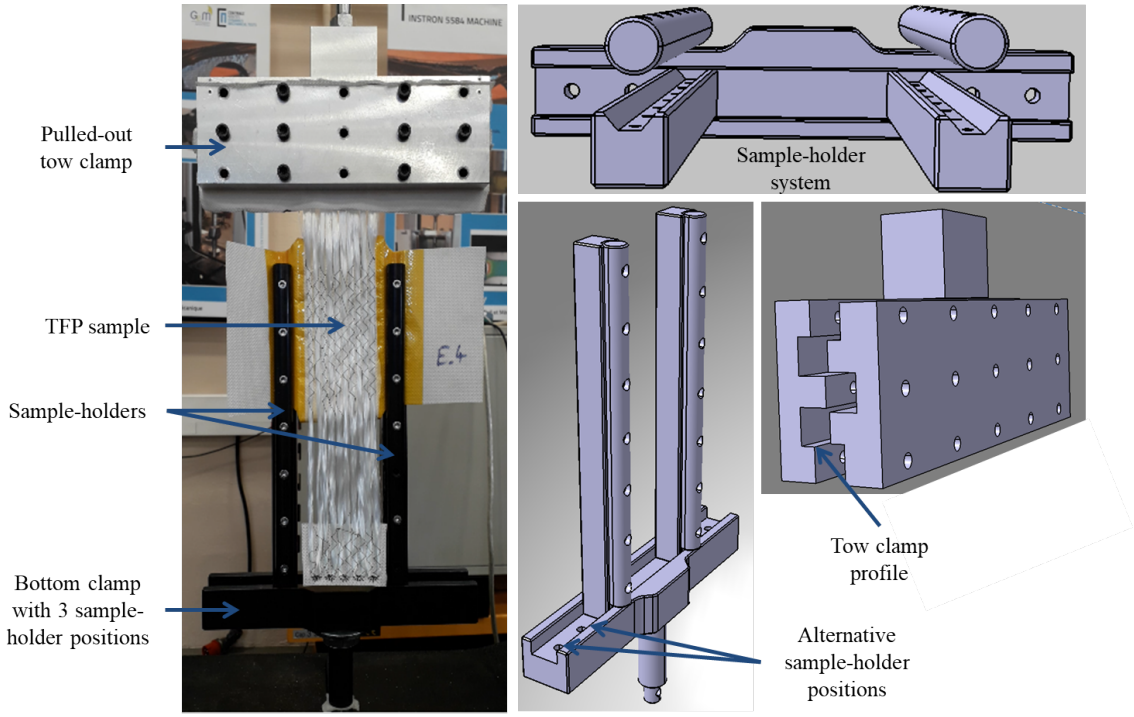

Figure 4.38: Pull-out device designed in this study with a sample (left) and its corresponding CAD (right)

locally modify the fibre volume fraction and in particular reduce the compression stiffness in comparison with conventional textiles. The effect of the stitching yarn parameters is of interest in this study.

Extracted fibre tow configurations In addition to the stitching parameters, the surroundings of the fibre tows will be shown to have a major impact on the fibre tow slippage. When considering a fibre tow in a TFP preform, three main configurations illustrated in Fig. 4.39 are considered. On the left configuration (Fig 4.39 (a)), the fibre tows are only in contact with the backing material and the stitching yarn. The middle and right configurations contain two layers. In the middle configuration (Fig 4.39 (b)), the fibre tows being pulled-out are in contact with the backing material, the stitching yarn, the fibre tows of the upper layer and on top of that they are overstitched. In the right configuration (Fig 4.39 (c)), the fibre tows of the upper layer are being pulled-out. This configuration is quite similar to the one in Fig 4.39 (a) except that the pulled-out fibre tows lie on the first layer rather than on the backing material.

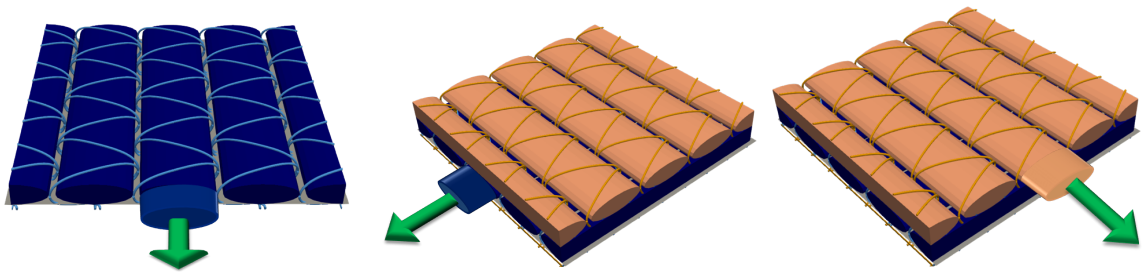

(a) Single layer **(b)** First layer fibre tow extraction **(c)** Second layer fibre tow extraction

Figure 4.39: Extracted fibre tow's surrounding configurations

Due to inter-layer overstitching, the fibre tow slippage in the middle configuration can be quite limited and difficult to interpret. Therefore, only the left configuration is considered. Moreover, since overstitching might compromise the interpretation of the pull-out results, intra-layer overstitching, as represented in Fig. 2.3 (b), has to be avoided. Preliminary tests demonstrated that intra-layer overstitching leads to high deformation of the backing material and considerably jams fibre tow slippage.

4.3.2.2 Design, preparation of the samples and materials

Sample design Tested samples consist in a single layer made of well-spaced fibre tows. Since a load cell of 1 kN capacity is used, the pull-out is achieved on multiple parallel fibre tows such that the measured friction force is high enough compared to the load cell resolution. Moreover, multiple fibre tows pull-out allows averaging measurement variations due to sample manufacturing, positioning or material variations. The friction force might depend on the trajectory of the fibre tow. Moreover, this study is limited to unidirectional fibre tows. Consequently, the effect of a curvilinear trajectory is not considered here.
The sample design is presented in Fig. 4.40 for the left configuration (1-layer). The area of interest is a rectangle of 50 mm × 100 mm containing 10 fibre tows being pulled-out. An extra length of 100 mm at the top is necessary to clamp the fibre tows. The additional length of 100 mm at the bottom will slip into the area of interest during the experiment. It allows measuring the friction behaviour without decreasing the total frictional surface as observed in woven fabric pull-out experiments when the number of fibre tow crossings decreases while the fibre tow is being pulled-out. The right image in Fig. 4.40 is a display of the sample design using the Python tool developed and introduced in section 3.1.4.1. For this experiment, this design tool allows manufacturing TFP sample where the stitch points are placed identically for every fibre tow.

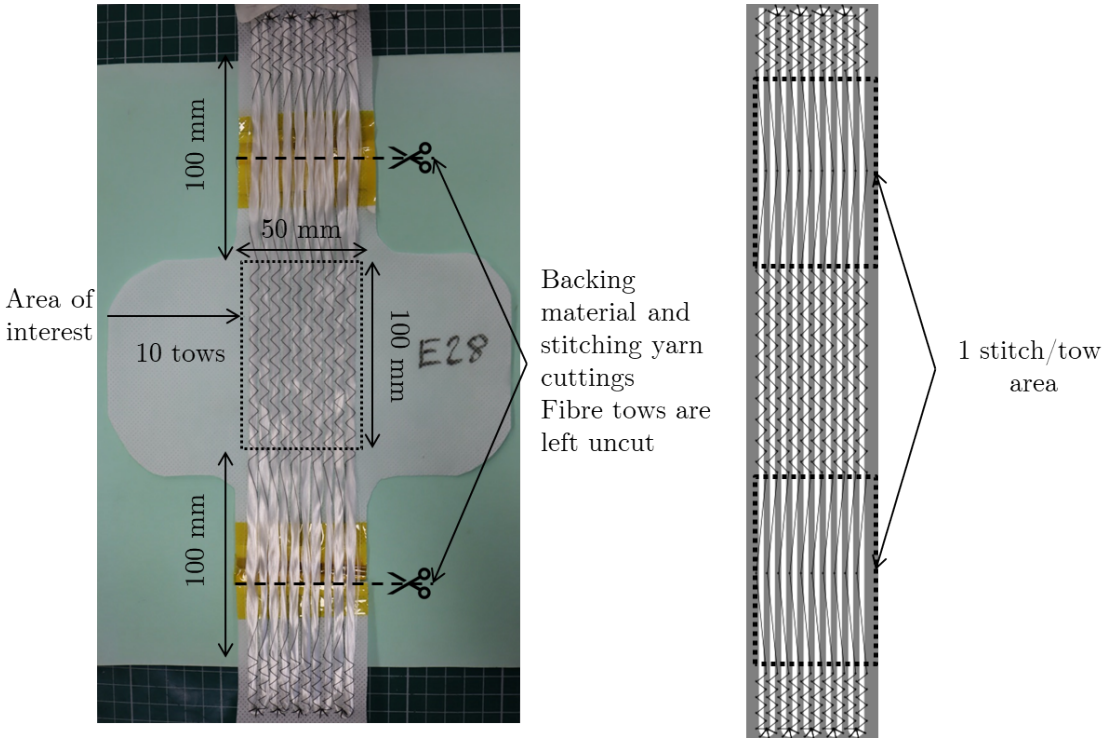

Figure 4.40: Pull-out sample design: manufactured sample (left), numerical design using the developed Python tool (right)

Sample preparations The top and bottom parts of the pulled-out fibre tows have to be isolated from the backing material and the stitching yarn. This is achieved by cutting the backing material and the stitching yarn. However, simply cutting the stitching yarn removes its tension. To maintain this stitching yarn tension, special care was taken to bond the stitching yarn on the backing material before cutting. Fig. 4.41 (c and d) show the bonding between the backing material and the stitching yarn (achieved before cutting and shown after cutting for more visibility). The stitching yarn was first stuck with additional tapes of backing material on the backing material using a thermally resistant adhesive tape to increase the bonding obtained by melting in a bag sealing unit. In Fig. 4.41 (b) the stitching yarn is located between the additional tapes of backing material and the backing material. In the sample design, one stitch per fibre tow was placed in the cut area to facilitate the isolation between the fibre tows and the stitching yarn.

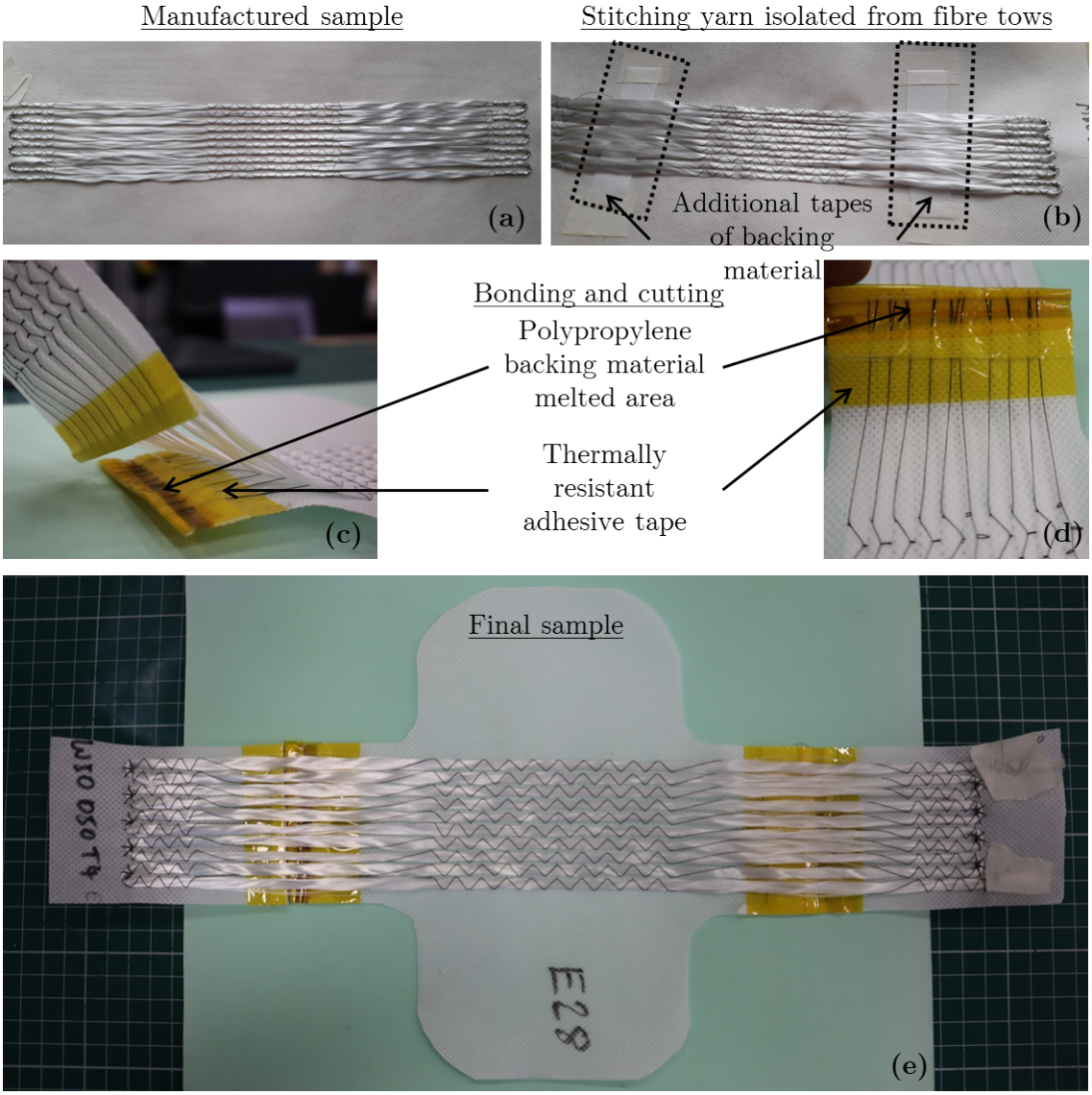

Figure 4.41: Bonding between backing material and stitching yarn: manufactured sample (a), isolation of the stitching yarn from the fibre tows (b), stitching yarn to backing material bonding (c and d), final sample (e)

Materials The fibre tow and stitching yarn materials are the ones used in the forming experiments in chapter 3. Besides, the same TFP machine is used to manufacture these samples.

Concerning the backing material, since many other backing materials can be used depending on the application, no specific choice was made. A non-woven polymer film was chosen for simplicity. The nature of the backing material is supposed to only affect the overall amplitude of the friction force without modifying the observed phenomena resulting from the interactions between the fibre tows and the stitching yarn.

Positioning the sample in the pull-out device To position the TFP sample in the pull-out device, both parts of the device are fixed on a rigid holding plate to ensure a perfect alignment and provide stability while positioning the sample (Fig. 4.42 (a)). The top of the fibre tows are firstly clamped. Due to the clamping jaw profile (Fig. 4.38), an additional length is needed (Fig. 4.42 (b)). Consequently, the backing material of the sample cannot be clamped in the sample-holders during this first operation otherwise an early stretch would be applied to the fibre tows. Once the fibre tows are clamped, the backing material is fixed by the sample-holders. This procedure allows a high reproducibility of the sample positioning.

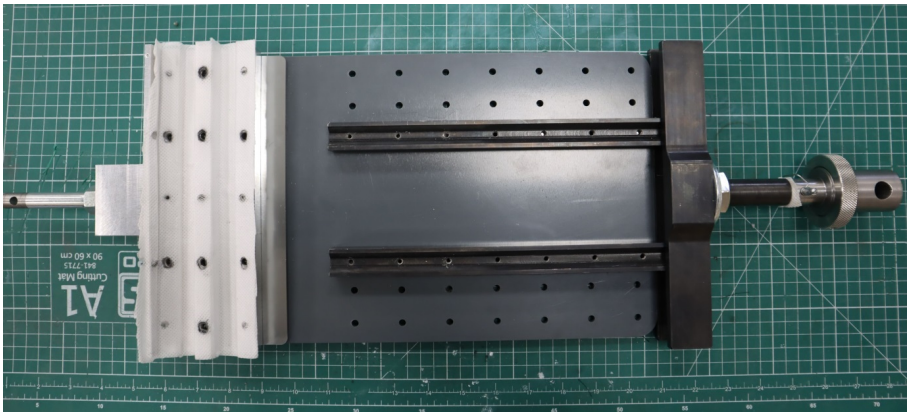

(a) Holding plate

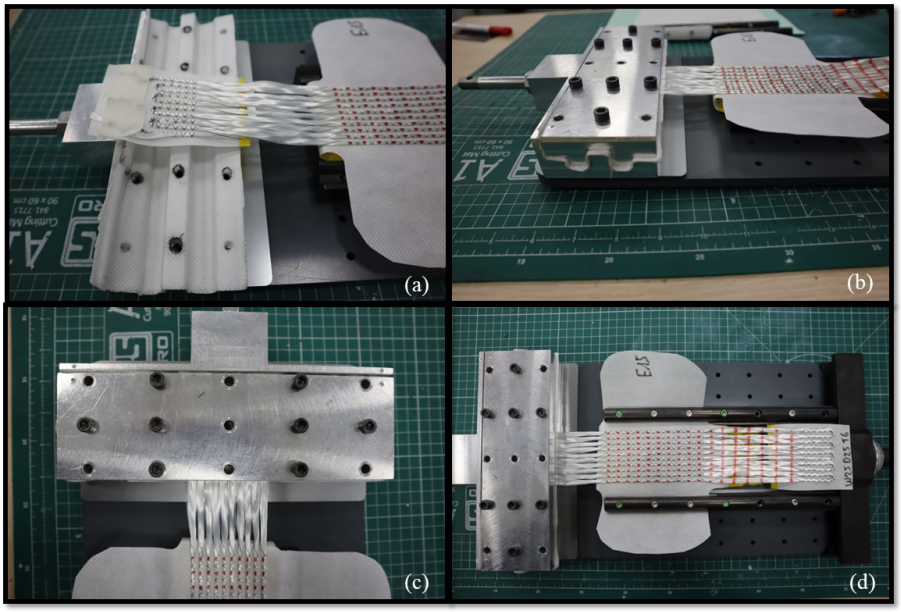

(b) Steps of the sample positioning procedure: placing top of the fibre tows (a), screwing the top clamp (b), checking alignment (c), clamping the backing material in the sample-holders(d)

Figure 4.42: Positioning of the sample in the pull-out device

Once the sample is positioned in the pull-out device, the latter can be easily handled and

mounted in the tensile testing machine thanks to the rigid holding plate maintaining the two-part device as a whole (Fig. 4.43). The rigid holding plate is then removed from the device before the test proceeds. The white board in the background of Fig. 4.43 is used to better contrast the sample and the device for further image processing.

To facilitate the camera positioning, four screws on the sample-holders have been painted green to be detected by the image processing. They are used to check the parallelism between the camera and the sample before every test (Fig. 4.44). Then, a real-time image processing allows drawing a frame (green lines) with the corner angles, a reference system (blue arrows) and a 2D grid (black lines).

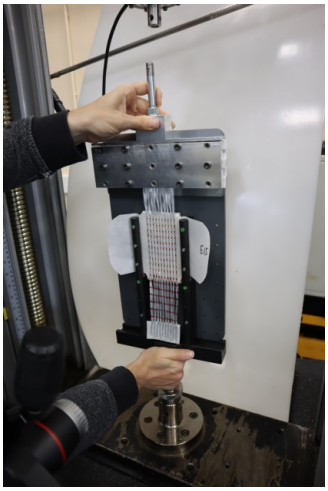

Figure 4.43: Mounting the pull-out device in the tensile machine

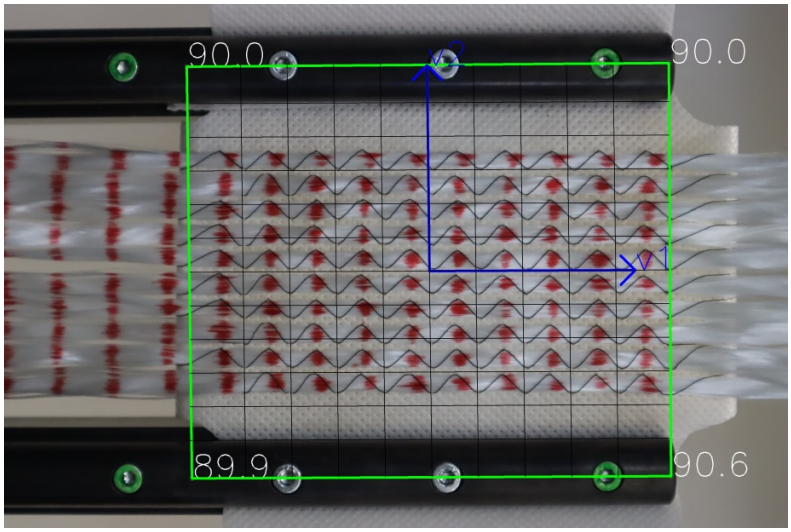

Figure 4.44: Checking camera positioning using real-time image processing drawing a frame (green rectangle), a reference system (blue arrows) and a 2D grid (black lines)

4.3.2.3 Parametric study

The characterization of the friction behaviour is mainly based on the analysis of the force-displacement data. Red-ink markers were drawn on the sample as shown in Fig. 4.45 to measure a displacement field. Since the fibre tows are not perfectly straight in the area of interest due to the TFP process induced waviness (section 1.4.1.3), measuring a displacement field was supposed to be of interest. Due to the waviness, fibre tows might first straighten before

slipping. Measuring the displacement field in the area of interest should allow highlighting this first deformation mode during pull-out tests. However, the post-processing of the recorded images has not been addressed in this work due to a lack of time. This measurement should have been carried out by using the same method presented in the forming experiments of chapter 3. Therefore, to characterize the effect of the stitching parameters, only the displacement-force curves are analysed.

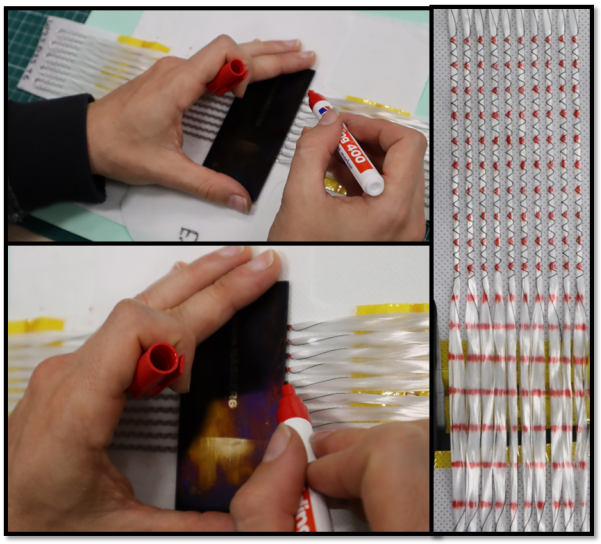

Figure 4.45: Drawing of red-ink markers for optical displacement field measurement

Design of experiments and factors' levels The main objective of this experimental study is to determine an analytical friction model to be implemented in the finite element solver to take into account the fibre tow slippage in Model I. This friction model is supposed to depend on the stitching parameters. That is why a parametric study has been designed. A full factorial design with two levels is considered. The levels for each of the three stitching parameters (factors) are reported in Table 4.7. The lower and upper values were chosen according to values reported in the literature. Besides, care had to be taken to ensure that no stitching point are missed during the manufacturing. In particular, the upper value of the stitching yarn tension was determined for a stitching speed of 400 pts/min. Higher stitching yarn tension led to manufacturing defects in the sample and requires reducing the stitching speed. It has to be noticed that the lower stitching yarn tension cannot be measured. Therefore, all the samples were manufactured with the same lower stitching yarn bobbin but the stitching yarn tension ratio is unknown. Adding features to control the lower stitching yarn tension in the TFP machine would be beneficial.

Table 4.7: Factors and levels of the parametric study

Factors Unit	Stitch width 1/10 mm	Stitch length 1/10 mm	Stitch tension g
Level 1	50	50	4
Level 2	25	25	6

Sample designs The chosen design of experiments results in eight different sample designs listed in Table 4.8. In particular, an image corresponding to 10 mm of a fibre tow is given for each design which allows a visual comparison of the effects of the stitching parameters on the fibre tow geometry. The id of the sample corresponds to the manufacturing order. Missing

number from 1 to 28 shows that some samples were removed due to defects. The id from 1 to 3 corresponds to the testing order within each design.

Table 4.8: Designs of the parametric study

Design	Stitch width w_s	Stitch length d_s	Stitch tension T_s	Samples' id 1	2	3	Stitching pattern
1	50	50	4	3	27	28	
2	25	50	4	4	25	26	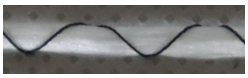
3	50	50	6	6	19	21	
4	50	25	6	7	17	18	
5	25	25	6	8	15	16	
6	25	25	4	9	13	14	
7	50	25	4	10	11	12	
8	25	50	6	22	23	24	

Transition

This section presented the pull-out experiments carried out to study the friction forces applied to the fibre tows in a single layer TFP preform with backing material. The sample design and manufacturing as well as the design of the parametric study were described. In the next section, results are examined. The pull-out displacement-force curves are analysed and an analytical friction model is proposed.

4.3.3 Determination of an analytical friction model

In this section, the force-displacement curves are firstly examined. Observations concerning the shape of the curves and the physical phenomena associated with peculiar regions are made. Next, the similarity between the curve shapes allows to propose a single analytical model to describe the force-displacement curve for all designs. The parameters of the analytical model are determined by fitting the experimental curve for each design. Finally, the relations between the model parameters and the studied stitching parameters are determined using a linear regression method.

4.3.3.1 Observations

General observations The results are shown in Fig 4.46 at the end of this section. The fourth top graphs correspond to a stitch tension of 4 g and the fourth bottom to 6 g. From left to right, the stitch width increases, while the stitch length increases from top to bottom. The experiments 9 and 16 cannot be exploited. Their strong deviation from the other repetitions is due to the presence of few oversticking points. In general, the curves for each design show a high repeatability. The curves have a specific trend shape that is similar from one design to

another. The following features can be identified:

- A static regime until a maximum is reached
- Damped oscillations

To explain the shape of the curves, two results are examined in details. One with the maximal stitching length (sample 4) and the other with the minimal stitch length (sample 14). In both results, the pull-out force increases until reaching a maxima (F_0, U_0). This region is similar to the static regime observed in pull-out of woven fabrics. Small deformation of the backing material and initial straightening of the fibre tows might cause the shape of the curve during this regime. Next, the pull-out force oscillates when fibre tow slippage really starts. For woven fabrics, oscillations are also observed and are due to the crimping. For the TFP samples, it seems that the oscillation period (T_1) is exactly twice the stitch length, which corresponds to the whole zig-zag pattern. Moreover these oscillations are damped. Assumed that the oscillations are actually related to the stitching pattern, then the plastic deformation of the cross-section of the fibre tows could cause the damping. When the fibre tow moves within the path prescribed by the stitching yarn, interactions between the stitching yarn and the fibre tows might lead to these oscillations. Therefore, the induced in-plane and out-of-plane wavinesses of the deposited fibre tows might explain this phenomena.

Besides, it has to be noticed that a second oscillation period (T_2) seems to be present as shown in Fig. 4.47. It is more visible for the sample with minimal stitch length (sample 14). It is difficult to see if damping occurs for this oscillation since only three periods can be observed. However, as it will be shown in the analysis presented hereafter, this second oscillation might be due to the fibre tow geometry.

4.3.3.2 Proposition of the analytical model and data fitting

Expression of the friction model Based on the observations of the force-displacement curves, a model is proposed to fit the data. This model has to take into account the static regime and the damped oscillations composed of two periods. For simplicity, the static regime is firstly ignored and the following model is considered:

$$f(u) = \underbrace{A_1 d(u) \cos(2\pi f_1 u + \phi_1)}_{\text{Oscillations due to stitching pattern}} + \underbrace{A_2 \cos(2\pi f_2 u + \phi_2)}_{\text{Oscillations due to fibre tow geometry}} + \underbrace{A_0}_{\text{mean value}} \tag{4.32}$$

where:

- A_1 is the amplitude of the oscillations associated to the stitching pattern
- $d(u)$ is a damping function
- f_1 is the frequency linked to the period T_1
- ϕ_1 is a phase
- A_2 is the amplitude of the oscillations due to the fibre tow geometry
- f_2 is the frequency linked to the period T_2
- ϕ_2 is a phase
- A_0 is the mean value

Fitting procedures based on minimisation algorithm require computing the raw data and the model at the same displacement values. A Savitzky-Golay filter was used with a window length

of 201 points and a polynomial degree of three to reduce the number of points and smooth the raw data.

Fitting procedure Due to the oscillations, determining the model parameters by a direct data fitting is not possible. Local minima are reached before the global one. Therefore, a step-by-step procedure has been developed to accurately extract the information from the force-displacement curves. The first step consists in identifying first guess values for the parameters associated with the oscillations, namely: A_1, f_1, ϕ_1, A_2, f_2, ϕ_2. In this step, a FFT analysis is performed on the force-displacement curve. The mean value of the curve is ignored to increase the accuracy of the analysis. The FFT analysis gives values for the six parameters. However, when plotting the model defined by:

$$h(u) = A_1 \cos(2\pi f_1 u + \phi_1) + A_2 \cos(2\pi f_2 u + \phi_2) \tag{4.33}$$

against the data, the peaks in the model are slightly shifted from the data. This might be due to the static regime. Therefore, an additional fitting using a minimisation algorithm with the function $h(u)$ is used to adjust the values of these parameters and obtain a better fit of the data. Fig 4.48 shows the raw data (red) plotted against the curve resulting from the FFT analysis (green) and the final one after the additional fitting step (blue). It is clear that a better match with the local minima and maxima is obtained with this additional minimising step. The amplitude of the curve does not match since damping is not taking into account in this first fitting step.

The second step is to identify the damping function $d(u)$ for the oscillations due to the stitching pattern. Since the parameters of the oscillations (f_1, ϕ_1, A_2, f_2, ϕ_2) are known, the local maxima and minima can be extracted from the data. Next, a linear interpolation of the local maxima and minima is performed, which gives the curves $F_{min}(u)$ and $F_{max}(u)$. The half of the difference between the two interpolated curves gives the damped amplitude from the data:

$$A_{data}(u) = \frac{F_{max}(u) - F_{min}(u)}{2} \tag{4.34}$$

A decaying exponential function given by:

$$d(u) = \exp\left(-\sqrt{\frac{u}{c}}\right) \tag{4.35}$$

and multiplied by A_1 was shown to give a good prediction of the damped amplitude $A_{data}(u)$. During this fitting step, A_1 is adjusted from the value determined in the previous step. Fig. 4.49 shows the damped amplitude form the data (blue circles) and the fitted damping amplitude function (red solid curve).

Final model For the static regime, which could include the straightening of the fibre tows, the following expression is used:

$$F_{static}(u) = F_0 \sqrt{\sin\left(\frac{\pi}{2}\frac{u}{U_0}\right)} \tag{4.36}$$

where F_0 and U_0 corresponds to the coordinates of the first peak of the pull-out force-displacement curve.

Therefore, the final analytic model is defined by:

$$\begin{cases} f(u) = F_0 \sqrt{\sin\left(\frac{\pi}{2}\frac{u}{U_0}\right)} & \text{if } u \leq U_0 \\ f(u) = A_1 \exp\left(-\sqrt{\frac{u}{c}}\right) \cos(2\pi f_1 u + \phi_1) + A_2 \cos(2\pi f_2 u + \phi_2) + A_0 & \text{if } u > U_0 \end{cases} \tag{4.37}$$

Model parameters of each design Fig 4.50 shows the result of the fitting procedure applied for each repetition of the design 1. In each case the analytical models are in good agreement with the experimental data.

The model parameters of a design are computed as the average of the values obtained for each repetition. Fig 4.51 shows the result of the fitting procedure for each design. The gray area corresponds to the interval of minimal and maximal values obtained from the repetitions of the raw data. In general, the model lies in the interval, which validates the fitting procedure for all designs. Table 4.9 reports the values of the model parameters for each design.

Table 4.9: Model parameters for all (8) designs

Model parameters	A_1 (N)	c (mm)	f_1 (mm^{-1})	ϕ_1 (radians)	A_2 (N)	f_2 (mm^{-1})	ϕ_2 (radians)	A_0 (N)	U_0 (N)	F_0 (N)
1	1.584	13.011	0.096	3.098	0.427	0.036	3.902	5.283	5.299	6.284
2	4.233	5.985	0.095	2.786	0.425	0.034	4.741	7.732	5.850	9.702
3	2.640	8.940	0.096	2.831	0.386	0.035	4.332	4.517	5.716	6.000
4	2.424	8.231	0.195	2.828	0.640	0.036	4.174	8.899	2.826	10.307
5	5.513	5.968	0.196	2.311	0.737	0.033	4.691	15.238	3.227	18.311
6	6.001	6.212	0.195	2.102	0.802	0.036	3.890	14.502	3.405	17.309
7	1.309	13.447	0.192	3.101	0.571	0.037	3.837	7.346	2.594	8.042
8	3.547	9.570	0.096	3.120	0.433	0.034	4.453	7.164	5.232	9.181

4.3.3.3 Determining the model parameters as function of the stitching parameters

The analytical model proposed fits accurately the data for each design. In this section, the values of the model parameters are analysed according to the stitching parameters. In particular, the hypotheses formulated during the first observations of the results are verified.

General observations As mentioned previously, the period of the oscillations due to the stitching pattern ($T_1 = \frac{1}{f_1}$) equals twice the stitch length. Moreover, the second frequency f_2 is constant across the designs, which means that this phenomena is due to the raw fibre tow specificities. Actually, when looking closely a fibre tow, an even undulation is visible and its period seems in the range of the detected one. The exact period of the observed undulations could be measured with a profilometer.
The mean value A_0 and the peak force F_0, increase as the stitching length and width decreases. This result is consistent because decreasing the stitching length and width, increases the fixation constraint on the fibre tow.

Linear regression The aim is to determine the dependency of the model parameters on the stitching parameters. Two levels were used for each factor. Therefore, the model parameters are a linear function of the stitching parameters at most. For each model parameter i, the following function has to be identified:

$$p_i(d_s, w_s, T_s) = a_0 + a_1 d_s + a_2 w_s + a_3 T_s + b_1 d_s w_s + b_2 d_s T_s + b_3 w_s T_s + c_1 d_s w_s T_s \tag{4.38}$$

where:

- a_0 is the overall mean
- a_1, a_2 and a_3 are the main effects
- b_1, b_2 and b_3 are the first order interactions

- c_1 is the second order interaction

To determine these coefficient, a linear regression is performed. It requires an equal number of repetitions for each design. For some design, only two repetitions were valid. Therefore, the linear regression is achieved using two repetitions. Due to the high repeatability observed during the experiments, using two repetitions is deemed satisfying. The open tool Jamovi (Navarro and Foxcroft, 2018) is used to perform the linear regression of each model parameter.

For each model parameter, the linear regression model is built step by step. In a linear regression, the p-value tests the null hypothesis of a predictor, namely, if it can be considered as having no effect. Therefore, a low p-value indicates that the predictor is meaningful. Therefore, the main effects are added one by one and kept in the model if their p-value is lower than 0.05. Next, the interactions between the factors whose main effect is meaningful are added and eliminated if their p-value is greater than 0.05. The correlation coefficient R indicates if the model represents accurately the data. This procedure, which is repeated for each model parameters, is detailed hereafter for one model parameter.

Example: application to the mean value A_0 Table 4.10 reports the results of the different steps to build the model for A_0. The predictor corresponds to a main effect or an interaction and the estimate is the value of the associated coefficient in the model. First, the model (a) is built with only the main effect d_s (stitch length). Since the p-value of this predictor is lower than 0.05, it is meaningful. This process is repeated by adding the main effect w_s (stitch width) which is also meaningful. It can be noticed that the correlation coefficient increases from 0.704 to 0.935 by adding the main effect w_s. Next, the main effect T_s (stitch tension) is added but shows to be insignificant since its p-value does not allow to reject the null hypothesis. Moreover, the correlation coefficient was not increased by adding T_s. Therefore, the two main effects d_s and w_s are significant. Then, only the interactions of the factors whose main effect is significant are tested. Model (d) shows that the interaction $d_s * w_s$ is meaningful. The correlation coefficient R is high and reaches a final value of 0.975.

Consequently, according to the linear regression, the mean value A_0 depends on the stitching length and width. More precisely, since the coefficient associated to the main effects is negative, decreasing the stitching length or width increases the mean value. Their effect is similar since their coefficients are close (-0.465 for d_s and -0.438 for w_s). Moreover, the interaction means that a change in the stitching length or width has an effect which depends on the current value of the stitching width or length respectively. Therefore, A_0 is expressed as:

$$A_0(d_s, w_s) = 33.238 - 0.465 d_s - 0.438 w_s + 0.00672 d_s w_s \tag{4.39}$$

The fact that the stitch tension has no effect on the mean pull-out force was not expected. As it will be shown hereafter, for each model parameters, the effect of the stitch tension is not detected. This might indicate that the two levels of stitch tension were to close to each other to lead to significant changes in the model parameters. In other words, the effect of the stitch tension might be hidden by the variations between repetitions. Therefore, the model parameters will only be function of the stitch length and width.

Results The results of the linear regression applied to each model parameters are reported in Table 4.11. In particular, the high value (> 0.90) of the correlation coefficient R shows that the linear regression gives accurate models for A_1, f_1, A_0, U_0 and F_0. As mentioned previously, f_1 is perfectly defined by the stitch length d_s while f_2 does not depend on the stitching parameters. A_1, A_0, and F_0 increases when the stitching length and width decreases, which is consistent. Moreover, the effect of the stitching length and width is similar. The damping velocity c depends only on w_s but the correlation coefficient is low. However, increasing the stitch width increases

Table 4.10: Step-by-step identification of the model for the mean value A_0

(a) Model Coefficient - $A_0(d_s)$ - $R = 0.704$

Predictor	Estimate	SE	t	p
Intercept	16.819	2.2682	7.41	<.001
d_s	-0.213	0.0574	-3.71	0.002

(b) Model Coefficient - $A_0(d_s, w_s)$- $R = 0.935$

Predictor	Estimate	SE	t	p
Intercept	23.790	1.6235	14.65	<.001
d_s	-0.213	0.0298	-7.15	<.001
w_s	-0.186	0.0298	-6.24	<.001

(c) Model Coefficient - $A_0(d_s, w_s, T_s)$ - $R = 0.935$

Predictor	Estimate	SE	t	p
Intercept	23.193	2.5612	9.055	<.001
d_s	-0.213	0.0298	-6.892	<.001
w_s	-0.186	0.0298	-6.018	<.001
T_s	0.119	0.3861	0.309	0.762

(d) Model Coefficient - $A_0(d_s, w_s)$ - $R = 0.975$

Predictor	Estimate	SE	t	p
Intercept	33.238	2.417	13.75	<.001
d_s	-0.465	0.0612	-7.60	<.001
w_s	-0.438	0.0612	-7.16	<.001
$d_s * w_s$	0.00672	0.0016	4.34	<.001

the damping velocity which is consistent since a higher stitch width reduces the stress applied to the fibre tow and facilitates its slippage. The amplitude A_2 associated to the oscillations related to the fibre tow geometry only depends on the stitch length. Increasing the stitch length increases this amplitude which is consistent since the induced in-plane and out-of-plane waviness could interact with the initial fibre tow geometry undulation.

Table 4.11: Coefficients of the linear regression models of the friction model parameters

	A_1	c	f_1	ϕ_1	A_2	f_2	ϕ_2	A_0	U_0	F_0
Intercept	13.63	2.96	0.295	1.635	0.953	0.0364	4.87	33.24	0.565	40.18
d_s	-0.24	-	-0.0039	0.0149	-0.011	-	-	-0.465	0.0977	-0.558
w_s	-0.16	0.159	-	0.0154	-	-	-0.017	-0.438	-	-0.547
$d_s * w_s$	0.00338	-	-	-	-	-	-	0.00672	-	0.00846
R	0.942	0.675	1	0.718	0.725	0.778	0.556	0.975	0.977	0.973
R^2	0.886	0.456	1	0.516	0.25	0.606	0.309	0.951	0.943	0.946

Discussion The parametric study associated to the linear regression method allows to understand the influence of the stitch length and width on the friction force. Even if only two levels were used per factor, numerous information has been extracted from these pull-out experiments. This parametric study could be completed with an additional and complementary

design of experiment to extend the observations out of the studied range.

Conclusion

This section presented the pull-out experiments carried out to characterize the frictional contact interactions between the fibre tows, the backing material and the stitching yarn. A specific test bench was designed based on previous works. Multiple fibre tows were extracted simultaneously from a single layer TFP preform. A parametric study has been performed to study the influence of the stitching parameters on the friction force. Next, an analytical model was developed to fit the data of the eight sample designs. Finally, the dependency of the model parameters on the stitching parameters was analysed using a linear regression.

This experimental study showed that the features observed in the pull-out force-displacement curves are related to the stitching design or the fibre tow nature. In particular, damped oscillations are associated to the stitching pattern. The developed analytical model provides an accurate fit of the data for all designs. Moreover, the linear regression models allow analysing the effect of the stitching parameters on the model parameters. Therefore, the effect of the stitching parameters on the friction force has been characterized. However, the difference between the two stitch tension levels in the parametric study was too small to produce significant changes in the friction force. Consequently, the effect of the stitch tension could not be distinguished from the data variations.

Nevertheless, this study gave a deep insight of the frictional behaviour of fibre tows in single layer TFP preforms. Its complexity is well described by the proposed analytical model. In the next section, the pull-out experiments will be simulated to address the validation of the ALE elements to model frictional slippage in TFP preforms.

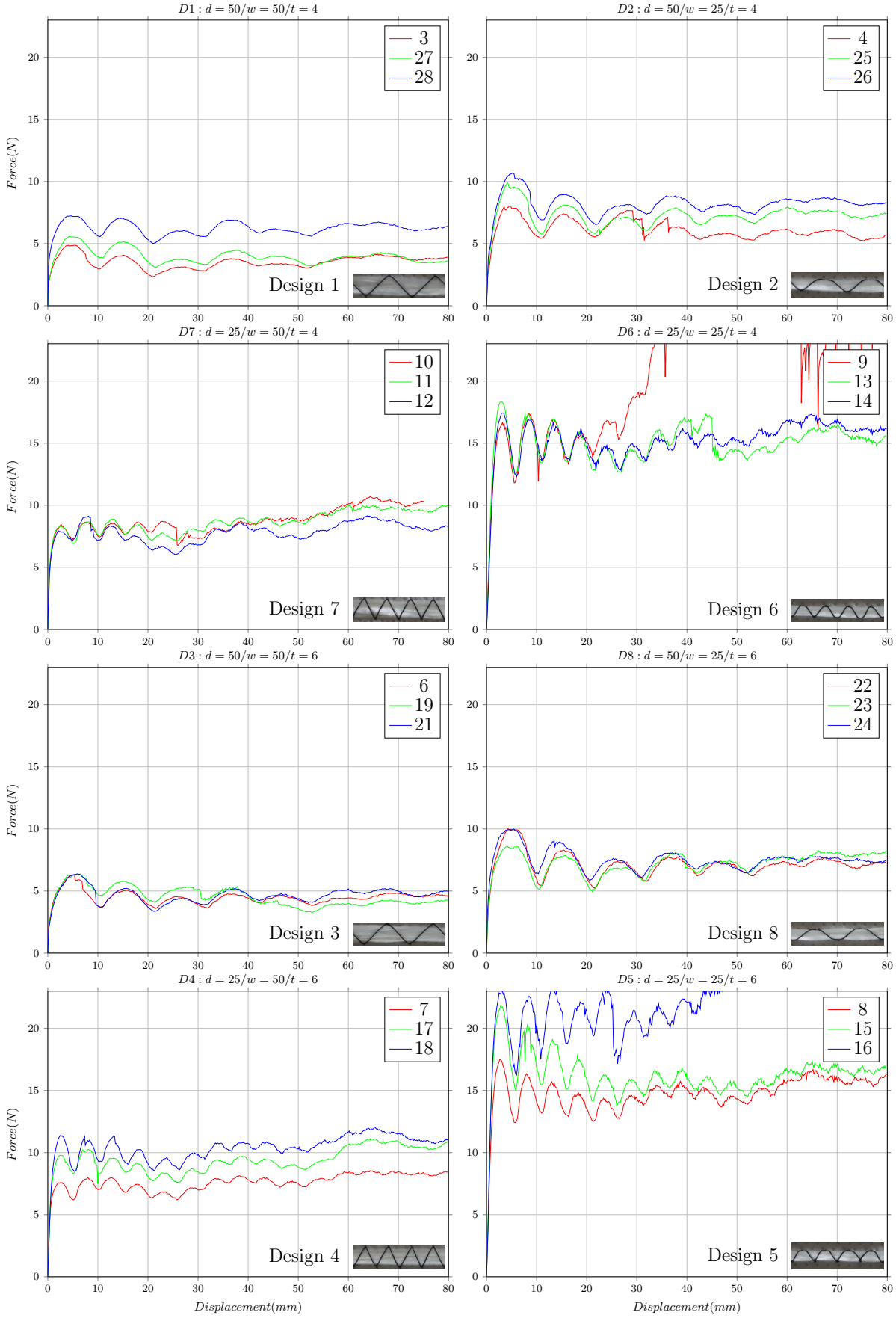

Figure 4.46: Force-displacement curves for the 8 designs shown in Table 4.8

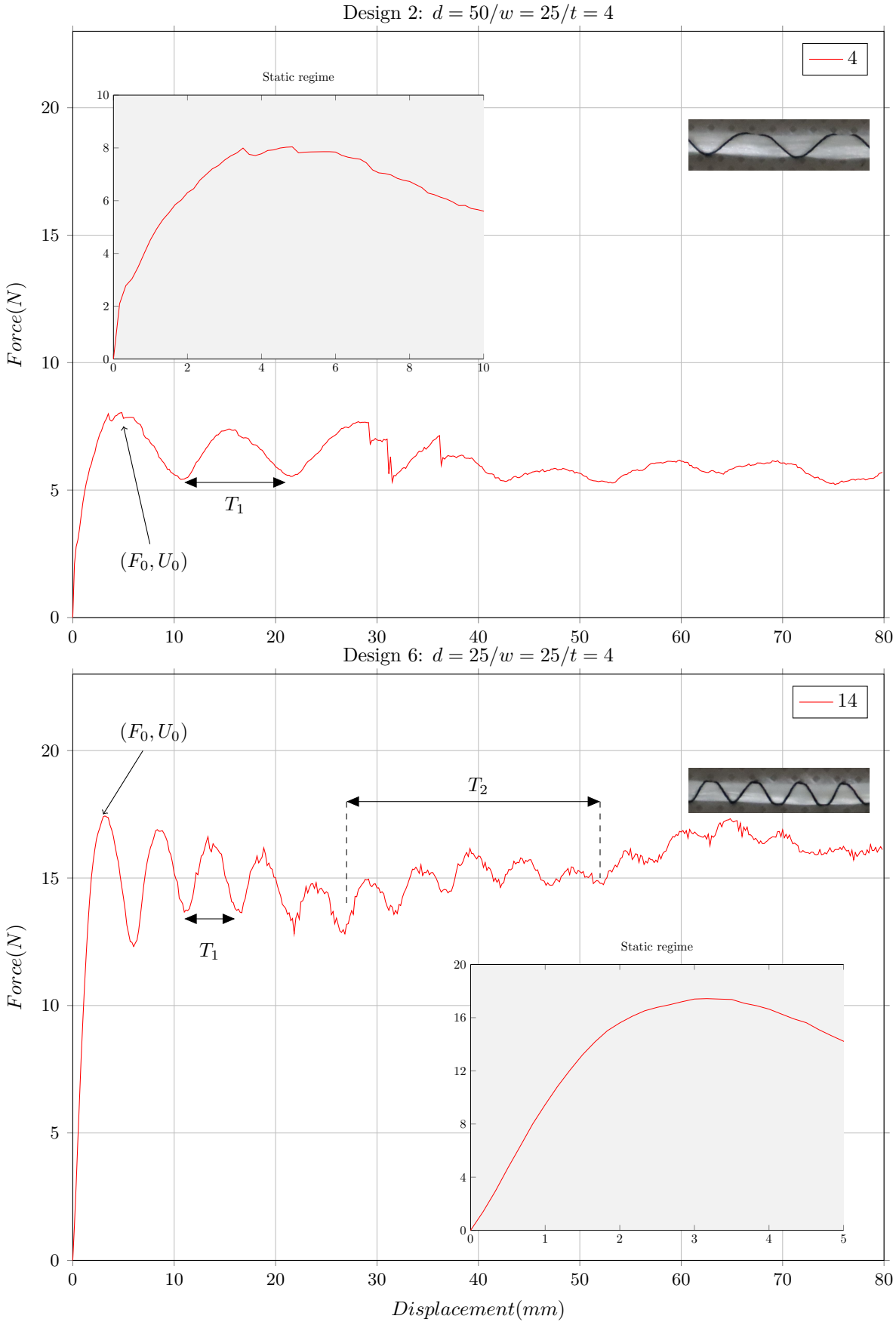

Figure 4.47: Identifying curves' features

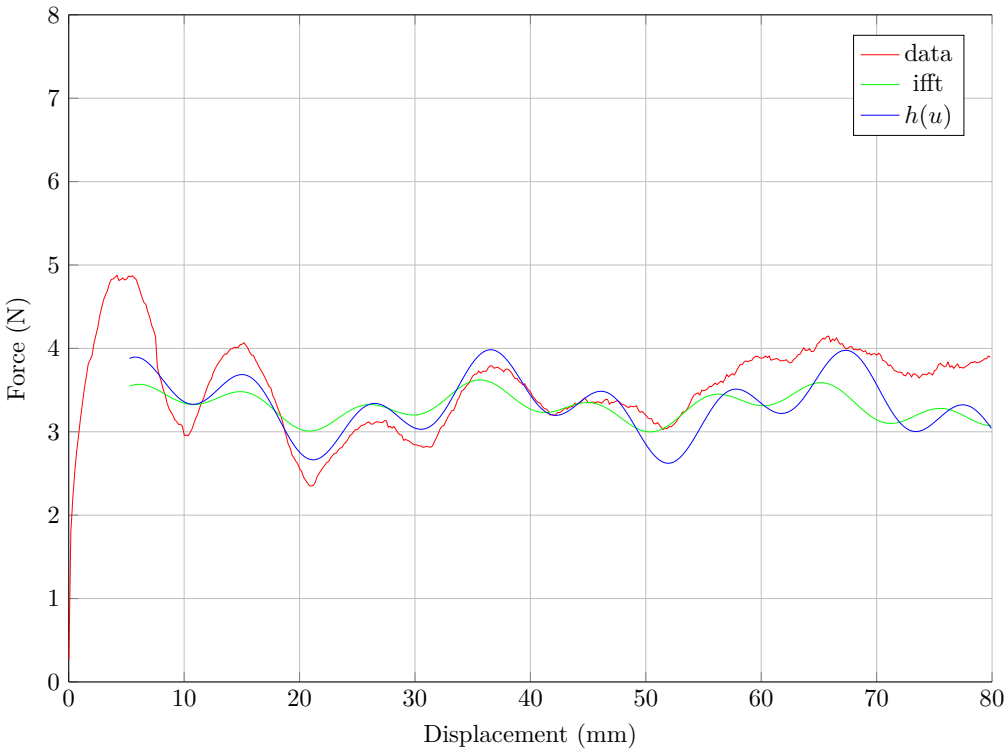

Figure 4.48: Comparison between the raw data, the curve obtained from IFFT and the curve after additional fitting (Design 1)

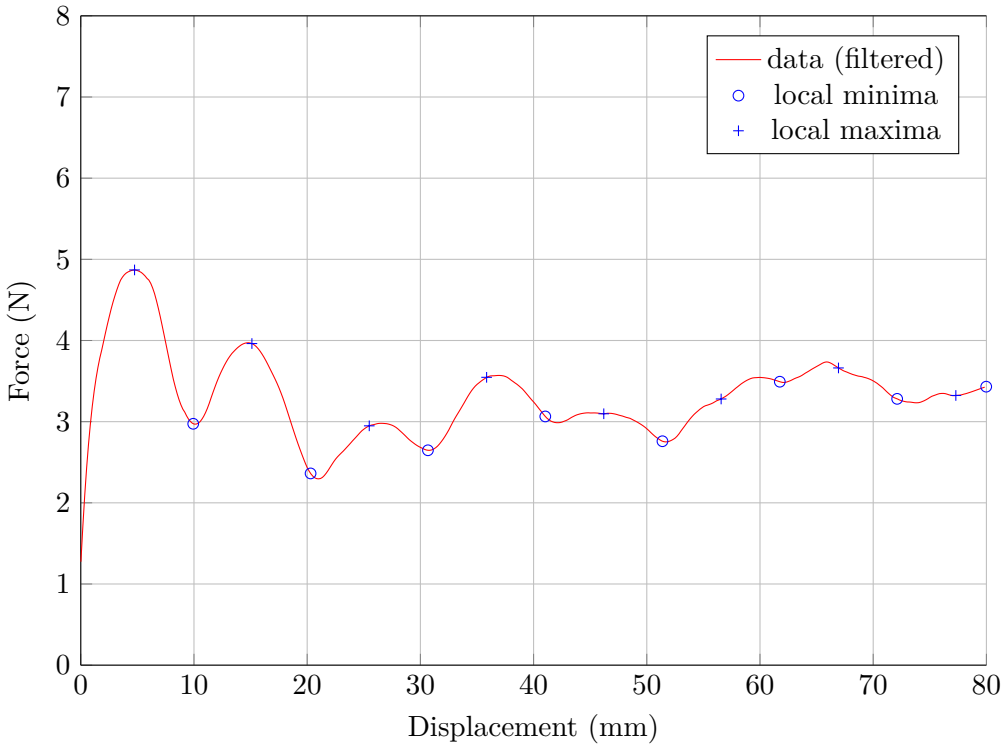

(a) Extracting local extrema

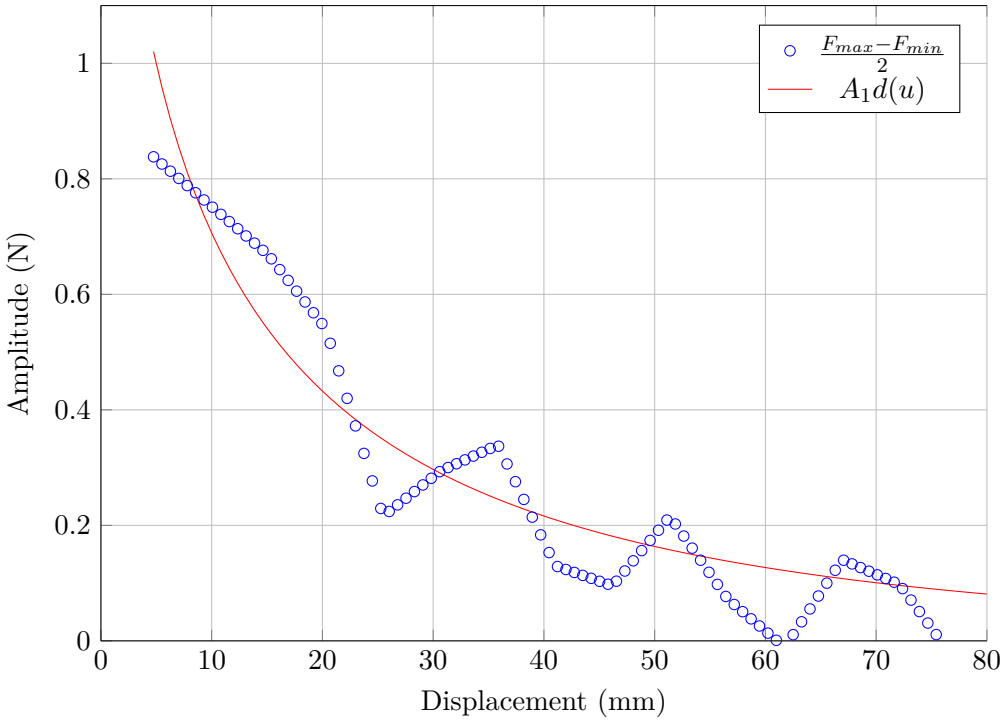

(b) Result of the damped amplitude fitting

Figure 4.49: Fitting of the damped amplitude

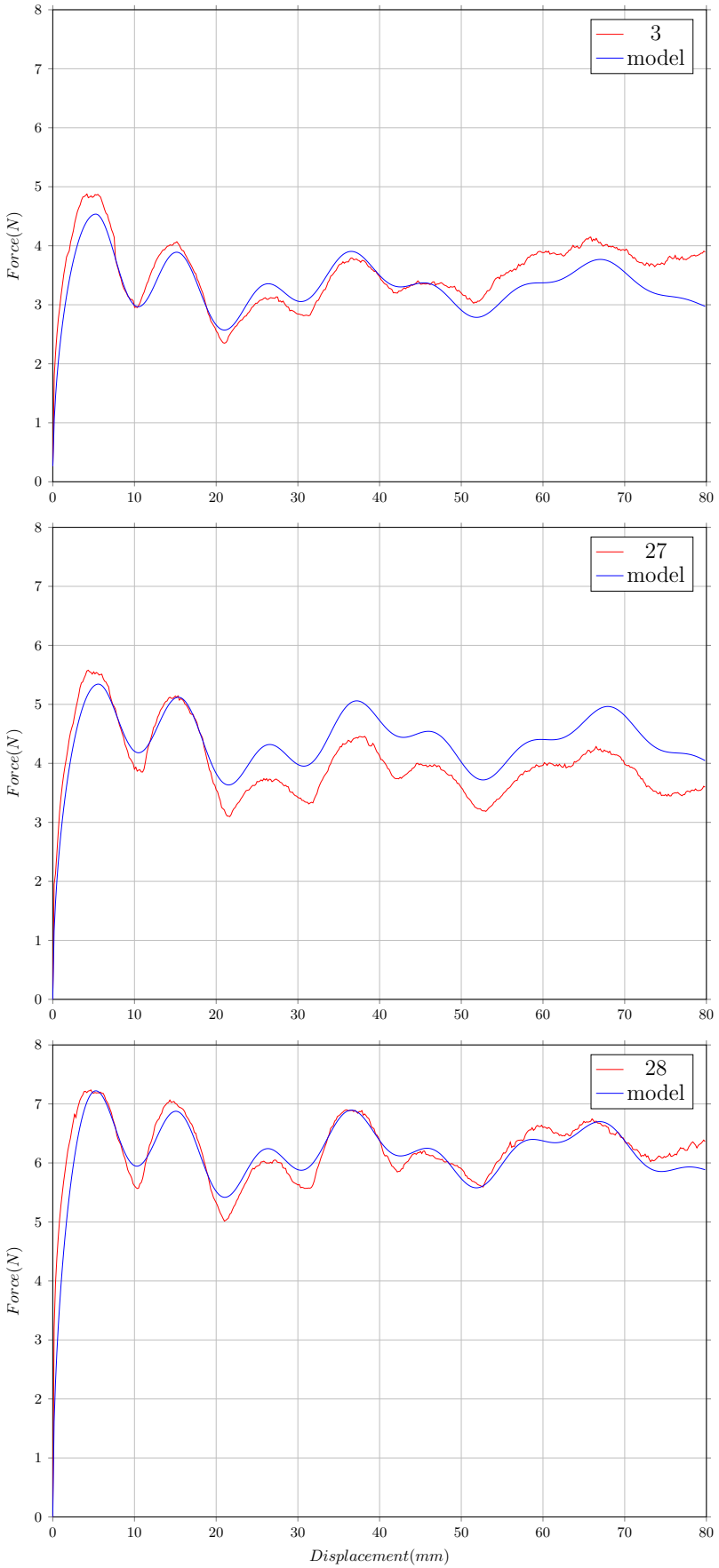

Figure 4.50: Data and fitted model for each repetition of design 1

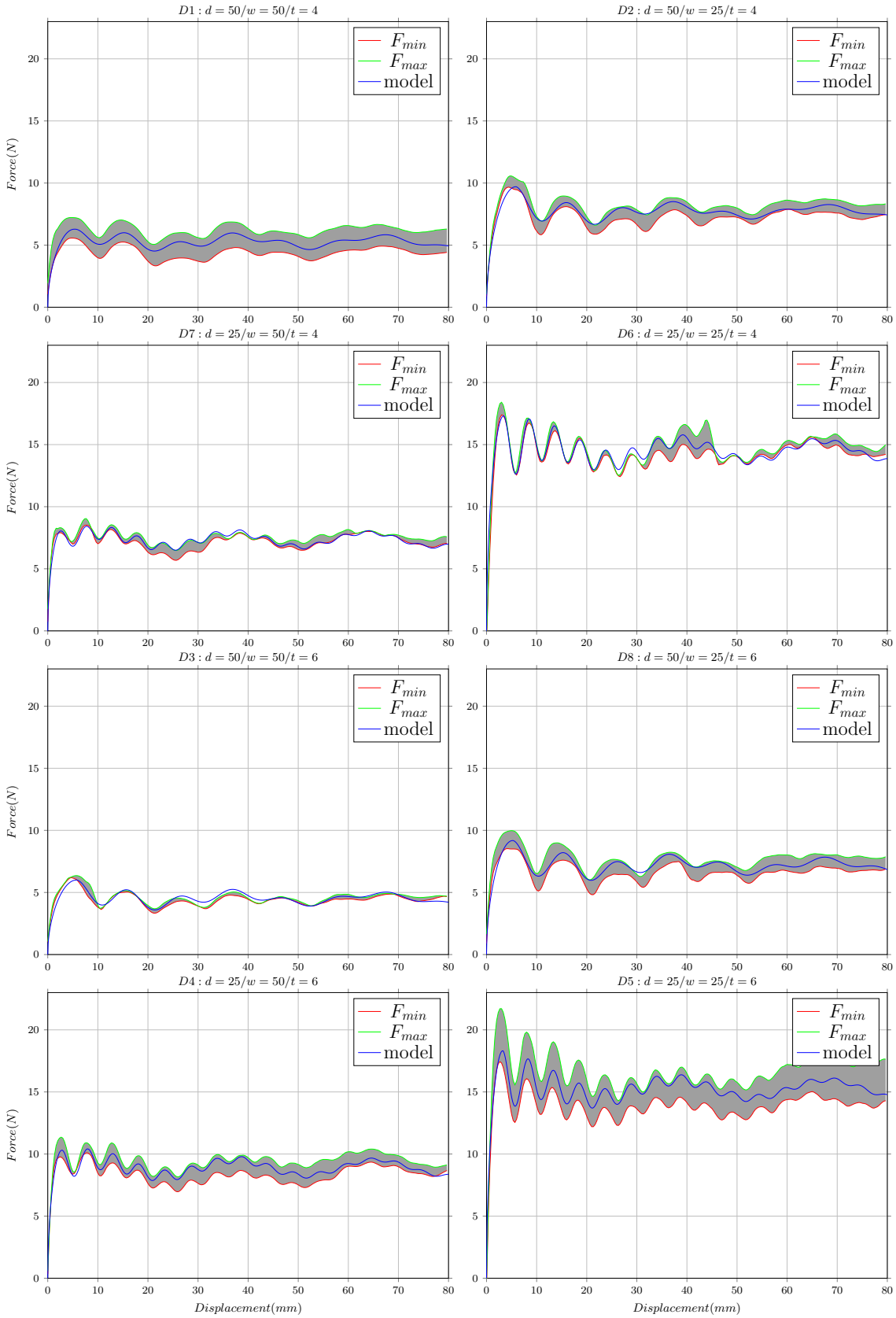

Figure 4.51: Analytical model for each design and minimal-maximal values interval from the repetitions

4.4 Application of the mixed embedded-ALE element approach to TFP preforms and extensions to conventional textiles

Introduction

This last section studies the benefits of integrating the 1D ALE element in the TFP preform models. First, the pull-out experiments presented in the previous section are simulated to evidence that the ALE elements can take into account complex frictional behaviours. Next, its application to Model I is addressed using the bias extension test of section 3.4.1. Finally, perspectives of application of the 1D ALE elements to the modelling of slippage in conventional textiles are presented. In particular, modelling of the fibre tow slippage in woven fabrics is achieved through the simulation of the bias extension test. Besides, a simplified approach to model the tufting yarn of tufted preforms is proposed and referenced elementary test cases are addressed.
Therefore, the objectives of this section are:

- Simulating the pull-out experiments
- Integrating the ALE elements in Model I
- Deploying the mixed embedded-ALE element formulation to the modelling of fibre slippage in conventional textiles

4.4.1 Integration of the 1D ALE element the TFP preform models

4.4.1.1 Simulation of the pull-out experiments

To further validate the implementation of the ALE elements, the pull-out experiments presented in the previous chapter are simulated. Since the pull-out force measured was rather low, the deformation of the backing material can be neglected and is not represented in the finite element model.

Finite element model The finite element model of the pull-out sample is shown in Fig. 4.52. The element size is 5 mm. The red nodes are Eulerian nodes (fixed in space) while the blue nodes are Lagrangian nodes. These Lagrangian nodes are kinematically driven by a reference point (black node). The displacement is imposed on this reference point. Due to the constraint imposed on the Lagrangian nodes, the pull-out force corresponds to the internal force of the reference point along the y-direction. The bottom part of the sample is simplified. In fact, the bottom part of the fibre tows are not represented but additional material flows through the bottom Eulerian nodes. The ALE truss element is used since the bending contribution is negligible in the pull-out configuration.

Implementation of the friction law The friction law is implemented at the node level. The analytical model developed in the previous section allows representing the pull-out force displacement curve at the sample scale. The static regime is the straightening of the fibre tows or the deformation of the backing material. Therefore, it does not describe the local friction behaviour on the fibre tows. Moreover, the phase parameter ϕ_1 is related to the beginning of the dynamic regime at the sample scale. Therefore, locally, the friction law reduces to:

$$f(u) = A_1 \exp\left(-\sqrt{\frac{u}{c}}\right) \sin(2\pi f_1 u - \pi) + A_2 \cos(2\pi f_2 u + \phi_2) + A_0 \tag{4.40}$$

The parameter of the analytical model have been determined for a whole sample. To implement the law at the fibre tow scale, the pull-out force is divided by the total fibre tow length L_{tot}

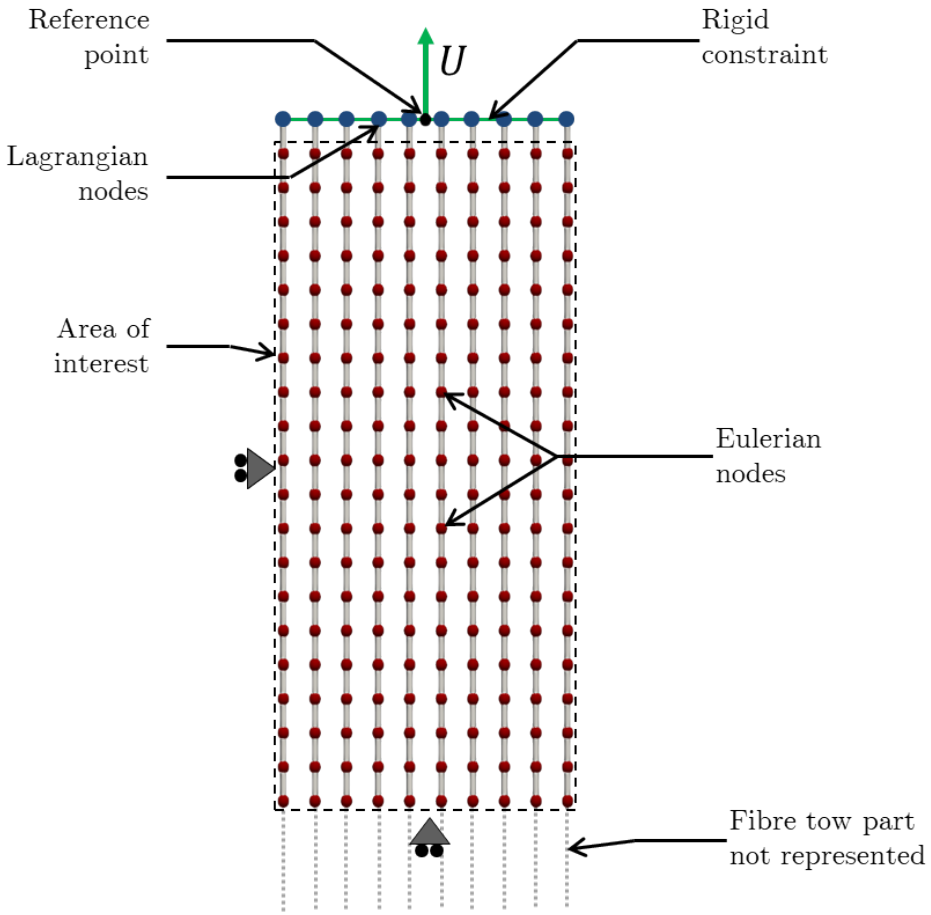

Figure 4.52: Finite element model of the pull-out experiments

in the area of interest of the sample, namely, 10^3 mm (100 mm $\times$ 10). Therefore, the friction forces are distributed along the fibre tows.

At a finite element ALE node, the friction force is defined as:

$$F_{ext}^{U_s}(U_s) = \frac{f(U_s)}{L_{tot}} * L \tag{4.41}$$

where L equals $\frac{L_i+L_{i+1}}{2}$ if the node i is connected to elements i and $i+1$ or $\frac{L_i}{2}$ if it is an end node.

No friction force is applied on the top Lagrangian nodes since the top elements are not in the area of interest of the sample.

For each design, the model parameters A_1, c, f_1, A_2, f_2, ϕ_2 and A_0 are those of Table 4.9. A_1, A_2, and A_0 are divided by L_{tot}.

Results The simulation results are plotted in Fig 4.53 along the model for each design. The simulations match the analytical model for each design. The slight horizontal shift visible for some design (D6 and D5) can be attributed to the static regime which is not perfectly represented since the fibre tows are already straight in the finite element model.

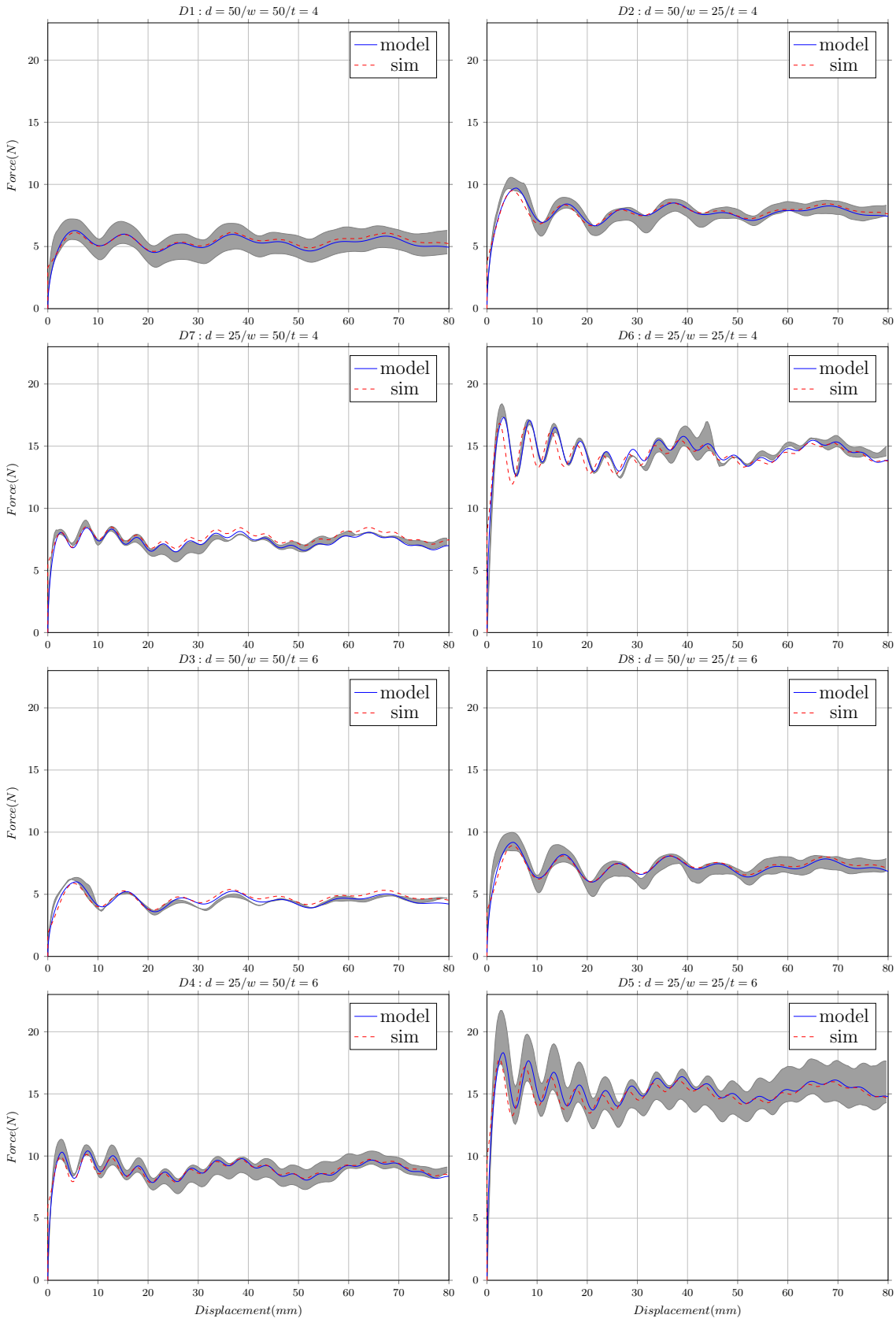

Figure 4.53: Results of the pull-out simulation for each design

4.4.1.2 Update of the simulation of a bias extension test with a TFP-reinforced conventional textile

As demonstrated in section 3.4.1, Model I leads to a very stiff behaviour when it is used to model the local reinforcement of another fibrous reinforcement. With the ALE elements, the no-slip condition can be relaxed. To show the benefit of introducing fibre tow slippage in Model I, the bias extension test performed in section 3.4.1 is addressed using the ALE elements to model the reinforcing fibre tow.

General settings The simulation is performed with both the ALE truss and the beam element. The material properties of the beam are the one used for the tetrahedral forming reported in Table 3.1. When the truss element is used, its tensile stiffness is those of the beam element. Scenarios with and without friction are considered. To simplify the friction behaviour, a static Coulomb friction law is used instead of the complex friction law determined in the previous section. The value chosen for the friction coefficient is 10^{-2} N/mm, which is in the same order of magnitude of the mean value $\frac{A_0}{L_{tot}}$ determined in the pull-out tests. The different configurations are labelled as:

- A: No hole and no reinforcement
- B: Hole and no reinforcement
- C: Hole and truss elements
- D: Hole and beam elements
- E: Hole and ALE truss (no friction)
- F: Hole and ALE beam (no friction)
- G: Hole and ALE truss (friction)
- H: Hole and ALE beam (friction)

Results The force-displacement curves of the simulations are plotted in Fig. 4.54 (a) along with the results of the simulations of section 3.4.1. Fig. 4.54 (b) shows the maximum force. For the cases without friction, the force is close to the one without reinforcement. As expected, the free slippage of the reinforcing fibre does not modify the behaviour of the conventional textile. When introducing friction, the force does not change. An increase might be measurable with more reinforcing fibre tows. The difference between the force required with a reinforcing truss or beam element is negligible is this case.

Fig. 4.55 shows the shear angle field for the configurations without reinforcement, with ALE trusses and ALE beams as well as the slip displacement of the fibre tow modelled with ALE trusses. The shear angle field are nearly the same meaning that the reinforcing fibre tows does not modify the behaviour of the conventional textile.

Discussion It has to be noticed that the out-of-plane bending mode has not been taken into account. Adding this deformation mode might lead to the creation of wrinkles for the stiffest solution and reduce the current shear angle. Nevertheless, relaxing the no-slip condition gives results which are more realistic compared to the ones obtained previously.

Transition

The 1D ALE elements allow modelling the fibre tow slippage in TFP preforms. In particular, they have been integrated in Model I to relax the strict embedding constraint

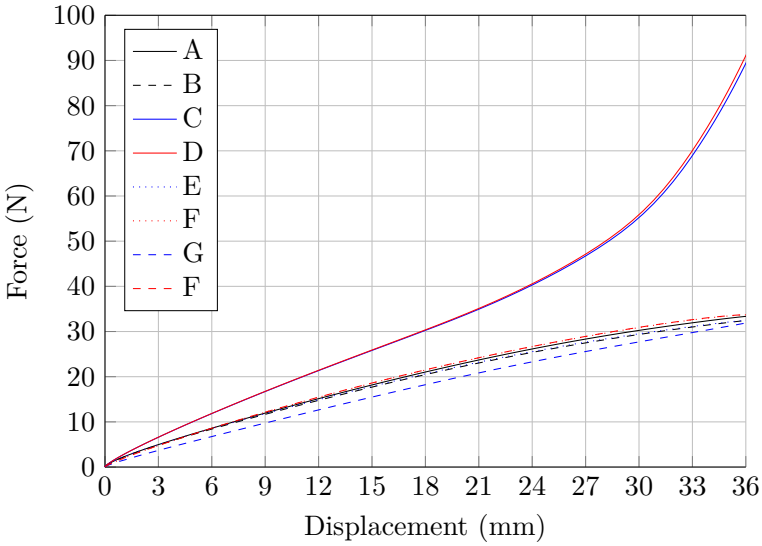

(a) Force-displacement curves for the different bias extension tests

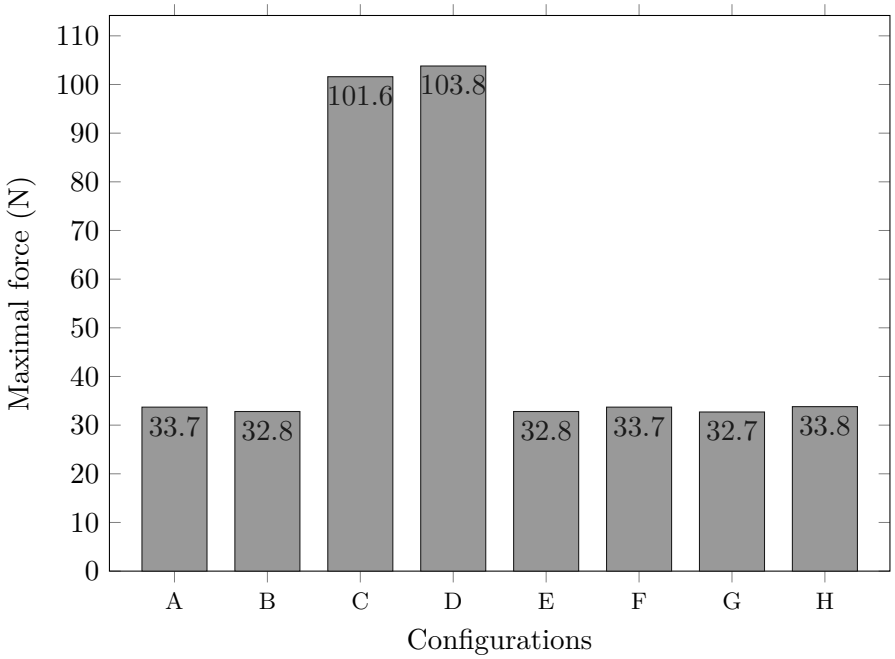

(b) Maximum force values

Figure 4.54: Result of the bias extension test with and without reinforcing fibre tows

which implied a no-slip condition between the fibre tows and the backing material. The resulting mixed embedded-ALE element formulation is very attractive to take into account fibre tow slippage when the TFP technology is used to locally reinforce another conventional textile. The next section discusses the extension of modelling strategy to model fibre slippage in conventional textiles.

4.4.2 Deploying the 1D ALE elements in conventional textile modelling

The 1D ALE elements used to enhance the TFP preform models allow modelling fibre slippage at the scale of the fibre tow without modelling explicitly the contact interactions. Moreover, complex friction laws can be implemented. This last section aims at highlighting the fact that

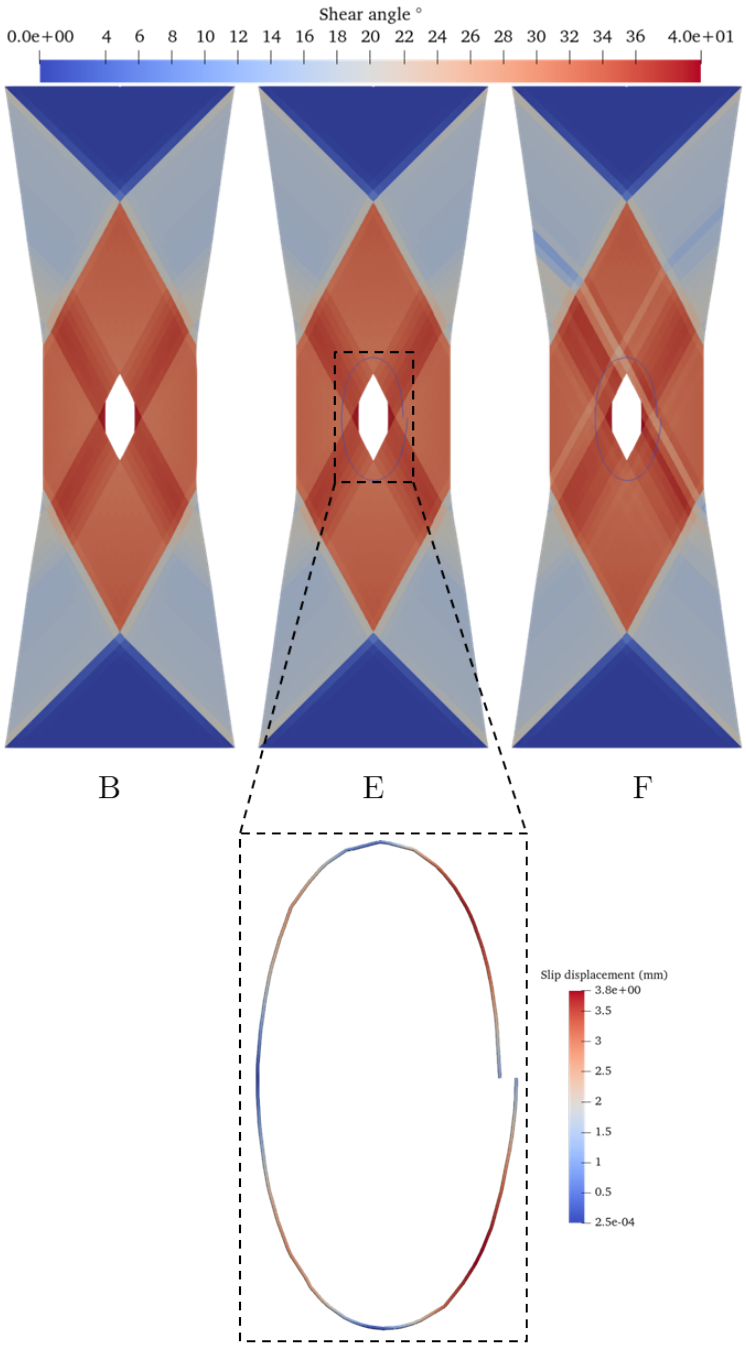

Figure 4.55: Shear angle for configuration B, E and F and slip displacement of the reinforcing fibre tows (E)

these elements could be used to model fibre slippage in conventional textiles. To this end, a model based on Model II is proposed to represent a woven fabric reinforcement. Then, a model is proposed to represent the tufting thread in tufted preforms. Numerical examples are addressed to demonstrate the potential of these models.

4.4.2.1 Modelling fibre tows slippage in woven fabrics

Objectives As mentioned in section 4.1.1.2, models of biaxial textiles taking into account the fibre slippage are mainly based on a Lagrangian description which implies modelling explicitly

the contact interactions between the fibre tows. Therefore, these models require a very fine description of the reinforcement features and are very time consuming. To the author's knowledge, only the model by Parsons et al. (2013) allows modelling fibre slippage in a continuum medium but was not used in forming applications. The model proposed here, which is based on Model II, is very similar to the latter but does not embed woven fabric unit cells in a continuum medium. Moreover, the effect of the crimp amplitude is not taken into account. A basic model is considered for demonstration but additional features can easily be added. Fibre slippage is a well-known deformation mode during bias extension test of textile reinforcement. Therefore, the demonstration is based on the simulation of this test. The areas where slippage are susceptible to happen are illustrated in Fig. 4.56.

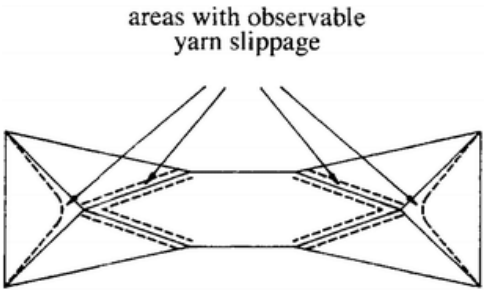

Figure 4.56: Area of observed slippage in bias extension test (Wang et al., 1998)

Finite element model A representation of the model is shown in Fig 4.57. The warp and weft fibre tows are represented using ALE beam elements. At the intersection of the warp and weft fibre tows, either the warp or weft node is embedded by the weft or warp node respectively. Contrary to Model II, both fibre tows have a node at the intersection. This allows to define the friction law at the node level rather than at the element level. However, it is possible to mesh independently the weft and warp fibre tows as in Model II. To take into account the resistance to rotation at the crossover points, non-linear torsional springs are used. The torsional moment is defined with the same law than the shear moment in the woven fabric model by Hamila et al. (2009). Therefore, the non-linear behaviour due to the lateral contact between fibre tows at high shear angles is taken into account. Since all nodes are located at crossover points, the friction law is directly applied on all nodes. A static Coulomb friction is considered for simplicity. The dependence of the friction force to the shear angle is not considered. This model is similar to the mesoscopic model by Gatouillat et al. (2013) where the shell elements are replaced by beam elements and the explicit contact interactions between the shell elements is managed by the mixed embedded-ALE formulation. Therefore, this model is supposed to considerably decrease the simulation time.

Bias extension test sample A sample of 250 mm length and 100 mm width is considered. The fibre tow density d_{tow} in each direction is set to 0.5 tow/mm. Therefore, the beam elements have a length of 2 mm. The properties of the beam elements and the torsional springs are reported in Table 4.12.

Table 4.12: Beam and torsional spring parameters

	Beam						Torsional spring		
Parameters	C_E	C_{Γ_1}	C_{Γ_2}	C_{K_1}	C_{K_2}	C_{K_3}	K_1	K_2	K_3
Values	2880	1440	1440	0.2	0.2	0.2	$6.44\ 10^{-4}$	$5.95\ 10^{-2}$	$1.07\ 10^{-1}$
Units	N	N	N	N.mm²	N.mm²	N.mm²	N.mm	N.mm	N.mm

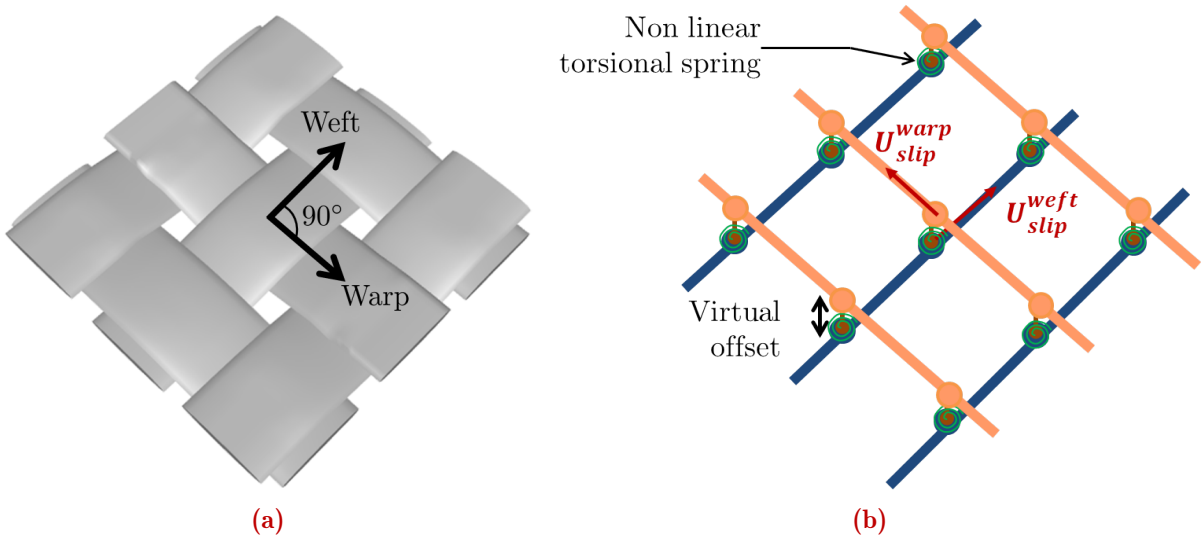

Figure 4.57: Mixed embedded-ALE beam model of woven fabric: (a) Texgen mesoscopic representation of woven fabrics, (b) corresponding finite element model

The maximal friction force before slip occurs at a crossover point is set to 0.5 N. To simplify the model, the ends of the fibre tows are not represented explicitly. The crossover points on the lateral sides of the sample corresponds to the last crossover points but the extra lengths of fibre tow are not modelled. This simplification avoids considering remeshing when a Lagrangian node (end of fibre tow) gets too close to an ALE node (crossover point). If the slip displacement at the last crossover points does not exceed the space between adjacent fibre tows, namely, 2 mm, then it will be appropriate.

Results Fig. 4.58 (a) and (b) shows the shear angle field with and without slippage. The transition layer between the three zones of constant shear are modified by the fibre slippage. Moreover, the shear angle in the central area is slightly smaller. As it is shown in Fig. 4.58 (c), the localisation of fibre slippage coincides with the observed area depicted in Fig 4.56. The maximal slippage value is 1.8 mm at the transition between the three shear zones. The fibre slippage on the sides of the central area do not exceed 1 mm. Therefore, the simplification concerning the fibre tows' ends is appropriate for this example.

Discussion The proposed modelling strategy, which takes into account fibre slippage in woven fabrics using a mixed embedded-ALE formulation, is very attractive. It considerably simplifies the modelling of the contact interactions between the fibre tows. Addressing a full-scale validation based on forming of a complex part, which is known to produce fibre slippage, would be the next step to develop this modelling strategy for biaxial textiles. However, a remeshing procedure to take into account the separation of the fibre tows would be required. To this end, the remeshing algorithm proposed by Liu et al. (2018) can be implemented.

4.4.2.2 A simplified approach to model the tufting thread in tufted preforms

Tufting principle and existing models Tufting is a through-the-thickness reinforcement technique of laminates. A thread, named tufting thread, passes totally or partially the thickness of the fibrous reinforcement layers (Fig. 4.59). The forming of such preform is strongly affected by the presence of the thread (Liu et al., 2015; Gnaba et al., 2021). A model has been proposed by Huang et al. (2021) to simulate the forming of tufted preforms and predict the creation of defects such as wrinkles. In this model, the interaction between the tufting thread and the

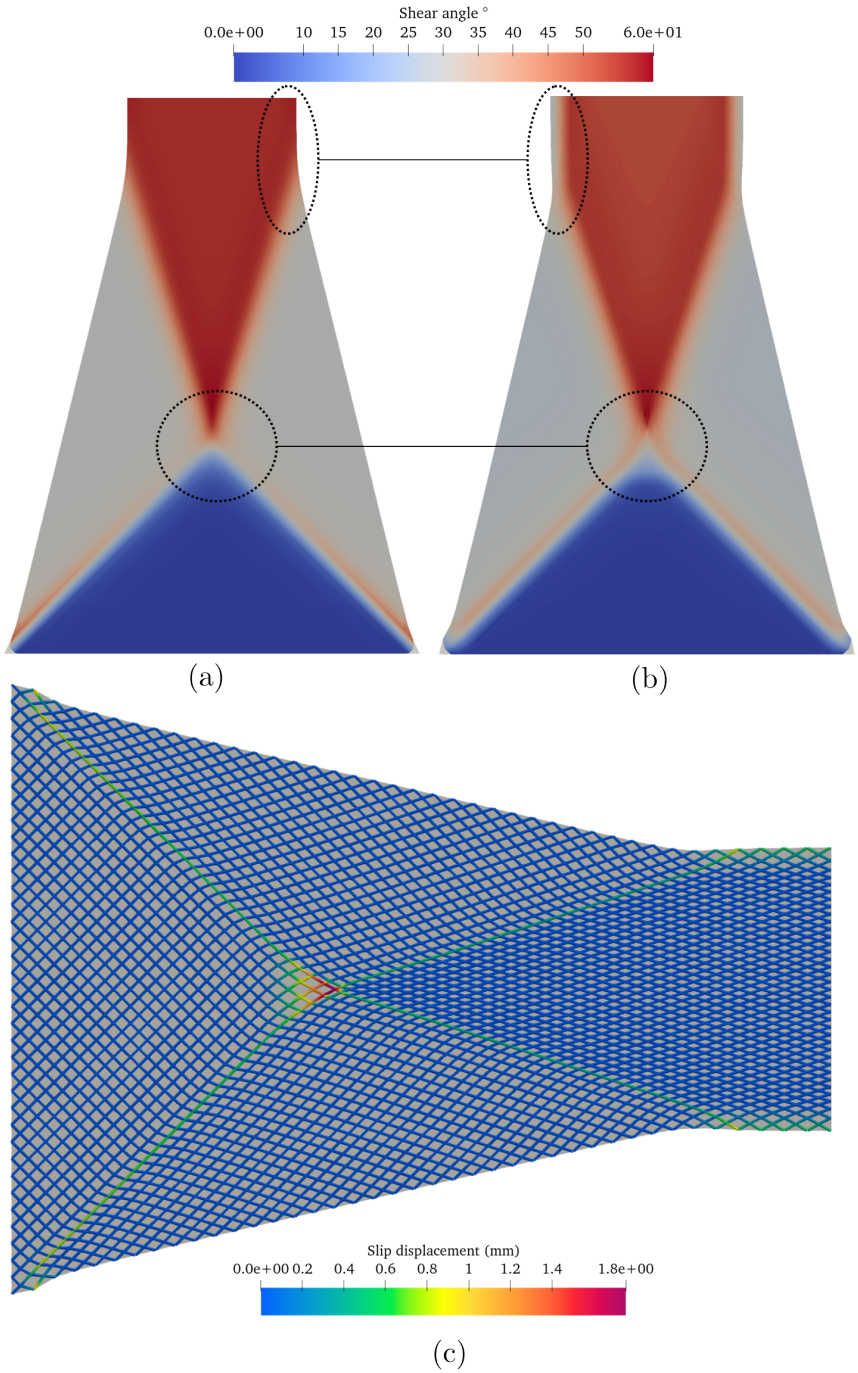

Figure 4.58: Bias extension test: Shear angle field (a) without slippage (Lagrangian beams), (b) with slippage and slip displacement field (c)

layers of reinforcement is modelled explicitly using a specific contact algorithm, which is able to model the slippage of the thread elements through the virtual holes of the layers' element as illustrated in Fig. 4.60. Two models were proposed with or without the simplification of the thread loop. The thread is modelled using 1D elements with tensile and bending stiffnesses and the fibrous reinforcement is modelled with the finite element by Hamila et al. (2009) previously used.

Due to the Lagrangian representation of the thread and the hole, a high number of elements is required to model the thread and avoid numerical instabilities due to the contact algorithm.

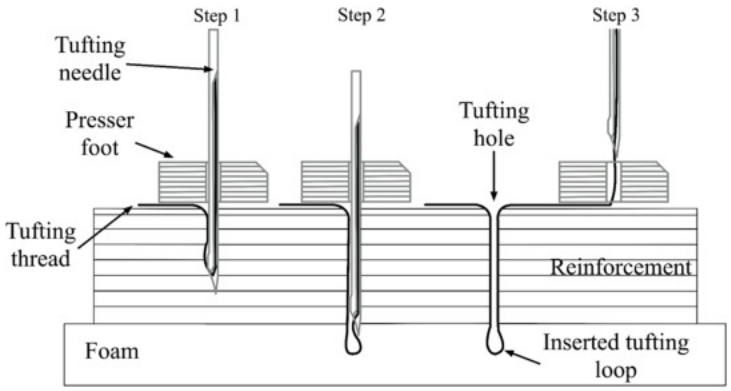

Figure 4.59: Principle of tufting (Huang et al., 2021)

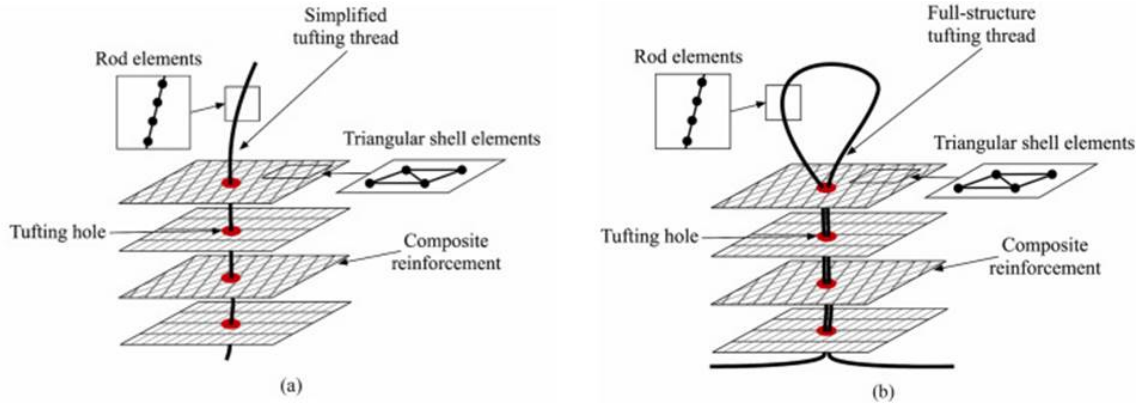

Figure 4.60: (a) Simplified model of the tufting (Model I) and (b) full-structure model of the tufting (Model II) (Huang et al., 2021)

The aim of this study is to show how the 1D ALE elements can be used to considerably simplify the model proposed by Huang et al. (2021).

Proposed models To simplify the contact interactions between the thread and the layers, the mixed embedded-ALE elements presented in this work and illustrated in Fig. 4.61 are used. The thread passing through the holes is modelled by ALE elements whose nodes are embedded in the element of the corresponding layer. Therefore, the thread material can flow through the thickness of the layers without the need of a specific and time consuming contact algorithm. A static Coulomb friction law can be considered at the nodes representing the holes. Moreover, the number of elements to discretize the thread is considerably reduced.

Elementary tests To demonstrate the feasibility of the proposed models, the two elementary tests performed by Huang et al. (2021) are addressed hereafter.

The first test concerns the tufting Model I. It consists of 4 reinforcement layers with a single tufting thread. The top and bottom layers are fixed while the middle layers are translated in the opposite direction. It results in a slippage of the tufting thread through the thickness. The initial and final configurations as well as the results by Huang et al. (2021) are shown in Fig. 4.62. They used 200 elements to model the tufting yarn. The proposed model used a single element per layer, namely, 4 elements for the whole thread.

With the proposed mixed embedded-ALE element model, one element between layers is enough. The slip dof of the node in the bottom layer is fixed (Lagrangian node). The extra length of thread on the top layer is not modelled explicitly but additional material can flow through the

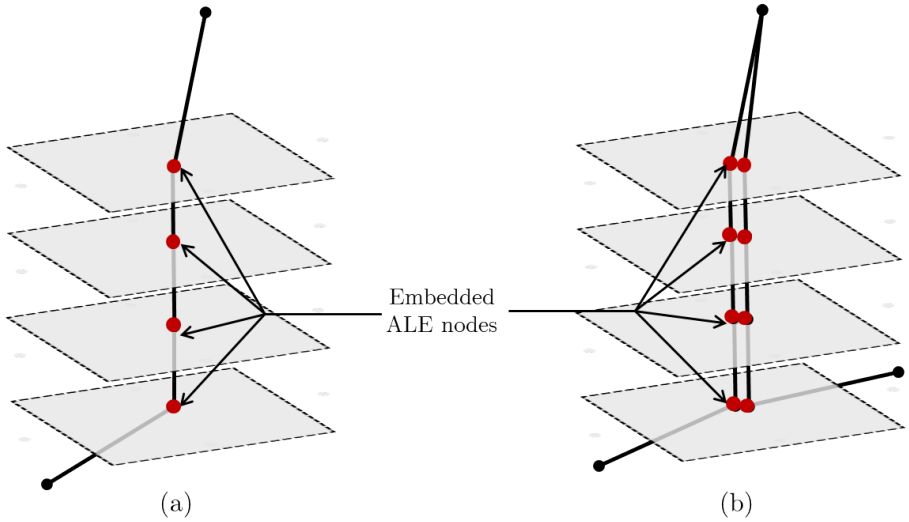

Figure 4.61: Proposed models based on mixed embedded-ALE elements: (a) Simplification of the tufting Model I and (b) tufting Model II

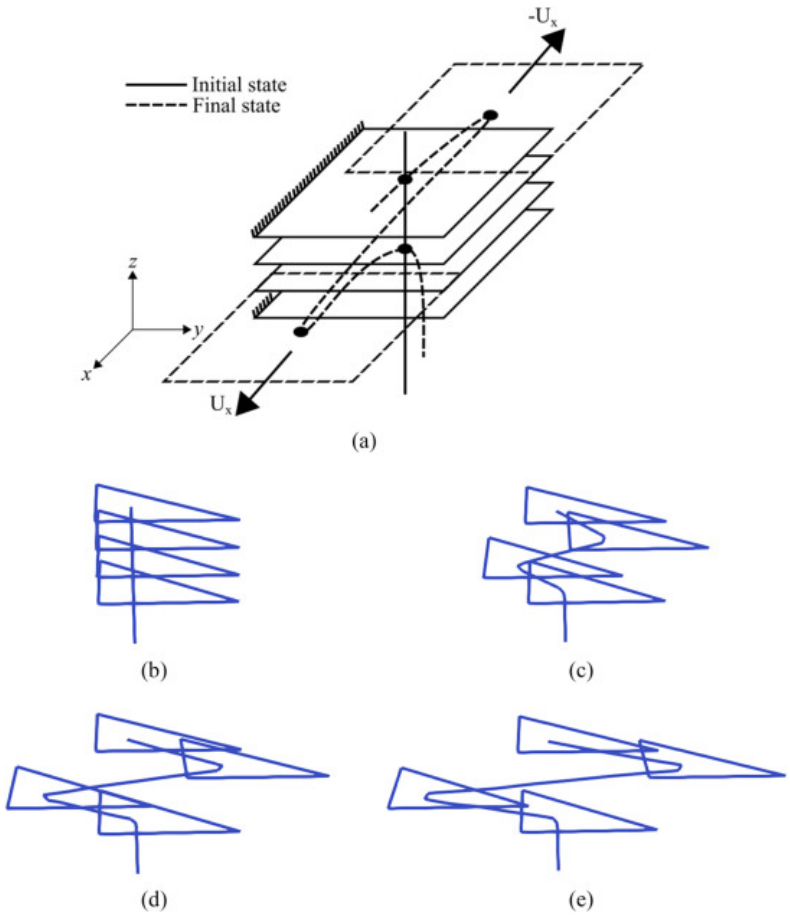

Figure 4.62: Test 1: (a) boundary condition, (b) Initial state, (c) 33% of the displacement, (d) 66% of the displacement, (e) 100% of the displacement (Huang et al., 2021)

top thread node. The result is shown in Fig 4.63. The slip displacement is linear from the bottom to the top nodes. No friction was applied. The deformation in the thread is lower than 10^{-9} which is consistent with the free slippage. Therefore, this test is validated for the proposed model.

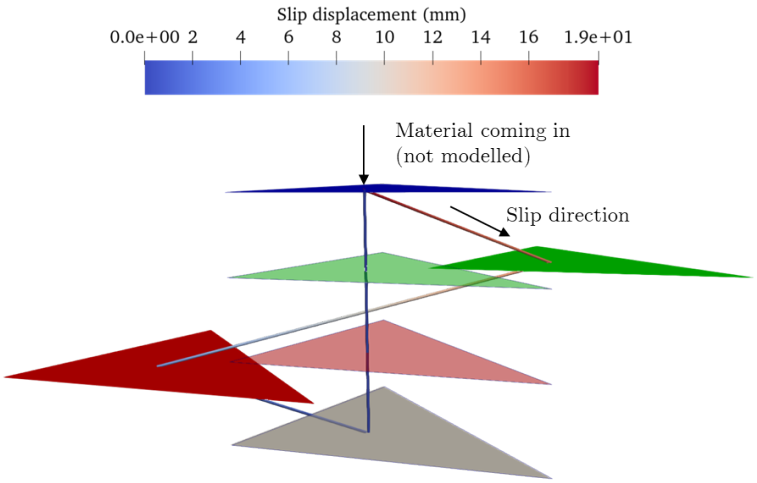

Figure 4.63: Proposed tufting Model I: Slip displacement field of the thread with initial state (light colors) and final state (dark colors)

The second test is quite similar to the first one but the thread forms a loop (Model II). The initial and final expected configurations as well as the results by Huang et al. (2021) are shown in Fig. 4.64.

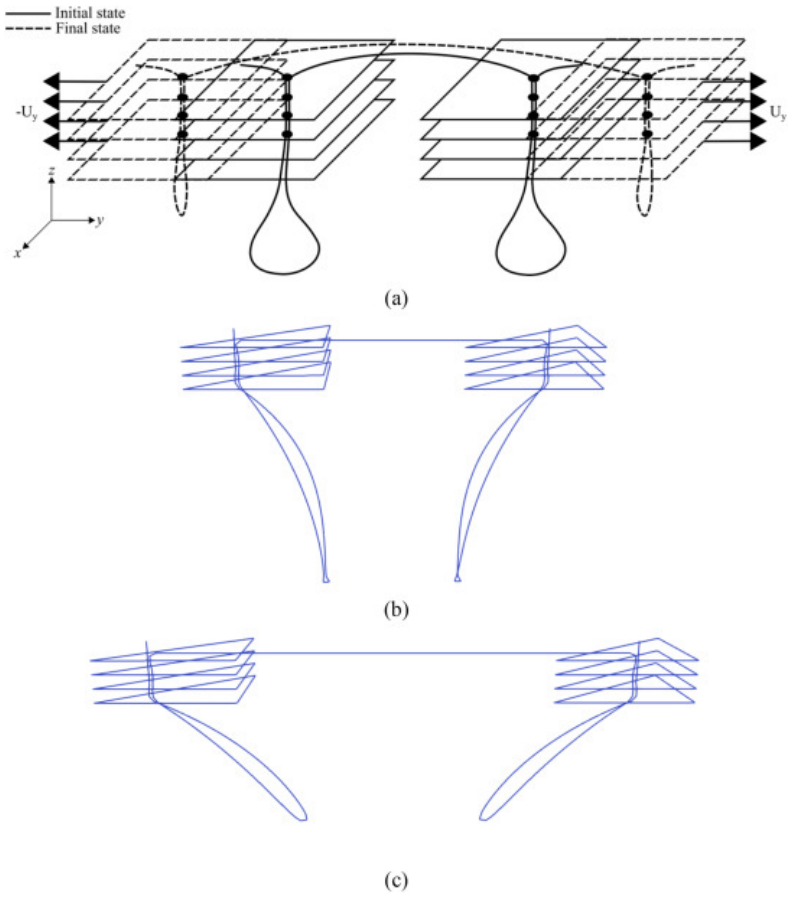

Figure 4.64: Test 2: (a) boundary condition, (b) 50% of the displacement, (c) 100% of the displacement (Huang et al., 2021)

In this second test, there is also one thread element between two layers. As shown in Fig. 4.65, the thread slip through the hole. No friction was applied but a static Coulomb friction law can be added.

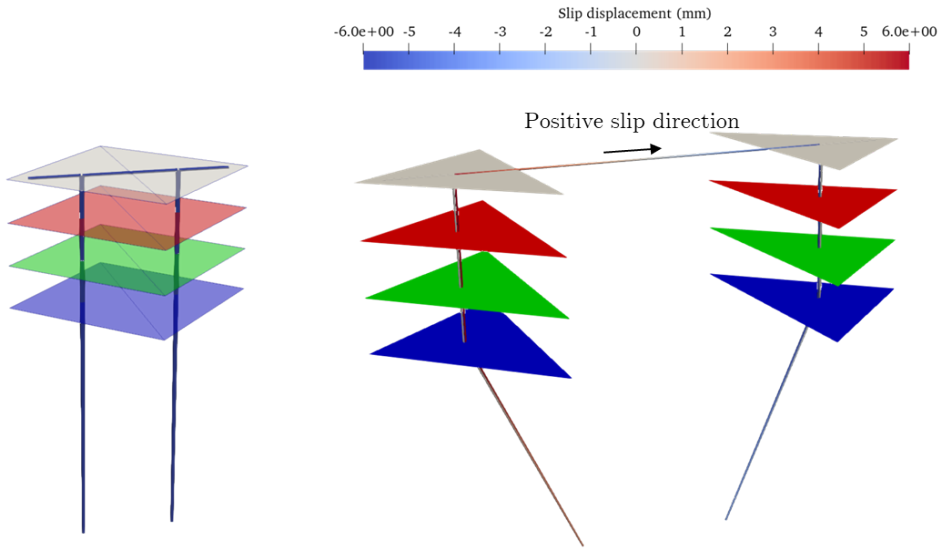

Figure 4.65: Proposed tufting Model II: Slip displacement field of the thread with initial state (light colors) and final state (dark colors)

Discussion Two elementary test cases have been addressed to show the potential of the mixed embedded-ALE elements to model the tufting thread. A next step to continue deploying this modelling strategy is to implement the deactivation of the embedding constraint of the hole nodes when the thread loop goes out of the hole. Then, full-scale validations could be addressed. The ALE truss element was used due to its simplicity. To take into account the bending rigidity of the tufting thread, the slip displacement dof can be easily added to the free-rotation 1D element used by Huang et al. (2021). If large slippage occurs, new Lagrangian nodes can be added to the tufting thread between successive layers. Node-to-surface contact is required for these additional Lagrangian nodes.

Conclusion

This section has presented the first validation of the mixed embedded-ALE element formulation to model the local reinforcement of conventional textiles with TFP. First, the pull-out experiments were successfully simulated. Next, the issue raised in section 3.4.1 concerning the very stiff behaviour of Model I has been addressed. The relaxation of the no-slip condition gives realistic results. Further full-scale validations based on forming are needed to validate the mixed embedded-ALE approach for Model I.
Moreover, this formulation can be used to model fibre slippage in conventional textiles. As a demonstration, fibre slippage in a woven fabric sample during a bias extension test has been simulated and gave consistent results. Addressing a forming simulation with this model would reveal the potential of this approach. Finally, the mixed embedded-ALE element formulation was applied to the modelling of the tufting thread in tufted preforms. Elementary tests were addressed. A full-scale forming simulation is required to demonstrate the consistency of this approach, in particular, the reduction of the computation time compared to the existing model.

Chapter conclusion

This chapter addressed the challenge of incorporating fibre slippage into the TFP models without modifying the initial ingredients introduced in Chapter 2. To this end, existing approach to model fibre slippage in conventional textile were reviewed. Among them, the use of the ALE description was deemed particularly attractive since it does not require the explicit modelling of the contact interactions. However, the model by Parsons et al. (2013) using the ALE description is only applicable to woven fabrics and uses 2D elements. Next, the ALE description was briefly introduced before presenting some modelling strategies developed for pulley-cable system applications that allow modelling material flow in 1D elements. Among them, the models by Peng et al. (2017) and Liu et al. (2018), which uses an additional dof to represent relative displacement between the mesh and the matter in truss and beam elements, have been deemed appropriate to enhance the TFP models. Consequently, both ALE truss and beam element formulations were detailed and numerical tests were addressed. These 1D ALE elements allow modelling the relative displacement between the fibre tows and the backing material while keeping the embedding constraint on the mesh of the fibre tows. To use this mixed embedded-ALE element formulation in Model I, the friction law which drives the material flow, had to be characterized. To this end, pull-out experiments have been carried out. A parametric study was performed to quantity the effect of the stitching parameters on the friction force. An analytical friction model has been proposed and its material parameters were related to the stitching parameters using a linear regression method. Finally, the pull-out experiments were simulated using the ALE elements to validate the implementation of the friction law for Model I. Next, the simulations showing the stiff behaviour of the initial Model I in the previous chapter were addressed using the mixed embedded-ALE element formulation. The relaxation of the no-slip condition gave realistic results. Therefore, the proposed mixed embedded-ALE element formulation allows facing the challenge raised at the beginning of this chapter.
Besides, the extension of this modelling strategy to model fibre slippage in conventional textiles has been addressed. In particular, fibre tow slippage in woven fabric was simulated through a bias extension test. Moreover, a solution has been proposed to more efficiently model the tufting thread in tufted preforms. Further full-scale simulations are required to validate and justify these extensions.

Bibliography

Allaoui, S., Boisse, P., Chatel, S., Hamila, N., Hivet, G., Soulat, D., and Vidal-Salle, E. (2011). Experimental and numerical analyses of textile reinforcement forming of a tetrahedral shape. *Composites Part A: Applied Science and Manufacturing*, 42(6):612–622.

Allaoui, S., Hivet, G., Soulat, D., Wendling, A., Ouagne, P., and Chatel, S. (2014). Experimental preforming of highly double curved shapes with a case corner using an interlock reinforcement. *International Journal of Material Forming*, 7(2):155–165.

Allaoui, S., Hivet, G., Wendling, A., Ouagne, P., and Soulat, D. (2012). Influence of the dry woven fabrics meso-structure on fabric/fabric contact behavior. *Journal of Composite Materials*, 46(6):627–639.

Aufaure, M. (1993). A finite element of cable passing through a pulley. *Computers & Structures*, 46(5):807–812.

Aufaure, M. (2000). A three-node cable element ensuring the continuity of the horizontal tension; a clamp–cable element. *Computers & Structures*, 74(2):243–251.

Bai, R., Li, W., Lei, Z., Ma, Y., Qin, F., Fang, Q., Chen, X., and Chen, Y. (2018). Experimental study of yarn friction slip and fabric shear deformation in yarn pull-out test. *Composites Part A: Applied Science and Manufacturing*, 107:529–535.

Bel, S., Hamila, N., Boisse, P., and Dumont, F. (2012). Finite element model for NCF composite reinforcement preforming: Importance of inter-ply sliding. *Composites Part A: Applied Science and Manufacturing*, 43(12):2269–2277.

Belytschko, T., Liu, W. K., Moran, B., and Elkhodary, K. (2013). *Nonlinear Finite Elements for Continua and Structures*. Wiley–Blackwell, Chichester, West Sussex, United Kingdon, 2nd edition edition.

Bilisik, K. and Korkmaz, M. (2011). Single and multiple yarn pull-outs on aramid woven fabric structures. *Textile Research Journal*, 81(8):847–864.

Bohler, P., Carosella, S., Goetz, C., and Middendorf, P. (2015). Path Definition for Tailored Fiber Placement Structures Using Numerical Reverse Draping Approach. *Key Engineering Materials*, 651-653:446–451.

Boisse, P., Hamila, N., Vidal-Sallé, E., and Dumont, F. (2011). Simulation of wrinkling during textile composite reinforcement forming. Influence of tensile, in-plane shear and bending stiffnesses. *Composites Science and Technology*, 71(5):683–692.

Capelle, E., Ouagne, P., Soulat, D., and Duriatti, D. (2014). Complex shape forming of flax woven fabrics: Design of specific blank-holder shapes to prevent defects. *Composites Part B: Engineering*, 62:29–36.

Chen, S., Harper, L. T., Endruweit, A., and Warrior, N. A. (2015). Formability optimisation of fabric preforms by controlling material draw-in through in-plane constraints. *Composites Part A: Applied Science and Manufacturing*, 76:10–19.

Coulibaly, J., Chanut, M.-A., Lambert, S., and Nicot, F. (2018). Sliding cable modeling: An attempt at a unified formulation. *International Journal of Solids and Structures*, 130-131:1–10.

Creech, G. and Pickett, A. K. (2006). Meso-modelling of Non-Crimp Fabric composites for coupled drape and failure analysis. *Journal of Materials Science*, 41(20):6725–6736.

Donea, J. and Huerta, A. (2003). *Finite Element Methods for Flow Problems*. John Wiley & Sons. Google-Books-ID: S4URqrTtSXoC.

Dong, Z. and Sun, C. (2009). Testing and modeling of yarn pull-out in plain woven Kevlar fabrics. *Composites Part A: Applied Science and Manufacturing*, 40(12):1863–1869.

Du, X., Du, J., Bao, H., Chen, X., Sun, G., and Wu, X. (2019). Dynamic Analysis of the Deployment for Mesh Reflector Antennas Driven With Variable Length Cables. *Journal of Computational and Nonlinear Dynamics*, 14(11).

Fial, J., Harr, M., Böhler, P., and Middendorf, P. (2018). Automated wet compression moulding of load-path optimised TFP preforms with low cycle times. *IOP Conference Series: Materials Science and Engineering*, 406:012018.

Gatouillat, S., Bareggi, A., Vidal-Sallé, E., and Boisse, P. (2013). Meso modelling for composite preform shaping – Simulation of the loss of cohesion of the woven fibre network. *Composites Part A: Applied Science and Manufacturing*, 54:135–144.

Gnaba, I., Soulat, D., Legrand, X., and Wang, P. (2021). Investigation of the formability behaviour of optimized tufted and un-tufted multi-layer carbon preforms during the stamping process. *ESAFORM 2021*.

Hamila, N., Boisse, P., Sabourin, F., and Brunet, M. (2009). A semi-discrete shell finite element for textile composite reinforcement forming simulation. *International Journal for Numerical Methods in Engineering*, 79(12):1443–1466.

Hautefeuille, A., Comas-Cardona, S., and Binetruy, C. (2019). Mechanical signature and full-field measurement of flow-induced large in-plane deformation of fibrous reinforcements in composite processing. *Composites Part A: Applied Science and Manufacturing*, 118:213–222.

Huang, J., Boisse, P., and Hamila, N. (2021). Simulation of the forming of tufted multilayer composite preforms. *Composites Part B: Engineering*, 220:108981.

Ju, F. and Choo, Y. S. (2005). Super element approach to cable passing through multiple pulleys. *International Journal of Solids and Structures*, 42(11):3533–3547.

Kan, Z., Li, F., Peng, H., Chen, B., and Song, X. (2021). Sliding cable modeling: A nonlinear complementarity function based framework. *Mechanical Systems and Signal Processing*, 146:107021.

Kan, Z., Peng, H., and Chen, B. (2019). A simple linear complementarity approach for sliding cable modeling considering friction. *Mechanical Systems and Signal Processing*, 130:293–314.

King, M. J., Jearanaisilawong, P., and Socrate, S. (2005). A continuum constitutive model for the mechanical behavior of woven fabrics. *International Journal of Solids and Structures*, 42(13):3867–3896.

Labanieh, A. R., Garnier, C., Ouagne, P., Dalverny, O., and Soulat, D. (2018). Intra-ply yarn sliding defect in hemisphere preforming of a woven preform. *Composites Part A: Applied Science and Manufacturing*, 107:432–446.

Liu, J.-P., Cheng, Z.-B., and Ren, G.-X. (2018). An Arbitrary Lagrangian Eulerian formulation of Geometrically Exact Timoshenko beam running through tube. *Acta Mechanica*, 229.

Liu, L., Zhang, T., Wang, P., Legrand, X., and Soulat, D. (2015). Influence of the tufting yarns on formability of tufted 3-Dimensional composite reinforcement. *Composites Part A: Applied Science and Manufacturing*, 78:403–411.

López-Gálvez, H., Rodriguez-Millán, M., Feito, N., and Miguelez, H. (2016). A method for inter-yarn friction coefficient calculation for plain wave of aramid fibers. *Mechanics Research Communications*, 74:52–56.

Mulvihill, D. M., Smerdova, O., and Sutcliffe, M. P. (2017). Friction of carbon fibre tows. *Composites Part A: Applied Science and Manufacturing*, 93:185–198.

Najjar, W., Pupin, C., Legrand, X., Boude, S., Soulat, D., and Dal Santo, P. (2014). Analysis of frictional behaviour of carbon dry woven reinforcement. *Journal of Reinforced Plastics and Composites*, 33(11):1037–1047.

Navarro, D. J. and Foxcroft, D. R. (2018). *Learning statistics with jamovi: a tutorial for psychology students and other beginners.* Danielle J. Navarro and David R. Foxcroft.

Parsons, E. M., King, M. J., and Socrate, S. (2013). Modeling yarn slip in woven fabric at the continuum level: Simulations of ballistic impact. *Journal of the Mechanics and Physics of Solids*, 61(1):265–292.

Parsons, E. M., Weerasooriya, T., Sarva, S., and Socrate, S. (2010). Impact of woven fabric: Experiments and mesostructure-based continuum-level simulations. *Journal of the Mechanics and Physics of Solids*, 58(11):1995–2021.

Peng, Y., Wei, Y., and Zhou, M. (2017). Efficient modeling of cable-pulley system with friction based on arbitrary-Lagrangian-Eulerian approach. *Applied Mathematics and Mechanics*, 38(12):1785–1802.

Salem, M. M., De Luycker, E., Delbe, K., Fazzini, M., and Ouagne, P. (2020). Experimental investigation of vegetal and synthetic fabrics cohesion in order to prevent the tow sliding defect via frictional and pull-out test. *Composites Part A: Applied Science and Manufacturing*, 139:106083.

Sjölander, J., Hallander, P., and Åkermo, M. (2016). Forming induced wrinkling of composite laminates: A numerical study on wrinkling mechanisms. *Composites Part A: Applied Science and Manufacturing*, 81:41–51.

Tourlonias, M. and Bueno, M.-A. (2016). Experimental simulation of friction and wear of carbon yarns during the weaving process. *Composites Part A: Applied Science and Manufacturing*, 80:228–236.

Tourlonias, M., Bueno, M.-A., Fassi, G., Aktas, I., and Wielhorski, Y. (2019). Influence of friction angle between carbon single fibres and tows: Experimental analysis and analytical model. *Composites Part A: Applied Science and Manufacturing*, 124:105478.

Wang, J., Page, J. R., and Paton, R. (1998). Experimental investigation of the draping properties of reinforcement fabrics. *Composites Science and Technology*, 58(2):229–237.

Zhang, Q.-b., Zhang, G.-b., Feng, Z.-w., and Chen, Q.-q. (2019). Finite Element Formulation for Modelling a Frictional Sliding Cable Element. In *Proceedings of the 2019 International Conference on Modeling, Analysis, Simulation Technologies and Applications (MASTA 2019)*, Hangzhou, China. Atlantis Press.

Zhou, B., Accorsi, M., and Leonard, J. (2004). Finite element formulation for modeling sliding cable elements. *Computers & Structures*, 82(2-3):271–280.

Zhou, Y., Ali, M., Gong, X., and Yang, D. (2019). An overview of yarn pull-out behavior of woven fabrics. *Textile Research Journal*, 89(2):223–234.

Zhu, B., Yu, T. X., Zhang, H., and Tao, X. M. (2011a). Experimental investigation of formability of commingled woven composite preform in stamping operation. *Composites Part B: Engineering*, 42(2):289–295.

Zhu, D., Soranakom, C., Mobasher, B., and Rajan, S. (2011b). Experimental study and modeling of single yarn pull-out behavior of kevlar® 49 fabric. *Composites Part A: Applied Science and Manufacturing*, 42(7):868–879.

Conclusions and Perspectives

Conclusions

Hybridization of the TFP technology with forming is an attractive solution to manufacture 3D shell-like composite parts with optimized mechanical properties. However, to the author's knowledge, a numerical tool to simulate the forming of TFP preform is still missing.

The overall objective of this thesis was to propose a first modelling strategy to predict the final fibre orientations in the part obtained by forming of flat TFP preforms.

Chapter 1 provided the necessary background to understand the key features of forming as well as the challenges associated with the numerical modelling of fibrous reinforcement. Numerical and experimental aspects concerning conventional textiles were presented as an introduction as they have been widely studied. This review of conventional textiles forming underlined the limits of these fibrous reinforcements in manufacturing optimised 3D shell-like composite parts. As a remedy, technologies based on fibre-steering were introduced. In particular, the TFP technology, which is the technology this thesis is concerned with, was detailed. A review of the literature highlighted both the capabilities and the potential of this technology as well as the missing tools whose development is required to fully take advantage of the TFP technology in combination with forming. This chapter ended with the objectives and the outline of the thesis.

Fig. 4.66 is the graphical abstract of the work achieved in this thesis illustrating the content of each chapter summed up hereafter.

In **Chapter 2**, two numerical models have been proposed to represent TFP preforms with (Model I) and without backing material (Model II) respectively. These models are based on the explicit discretisation of the fibre tows to capture directly the fibre orientation changes. The stitching yarn, which ensures the cohesion between the fibre tows and the backing material in Model I, or between adjacent layers in Model II, was modelled implicitly through the use of an embedded element formulation. In Model I, the 1D elements representing the fibre tows are embedded in the backing material modelled with 2D elements. In Model II, the 1D elements representing the fibre tows of a layer are embedded within those of the previous layer. The embedded element formulation assumes no-slip between the constituents of the TFP preforms. The formulation, implementation and elementary numerical testing of the models' features was presented.

Chapter 3 addressed the full-scale validation of Model II. To this end, the numerical and experimental forming of complex doubly-curved parts from flat TFP preforms without backing material was achieved. A hemisphere shape, which is a well-known case study, and a tetrahedral shape, which has a direct industrial application, were selected. To validate Model II and at the same time demonstrate the potential of this hybrid solution, specific flat TFP patterns were designed to obtained orthotropic parts. The numerical and experimental results are in good agreement and nearly orthotropic parts are obtained which validated Model II. Concerning Model I, numerical simulations carried out to investigate the local reinforcement of a conventional textiles using TFP showed an unrealistic stiff behaviour, which was attributed to the

no-slip condition.

Chapter 4 proposed a solution to the issue raised concerning Model I. It addressed the challenge of introducing fibre slippage in the TFP preform models developed in **Chapter 2** without modifying their initial ingredients. To this end, modelling of fibre slippage in conventional textiles was firstly reviewed. The ALE description was deemed a suitable approach to include fibre slippage. Based on the literature concerning the modelling of pulley-cable systems, ALE truss and beam elements taking into account material flow were formulated, implemented and numerically tested. Next, the friction law to be implemented in the enhanced Model I was determined using pull-out experiments. A parametric study was performed to characterise the effect of the stitching parameters on the friction force required to extract the fibre tows from the TFP preform. This friction law was implemented in the ALE elements and the pull-out experiments were simulated accurately. The mixed embedded-ALE formulation was used in Model I to demonstrate the benefits of introducing fibre tow slippage. The very stiff behaviour observed in the simulations of **Chapter 2** was eliminated. Finally, the extension of the mixed embedded-ALE formulation to the modelling of fibre slippage in woven fabrics and of the tufting thread in tufted preforms was introduced.

Perspectives and future works

This work proposes a first numerical tool to model the forming of TFP preforms. It offers the possibility to model TFP preforms with or without backing material. The mixed embedded-ALE formulation allows to consider the local reinforcement of any type of 2D-like backing material such as conventional textiles. Predicting the forming of TFP preforms allows to check the manufacturability of a given part for a given flat TFP design. However, to fully exploit the TFP technology, determining the flat TFP design from the targeted 3D part, known as flattening, is also desirable. With this numerical forming tool in hands, it is possible to develop a flattening tool whose results can be checked numerically by forming. Moreover, if the development of a direct flattening algorithm is not possible, an iterative approach combining successive flattening and forming with fibre orientation corrections can be achieved. The following points could serve as interesting next steps in continuation of the achievements of this thesis:

- Addressing the full-scale validation of the mixed embedded-ALE formulation for Model I and study its extension to Model II for cases where fibre tow slippage can increase the preform formability.
- Improving the proposed TFP preform models. This could implies to use non-linear torsional springs to model the stitching yarn contribution at fibre tow intersections and add the lateral contact interactions between the fibre tows within the same layer. Moreover, a beam element with deformable cross-section could be used. For thick TFP preforms, enrichment of the embedded formulation to take into account the through-the-thickness offset would be required.
- As demonstrated, the mixed embedded-ALE formulation can be used to model fibre slippage in woven fabrics or the tufting thread in tufted preforms. Addressing full-scale simulations would allow to confirm the suitability of these models.
- Developing a numerical flattening tool to determine the flat TFP design from the targeted 3D parts has to be addressed to fully take advantage of the TFP technology. The numerical forming tool develop in this work can either be used to numerically validate the flattening tool or as part of the flattening algorithm in an iterative minimisation approach.

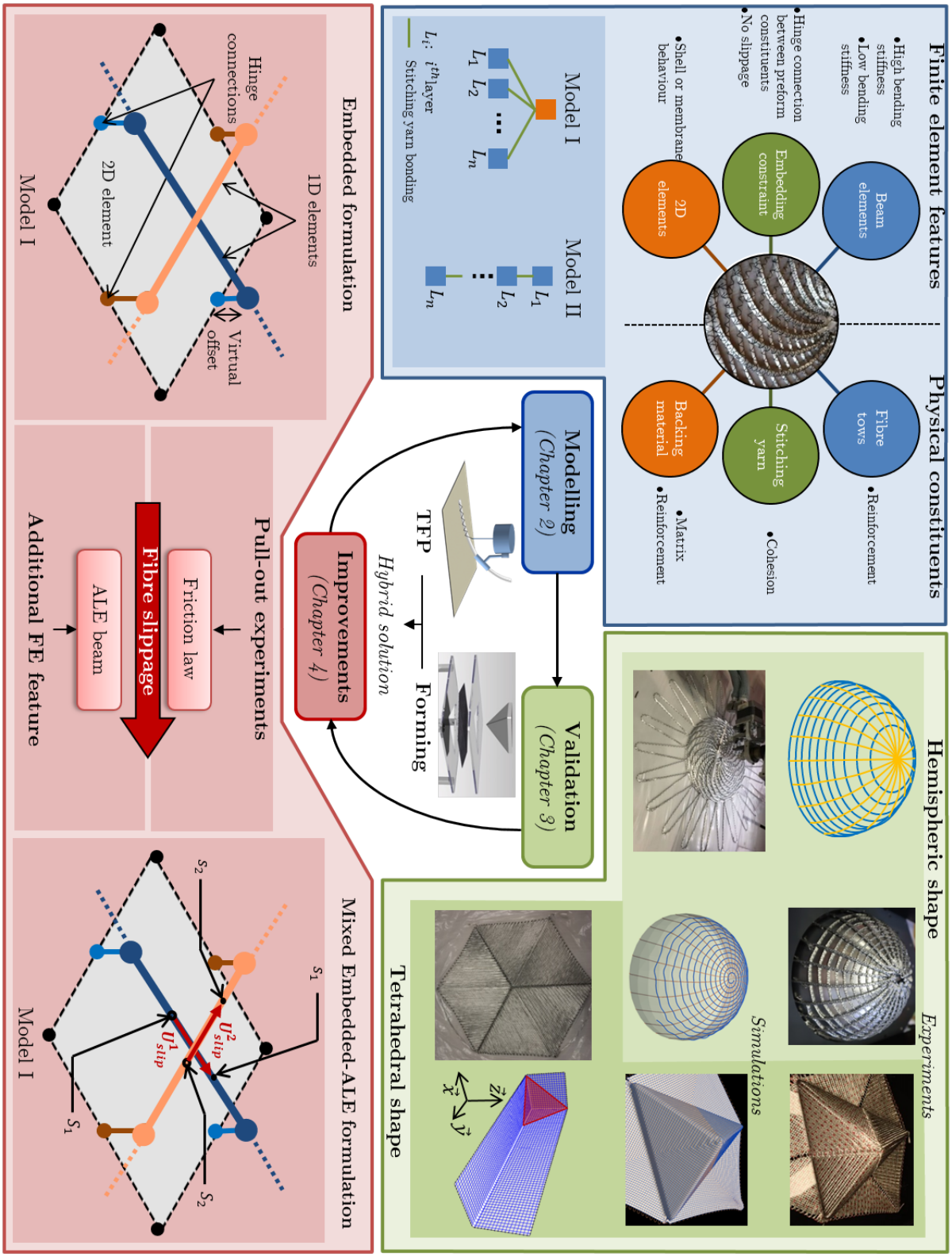

Figure 4.66: Graphical abstract of the thesis

CENTRALE NANTES

Titre : Simulation numérique et investigation expérimentale du formage de préformes fabriquées par la technologie tailored fibre placement : une formulation mixte élément fini embarqué-ALE

Mots clés : Tailored Fibre Placement, Formage, Eléments finis, Méthode ALE

Résumé : La technologie Tailored Fibre Placement (TFP) permet de fabriquer des préformes fibreuses planes à orientation et épaisseur continûment variables. L'hybridation du TFP et du formage est une solution attractive pour produire des pièces composites 3D optimisées. Au cours du formage de pièces complexes, les changements de trajectoires curvilignes des fibres sont inévitables. La prédiction de l'état final de la préforme TFP est nécessaire pour utiliser pleinement le potentiel de cette solution hybride dans le monde industriel.

Une première approche de modélisation est proposée pour simuler le formage de préformes TFP. Deux modèles semi-discrets basés sur des éléments finis embarqués sont développés pour représenter des préformes avec et sans matériau support. Dans ces deux modèles, les mèches de fibres sont représentées explicitement avec des éléments finis de poutre et le glissement entre les constituants de la préforme est d'abord négligé.

La validation du modèle sans matériau support est réalisée au travers du formage sur des poinçons hémisphérique et tétraédrique avec obtention d'orientations orthotropes.

Finalement, une formulation mixte d'éléments embarqués ALE (Lagrangienne-Eulérienne Arbitraire) est proposée pour introduire le glissement des mèches sans modifier les ingrédients initiaux des modèles. Une étude paramétrique expérimentale d'extraction de mèches est menée pour caractériser le comportement en friction à implémenter dans les modèles. La validation de cette stratégie de modélisation pour le TFP est réalisée et son extension pour le renforcement local des textiles conventionnels est abordée.

Title : Numerical simulation and experimental investigation of the forming of tailored fibre placement preforms: a mixed embedded-ALE finite element formulation

Keywords : Tailored Fibre Placement, Forming, Finite elements, ALE method

Abstract: Tailored Fibre Placement (TFP) allows manufacturing flat, net shape fibrous reinforcements with continuously varying orientation and thickness. The hybridisation of TFP and forming is an attractive solution to manufacture mechanically optimized 3D shell-like composite parts. During the forming of complex parts, inevitable fibre path changes occur in the TFP preform. Prediction of the final state of TFP preforms is required to take full advantage of this hybrid solution in the industry.

A first numerical modelling strategy is proposed to address the forming of flat TFP preforms. Two semi-discrete models based on an embedded formulation are developed to offer the possibility of removing or keeping the backing material. Both finite element models use an explicit discretisation of the fibre tows using beam elements and assumes no slippage between the preform constituents.

Full-scale validations of the model without backing material are successfully addressed by forming hemispherical and tetrahedral parts with final orthotropic orientations.

Finally, a mixed embedded element-ALE (Arbitrary Lagrangian Eulerian) formulation is proposed to introduce fibre slippage into the models without modifying their initial ingredients. A parametric study of pull-out experiments is performed to characterize the friction behaviour to be implemented in the models. Numerical validations for TFP preforms and an extension to model fibre slippage in conventional textiles are proposed.